HORIZONTAL RECEIVER AZIMUTH ORIENTATION ESTIMATES AND POSTSTACK INVERSION

by

Jacquelyn Daves

A thesis submitted to the Faculty and the Board of Trustees of the Colorado School of Mines in partial fulfillment of the requirements for the degree of Master of Science (Geophysics).

Golden, Colorado

Date _____

Signed: _____

Jacquelyn Daves

Signed: _____

Dr. Jim Simmons

Thesis Advisor

Golden, Colorado

Date _____

Signed: _____

Dr. John Bradford

Professor and Head

Department of Geophysics

ABSTRACT

The oil and gas industry is inherently volatile, and as a result, industry downturns force companies to become more efficient. Companies that adapt and successfully control operating costs, while maximizing reserves, survive these downturns relatively unscathed. Unconventional reservoir plays can be prolific hydrocarbon producers, but require hydraulic fracturing to enhance production. These reservoirs are generally complex, heterogeneous, and reservoir characterization becomes extremely difficult, yet is critical for success. Utilizing time-lapse (4-D), nine-component (9-C) seismic data to characterize these reservoirs can aid recovery. My 4-D, 9-C datasets are from the Wattenberg Field, Colorado, USA, and the reservoir targets are chalk formations within the Niobrara Formation and the Codell member of the Carlile Formation.

I performed a post stack sparse-layer inversion that appears to resolve the chalk benches within the Niobrara Formation. These results are compared to published regional sequence stratigraphic framework. In addition, this inversion was performed in a time-lapse sense to monitor how the reservoir has changed after two years of production. These time lapse results correlate well with microseismic events and modeled hydraulic fracture conductivity. There is an overall increase in time lapse-change in the North-Western portion of the section that correlates with higher production.

Analysis and interpretations of seismic data are critical to successful reservoir characterization, but when there are dataset issues (pertaining to acquisition and/or processing) this leads to incorrect interpretations. In addition to the post stack inversion, I expose errors in the H_1 orientation for the Monitor 1 survey (acquired immediately post-hydraulic fracturing) that are consistent enough to produce coherent converted-wave (C-wave), and shear-wave (S-wave), reflection signal on the crossterms after rotation to radial-transverse coordinates. I then utilize two scanning methods to estimate the H_1 azimuth orientation for each receiver

gather. All three surveys were then re-rotated into radial-transverse coordinates with the appropriate H_1 orientation azimuths.

TABLE OF CONTENTS

ACKNOWLEDGMENTS

To my Grandmothers who have shown me how to be both strong and soft.

CHAPTER 1

INTRODUCTION

The Wattenberg Project has been the primary focus of the Reservoir Characterization Project (RCP) research consortium at the Colorado School of Mines since the fall of 2013. This is an integrated effort between Petroleum Engineering, Economics, Geology and Geophysics and a collaborative effort with Anadarko Petroleum Corporation (APC). The objective of this research is to conduct dynamic reservoir characterization to further understand how to increase the recovery factor in the Niobrara Shale Reservoir, Wattenberg, Colorado. This project study area is located in Weld County, approximately 35 miles North of Denver, Colorado (Figure 1.1). The development of recommended workflows that utilize time-lapse (4-D) multicomponent seismic data is a critical factor of this project's objective and a topic of this thesis.

4-D, nine-component (9-C) seismic data have the ability to characterize fracture networks, stress changes, and to potentially increase the hydrocarbon recovery factor from unconventional reservoirs (Riazi and Clarkson, 2017; Farfour and Yoon, 2016). Potential value added from 4-D 9-C data lies in the ability to detect spatial and temporal changes in the induced fractures within the reservoir from shear-wave (SS or S-wave) and converted-wave (PS or C-wave) splitting, Amplitude-Versus-Azimuth (AVAZ) analyses, and Velocity-Versus-Azimuth (VVAZ) analyses. In addition, time-lapse compressional-wave (PP or P-wave), C-wave and S-wave azimuthal travel time analysis of full azimuth and offset data is a good monitoring tool of stress field and fracture variance.

In this project, the unmigrated, fully processed P-wave, C-wave and S-wave gathers from the Turkey Shoot surveys were sorted into Common Offset, Common Azimuth (COCA) volumes to assess the travel time variance within the reservoir. The preliminary analysis shed light on issues with the Monitor 1 shear-wave data. The S-wave crossterms (**RT**, and

1

TR) and the C-wave crossterm (**T**) for this survey appeared as scaled down versions of the principal components, where this energy could not be attributed to anisotropy. Initially, the scaled down energy, or cross-component leakage, was attributed to surface conditions present during acquisition.

This thesis identifies the anomalous S-wave and C-wave reflections (cross-component leakage) on the time-lapse 9-C seismic, exposes and determines the cause of the anomalous signal, recreates this signal with prestack modeling, then estimates corrections to properly rotate the prestack data into radial-transverse coordinates. Standard 9-C and 3 component (3-C) multicomponent data processing steps are proposed. The corrected data are then compared to the original field data.

The second portion of this thesis details a thin-bed reflectivity inversion approach for reservoir characterization. For controls, both a well data derived synthetic and a simple wedge model are run through both a thin-bed reflectivity inversion and a post stack model based inversion. Results of the synthetic inversions area analyzed. Once confidence in the inversion is established, the inversion is performed on field data, both in a static and dynamic sense. The static inversion is related to geology, and the dynamic inversion results are interpreted with regard to hydrocarbon production.

I begin with a general literature review regarding multicomponent receiver orientation and post stack seismic inversion. I then summarize data availability and details of the study area, provide an overview of the geology, and background theory necessary for this thesis. Chapters 2 and 3 discuss the multicomponent receiver orientation, while Chapters 4 and 5 detail the thin-bed reflectivity inversion.

1.1   Literature Review

The first main topic discussed in this thesis is multicomponent receiver rotations. Although P-wave energy has been the dominant component in exploration seismology, the use of both vertically and horizontally polarized sources and multicomponent receivers has become more common (Tatham and McCormack, 1991). The radial-transverse coordinate system is

Figure 1.1: The Wattenberg Field location is shown within the green colored shade. The area specific to this study is in the southern part of the Wattenberg Field (RCP, 2017).

essential for processing and interpretation of multicomponent data (Gaiser, 1999). Simmons and Backus (2001a) also illustrate the important concepts of the radial-transverse coordinate system and its application in detecting shear-wave splitting. Grossman and Couzens (2012) present a case of improper rotations leading to misinterpretations and suggest an automated receiver rotation. Additional rotation methods are discussed in Gaiser (2003), Nagarajappa et al. (2013) and, Burch et al. (2005).

The second topic in this thesis is a P-wave post stack thin-bed reflectivity inversion. Direct inversion comes in many forms: direct inversion for impedance (Turin, 1957), recursive trace integration (Lindseth, 1979), layer stripping (Goupillaud, 1961; Robinson, 1978), among others. The most commonly used inversion within RCP is a model based inversion (Cooke and Schneider, 1983; Russell and Hampson, 1991), which has been used as Utley (2017), Copley (2018), Harryandi (2017), White (2015), MacFarlane (2014), among others. The thin-bed reflectivity inversion (which does not require an initial model) attempts to estimate bed thickness and reflectivity in the frequency domain and has been popular among Puryear and Castagna (2008), Portniaguine and Castagna (2004, 2005), Chopra et al. (2006), and others. This type of inversion has also been conducted in the time domain and has been published by Simmons and Backus (1994), Simmons and Backus (1996), Zhang and Castagna

(2011), Chen et al. (2001), and others.

1.2 Data Availability

Data provided by APC and RCP includes: microseismic, well logs, cores, tracer data, DFIT, completion data, production data, and a time-lapse 9-C seismic data that includes one baseline survey and two monitors (Figure 1.2). The 4-D, 9-C surveys were acquired over the Wishbone section after drilling of 11 horizontal wells (Baseline), immediately after completion and hydraulic fracturing (Monitor 1), and after two years of production (Monitor 2) (Figure 1.3). Each survey was acquired with a single layout of 3-C geophones. Horizontal-receiver H_1 was oriented at a nominal azimuth of $H_1 = 0°$ (North), which paralleled the receiver lines. Compass headings were recorded for the horizontal vibrators, S_1 and S_2, at each shotpoint location. C-wave and S-wave data were processed in radial-transverse coordinates assuming $H_1 = 0°$, and using the measured S_1 azimuth (with S_2 perpendicular) for the S-wave source data (Gaiser, 1999; Simmons and Backus, 2001b).

The crossterms were not migrated, thus, the premigrated fully processed gathers were used for the multicomponent analysis. The migrated P-wave data were inputs into the thin-bed reflectivity inversion. Data processing of the three surveys was done commercially and followed a standard 4-D time-processing flow shown in Figure 1.4.

The horizontal wells trend North-South semi-perpendicular to the local maximum stress direction of N70°W. A schematic cross section showing the idealized horizontal well placement is shown in Figure 1.5. Each well is numbered by the chronological order of drilling. Well spacing is variable. Average depth separation between the Niobrara C chalk and the Codell sandstone is 150 feet. Lateral extent of each of the wells is a little over 1 mile, with 337 stages completed in the section. 10 horizontal wells were stimulated using sliding sleeve and 1 horizontal well was stimulated using a plug-n-perf system. Three wells (7N, 8C, and 9N) in the section were completed with a zipper fracture. The zipper fracture process fractures adjacent wells in a sequence which allows one well to hold fracture pressure while the adjacent well is hydraulically fractured. Every well was hydraulically fractured using cross-
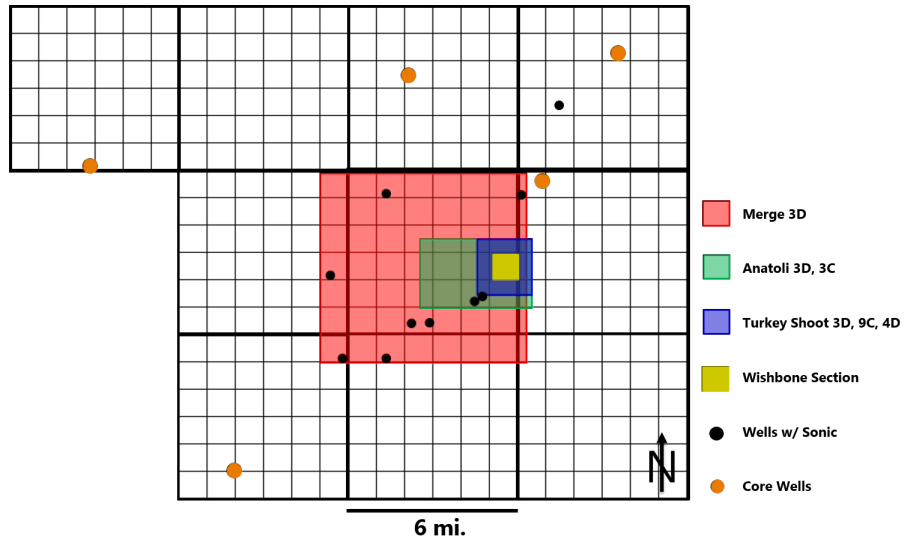
Figure 1.2: Map view of data availability (RCP, 2017).
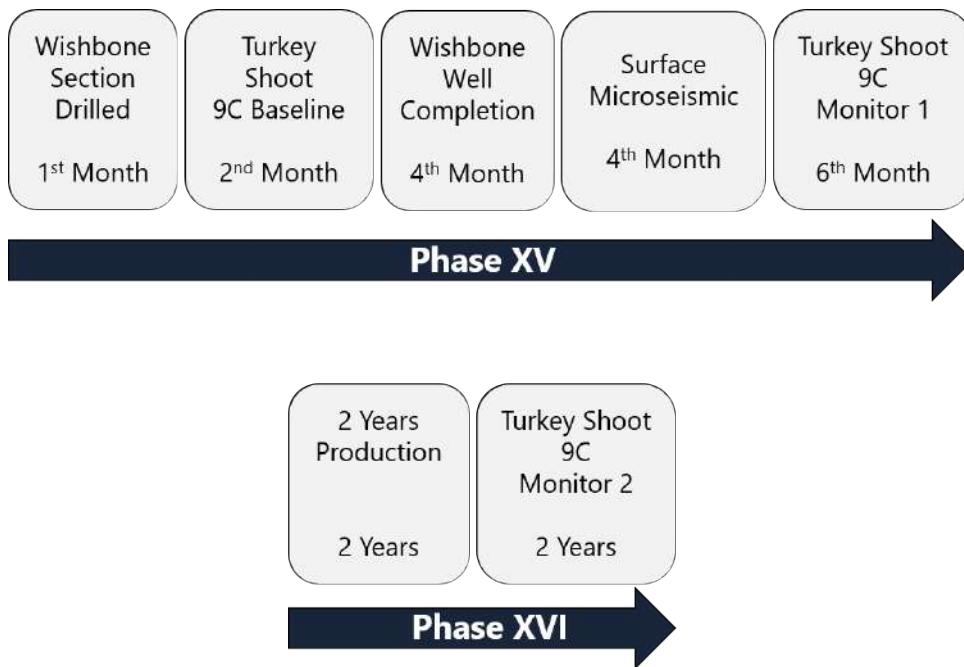
Figure 1.3: Timeline of data acquisition (RCP, 2017).

link gel in the first five stages, on average, and slickwater for the remaining stages in the well. The wells were hydraulically fractured and stimulated from East to West. In summary, there is large variability in well placement and fracture treatment.

P-wave	S-wave	C-wave
Layered refraction statics	Shear source orientation analysis	Geophone orientation analysis
Surface consistent deconvolution	Rotation into radial/transverse	Rotation into radial/transverse
Surface consistent residual statics	Layered shear refraction statics	P-wave refraction statics for source
3D noise removal	Surface consistent deconvolution	S-wave refraction statics for receiver
Surface consistent repeatability	Surface consistent residual statics	Surface consistent deconvolution
Differencing analysis	3D noise removal	Surface consistent residual statics
PreStack Kirchhoff Time Migration	Surface consistent repeatability	3D noise removal
	Differencing analysis	Surface consistent repeatability
	Primary shear modes PreStack Kirchhoff Time Migration	Differencing analysis
		Primary shear modes PreStack Kirchhoff Time Migration

Figure 1.4: Processing sequence for all components

1.3 Geologic Overview

Before any seismic interpretation it is extremely critical to understand the data limitations. It is equally important to understand the basic geologic history before interpretation. This section will provide a basic overview of the geologic history of the Wattenberg field and specifics within our study area.

The Wattenberg Field is the most prolific portion of the larger Denver Julesberg (DJ) Basin. Encompassing 70,000 square miles, the DJ Basin is bounded on the west by the Colorado Rocky Mountains and extends to Wyoming, Nebraska and Kansas. This basin is an asymmetric foreland basin that is steeply dipping to the west and gently dipping to the east (Figure 1.6) (Higley, Debra K and Cox, 2007). Reaching an approximate area of 1600 square miles, the Wattenberg Field has been in production since the 1970s. Early conventional development focused on gas production within the Lower Cretacous D and J Sandstone (shown in Figure 1.7 at depths 7600-7800ft). As production progressed in the Wattenberg

6
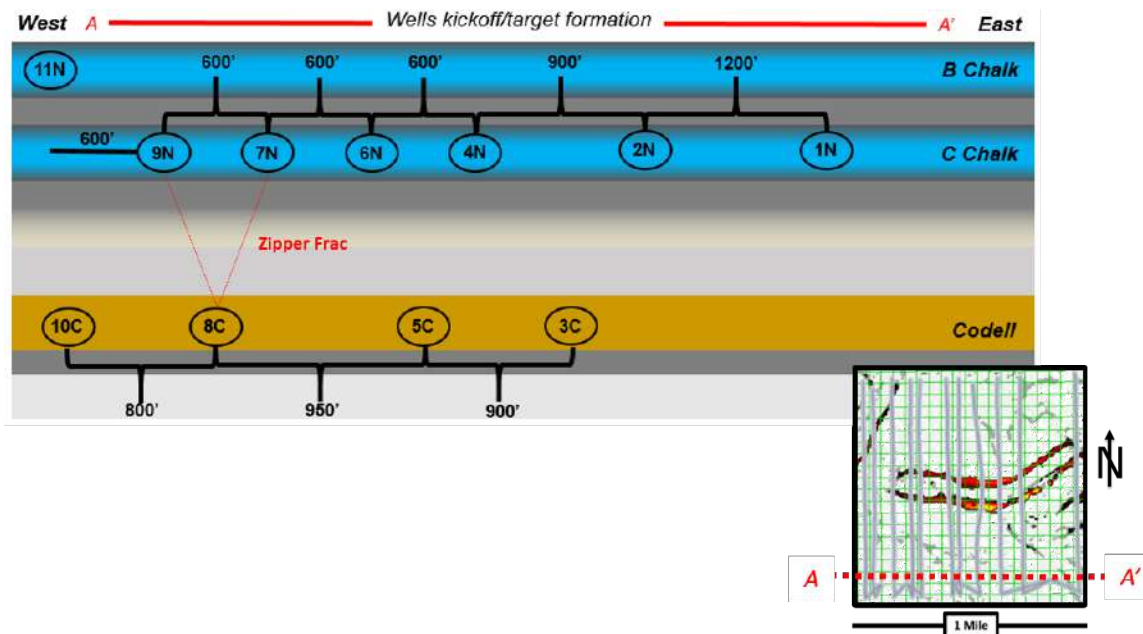
Figure 1.5: Cross section view through A-A' providing relative well locations. Notice the variability in well placement both spatially and in depth. A zipper fracture was conducted with wells 9N, 8C and 7N.

Field, it was realized that the field had multiple pay intervals increasing the reserves. As unconventional development took flight, the focus shifted to the Niobrara Formation and Codell Sandstone of the Carlile Formation (shown in Figure 1.7 at depths 6800-7100ft and colored blue in Figure 1.6). These reservoirs are considered unconventional due to their low matrix porosity and permeability and require hydraulic stimulation for production.

Both the Niobrara Formation and the Codell Sandstone were deposited in the Western Interior Cretaceous (WIC) Seaway (Figure 1.8). This was an asymmetric foreland seaway that extended from the Arctic to the Gulf of Mexico. The Niobrara Formation was deposited during higher sea level conditions which resulted in coccolith-rich carbonate sediment (Smith, 2015; Sonnenberg, 2013). The sea level and climate was in constant fluctuation during this depositional period. During times of transgression, warmer gulf currents deposited cocolith-rich carbonate chalks and during regression cooler currents from the north deposited anoxic marls (Figure 1.9). This formation is composed of inter-bedded chalks and marls and ranges in total thickness from 200-400ft with the individual benches ranging 30-50ft. Although

7

difficult to interpret on well logs, the chalks can be identified with higher resistivity, lower gamma ray and higher permeability and porosity.

The Codell Sandstone was regionally deposited in low stand conditions in the Eastern portion of the WIC seaway. The sandstone is a hummocky, cross-stratified, bioturbated, clay-rich siltstone that was deposited in the eastern portion of the seaway and is age equivalent to the Eagle Ford Shale. On well logs the gamma ray appears as a dirty sand/shale, the resistivity ranges from 4-6 ohmms, porosity ranges from 12-16% and permeability is usually greater than 0.01 mD (Smith, 2015).
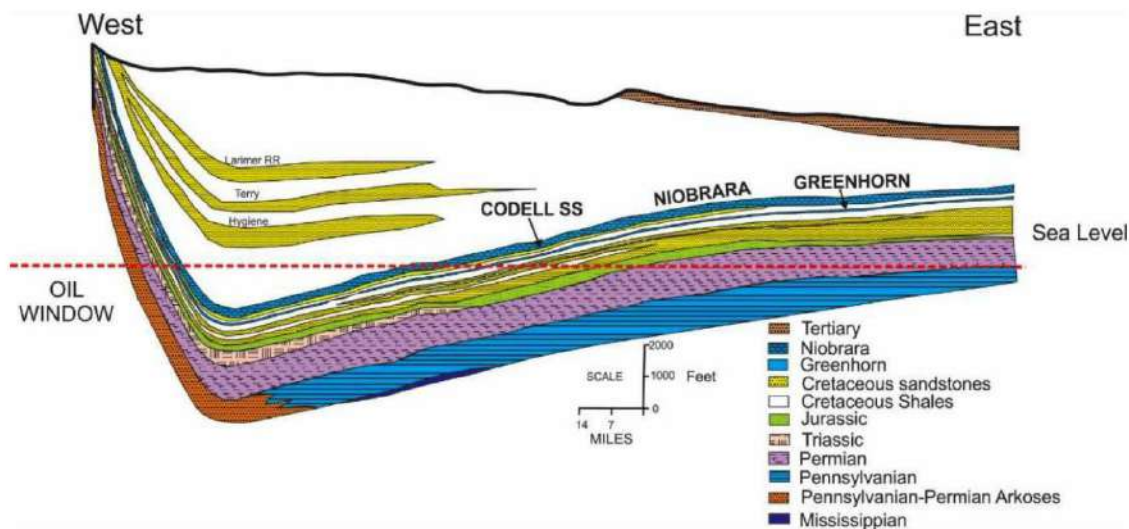
Figure 1.6: West to east cross section through the DJ Basin (Sonnenberg, 2013).

The tectonics responsible for the formation of the DJ Basin begin with subsidence from the WIC Seaway and the deposition of the Fountain Formation in the Late Pennsylvanian. The Laramide Orogeny (67.5-50 Ma) was a period of compression resulting in basement involved, right lateral wrench faulting that run Southwest-Northeast (Sonnenberg, 2013). Associated with the wrench fault zones are high concentrations of normal faults. During the mid-Tertiary, a period of extension caused the previously compressed basin to adjust. The extensional stresses formed a series of grabens. Figure 1.10 shows a fault map over the Wishbone section, the two parallel faults in the middle of the section is referred to as the
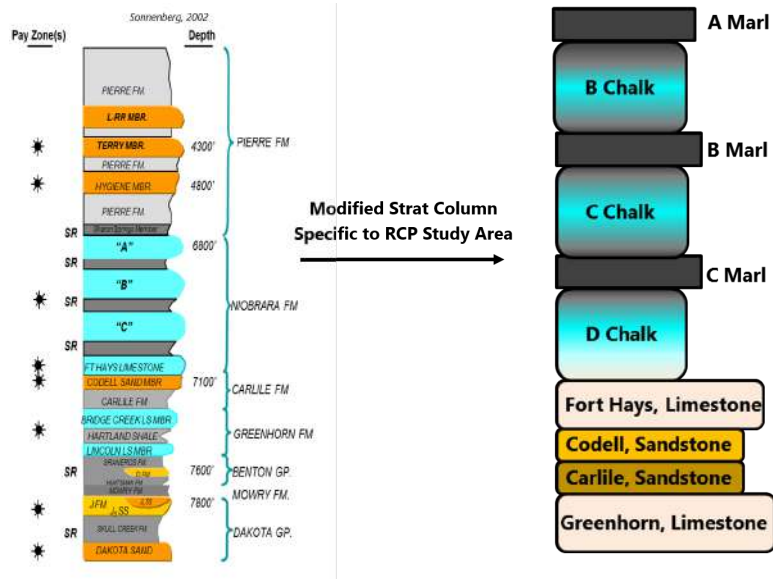
Figure 1.7: Generalized stratigraphic column of the DJ Basin and the modified stratigraphic column modified to represent the geology within the study area (Sonnenberg, 2007; RCP, 2017).

Figure 1.8: Paleo-geographic map of the Late Cretaceous illustrating the WIS from the present day Artic Ocean to the Gulf of Mexico (Blakey, 2014).
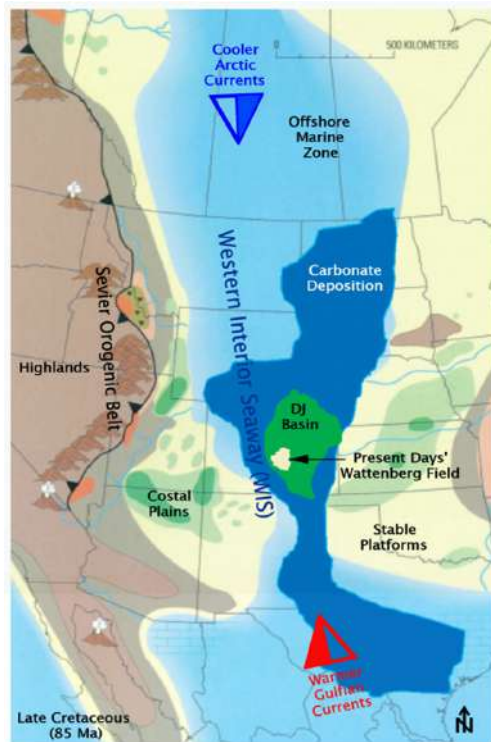
Figure 1.9: Map of the deposition of the Late Creteceous Niobrara showing warmer gulf currents from the South and cooler Arctic currents from the North (Locklair and Sageman, 2008; Hettinger and Kirschbaum, 2002).
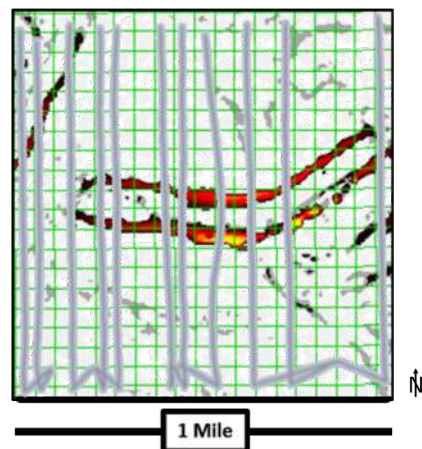
Figure 1.10: Top Niobrara fault map over the Wishbone section. The graben in the middle of the section is refered to as the central graben.

central graben.

The World Stress Map from 2008 suggests that within the Wattenberg field the modern day stress direction is around N20°W (Grechishnikova, 2017). Specifically within the RCP study area, Dudley (2015) conducted a local maximum stress analysis (Figure 1.11). Dudley analyzed fracture image (FMI) logs from three different horizontal wells within the Wishbone section and determined that the local average maximum horizontal stress direction is N68°W. The fractures within the Codell Sandstone were oriented N65°W and within the two Niobrara wells Dudley (2015) identified the dominant fracture orientations: 1) N60°W and N90°W within one well and 2) N50°E and N80°W in the other. Within the Niobrara wells there was no visual difference in fracture intensity between the chalk and marl benches, although it was determined that the Niobrara had a lower fracture count than the Codell Sandstone (Dudley, 2015).
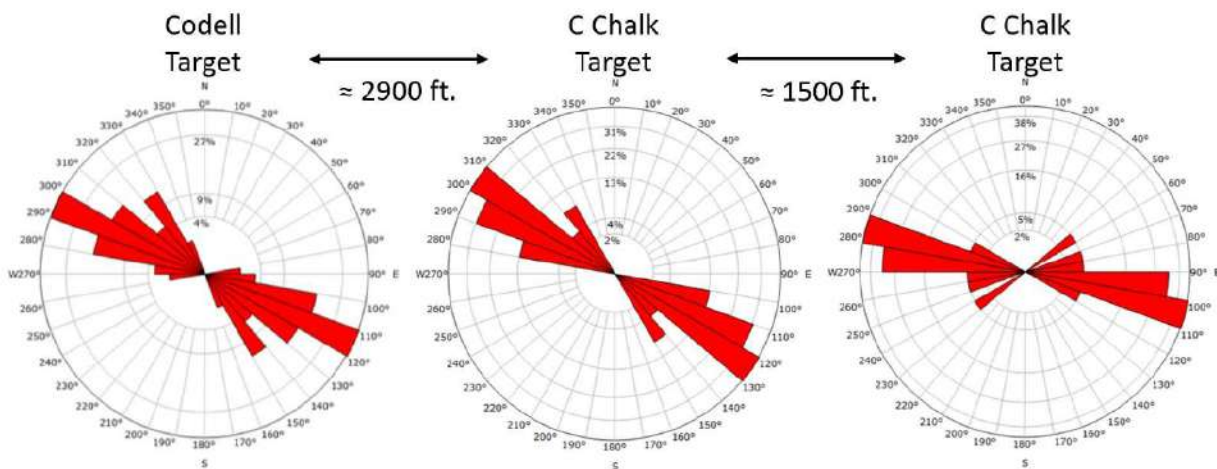
Figure 1.11: Maximum horizontal stress directions average at N68°W - derived from FMI log interpretations from three horizontal wells (one targeting the Codell formation and two targeting the Niobraray C chalk interval). The wells strike NS. (modified from Dudley, 2015).

1.4 Background Information

This section details the basics needed to understand the work presented in this thesis. These topics include acquisition of 9-C data, the purpose and generation of COCA gathers,

and the process of developing the Wattenberg synthetic model.

Acquisition of 9-C multicomponent data utilizes both vertical and horizontal sources and 3-C receivers (two horizontal components and one vertical). P-wave data acquisition utilizes a vertical source that generates particle motion parallel to the direction of wave propagation. For pure P-wave data, the particle motion is observed on the vertical and horizontal receiver components. The distribution of P-waves on the vertical and horizontal receivers is dependent upon the angle of emergence at the receiver. The P-wave dataset used for processing and analysis is taken from the vertical receiver component only. I make use of the fact that P-waves are recorded on the horizontal receivers for the horizontal-receiver azimuth orientation in Chapters 2 and 3.

Converted-wave (PS or C-wave) data are generated with a vertical source and the particle motion is observed on the horizontal components. C-waves recorded on the vertical receiver, again due to a non-vertical emergent angle, are neglected. C-wave reflections are generated by an incident (down traveling) P-wave reflecting as an SV-wave and observed on the radial component ($\mathbf{R}$) as the radial direction is inline with the source-receiver azimuth. The transverse component $\mathbf{T}$ is oriented orthogonal to $\mathbf{R}$, and is used as a diagnostic indicator of shear-wave splitting when non-zero.

Two orthogonal, horizontal sources generate particle motion perpendicular to the direction of wave propagation during S-wave data acquisition. Data acquired in field coordinates are rotated to radial-transverse coordinates for processing and analysis. The radial-source radial-receiver component is denoted as $\mathbf{RR}$ and is a proxy for SV-waves, while the transverse-source transverse-receiver $\mathbf{TT}$ is a proxy for SH-waves (Omar, 2018). Cross-terms $\mathbf{RT}$ (radial-source transverse-receiver) and $\mathbf{TR}$ (transverse-source radial-receiver) are indicators of shear-wave splitting when non-zero. Note that ideally $\mathbf{RT} = \mathbf{TR}$ in the presence of split shear-waves.

In a purely isotropic world, energy will only be observed on the principle components $\mathbf{R}$, $\mathbf{RR}$ and $\mathbf{TT}$. Conversely, energy observed on the crossterm components $\mathbf{T}$, $\mathbf{RT}$ and $\mathbf{TR}$ is

indicative of shear-wave splitting and anisotropy.

COCA gathers allow for azimuthal information preservation and the visualization of anisotropy (Gray, 2007). COCA gathers are built by binning prestack data primarily by CMP super gather location (with a large binning radius) with offset as the secondary sorting key. Different from the common-offset stack, the tertiary sorting key is azimuth (Figure 1.12).
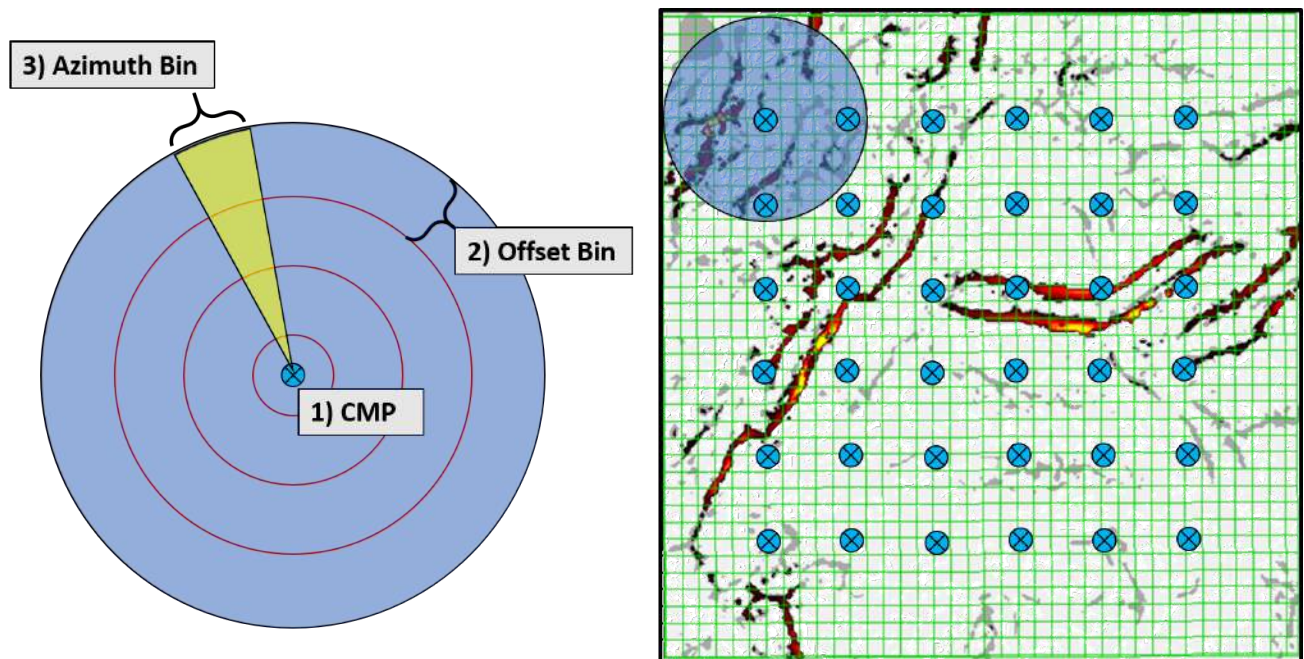
Figure 1.12: The basemap at the right shows a number of COCA super gather locations (blue). The backdrop shows the faults on the top Niobrara level. COCA gathers are formed by sorting the data within each binning radius by offset plane (secondary) and azimuth bin (tertiary).

Created by Todd, 2018, the Wattenberg synthetic model included input from all 10 vertical wells within the Turkey Shoot survey. Density and sonic logs were used to derive P-impedance. The derived P-impedance and seismically derived horizons were used to populate the model (the interpolation method was a weighted average), Figure Payson 1.13 is the result. To convert the model to time a velocity model was built. Once the model is populated in time it was converted into reflection coefficients and convolved with a zero-phase 30hz Ricker wavelet.
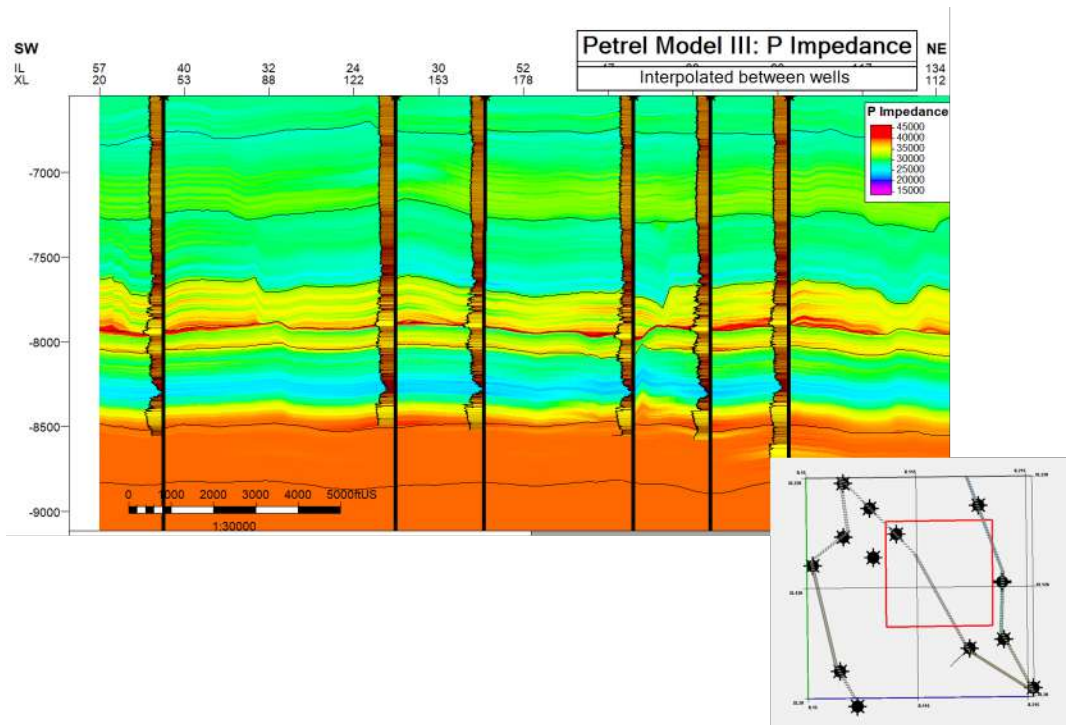
Figure 1.13: Wattenberg Synethic Model - cross section through the Turkey Shoot survey. Star represent well locations, the black line is the cross section. The red box indicates where the Wishbone section is located (Todd, 2018)

SHEAR-WAVE REFLECTION-SIGNAL LEAKAGE IDENTIFICATION

2.1 Summary

Shear-wave (S-wave) and Converted-wave (C-wave) COCA gathers are used to expose, and interpret, anomalous reflection signal on the Monitor 1 data. Reflections on the *cross-components*, typically used as a diagnostic of shear-wave splitting when reflection energy exists, are seen in the overburden above the Niobrara interval where the hydraulic fracturing occurred. S-wave COCA gathers show apparent S-wave reflections that are unrealistic, and unrelated to anisotropy. C-wave COCA gathers pinpoint the cross-component leakage as a global error in the nominal azimuth of the horizontal receiver H_1 during data acquisition ($\phi_{H1} \approx 10°$, rather than $\phi_{H1} = 0°$ as assumed in the rotation to radial-transverse coordinates).

Synthetic S-wave and C-wave COCA gathers qualitatively model the cross-component leakage caused by $\phi_{H1} = 10°$, which confirms the hypothesis derived from the interpretation of Monitor 1 COCA gathers. Evidence that the leakage is caused by a global error in the nominal azimuth orientation of H_1 became obvious only from examination of the C-wave transverse **T** component. C-waves only require a receiver rotation, thus, a global error in the nominal H_1 orientation will not cancel in the COCA gathers, and the leakage will exist throughout the dataset.

The global H_1 azimuthal error during data acquisition is likely due to confusion between true north, $\phi_{H1} = 0°$, and magnetic north $\phi_{H1} = 8°$ (or $\phi_{H1} = $ N8°E).

2.2 Basics

Simple synthetic examples illustrate the principles of particle motion involved in the P-wave first-arrival, and C-wave reflection methods for estimating the H_1 azimuthal field orientation. A basemap of nine shotpoints (blue) and one receiver (green) is shown in Figure

2.1a. Shots are located at the same relative offset from the receiver and are separated by 20° azimuth increments from Shotpoint A to Shotpoint B. Horizontal receivers are oriented North (N) and East (E) as shown in green.

Seismograms recorded on the N and E receivers from each shotpoint are shown in Figure 2.1b. Simple convolutional modeling generates the seismograms, and the source-receiver azimuth determines the distribution of energy onto the horizontal receiver components. The polarity convention for particle motion is positive to the North and East. For example, shotpoint A located due North of the receiver generates a P-wave traveling South, thus, the polarity is negative (red trough). Shotpoint B, which is almost due South of the receiver, produces particle motion on the N component to the North, thus, the waveform is positive polarity.

These concepts are applicable to both the P-wave first arrival and C-wave reflection methods for horizontal-receiver orientation. For the first-arrival and C-wave reflection methods, the data are presumed to be direct P-wave arrivals and C-wave (P-SV) reflections, respectively. Both types of events are assumed to have particle motion in the sagittal plane (the vertical-radial plane between source and receiver) as shown in Figure 2.1b.

The data in Figure 2.1b are not easily interpretable due to the azimuth-dependent signal distribution onto the $N = H_1$ and $E = H_2$ receivers. Rotating the horizontal receivers H_1 and H_2 into radial-transverse coordinates (**R**=Radial,**T**=Transverse) is essential for multicomponent processing and interpretation as the azimuthal dependence of the source-receiver orientation is removed (Gaiser, 1999). Azimuthal rotation to $R - T$ coordinates (ϕ_{ROT}^R) requires knowledge of the source-receiver azimuth (ϕ_{SR}) and the azimuth of the H_1 receiver (ϕ_{H1}) (H_2 is orthogonal). ϕ_{SR} is calculated from the source and receiver locations. Generally, an attempt is made to orient ϕ_{H1} parallel to the receiver-line layout prior to data acquisition.

Three simple examples of the R-T rotation are shown in Figure 2.2 using Equations 2.1 and 2.2. The source is depicted as the black circle, the red and blue arrows are H_1 and H_2, respectively. The green and purple arrows indicate ϕ_{SR} for receivers 2 and 3, respectively.

Rotation from H_1 - H_2 coordinates to R-T coordinates is given mathematically as

$$\begin{bmatrix} R \\ T \end{bmatrix} = \begin{bmatrix} \cos(\phi_{ROT}^R) & \sin(\phi_{ROT}^R) \\ -\sin(\phi_{ROT}^R) & \cos(\phi_{ROT}^R) \end{bmatrix} \begin{bmatrix} H_1 \\ H_2 \end{bmatrix} \tag{2.1}$$

where

$$\phi_{ROT}^R = \phi_{SR} \text{ - } \phi_{H1}. \tag{2.2}$$

where ϕ_{SR} is the source-receiver azimuth, and ϕ_{H1} is the azimuth of the H_1 receiver ($\phi_{H1} = 0°$ for this example).

S-wave data consist of the horizontal receivers H_1 and H_2 recorded from each of the two horizontal vibrators (S_1 and S_2) as S_1H_1, S_1H_2, S_2H_1, and S_2H_2. These data are rotated to radial-transverse coordinates (Simmons and Backus, 2001b) as

$$\begin{bmatrix} RR & RT \\ TR & TT \end{bmatrix} = \begin{bmatrix} \cos(\phi_{ROT}^R) & \sin(\phi_{ROT}^R) \\ -\sin(\phi_{ROT}^R) & \cos(\phi_{ROT}^R) \end{bmatrix} \begin{bmatrix} S_1H_1 & S_1H_2 \\ S_2H_1 & S_2H_2 \end{bmatrix} \begin{bmatrix} \cos(\phi_{ROT}^S) & -\sin(\phi_{ROT}^S) \\ \sin(\phi_{ROT}^S) & \cos(\phi_{ROT}^S) \end{bmatrix} \tag{2.3}$$

with

$$\phi_{ROT}^S = \phi_{SR} - \phi_{S1}. \tag{2.4}$$

The S-wave data in radial-transverse coordinates are **RR**. **RT**, **TR**, and **TT** where **RR** is defined as radial source - radial receiver, **RT** as radial source - transverse receiver, etc. Note that the azimuth orientation of source S_1 (ϕ_{S1}) is required, and it is assumed that $S_2 \perp S_1$. Shear-waves in radial-transverse coordinates are examined later.

Now I consider the C-wave problem of Figure 2.2. Every H_1 receiver is oriented North, thus, $\phi_{H1} = 0°$ for all receivers. The parameter that varies for each receiver is ϕ_{SR}, as the source-receiver azimuth changes per location. For receiver 1, $\phi_{SR} = 0°$ and from Equation 2.2, $\phi_{ROT}^R = 0°$. Moving clockwise, $\phi_{SR} = 45°$ for receiver 2. In this case, as Equation 2.2 shows, $\phi_{ROT}^R = 45° - 0°$. For receiver 3, $\phi_{SR} = 90°$, and consequently $\phi_{ROT}^R = 90°$.

17
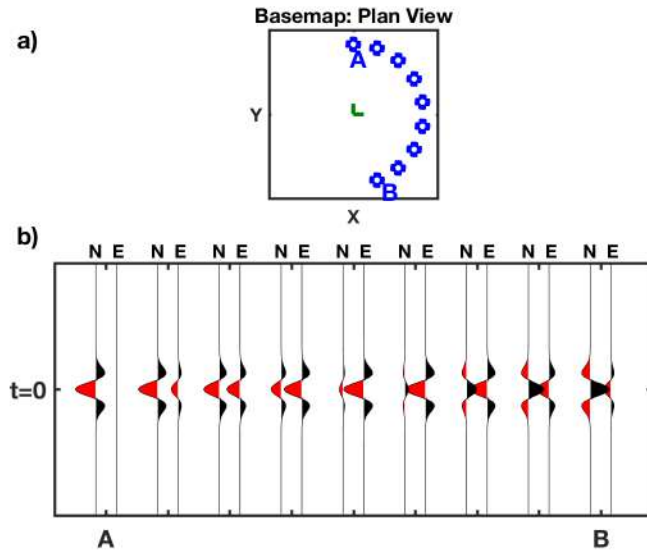
Figure 2.1: Illustration of P-wave (and/or C-wave) particle motion as recorded on horizontal receivers as a function of source-receiver azimuth. a) Basemap with horizontal receivers oriented North and East at the center of the map in green. Shotpoints are shown in blue, and are spaced at 20° azimuth increments from shotpoint A to shotpoint B. b) Data recorded on the North (N) and East (E) oriented receivers for each shotpoint. The inherent assumption is that the wave arriving at the receiver from each shotpoint propagates in the sagittal plane (vertical plane containing source and receiver).
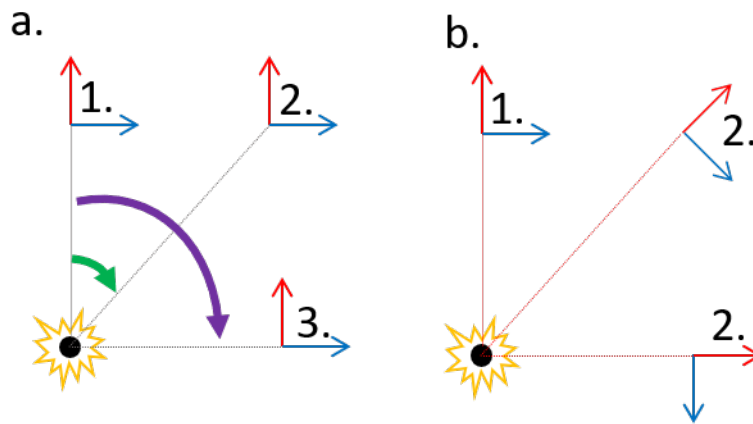
Figure 2.2: Schematic illustration of the rotation of the horizontal-receiver components from a) North (N) and East (E) to b) Radial (R) and Transverse (T). This figure depicts a basemap in plan view of a shotpoint (black circle) and three receivers (1, 2, and 3). Radial-Transverse rotation needs the source-receiver azimuth as determined from the (x,y) locations, and the field azimuth of the North receiver (the East receiver is orthogonal). The radial component (red arrow in b) is oriented away from the shot along the source-receiver azimuth, with the transverse component perpendicular in the clockwise direction.

Data recorded from the shotpoints in Figure 2.1a are shown again in Figure 2.3 with the radial-transverse data below (Figure 2.3b). These data are rotated using Equation 2.1 with $\phi_{H1} = 0°$, and the appropriate ϕ_{SR} for each shotpoint. All data are now contained on **R** for all shotpoints (azimuths), with **T**=0.
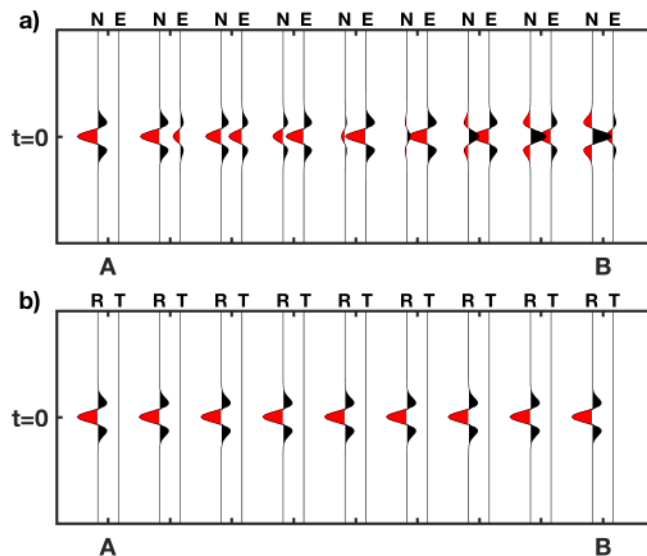
Figure 2.3: Rotation of the data in Figure 2.1b from North and East to Radial and Transverse (R, T). a) Data recorded on the North (N) and East (E) horizontal receivers (as in Figure 2.1b). b) Rotated to Radial **R** and Transverse **T** coordinates.

The radial-transverse rotation uses the correct azimuth of the North receiver, $\phi_{H1} = 0°$. In 3-D multicomponent data acquisition, field crews generally try to orient H_1 along the receiver lines. H_2 is then orthogonal by nature of the 3-C geophone design. The source-receiver azimuth, ϕ_{SR} is determined from the source and receiver (x,y) locations. Multicomponent acquisition is imperfect, however, particularly with regard to the assumption of a constant and consistent H_1 orientation. Variance of the H_1 azimuth, which can potentially vary at each receiver location, must be identified and corrected during processing. An incorrect assumption of ϕ_{H1} can lead to improper radial-transverse rotations. Residual energy will remain on **T**, with **R** consequently having incorrect amplitudes. Note that reflection energy on the transverse component $\mathbf{T} \neq 0$ is generally a diagnostic indicator of shear-wave splitting for C-wave data.

2.3 Improper Rotation to R-T Coordinates: Simple Synthetic Example

The simple synthetic data produced with misoriented horizontal receivers are shown in Figure 2.4. Here $\phi_{H1} = 20°$ (with $\phi_{H2} = 110°$), as shown in green on the basemap in Figure 2.4a. The data are shown below in Figure 2.4b. Note that the shot located at an azimuth of $\phi_{SR} = 20°$ (clockwise from North), now contains all energy on N' (with $E' = 0$). For this source-receiver azimuth N' is actually the radial component $\mathbf{R}$ since from Equation 2.2, $\phi_{ROT}^{R} = 0°$ (and E' is the transverse component $\mathbf{T}$).

Results of the radial-transverse rotation assuming $\phi_{H1} = 0°$, rather then the correct value of $\phi_{H1} = 20°$, are shown in Figure 2.5. Residual energy remains on $\mathbf{T'}$, and consequently, the amplitudes of $\mathbf{R'}$ are in error.

Data recorded with the misoriented receivers and rotated to radial-transverse coordinates using $\phi_{H1} = 20°$ are shown in Figure 2.6. The data are now properly rotated onto the true $\mathbf{R}$ and $\mathbf{T}$ components.
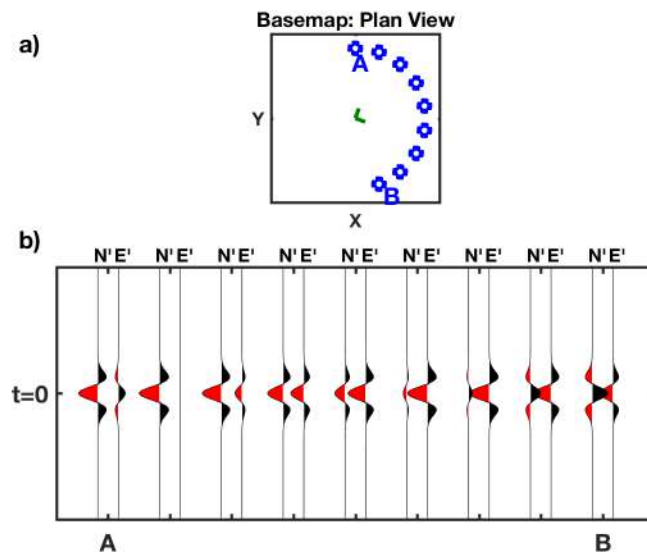
Figure 2.4: Misorientation of the North (N) and East (E) receiver components by 20°. a) The North and East receivers are rotated by 20° to the East (green), with the same shotpoint locations as in Figure 2.1a. The mis-oriented N and E components are now denoted as N' and E', respectively. b) Data recorded on the N' and E' components. Note now that the shotpoint located 20° East of North has all data contained on the N' component, whereas E' = 0. This shotpoint is radial to N', while E' is transverse.
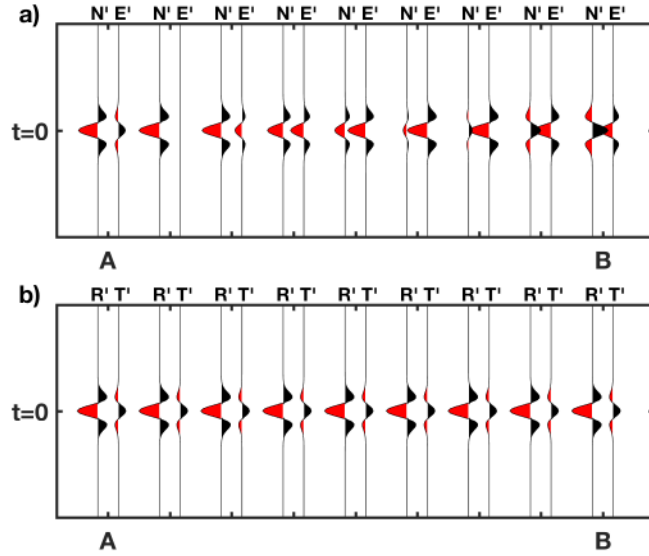
Figure 2.5: Radial-Transverse rotation of the data with the North receiver misoriented by 20° to the East. a) Data recorded on the N' and E' components from the geometry of Figure 2.4a. b) Data in radial-transverse coordinates. The N' and E' components have been rotated to **R'** and **T'** assuming that the North receiver is actually oriented North ($\phi_{H1} = 0°$). Note the energy on **T'**, and as a result, the energy on **R'** is less than it should be.

2.4 Field Data: Anomalous Crossterm Energy

C-wave and S-wave data from the Baseline and Monitor 2 surveys were judged to show no evidence of shear-wave splitting during commercial data processing. Monitor 1 S-wave common-shot stacks (Figure 2.7) do show apparent reflection signal on the *crossterms* **RT** and **TR**. Note that these S-wave crossterms are the equivalent indicator of shear-wave splitting as is the C-wave **T** component (Omar, 2018).

The Niobrara interval is at 3500 ms, within which the hydraulic fracturing occurred. The reflection signal in the overburden is anomalous and cannot be explained in terms of anisotropy. This anomalous signal was described as leakage, somehow attributed to wet surface conditions present during data acquisition, with no additional explanation or analysis provided.

Consequently, only the C-wave radial component **R**, and the S-wave **RR** and **TT** components from all three surveys were prestack time migrated. The C-wave **T** component, and
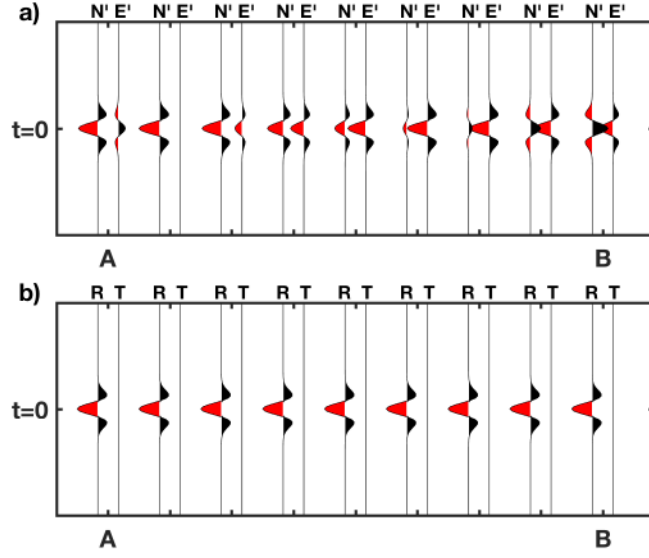
Figure 2.6: Correct radial-transverse rotation assuming that the azimuth of $N' = 20°$. a) Input data in N', E' coordinates. b) Output data in radial-transverse coordinates. All energy is rotated onto $\mathbf{R}$ given that the correct ϕ_{H1} is used in the rotation.

the S-wave $\mathbf{RT}$ and $\mathbf{TR}$ components were dropped after preprocessing.

In order to examine the anomalous Monitor 1 signal (Figure 2.7), I use the preprocessed unmigrated data for the following COCA gather analysis since all C-wave and S-wave data components are available.

COCA gathers for a super bin from the Baseline and Monitor 1 surveys are shown in Figure 2.8. Isotropic 1-D traveltime moveout corrections have been applied to the preprocessed gathers, along with a bandpass filter. Each of the components were then super binned (bins of 2500 ft by 2500 ft), stacked within 500-ft offset planes and 20° azimuth sectors, to produce the COCA gathers.

Three reflections ($\mathbf{A}$,$\mathbf{B}$,$\mathbf{C}$) are indicated along the time (vertical) axis. Reflections $\mathbf{A}$ and $\mathbf{B}$ are in the overburden, while reflection $\mathbf{C}$ is at the depth where the hydraulic fracturing occurred. Gathers from the Baseline survey (Figure 2.8a) show minimal energy on the crossterms $\mathbf{RT}$, $\mathbf{TR}$, and $\mathbf{T}$, and the clear separation of SV-waves onto $\mathbf{RR}$, and SH-waves onto $\mathbf{TT}$, as expected. Monitor 1 gathers (Figure 2.8b) show the leakage. Reflections $\mathbf{A}$, $\mathbf{B}$, and $\mathbf{C}$ appear on $\mathbf{RT}$, $\mathbf{TR}$, and $\mathbf{T}$ as scaled versions of $\mathbf{RR}$, $\mathbf{TT}$, and $\mathbf{R}$, respectively. Note
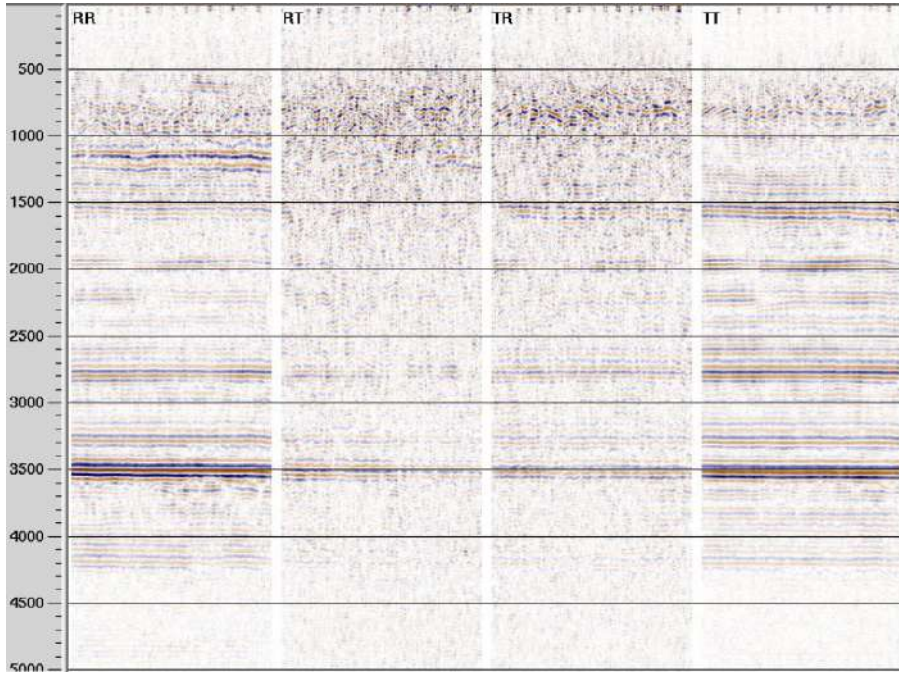
Figure 2.7: Monitor 1 S-wave common-shot stacks from the data-processing report showing undesirable energy on **RT** and **TR** throughout the section.

that **RT** is reversed polarity relative to **RR** (most obvious for Reflection **C**).

S-wave and C-wave data from Monitor 1 are unusable in this form as reported by the data processing contractor. This characteristic is observed on the COCA gathers throughout the entire survey. S-wave data (**RR**, **RT**, **TR**, **TT**) involve a source-side rotation which assumes orthogonality between S_1 and S_2, and known azimuthal orientations of S_1 (ϕ_{S1}) and H_1 (ϕ_{H1}) as seen in Equation 2.3. Small random errors in these orientations tend to cancel in the large spatial bin COCA gathers, but the crossterm energy has not canceled out. The energy is coherent and not characteristic of HTI media. This analysis of the S-wave data indicates that signal leakage is a source and/or receiver orientation issue not accounted for during processing.

C-wave COCA gathers also show the crossterm leakage as seen on the **T** component in Figure 2.8. Only a receiver-side rotation is required for C-wave data which indicates that an error in the H_1 azimuth orientation is the first-order cause of the signal leakage on the **T**, **RT**, and **TR** components.

23
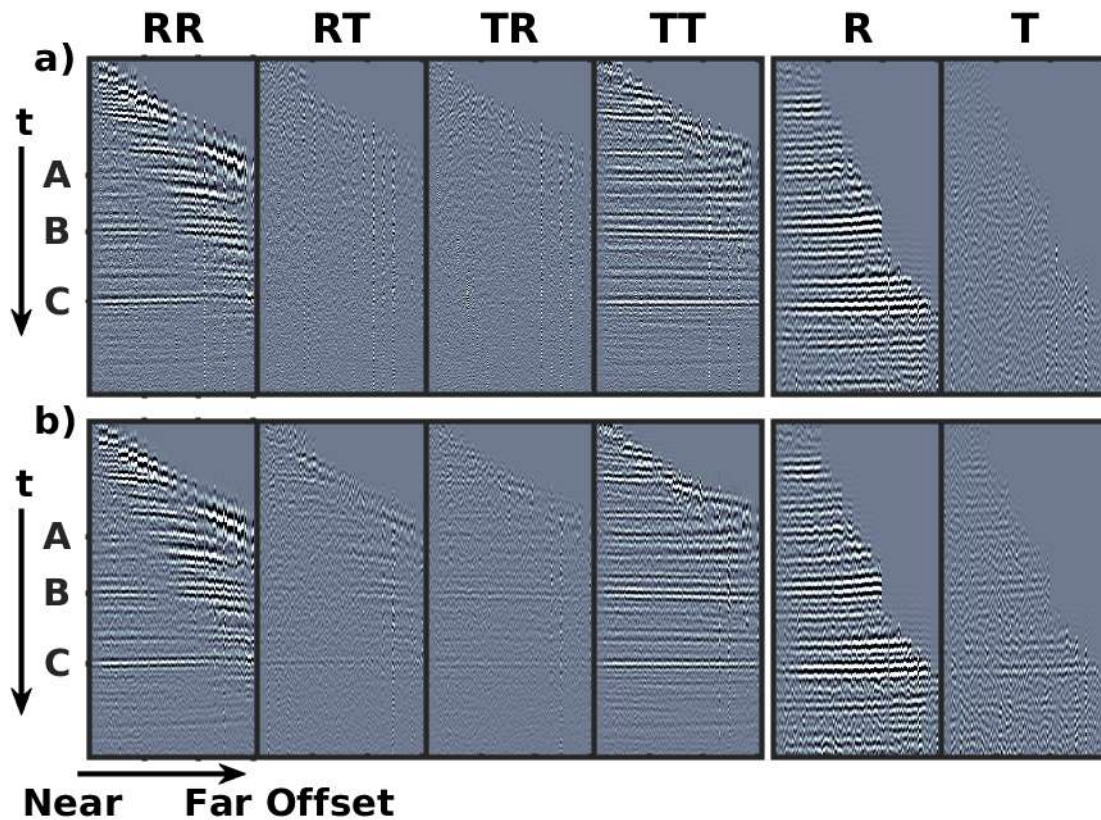
Figure 2.8: COCA gathers, real data. The nominal $\phi_{H1} = 0°$ is used for the radial-transverse rotation. a) Baseline survey. b) Monitor 1 survey. The C-wave gathers (right) have been approximately registered with the S-wave gathers. Note the leakage of reflections onto **RT**, **TR**, and **T** in b), even for reflections **A** and **B** which are considerably shallower than the hydraulically fractured interval **C**.

24

2.5 COCA Gathers: Prestack Synthetic Seismograms

The cross-component leakage was modeled using 9-C synthetic prestack data generated by anisotropic reflectivity modeling (Fryer and Frazer, 1984; Fryer and Frazer, 1987; Kennett, 1983). Any, or all, layers may be generally anisotropic with the restriction that the layers be flat and homogeneous. Vertical and orthogonal horizontal forces are located at the center of a square (x, y) grid, with 3-C receivers uniformly spaced in x and y. Plane waves are propagated through the layered medium as a function of frequency ω, and horizontal wavenumbers k_x and k_y, the reflectivity response is calculated, $R(\omega, k_x, k_y)$, and then a 3-D inverse Fourier Transform produces the 9-C prestack data cubes in the time-space domain (t, x, y).

The square acquisition grid, with the sources at the center, provides data at all azimuths and offsets. Horizontal receivers H_1 and H_2 are oriented north and east ($\phi_{H1} = 0°$, $\phi_{H2} = 90°$), as are the horizontal-force sources S_1 and S_2 ($\phi_{S1} = 0°$ and $\phi_{S2} = 90°$, respectively). The earth model consists of an isotropic overburden (five layers), with an anisotropic (HTI) target interval (four layers). Prestack data are rotated into radial-transverse coordinates assuming $\phi_{H1} = 0°$, and $\phi_{S1} = 0°$ for the shear-wave source components.

Spherical divergence and traveltime moveout corrections are applied, then the data are stacked into COCA gathers (Figure 2.9a). Reflections from within the isotropic overburden are indicated as **A** and **B**, with the HTI target interval identified as **C**. SV reflections are contained on **RR**, SH reflections on **TT**, with the cross terms (**RT** and **TR**) containing the split shear waves. P-SV reflections are contained on **R**, with **T** containing the split shear waves. Omar (2018) provides examples of P-wave, C-wave, and S-wave COCA gathers for several different anisotropic models.

I model a global error in the H_1 azimuth occurring during data acquisition by rotating H_1 and H_2 for each source to $\phi_{H1} = 10°$ ($\phi_{H2} = 100°$), and *then* rotating the C-wave and S-wave data to radial-transverse coordinates. I assume $\phi_{H1} = 0°$ in the rotation to radial-transverse coordinates, using the correct value of $\phi_{S1} = 0°$ for the S-wave source rotation.
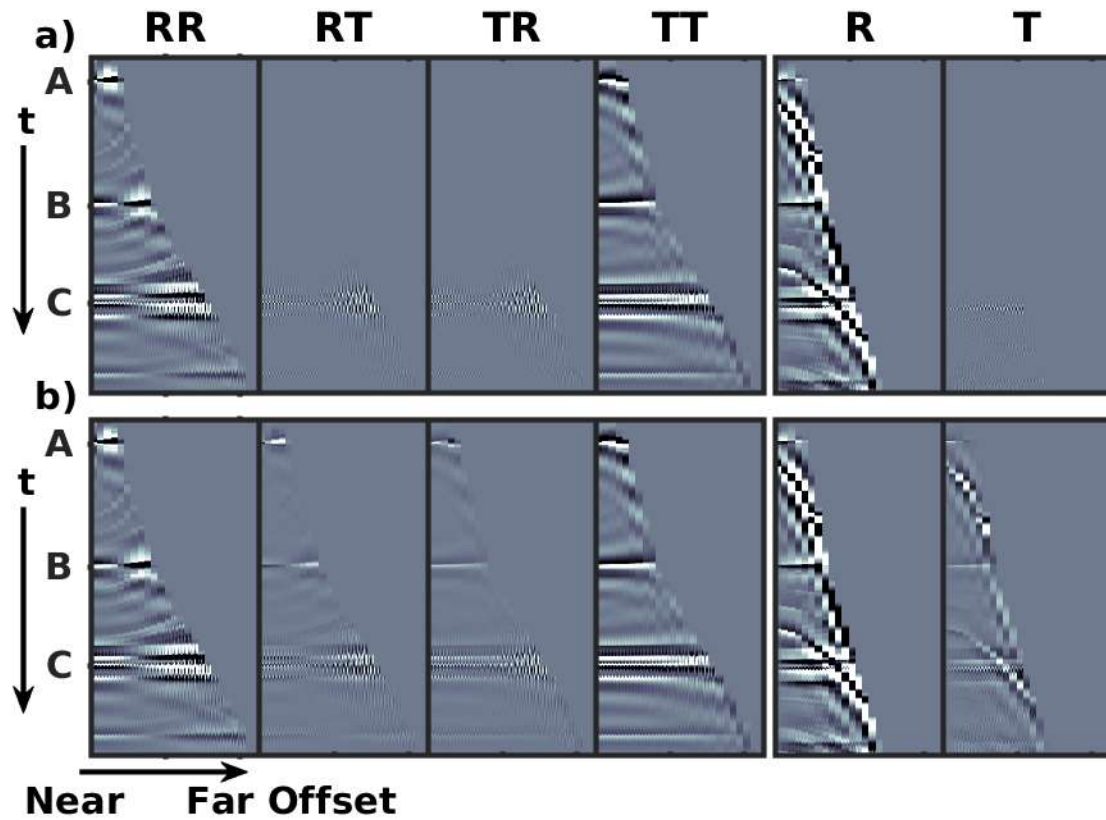
Figure 2.9: COCA gathers, synthetic data. a) Rotated with the correct $\phi_{H1} = 0°$. b) The actual $\phi_{H1} = 10°$, but the radial-transverse rotation assumes $\phi_{H1} = 0°$. Note the cross-component leakage on **RT, TR**, and **T**. Consequently, the amplitudes on **RR, TT** and **R** are in error.

The corresponding COCA gathers are shown in Figure 2.9b. This procedure mimics my interpretation of the Monitor 1 data. An unrecognized global error of $\phi_{H1} = 10°$ causes isotropic reflection energy (reflections **A** and **B**) to appear on the crossterms (**RT**, **TR**, and **T**). Note that **RT** is a scaled version of **RR**, **TR** is a scaled version of **TT**, and **T** is a scaled version of **R**. Also note that **RT** is reversed polarity relative to **RR**. These data are not interpretable with regard to shear-wave splitting and/or AVAZ (Cary, 2002; MacBeth et al., 1994).

2.6   Discussion

Rotation of horizontal receivers H_1 and H_2 to radial-transverse coordinates is critically important for C-wave and S-wave data processing and analysis. Geophone layout prior to data acquisition attempts to align the H_1 azimuth, ϕ_{H1} to a fixed direction, generally this nominal direction is parallel to the receiver lines ($\phi_{H1} = 0°$ for Wattenberg). COCA gathers of the Monitor 1 C-wave and S-wave data, suggest a general error in the nominal H_1 azimuth, as $\phi_{H1} \neq 0°$.

Initial analysis focussed on the S-wave COCA gathers. The cross-component leakage became clearly apparent looking at these prestack gathers including the overburden data. S-wave rotation to radial-transverse coordinates involves ϕ_{SR}, ϕ_{H1}, and the field orientation of ϕ_{S1} (assuming that the field orientation of $\phi_{S2} \perp \phi_{S1}$). At this stage, however, the source of the leakage was uncertain; receiver side due to a mis-orientation of H_1, source-side due to the mis-orientation of S_1, or some combination thereof.

Analysis of the C-wave COCA gathers confirmed a receiver-side issue with the field orientation of H_1. No source rotation is involved for C-waves recorded from a vertical vibrator. Visual inspection of COCA gathers from the Baseline, Monitor 1, and Monitor 2 surveys suggested that the Monitor 1 data were most affected. It is important to note, however, that the magnitude of shear-wave splitting within the Niobrara interval is expected to be very small (Omar, 2018). Consequently, the *crossterms* (C-wave **T** component, and the S-wave **RT** and **TR** components) will be weak in amplitude. As a result, estimation of the

true H_1 azimuth orientations is extremely important since the crossterm energy is diagnostic of shear-wave splitting, and preservation of the correct crossterm energy is needed for C-wave (Simmons, 2009), and S-wave (Alford, 1986) splitting inversions.

The simple synthetic example shows that a mis-orientation of $\phi_{H1} = 20°$, produces an amplitude error in $\mathbf{R'}$ when the data are rotated to radial-transverse coordinates assuming $\phi_{H1} = 0°$. This is relevant to the Wattenberg data processing. C-wave and S-wave preprocessing generally derives processing parameters from the $\mathbf{R}$, $\mathbf{RR}$, and $\mathbf{TT}$ components (surface-consistent amplitudes, surface-consistent deconvolution filters, reflection statics, etc.) and then applies these parameters to respective crossterm components. Errors in the ϕ_{H1} values used for radial-transverse rotation, may compromise the quality of products created during the seismic processing flow.

The cross-component leakage on the Monitor 1 survey was initially identified on S-wave COCA gathers. Reflection signal leakage on S-wave data could be attributed to receiver mis-orientations, and/or shear-source non-orthogonality and/or receiver mis-orientations. Leakage on the C-wave COCA gathers indicated that there was a receiver side (H_1) acquisition issue. Utilizing both the S-wave and C-wave data were crucial in determining the cause of the cross-component leakage. The receiver mis-orientation hypothesis was qualitatively confirmed through synthetic prestack modeling. The following chapter details two methods that estimate H_1 azimuth orientations, compares the methods, exposes a global rotation error of the Monitor 1 data, and provides local receiver ϕ_{H1} estimates for the Baseline, Monitor 1 and Monitor 2 surveys.

HORIZONTAL-RECEIVER AZIMUTH ESTIMATION

3.1   Summary

This chapter details two approaches to estimate the azimuth orientation of H_1 for each C-wave receiver gather to optimally rotate the horizontal receivers from field coordinates into radial-transverse coordinates. Concepts are illustrated on the simple synthetic example of Chapter 2, then applied to the Turkey Shoot data.

The first approach uses P-wave first-arrival energy to drive the algorithm and is often employed on land and marine multicomponent data. The second approach uses C-wave reflections on Limited-Azimuth-Stacks (LAS). Input data are common-receiver gathers of the horizontal-receiver components, H_1 and H_2, as acquired in the field. Both approaches search for the optimal H_1 azimuth for each receiver (ϕ_{H1}^{est}), which when used to rotate the data to radial-transverse coordinates, minimizes the energy on the transverse component, and maximizes the energy on the radial component.

I find that the P-wave first-arrival method recognizes a *global error* in the Monitor 1 H_1 azimuth orientation of $\approx 8°$ as summarized in histograms of the ϕ_{H1}^{est} values. Baseline and Monitor 2 histograms are centered around $\phi_{H1}^{est} \approx 0°$. Spot checking some of the Monitor 1 histogram outliers suggested that these values may be in error. Some authors have noted with problems with this approach, particularly for onshore data which tends to have a lower signal-to-noise ratio than Ocean-Bottom-Cable or Ocean-Bottom-Node data.

The C-wave reflection approach finds the optimal H_1 azimuth that minimizes transverse reflection energy in the overburden. It is interesting the two approaches give very simi-

lar looking ϕ_{H1}^{est} histograms, with the spread being considerably tighter with the reflection method. The ϕ_{H1}^{est} estimates from this approach are then used to correct the preprocessed C-wave and S-wave data for further analysis.

3.2 Introduction

Various approaches to estimating the horizontal-geophone azimuth orientation (ϕ_{H1}) have been proposed. Hodograms are often used for Vertical-Seismic-Profile (VSP) data (DiSiena et al., 1984) due to the relatively small number of receivers since this is an interactive, graphical approach. Generally, the analysis window is guided by the P-wave first arrival at each receiver level. The horizontal receivers at each depth level have an unknown azimuth orientation, and as a result, the direct P-wave arrival is recorded on both the H_1 and H_2 receivers. A hodogram is simply the crossplot of the seismic trace amplitudes within a specified time window encompassing the P-wave first arrival.

Hodograms for the simple synthetic data of Figure 2.1 are shown in Figure 3.1. One looks for *linearity* in these crossplots, whereby one then infers the azimuth of one of the horizontal receivers. For example, for shotpoint A all energy is on the North (N) component. If the shotpoint A hodogram instead looked like the top row, right, knowing the source-receiver azimuth (from shotpoint A to the receiver) one could estimate the misalignment of the North receiver. Crossplots of the East (horizontal) and North (vertical) show linear trends for each shotpoint from which the ϕ_{H1} is inferred from the slope of a line fit to the crossplot. In this case, the azimuths of the linear trends are the source-receiver azimuths.

Another common, more automated approach is to form the covariance matrix (Kanasewich, 1981; Zeng and McMechan, 2006) of the H_1 and H_2 amplitudes of common-receiver gathers as

$$cov(H_1, H_2) = \begin{bmatrix} \sum_{offset} \sum_{time} H_1^2 & \sum_{offset} \sum_{time} H_1 H_2 \\ \sum_{offset} \sum_{time} H_2 H_1 & \sum_{offset} \sum_{time} H_2^2 \end{bmatrix} \tag{3.1}$$

30
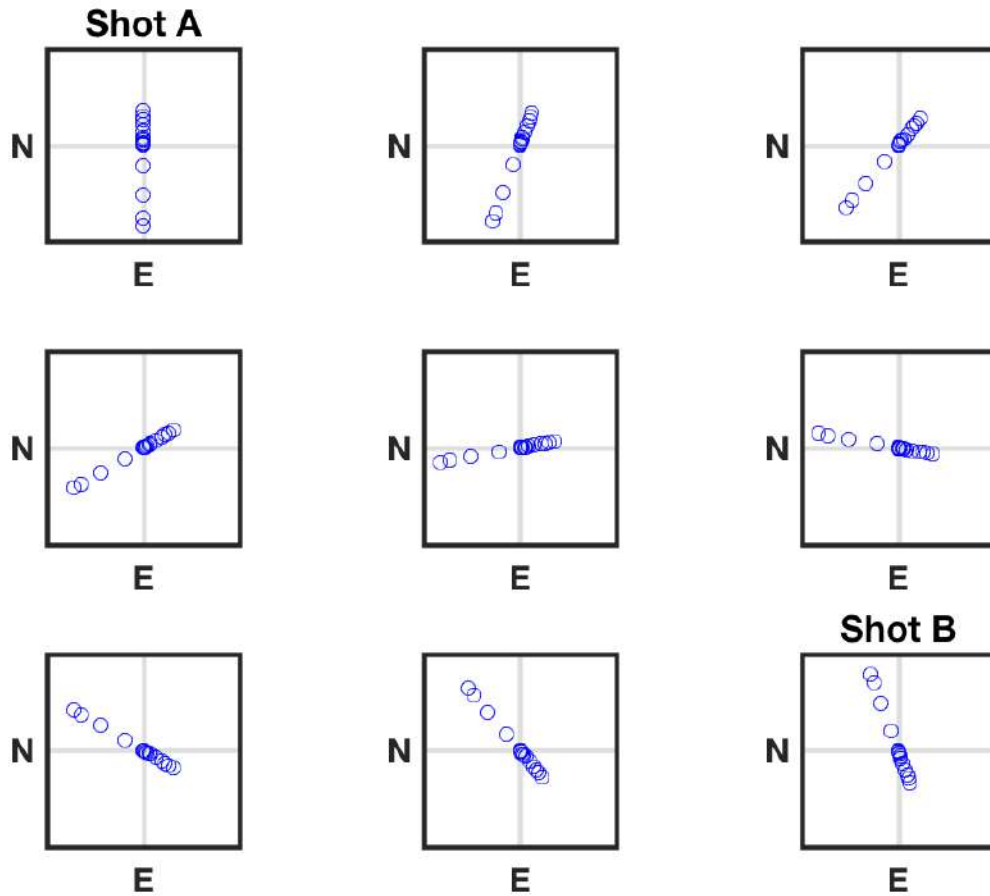
Figure 3.1: Hodograms of the data recorded on the North (N) and East (E) horizontal receivers (Figure 2.1a). Each row shows the shots moving clockwise from shotpoint A to shotpoint B. A hodogram is simply the crossplot of the seismic trace amplitudes (East is along the horizontal axis, North is along the vertical axis).
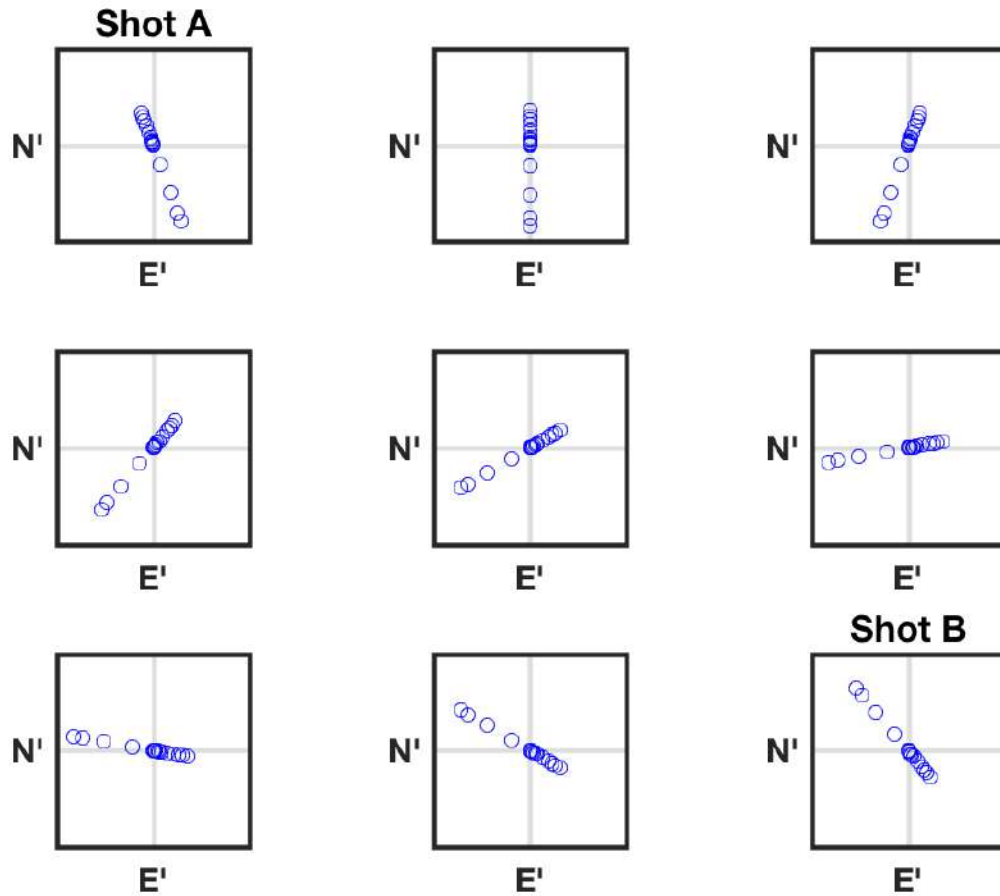
Figure 3.2: Hodograms of the data recorded on the North (N') and East (E') horizontal receivers when the North receiver is oriented at $H_1 = 20°$. Now the azimuth inferred by linear trend (slope) of the crossplots does not equal the source-receiver azimuth. The data are those of Figure 2.4.

where the summations are taken over the time window and the spatial (offset) window of the analysis. The covariance matrix is then directly solved, and the ϕ_{H1} orientation angle is determined from the eigenvalues and eigenvectors . This direct solution can be susceptible to noise in the data, limited shotpoint azimuthal coverage, and the polarity is ambiguous. In addition, there is no quality control mechanism readily available with this method.

Both the P-wave first-arrival and C-wave reflection methods utilize a scanning procedure (Nagarajappa et al., 2013) that operates on H_1 and H_2 common-receiver gathers to estimate the optimal ϕ_{H1} for each gather as

$$\begin{bmatrix} R' \\ T' \end{bmatrix} = \begin{bmatrix} \cos(\phi_{SR} - \phi_{H1}^{trial}) & \sin(\phi_{SR} - \phi_{H1}^{trial}) \\ -\sin(\phi_{SR} - \phi_{H1}^{trial}) & \cos(\phi_{SR} - \phi_{H1}^{trial}) \end{bmatrix} \begin{bmatrix} H_1 \\ H_2 \end{bmatrix} \qquad (3.2)$$

where ϕ_{SR} is the source-receiver azimuth, and ϕ_{H1}^{trial} is a trial value of the H_1 azimuth. Each trace of the H_1 and H_2 receiver gathers is rotated by $\phi_{SR} - \phi_{H1}^{trial}$ producing R' and T' receiver gathers. For each ϕ_{H1}^{trial}, the RMS amplitudes of $\frac{T'}{R'}$ are calculated within the analysis window, and the minimum value yields the optimal ϕ_{H1}. The objective function is, thus, $\frac{T'}{R'}(\phi_{H1}^{trial})$ and is displayed in decibels relative to $\frac{T'}{R'}(\phi_{H1}^{nom})$, where ϕ_{H1}^{nom} is the nominal ϕ_{H1} generally oriented parallel to the receiver lines ($\phi_{H1}^{nom} = 0°$ for the Wattenberg field data).

Objective functions are used in all inversion problems. In many problems, the objective function involves the data misfit (difference between the observed and predicted data) and a model regularization term. Generally, the objective function is monitored and iterations of the inversion cease when the objective function is no longer decreasing. In the following examples, I display the objective function values for the entire range of ϕ_{H1}^{trial} for illustrative, and potentially, interpretive purposes.

The ϕ_{H1}^{trial} scanning algorithm is applied to the simple synthetic data, and the results are shown in Figures 3.3 - 3.4. Input data are that of Figure 2.4b, but now displayed as receiver gathers (A and B indicate the traces recorded from shotpoints A and B, respectively of Figure 2.4a). Each panel of Figure 3.3 shows the output of Equation 3.2 using the ϕ_{H1}^{trial} value indicated by the azimuth icon. The energy of T' decreases from upper left to lower left

33

(moving left to right across each row) as ϕ_{H1}^{trial} approaches the correct value of $\phi_{H1}^{est} = 20°$.

The objective function is shown in Figure 3.4 as the RMS ratio $\frac{T'}{R'}$ (top), and in decibels relative to the ratio at ϕ_{H1}^{nom} (bottom). A virtue of displaying the objective function in decibels relative to the value at ϕ_{H1}^{nom} is that objective functions can be more easily compared.
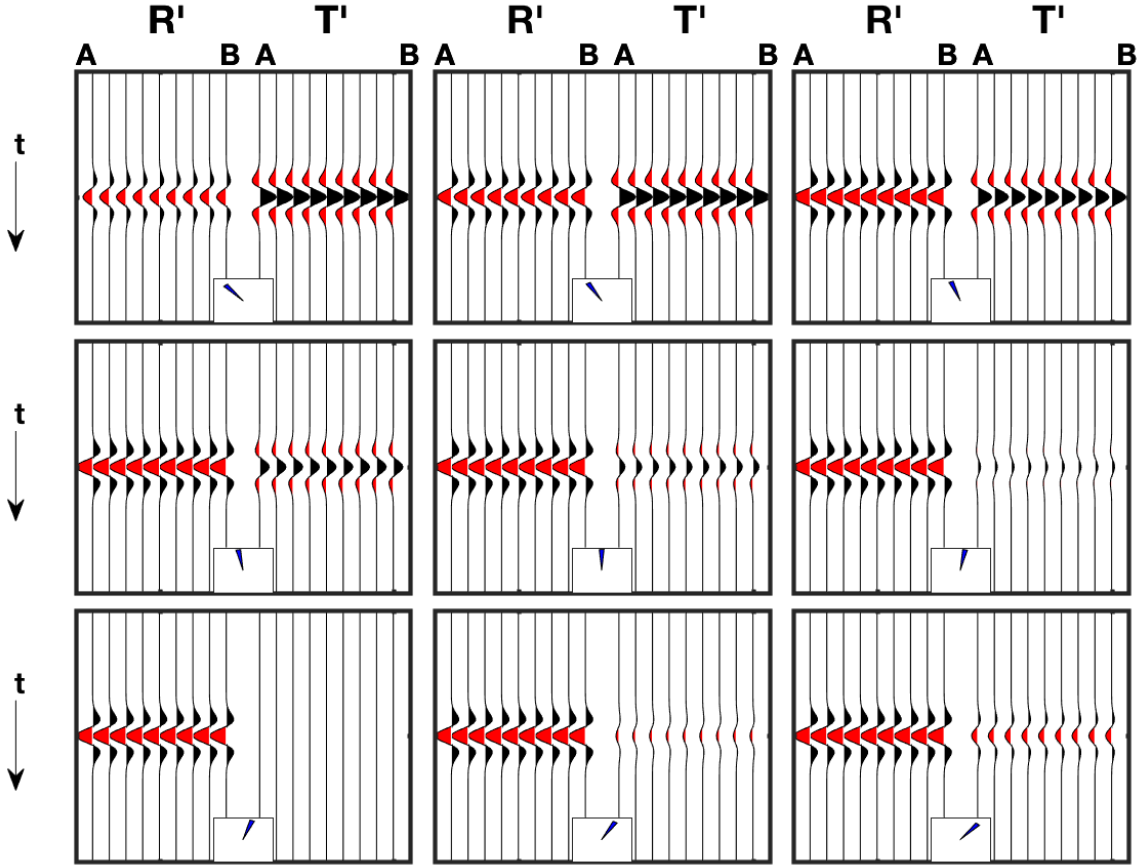
Figure 3.3: Example of the H_1 azimuth-scan algorithm applied to the simple synthetic data of Figure 2.4b. Each panel shows the radial and transverse components (R', T'), ordered as gathers, obtained using a ϕ_{H1}^{trial} in the radial-transverse rotation of Equation 3.2. The icons at the bottom center of each panel indicate the ϕ_{H1}^{trial} trial values. $\phi_{H1}^{trial} = -40°, -30°, -20° \dots 40°$ from the upper left to lower right.

3.3 H_1 Azimuth Orientation Estimation: Field Data, P-wave First Arrivals

An optimal ϕ_{H1}^{est} for each C-wave receiver gather is obtained using the scanning procedure outlined in Equation 3.2, and illustrated in Figures 3.3 - 3.4. Field data H_1 and H_2 receiver gathers, are minimally processed on input to the scan algorithm. Gain as $t^{1.8}$ is applied,
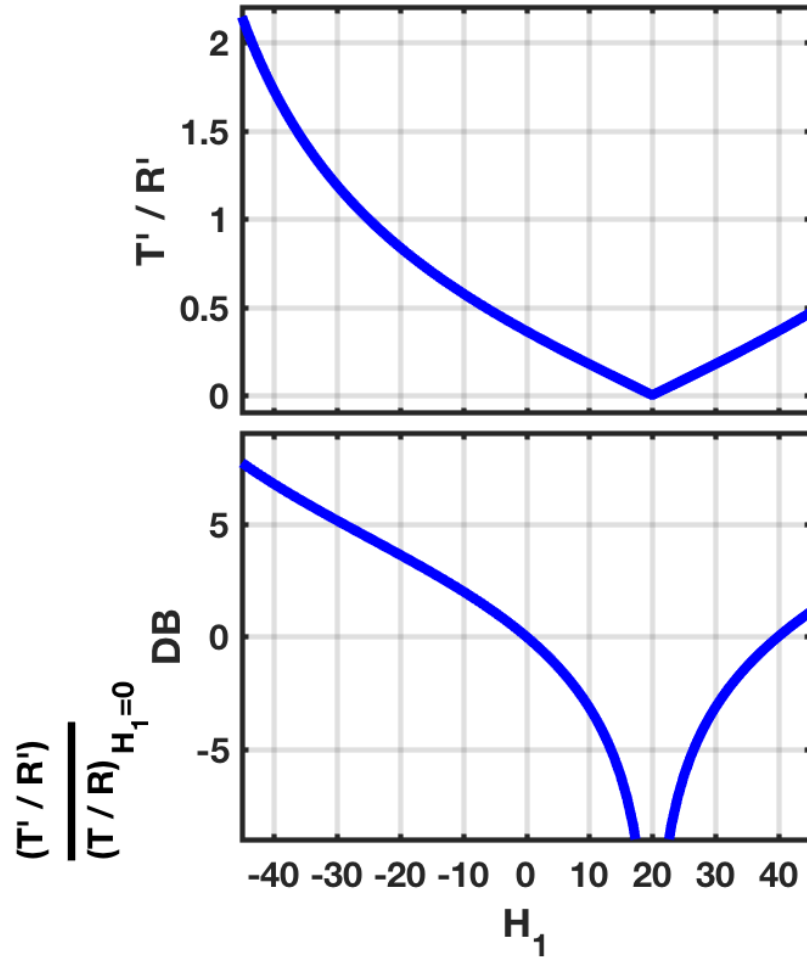
Figure 3.4: Objective function for the H_1 trial azimuth-scan inversion shown in Figure 3.3. a) Ratio of T'/R' RMS amplitude values as a function of ϕ_{H1}^{trial}. b) Ratio of T'/R' RMS values divided by the ratio obtained for the $\phi_{H1}^{nom} = 0°$ trial (the presumed nominal H_1 azimuth). Results are displayed in decibels. The minimum of the objective function gives the optimal $\phi_{H1}^{est} = 20°$.

where t is two-way traveltime, the data are time aligned using P-wave first arrival picks, and then noise bursts are attenuated using a time-frequency domain median filter.

Trace amplitudes within an 80 ms time window following the time-aligned P-wave first arrivals are considered in the analysis for the objective function calculation. Data input to the objective function are also offset limited to include only shotpoints having offsets from $1500 \leq x \leq 5000$ ft, where x is the source-receiver offset. The trial azimuths $\phi_{H_1}^{trial}$ range from $-90° \ldots 90°$, Equation 3.2 is applied, and the RMS values of T' and R' are calculated for each $\phi_{H_1}^{trial}$.

Baseline and Monitor 1 time-aligned receiver-gathers from various receivers across the survey are shown in Figures 3.5-3.11, and 3.12-3.18, respectively. The H_1, and H_2 input gathers are at the left. Radial and transverse gathers obtained using $\phi_{H1}^{nom} = 0°$ (R_{nom}, T_{nom}), and the optimal ϕ_{H1}^{est} from the scanning algorithm (R_{est}, T_{est}), are shown in the middle, and at the right, respectively. Energy on T_{est} is generally reduced relative to that of T_{nom}, although the amount of decrease is often very small.

The objective function is shown at the upper right of the T_{est} panel. A virtue of the scan method is that it produces an objective function that can be further examined, for the depth of the minimum in particular. As discussed in Figure 3.4 , the objective function is displayed in decibels relative to the value for $\phi_{H1}^{nom} = 0°$, which is the nominal H_1 azimuth during acquisition. The minimum of the objective function gives the ϕ_{H1}^{est} that minimizes energy on the transverse component after applying Equation 3.2.

The H_1 azimuth scan is applied to all receiver gathers from the three surveys. Histograms of the ϕ_{H1} estimates for Baseline, Monitor 1 and Monitor 2 surveys are shown in Figure 3.19. Histograms for Baseline and Monitor 2 have their mode near the nominal $\phi_{H1} = 0°$, while the mode for Monitor 1 $\phi_{H1} \approx 8°$. This global skew of the Monitor 1 data causes the cross-component leakage seen in the COCA gathers of Figure 2.8b, and in the synthetic COCA gathers of Figure 2.9b.
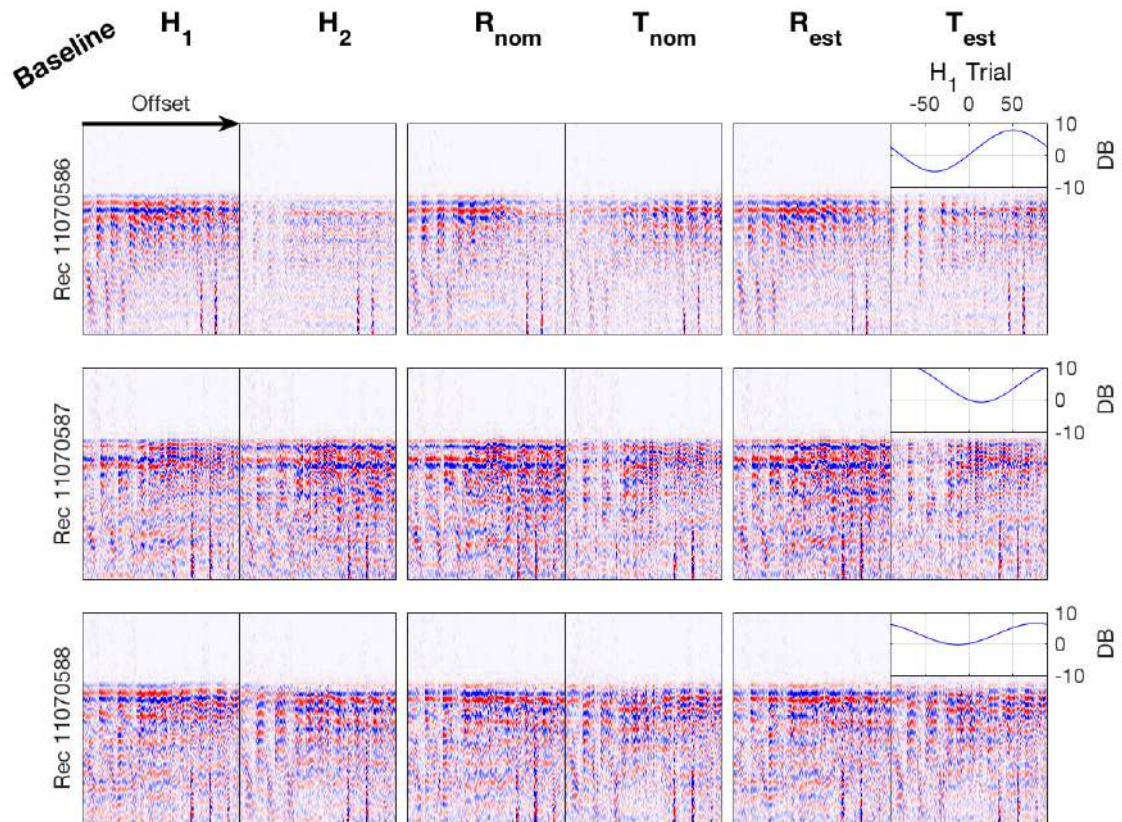
Figure 3.5: H_1 azimuth estimation results. a) Baseline common-receiver gathers. Data are aligned on the P-wave first arrival. H_1, H_2 as acquired in the field, after rotation to radial-transverse assuming $\phi_{H1}^{nom} = 0°$ (R_{nom}, T_{nom}), and after rotation to radial-transverse using the estimated ϕ_{H1}^{est} (R_{est}, T_{est}).
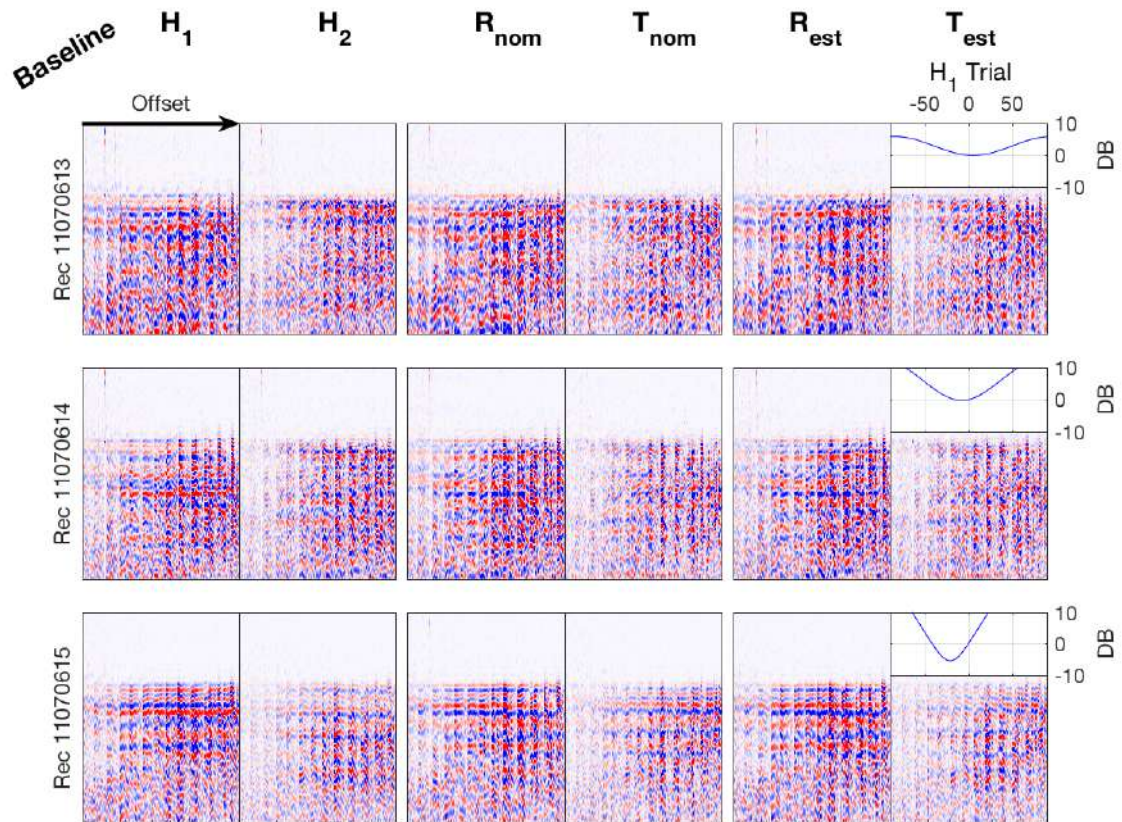
Figure 3.6: H_1 azimuth estimation results. a) Baseline common-receiver gathers. Data are aligned on the P-wave first arrival. H_1, H_2 as acquired in the field, after rotation to radial-transverse assuming $\phi_{H1}^{nom} = 0°$ (R_{nom}, T_{nom}), and after rotation to radial-transverse using the estimated ϕ_{H1}^{est} (R_{est}, T_{est}).
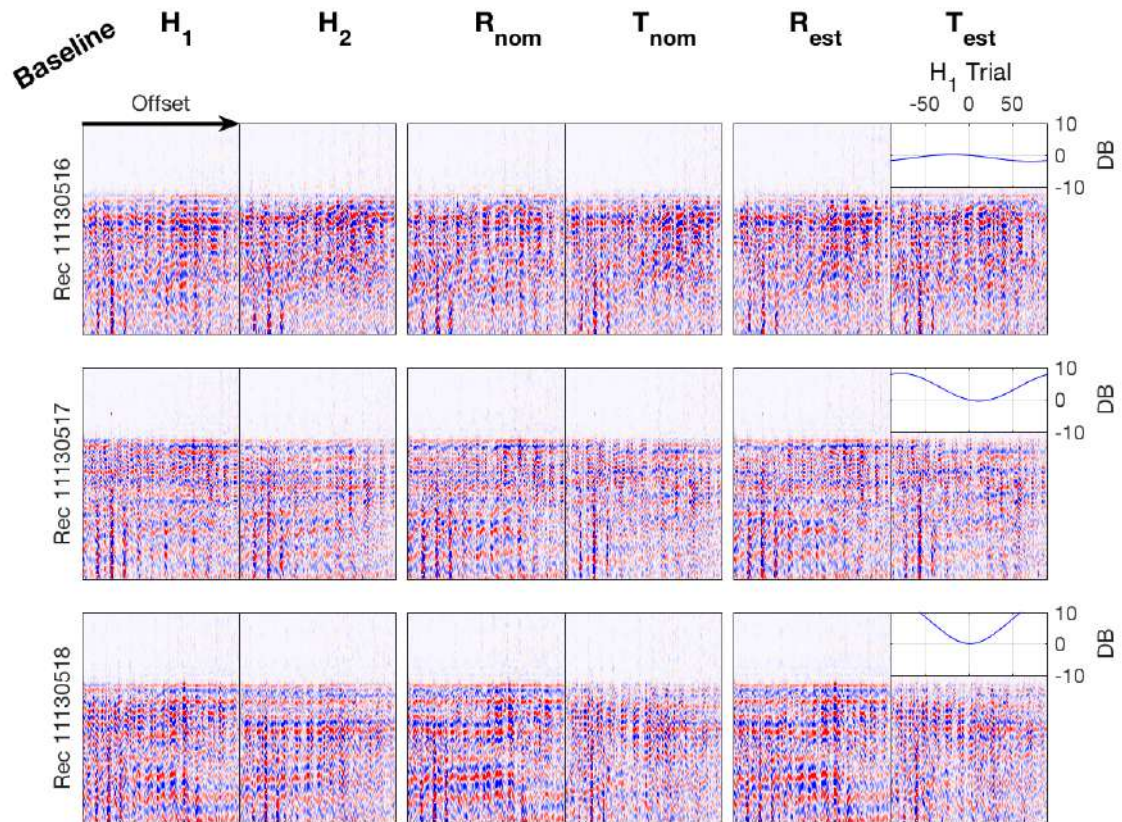
Figure 3.7: H_1 azimuth estimation results. a) Baseline common-receiver gathers. Data are aligned on the P-wave first arrival. H_1, H_2 as acquired in the field, after rotation to radial-transverse assuming $\phi_{H1}^{nom} = 0°$ (R_{nom}, T_{nom}), and after rotation to radial-transverse using the estimated ϕ_{H1}^{est} (R_{est}, T_{est}).
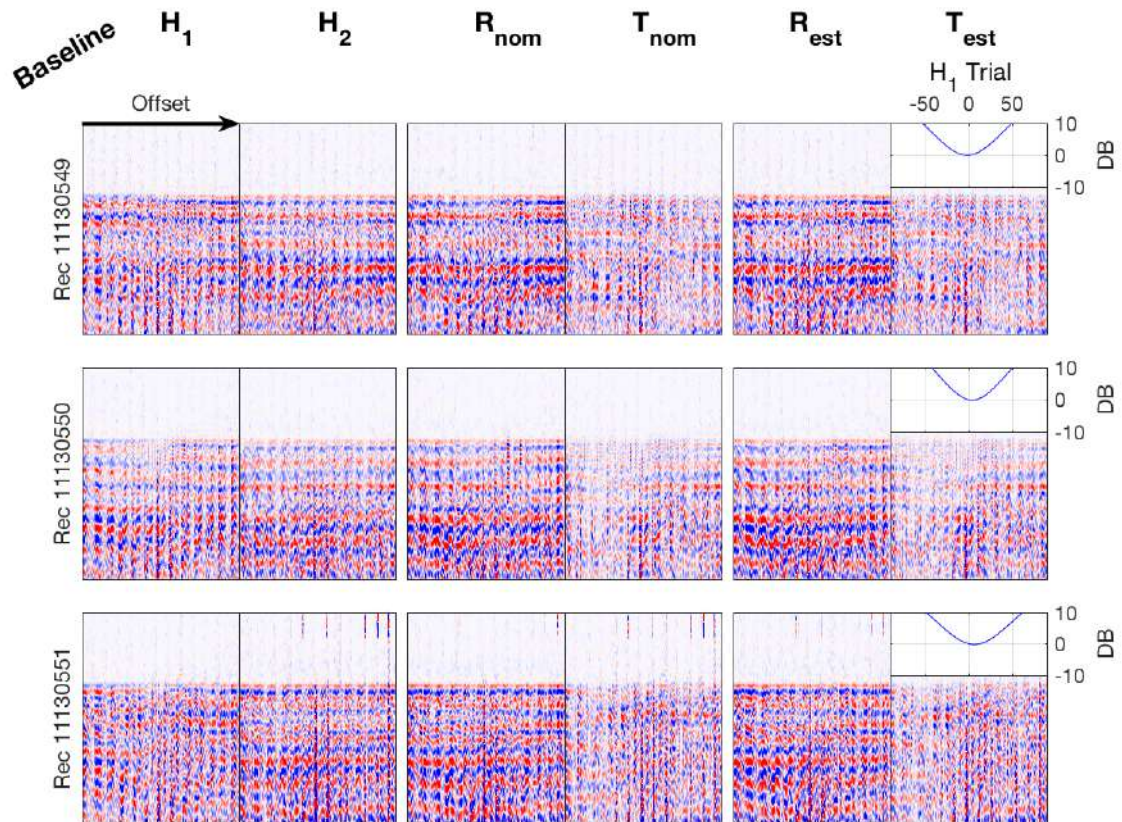
Figure 3.8: H_1 azimuth estimation results. a) Baseline common-receiver gathers. Data are aligned on the P-wave first arrival. H_1, H_2 as acquired in the field, after rotation to radial-transverse assuming $\phi_{H1}^{nom} = 0°$ (R_{nom}, T_{nom}), and after rotation to radial-transverse using the estimated ϕ_{H1}^{est} (R_{est}, T_{est}).
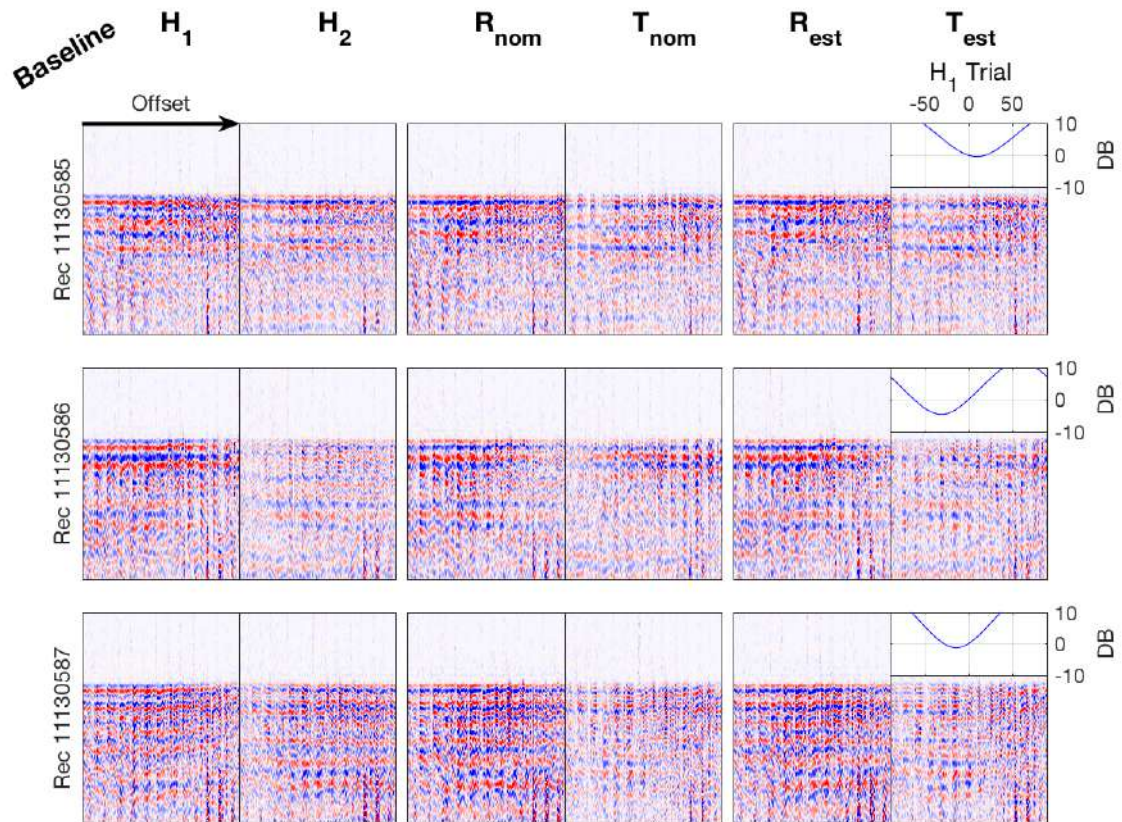
Figure 3.9: H_1 azimuth estimation results. a) Baseline common-receiver gathers. Data are aligned on the P-wave first arrival. H_1, H_2 as acquired in the field, after rotation to radial-transverse assuming $\phi_{H1}^{nom} = 0°$ (R_{nom}, T_{nom}), and after rotation to radial-transverse using the estimated ϕ_{H1}^{est} (R_{est}, T_{est}).
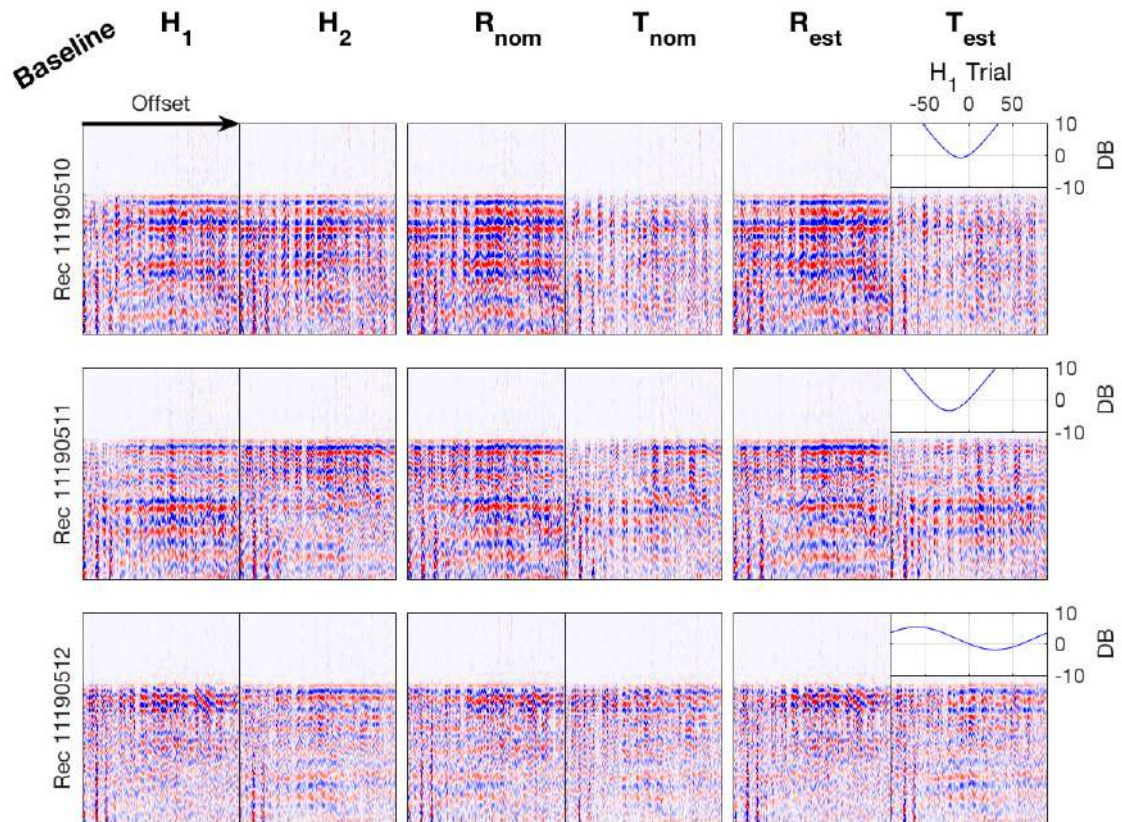
Figure 3.10: H_1 azimuth estimation results. a) Baseline common-receiver gathers. Data are aligned on the P-wave first arrival. H_1, H_2 as acquired in the field, after rotation to radial-transverse assuming $\phi_{H1}^{nom} = 0°$ (R_{nom}, T_{nom}), and after rotation to radial-transverse using the estimated ϕ_{H1}^{est} (R_{est}, T_{est}).

42
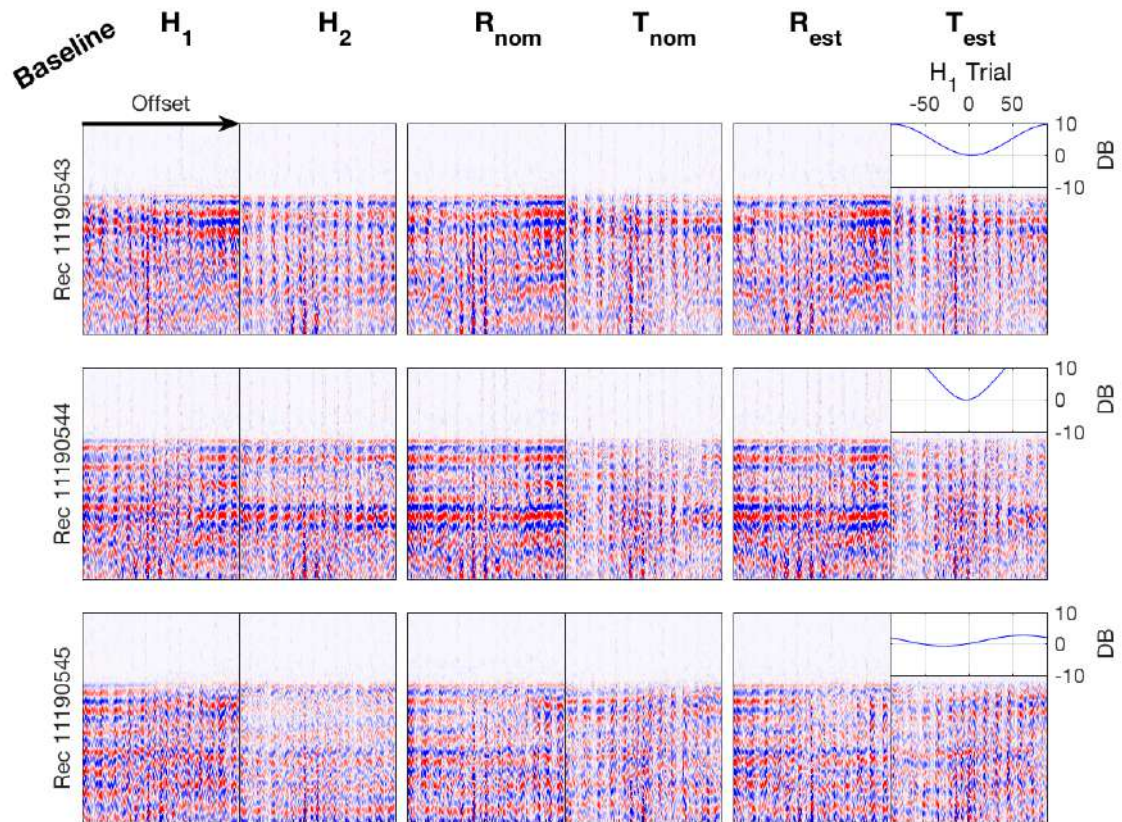
Figure 3.11: H_1 azimuth estimation results. a) Baseline common-receiver gathers. Data are aligned on the P-wave first arrival. H_1, H_2 as acquired in the field, after rotation to radial-transverse assuming $\phi_{H1}^{nom} = 0°$ (R_{nom}, T_{nom}), and after rotation to radial-transverse using the estimated ϕ_{H1}^{est} (R_{est}, T_{est}).

43
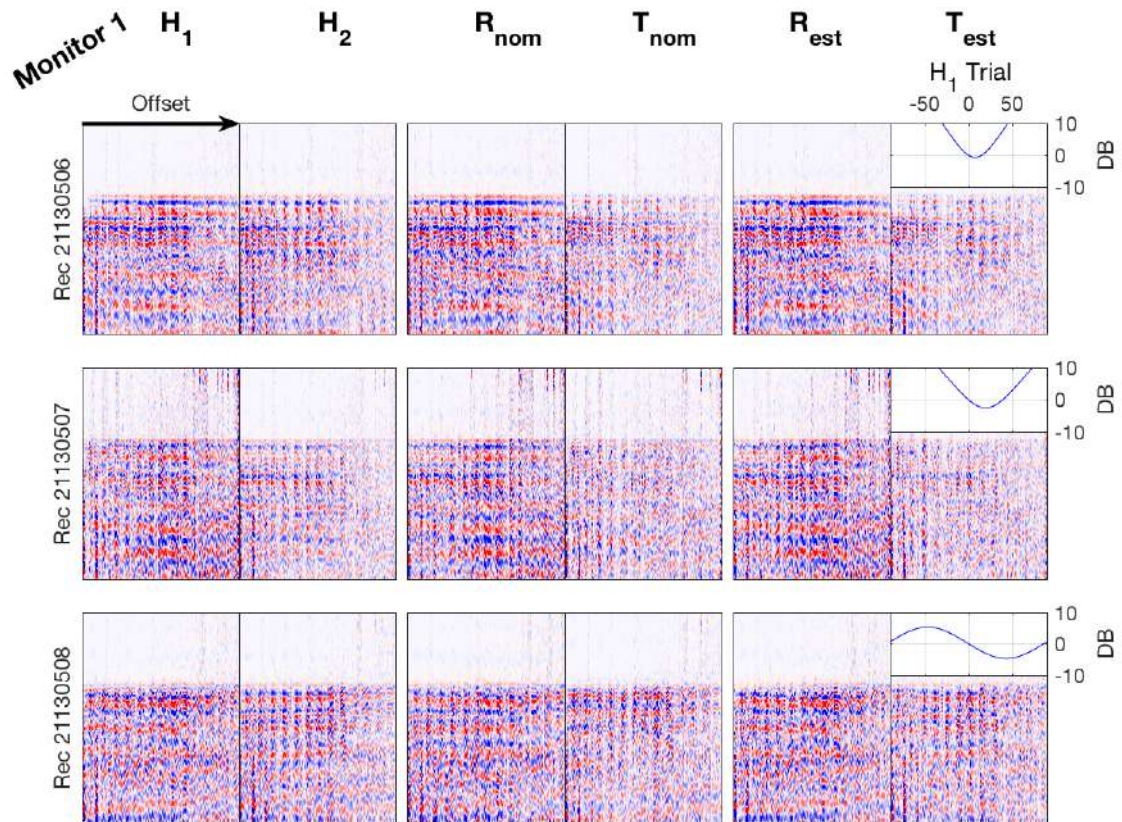
Figure 3.12: H_1 azimuth estimation results. a) Monitor 1 common-receiver gathers. Data are aligned on the P-wave first arrival. H_1, H_2 as acquired in the field, after rotation to radial-transverse assuming $\phi_{H1}^{nom} = 0°$ (R_{nom}, T_{nom}), and after rotation to radial-transverse using the estimated ϕ_{H1}^{est} (R_{est}, T_{est}).
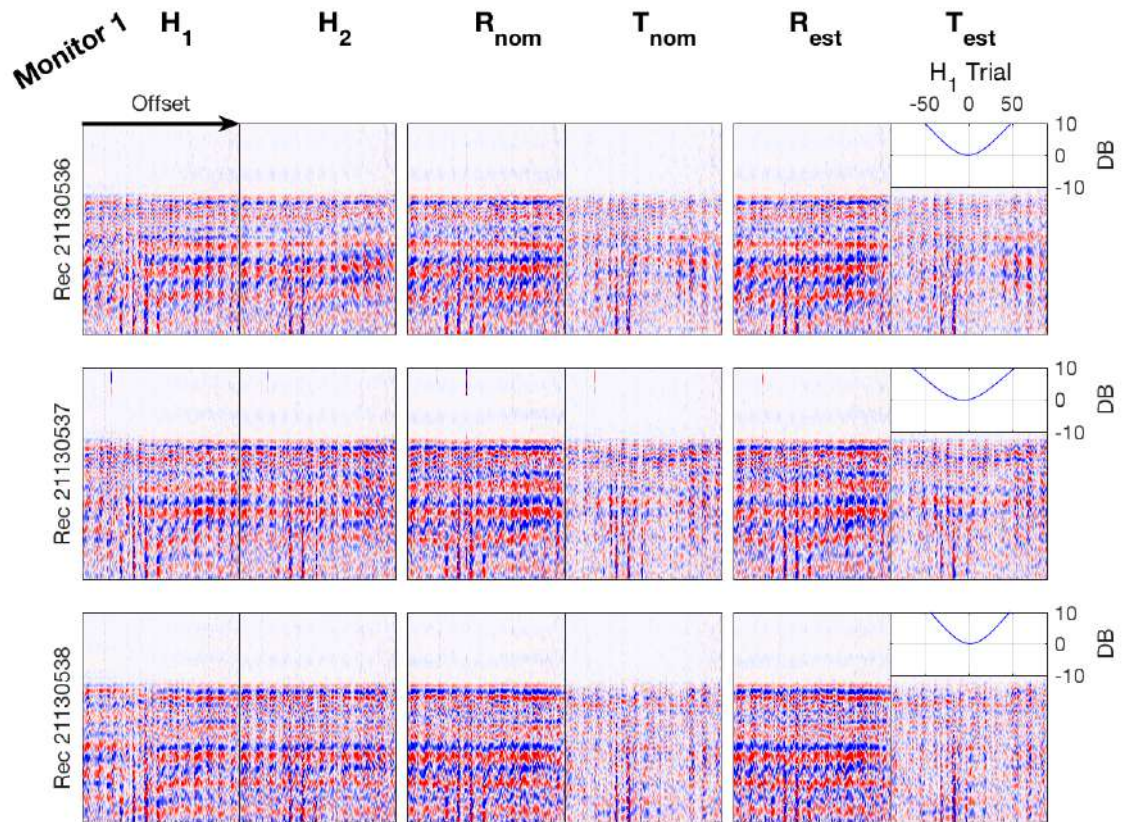
Figure 3.13: H_1 azimuth estimation results. a) Monitor 1 common-receiver gathers. Data are aligned on the P-wave first arrival. H_1, H_2 as acquired in the field, after rotation to radial-transverse assuming $\phi_{H1}^{nom} = 0°$ (R_{nom}, T_{nom}), and after rotation to radial-transverse using the estimated ϕ_{H1}^{est} (R_{est}, T_{est}).
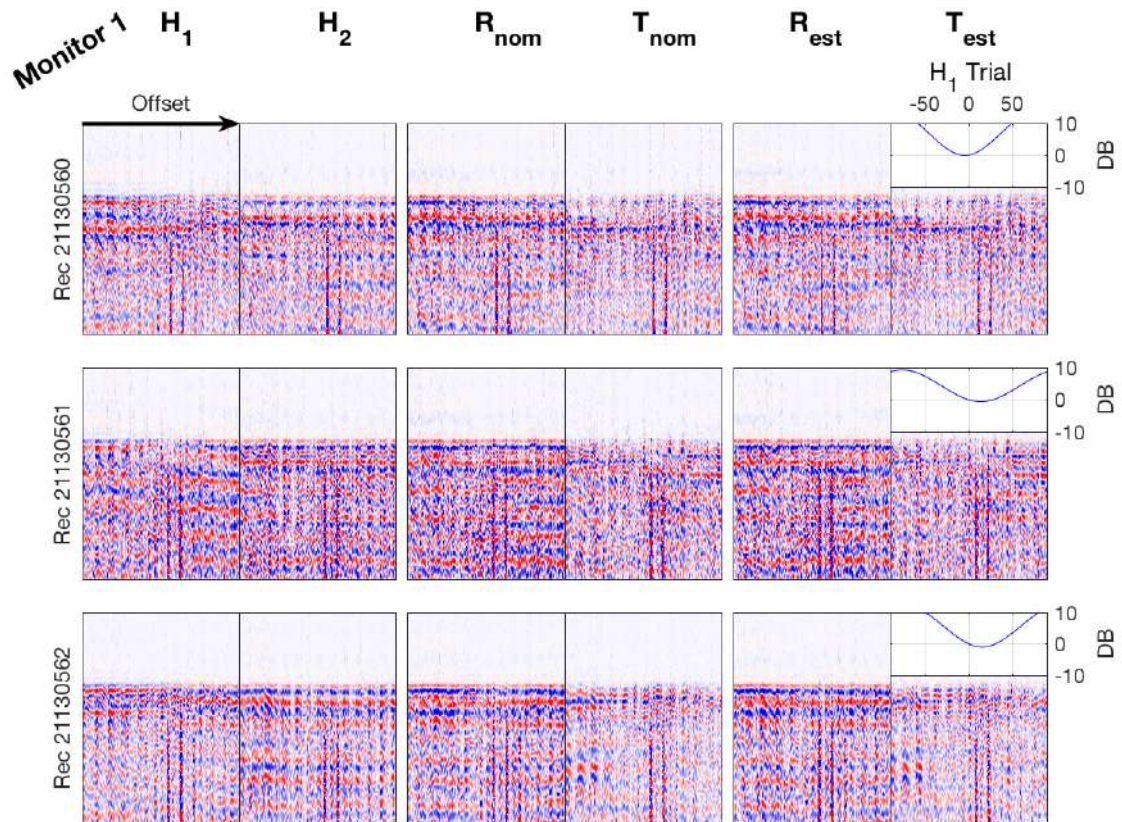
Figure 3.14: H_1 azimuth estimation results. a) Monitor 1 common-receiver gathers. Data are aligned on the P-wave first arrival. H_1, H_2 as acquired in the field, after rotation to radial-transverse assuming $\phi_{H1}^{nom} = 0°$ (R_{nom}, T_{nom}), and after rotation to radial-transverse using the estimated ϕ_{H1}^{est} (R_{est}, T_{est}).
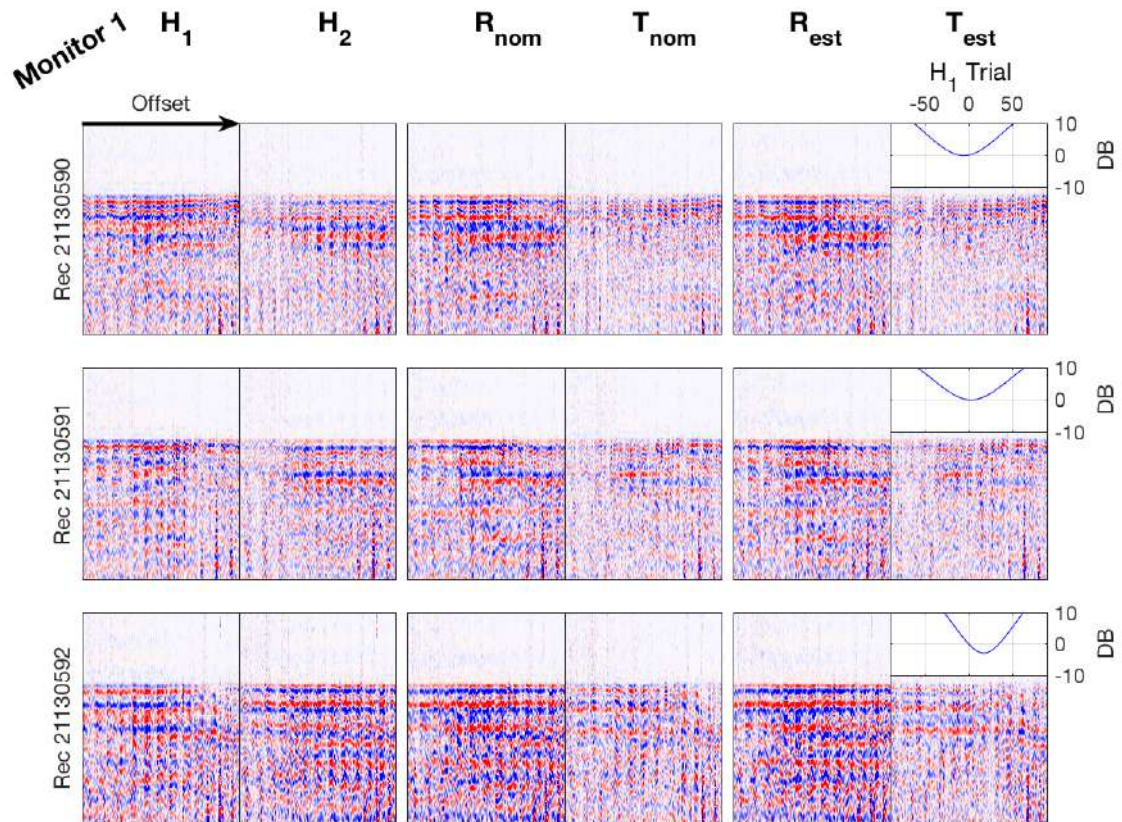
Figure 3.15: H_1 azimuth estimation results. a) Monitor 1 common-receiver gathers. Data are aligned on the P-wave first arrival. H_1, H_2 as acquired in the field, after rotation to radial-transverse assuming $\phi_{H1}^{nom} = 0°$ (R_{nom}, T_{nom}), and after rotation to radial-transverse using the estimated ϕ_{H1}^{est} (R_{est}, T_{est}).
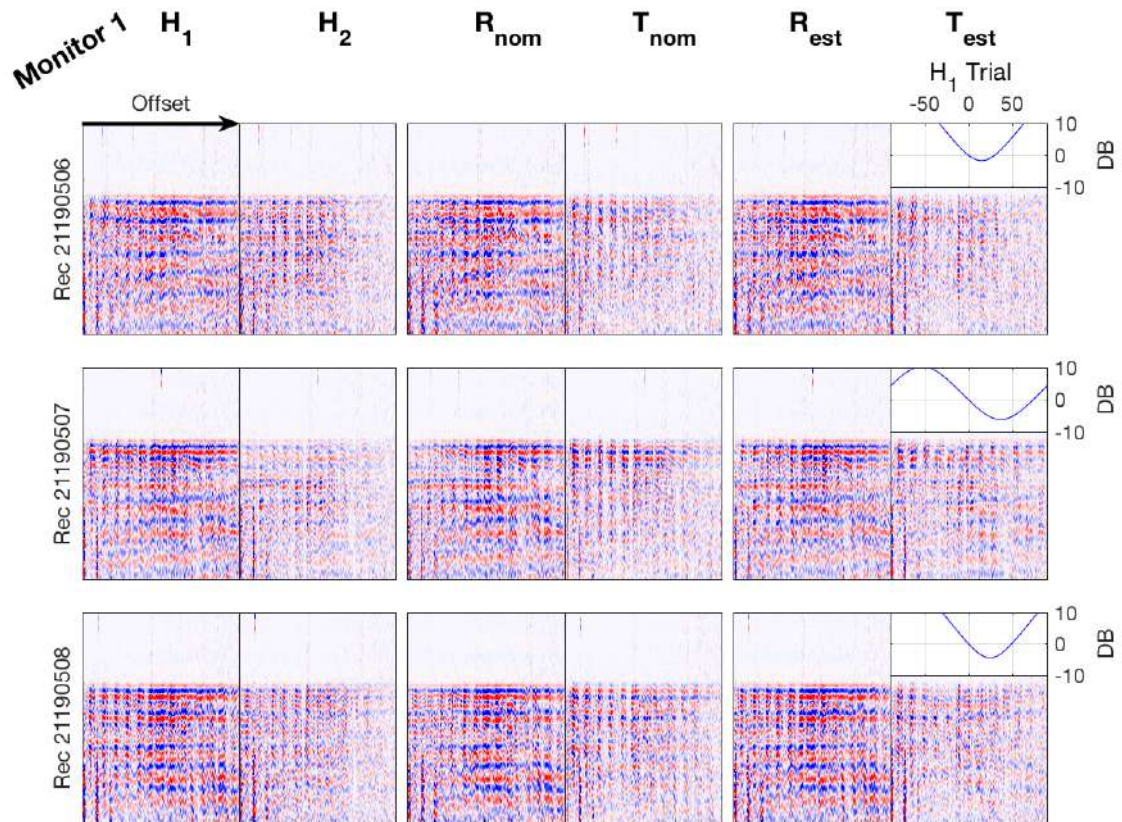
Figure 3.16: H_1 azimuth estimation results. a) Monitor 1 common-receiver gathers. Data are aligned on the P-wave first arrival. H_1, H_2 as acquired in the field, after rotation to radial-transverse assuming $\phi_{H1}^{nom} = 0°$ (R_{nom}, T_{nom}), and after rotation to radial-transverse using the estimated ϕ_{H1}^{est} (R_{est}, T_{est}).
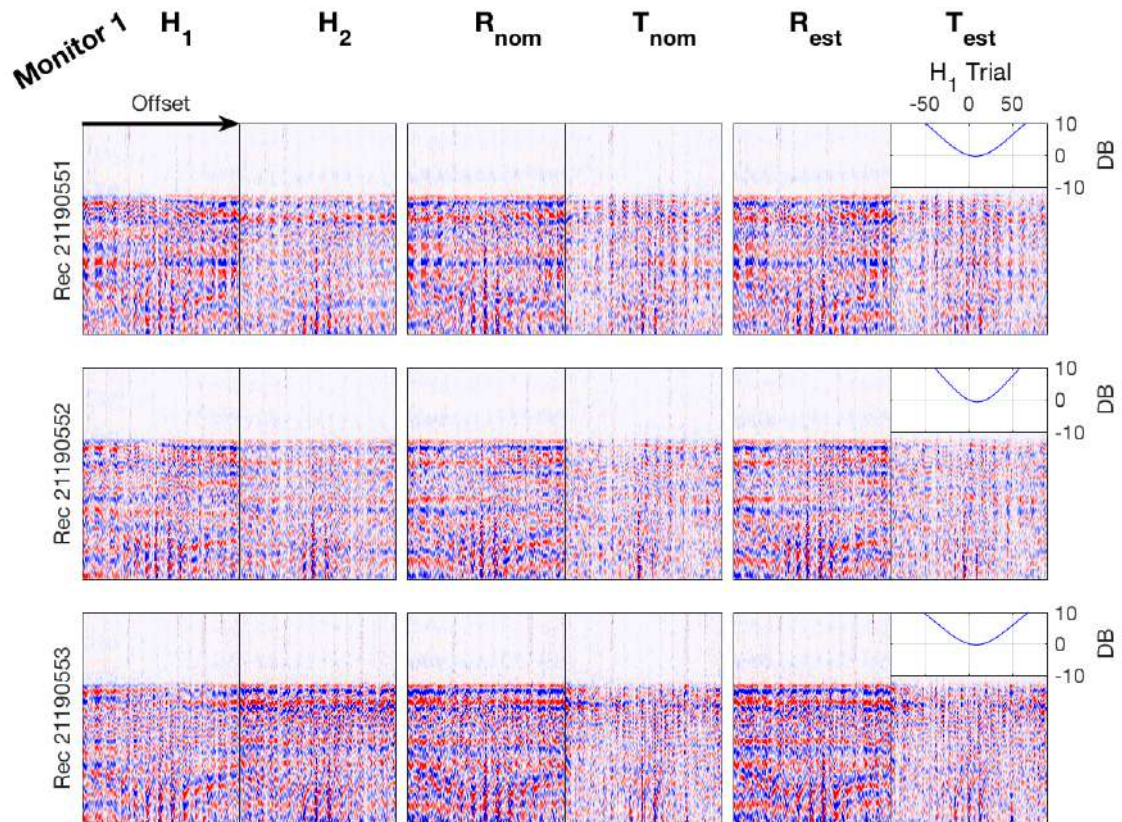
Figure 3.17: H_1 azimuth estimation results. a) Monitor 1 common-receiver gathers. Data are aligned on the P-wave first arrival. H_1, H_2 as acquired in the field, after rotation to radial-transverse assuming $\phi_{H1}^{nom} = 0°$ (R_{nom}, T_{nom}), and after rotation to radial-transverse using the estimated ϕ_{H1}^{est} (R_{est}, T_{est}).

49
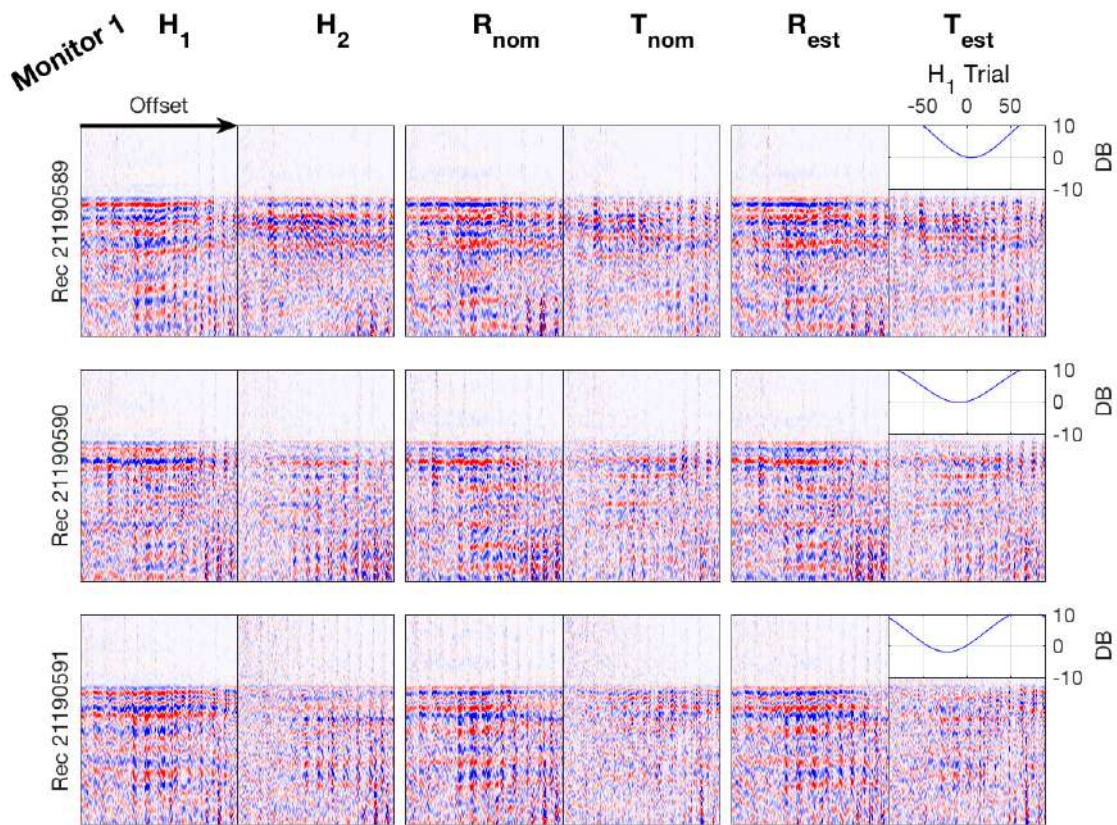
Figure 3.18: H_1 azimuth estimation results. a) Monitor 1 common-receiver gathers. Data are aligned on the P-wave first arrival. H_1, H_2 as acquired in the field, after rotation to radial-transverse assuming $\phi_{H1}^{nom} = 0°$ (R_{nom}, T_{nom}), and after rotation to radial-transverse using the estimated ϕ_{H1}^{est} (R_{est}, T_{est}).
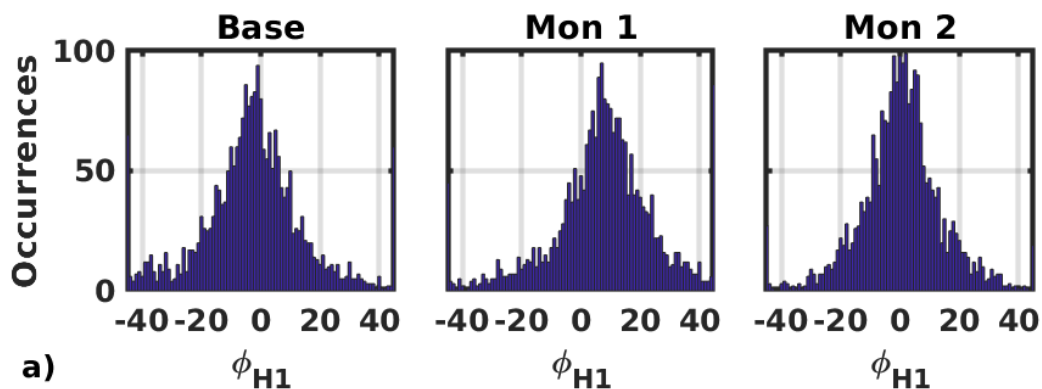
Figure 3.19: Histograms of the ϕ_{H1} estimates from the Baseline, Monitor 1, and Monitor 2 surveys. Baseline and Monitor 2 surveys have their mode near $\phi_{H1} = 0°$, whereas the Monitor 1 mode is shifted to $\phi_{H1} \approx 8°$.

Many of the minima of the objective functions in Figures 3.5 - 3.18 are near the $dB = 0$ line, which means only a very slight reduction in energy on the transverse component. Others show a considerable reduction in transverse energy. The shape of the objective function may be meaningful, in particular, the difference between the maximum and minimum values (the depth of the minimum). For example, in Figure 3.11 the objective function for the receiver in the bottom row has a much smaller difference between the maximum and minimum values, than do the other two gathers. Note that the vertical scale is restricted to ± 10 dB, the actual maximum value over the azimuth scan range may be larger than what is shown.

A conjecture is that the *flatter* objective functions, which have a relatively small difference between maximum and minimum values, may be more uncertain than those objective functions that show more clearly defined minima, and may account for the scatter in the ϕ_{H1} estimates. Histograms of the objective function differences (maximum - minimum) are shown in Figure 3.20 (left), along with the ϕ_{H1}^{est} histograms (middle). The relative asymmetry of the Monitor 1 objective function histogram is most noticeable (left, middle panel). The right column in Figure 3.20 shows histograms of ϕ_{H1}^{est} for the receiver gathers restricted to those with a difference in the objective function ≤ 3 dB. In general, these flatter objective functions account for some of the more anomalous ϕ_{H1}^{est} values, but not all. A number of these values exist at the modes of the ϕ_{H1}^{est} histograms.

Visual inspection of C-wave *reflection data* (receiver gathers in the form of LAS) having $\phi_{H1}^{est} \approx \pm 45°$ was made to qualitatively validate (or not) outliers from the histogram modes. The LAS receiver gathers inspected after applying Equation 3.2 did not show reduced energy on the output transverse component.

The first-arrival ϕ_{H1}^{est} method is successful at finding the values of the histogram modes, in general, but the outliers from the modes are suspect. Noise in the input data is a potential cause, as is potential "out of the sagittal plane" P-wave polarization on the horizontal receivers as pointed out by several authors (Burch et al., 2005).

In the next section I apply the same scan algorithm as shown in Equation 3.2 to C-wave reflection data, LAS of common-receiver gathers, to attempt to obtain more robust ϕ_{H1}^{est} values.
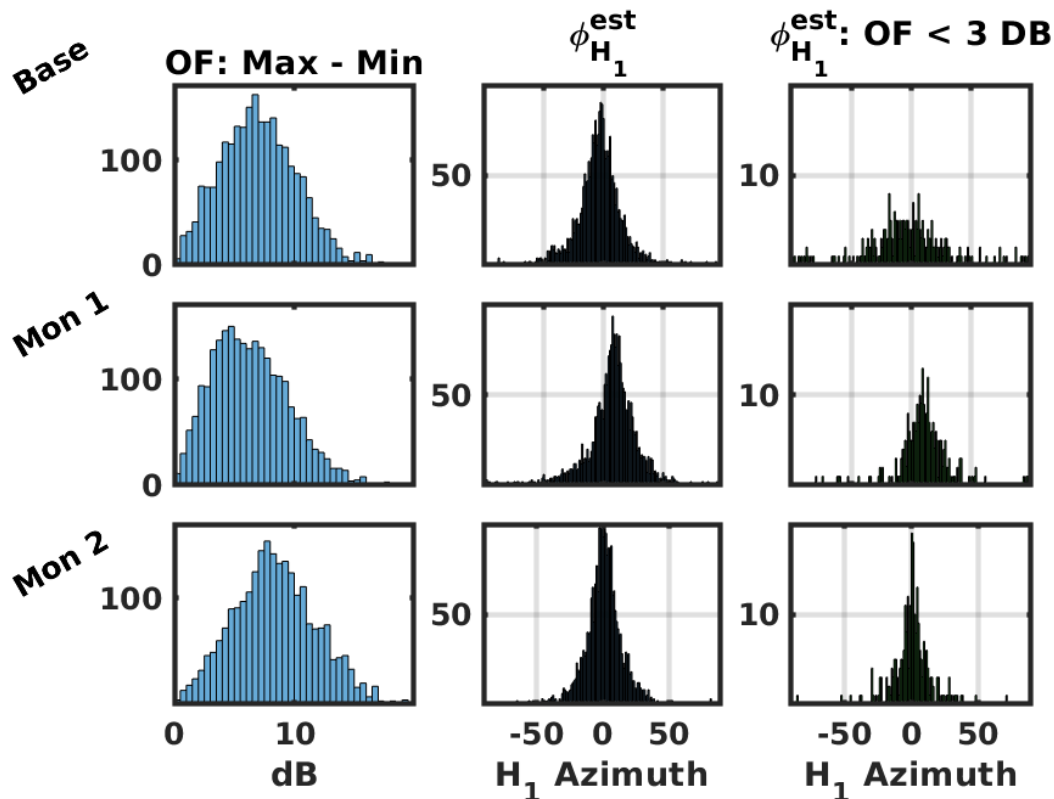
Figure 3.20: Histograms resulting from the P-wave first-arrival method. At the left are histograms of the objective functions *maximum - minimum* values in decibels. These summarize the depth of the objective function minima. In the middle are histograms of the ϕ_{H1}^{est} values. At the right are histograms of ϕ_{H1}^{est} associated with objective function values below 3 dB. The aim is to see if the outliers of the ϕ_{H1}^{est} histograms correlate with *shallow* objective functions. They do to some extent, but values near the ϕ_{H1}^{est} histogram modes also appear.

3.4 Horizontal-Geophone Azimuth Estimation: C-wave Reflection Data

The assumption of a simple earth model used in the P-wave first arrival method does not always hold (Burch et al., 2005). Complexities in the near surface, and noise in the data, complicate the P-wave first arrival amplitudes resulting in unreliable source-receiver azimuths. A possibly more reliable method utilizes reflected C-wave reflections (Gaiser, 2003; Nagarajappa et al., 2013).

The C-wave (P-SV) reflection method also assumes propagation in the sagittal plane (vertical plane between the source and the receiver). In general, C-wave reflections will be recorded on the H_1 and H_2 receiver components, and the scan method can be directly applied. To increase the signal to noise ratio and preserve azimuth information, receiver gather LAS are used. The input data has been fully preprocessed by the data-processing contractor.

Similar to the P-wave first-arrival method, this approach maximizes the C-wave reflection energy on the radial component and minimizes the energy on the transverse component. An optimal ϕ_{H1}^{est} is estimated for each C-wave receiver LAS using the scanning procedure of Equation 3.2 where now C-wave reflections are used to drive the algorithm.

An example of the C-wave reflection-scan output for nine ϕ_{H1}^{trial} values is shown in Figure 3.21. Output R' and T' LAS stacks (20° azimuth sectors) from Equation 3.2 are shown, along with the ϕ_{H1}^{trial} which is indicated in the azimuth icon positioned above each R', T' pair. The time window for analysis is indicated by the black bar (0.9 - 2.2 s) and is restricted to the overburden. Hydraulic fracturing occurred deeper within the Niobrara interval at $\approx$ 2.6s.

For each ϕ_{H1}^{trial}, the RMS energy within the analysis window is measured for the R', T' output of Equation 3.2. Detailed examples are shown in Figures 3.22 - 3.25. The objective function is shown as the solid line produced by scanning over all ϕ_{H1}^{trial}, with the circle showing the objective function value for LAS gathers below. Output transverse energy decreases, and output radial energy increases, as the ϕ_{H1}^{trial} producing the minimum of the objective function is reached Figure 3.24.

The C-wave reflection method is applied to all receiver gather LAS for Baseline, Monitor 1, and Monitor 2 surveys. Histograms of the ϕ_{H1}^{est} values are shown in Figure 3.26, along with the histograms from the P-wave first-arrival method. The reflection method results show similar histogram modes as does the first-arrival method, with considerably less variance in the ϕ_{H1}^{est} values.
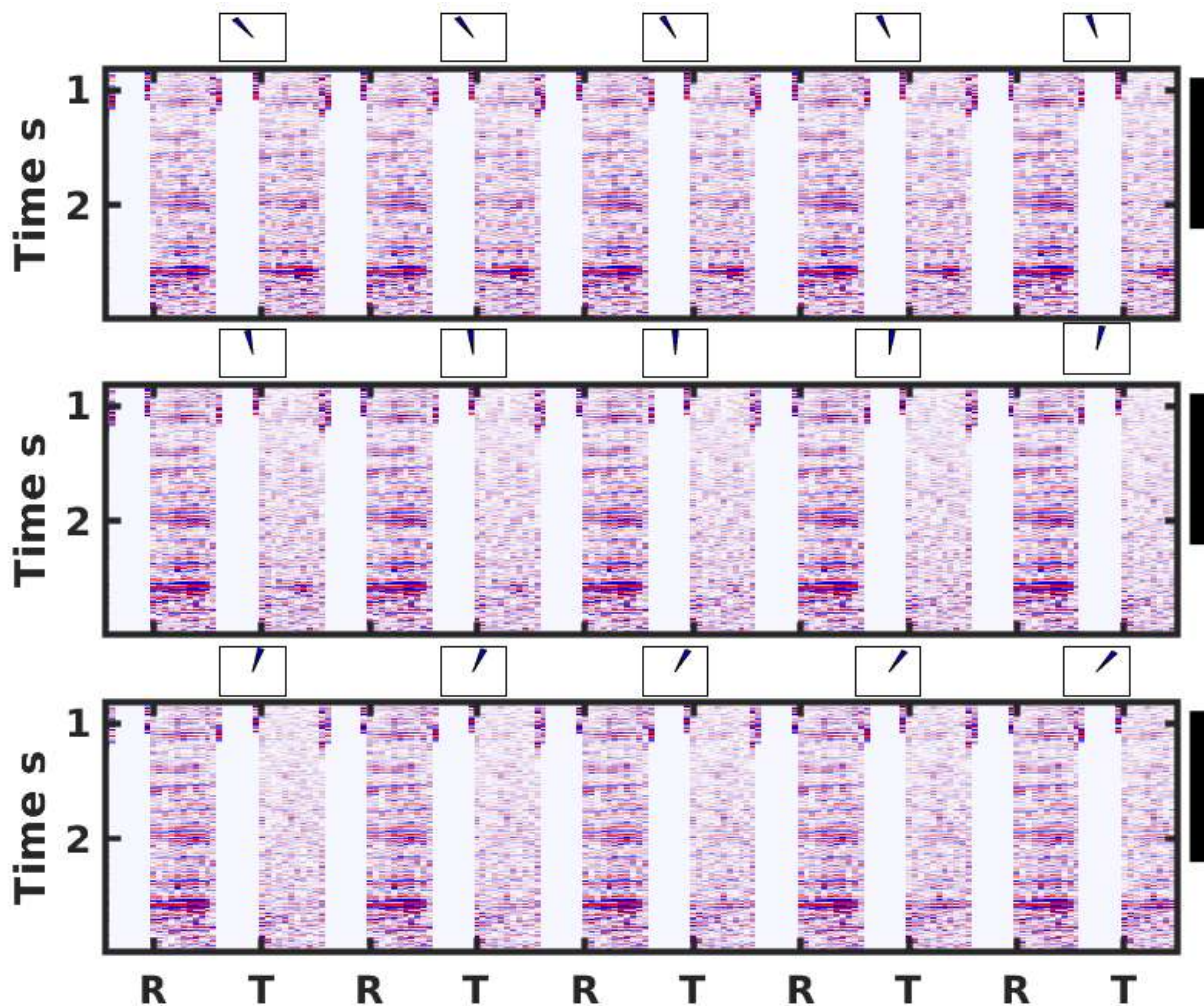
Figure 3.21: C-wave reflection scan method. Radial **R** and Transverse **T** receiver-gather LAS stacks are shown for a single receiver gather (20° azimuth sectors). The azimuth icon above each LAS pair indicates the $\phi_{H_1}^{trial}$ value used in Equation 3.2. The analysis time window is indicated by the black bar, and is restricted to the overburden (the Niobrara is at 2.6 s). The optimal $\phi_{H_1}^{trial}$ minimizes energy on T.
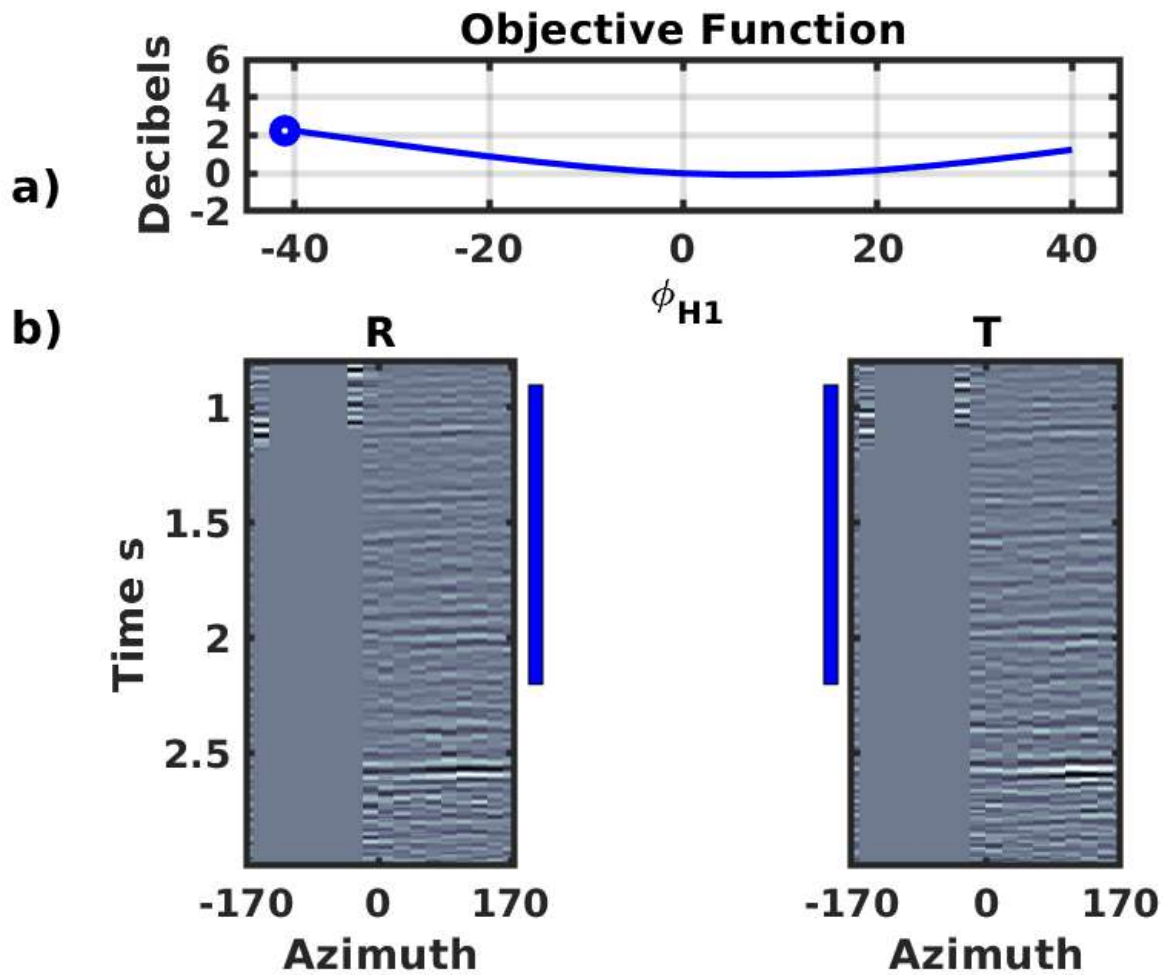
Figure 3.22: Detailed view of the C-wave reflection scanning method. a) The objective function for all ϕ_{H1}^{trial} values (solid line), and the current trial value (blue circle). b) Output LAS using the current trial value. Note the similarity of **R** and **T** when the trial value is far from the objective function minimum.
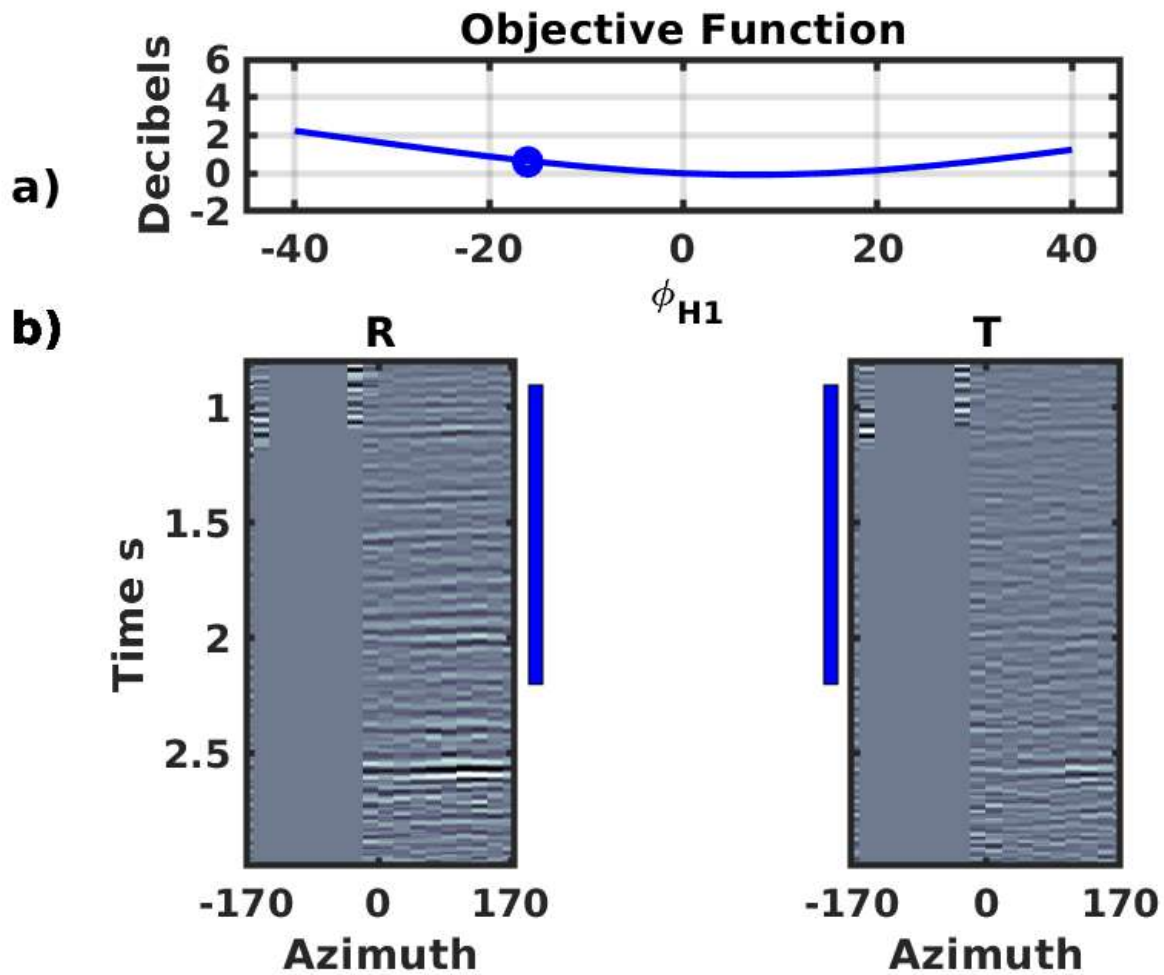
Figure 3.23: Detailed view of the C-wave reflection scanning method. a) The objective function for all ϕ_{H1}^{trial} values (solid line), and the current trial value (blue circle). b) Output LAS using the current trial value. As the trial value approaches the objective function minimum, energy on $\mathbf{T}$ is reduced relative to $\mathbf{R}$.
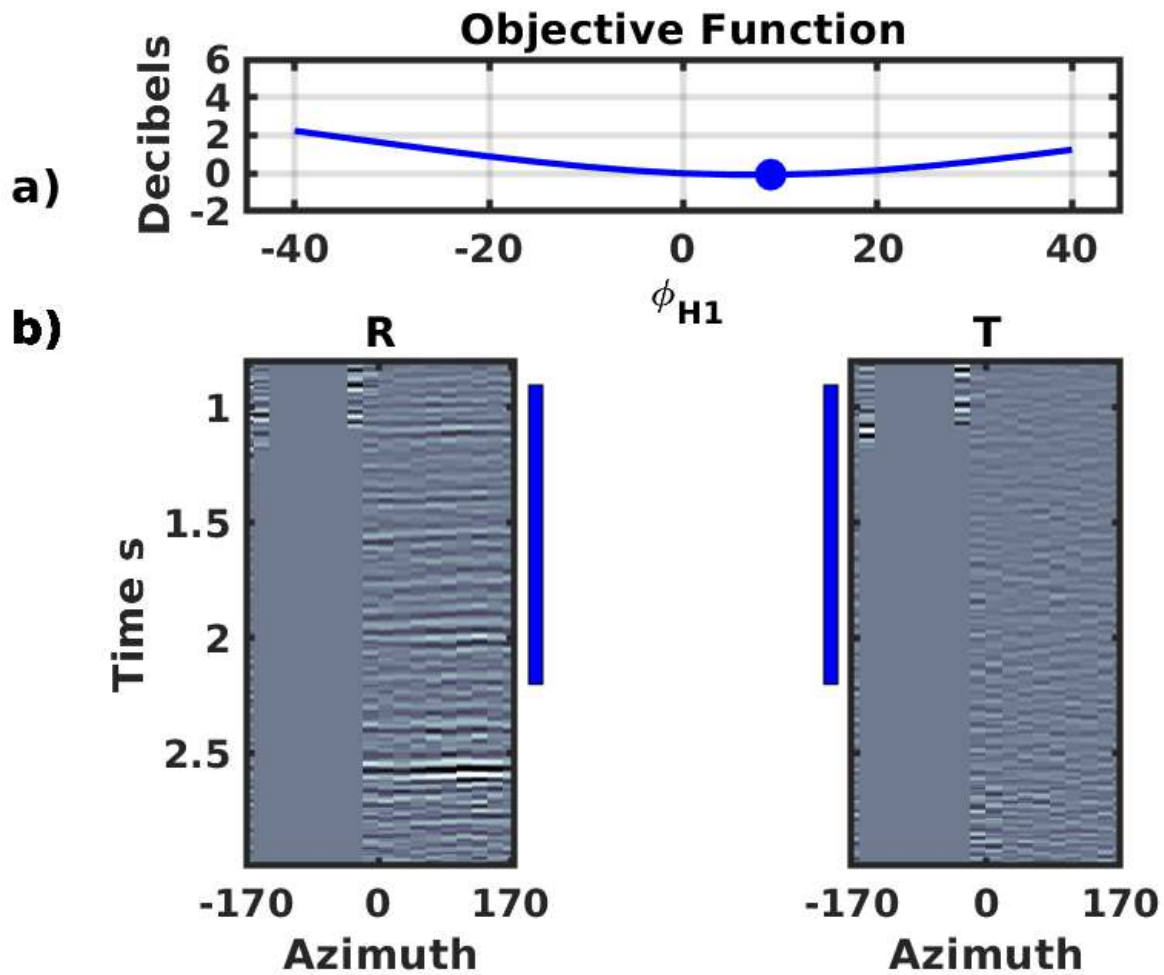
Figure 3.24: Detailed view of the C-wave reflection scanning method. a) The objective function for all ϕ_{H1}^{trial} values (solid line), and the current trial value (blue circle). b) Output LAS using the current trial value. At the objective function minimum, there is no coherent energy on **T**, and the energy on **R** is maximized.
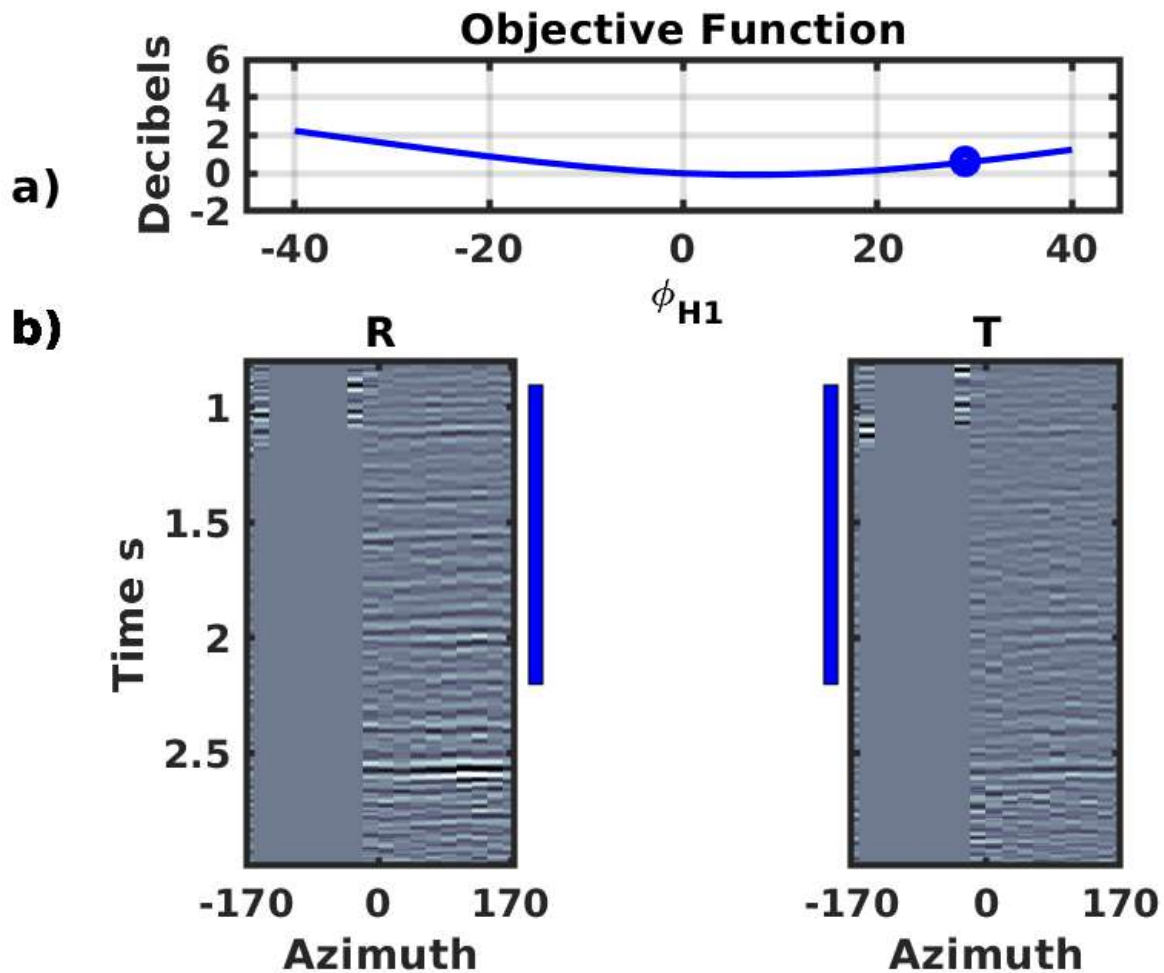
Figure 3.25: Detailed view of the C-wave reflection scanning method. a) The objective function for all ϕ_{H1}^{trial} values (solid line), and the current trial value (blue circle). b) Output LAS using the current trial value. Energy increases on **T** as ϕ_{H1}^{trial} moves away from the objective function minimum.

The C-wave reflection method is considerably more robust, in that the spread of the histograms is less, than is the first-arrival method. It is interesting, however, that both approaches give similar estimates of the histogram modes, and recognize the "global skew" of $\phi_{H1} \approx 8°$ for Monitor 1. This skew is most likely due to confusion between true North versus magnetic North during geophone layout.

Results from the C-wave method are judged to be more reliable and are used to optimally rotate the C-wave and S-wave data to radial-transverse coordinates for all three surveys.
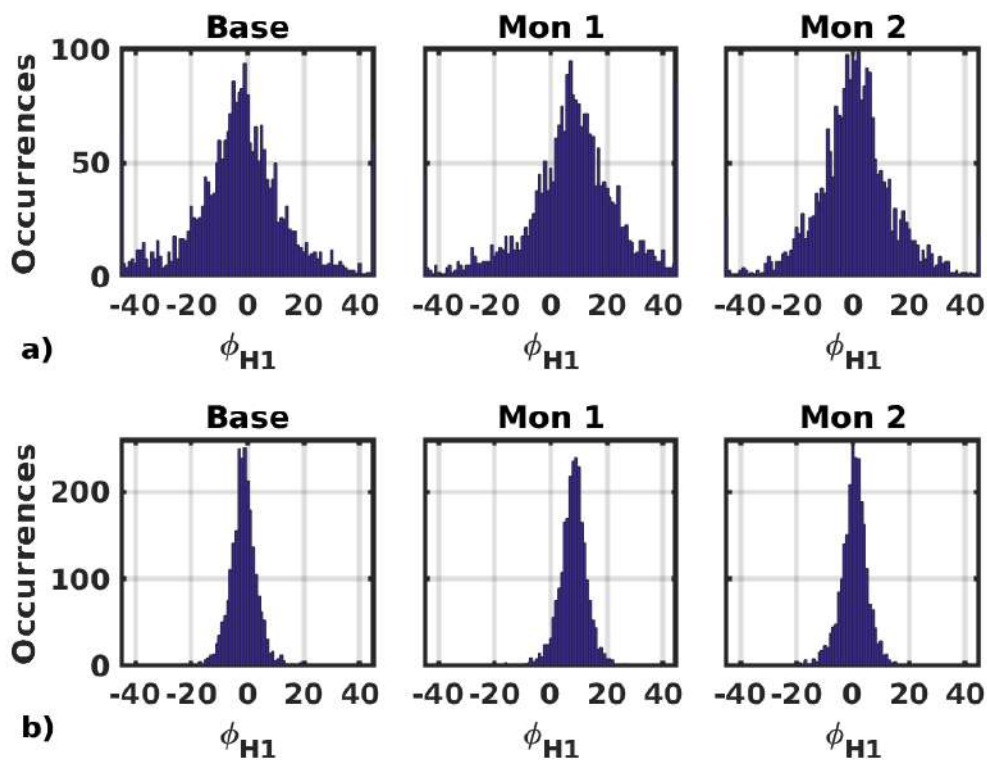
Figure 3.26: ϕ_{H1}^{est} comparison. a) P-wave first-arrival method. b) C-wave reflection-stack method. The two approaches give very similar histogram modes, but the C-wave reflection-stack method has reduced scatter about the modes.

3.5 Cross-Component Shear-Wave Leakage Compensation

Preprocessed data were provided as **R**, **T**, **RR**, **RT**, **TR**, and **TT** gathers. These data were rotated back to field coordinates using $\phi_{H1} = 0°$, and then rotated to radial-transverse coordinates using the ϕ_{H1}^{est} values from the reflection-stack method.

59

The large and apparent global skew in the H_1 azimuth from the Monitor 1 survey was easily identified with the P-wave first arrival approach, but it is difficult to confidently utilize the H_1 estimates for local rotations on Baseline, Monitor 1, and Monitor 2. Although the local variations in the P-wave first arrival histograms were not reliable, the modes indicate the global H_1 orientations. Histograms from the reflection-stack method have the same modes as the P-wave first arrival method with more reliable local variations for H_1 azimuth estimates (Figure 3.26).

The reflection-stack ϕ_{H1}^{est} values for each receiver are used to optimally rotate the Baseline, Monitor 1, and Monitor 2 data into radial-transverse coordinates. COCA gather comparisons are shown in Figures 3.28 - 3.42.
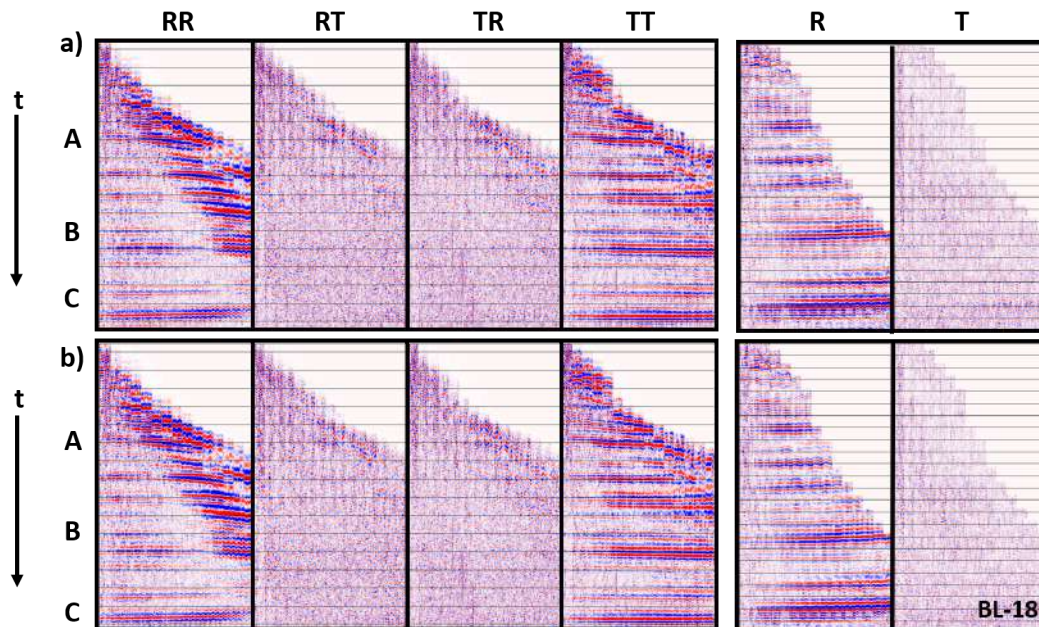
Figure 3.27: Baseline COCA gathers. a) S-wave (**RR**, **RT**, **TR**, **TT**) and C-wave (**R**, **T**) obtained using the nominal $\phi_{H1}^{nom} = 0°$. b) COCA gathers obtained using the C-wave reflection scan ϕ_{H1}^{est} values.
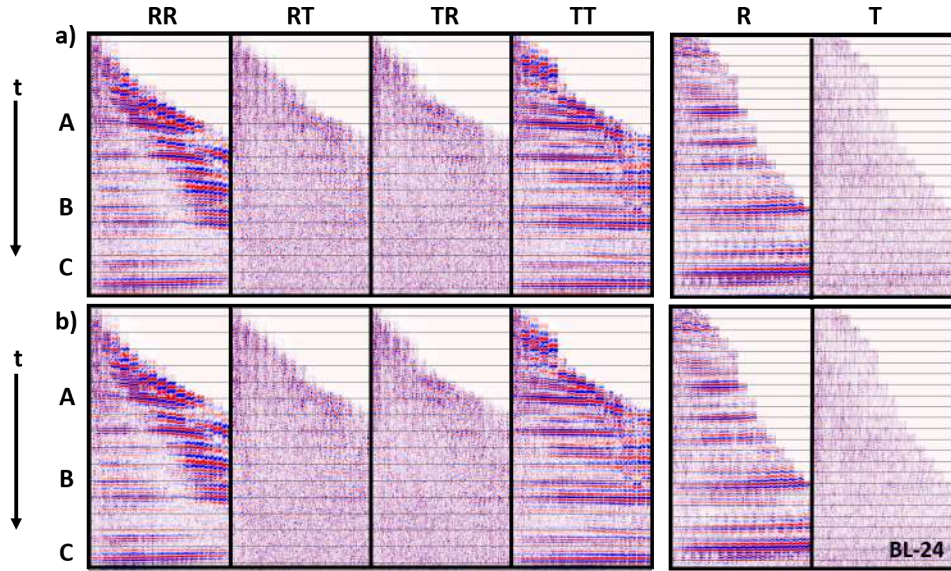
Figure 3.28: Baseline COCA gathers. a) S-wave (**RR**, **RT**, **TR**, **TT**) and C-wave (**R**, **T**) obtained using the nominal $\phi_{H1}^{nom} = 0°$. b) COCA gathers obtained using the C-wave reflection scan ϕ_{H1}^{est} values.
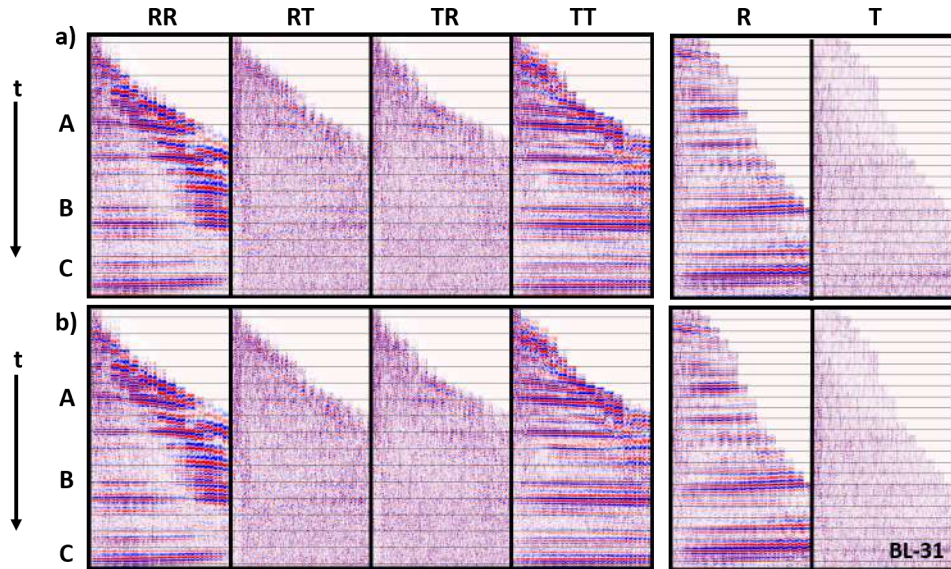
Figure 3.29: Baseline COCA gathers. a) S-wave (**RR**, **RT**, **TR**, **TT**) and C-wave (**R**, **T**) obtained using the nominal $\phi_{H1}^{nom} = 0°$. b) COCA gathers obtained using the C-wave reflection scan ϕ_{H1}^{est} values.
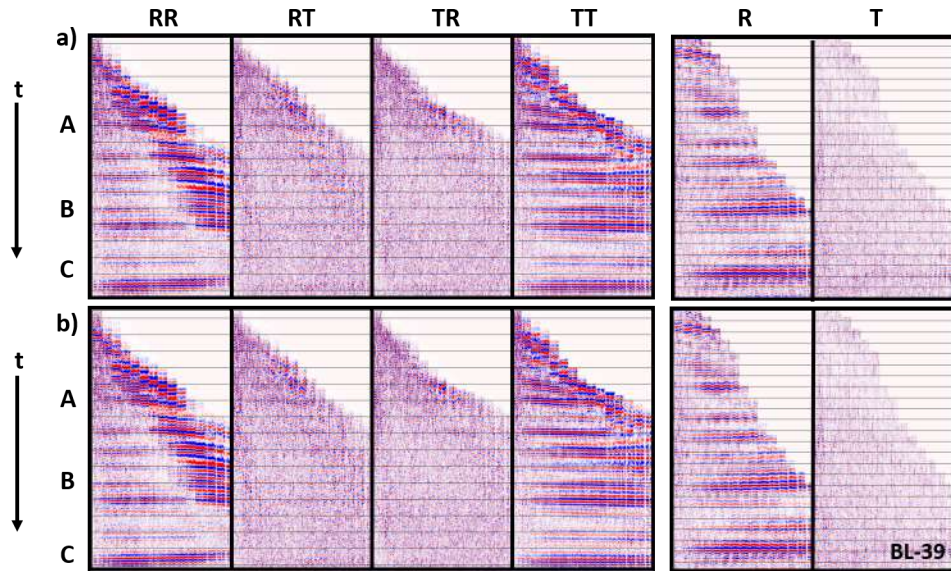
Figure 3.30: Baseline COCA gathers. a) S-wave (**RR**, **RT**, **TR**, **TT**) and C-wave (**R**, **T**) obtained using the nominal $\phi_{H1}^{nom} = 0°$. b) COCA gathers obtained using the C-wave reflection scan ϕ_{H1}^{est} values.
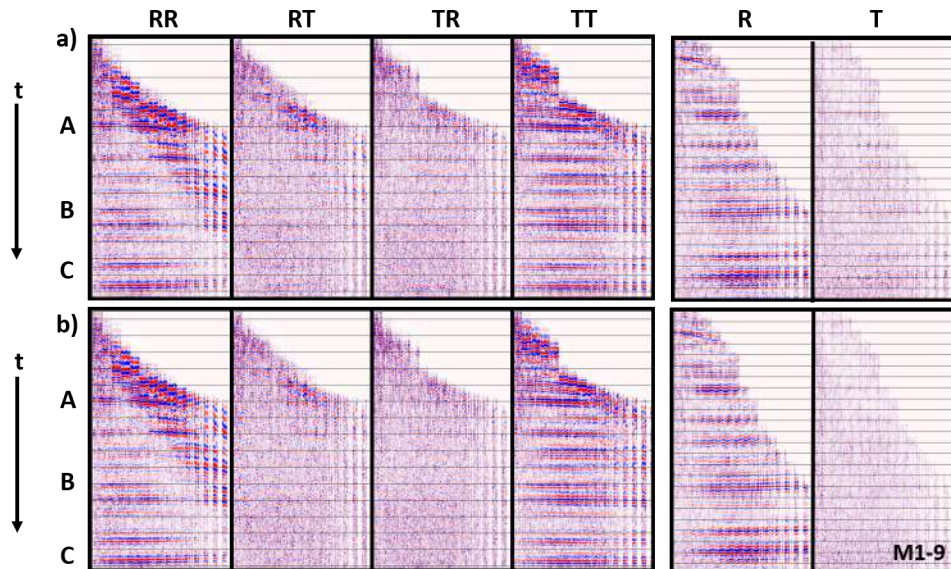
Figure 3.31: Monitor 1 COCA gathers. a) S-wave (**RR**, **RT**, **TR**, **TT**) and C-wave (**R**, **T**) obtained using the nominal $\phi_{H1}^{nom} = 0°$. b) COCA gathers obtained using the C-wave reflection scan ϕ_{H1}^{est} values.
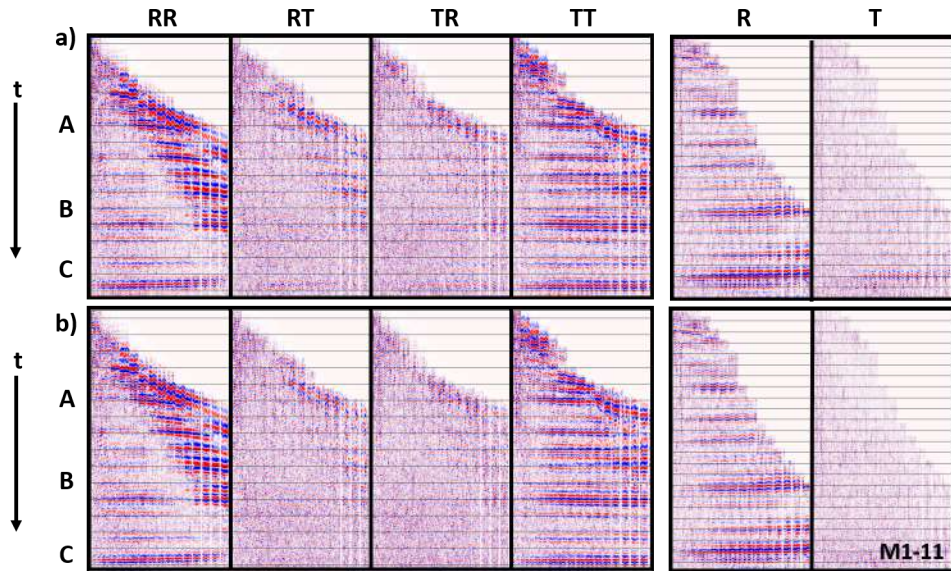
Figure 3.32: Monitor 1 COCA gathers. a) S-wave (**RR**, **RT**, **TR**, **TT**) and C-wave (**R**, **T**) obtained using the nominal $\phi_{H1}^{nom} = 0°$. b) COCA gathers obtained using the C-wave reflection scan ϕ_{H1}^{est} values.
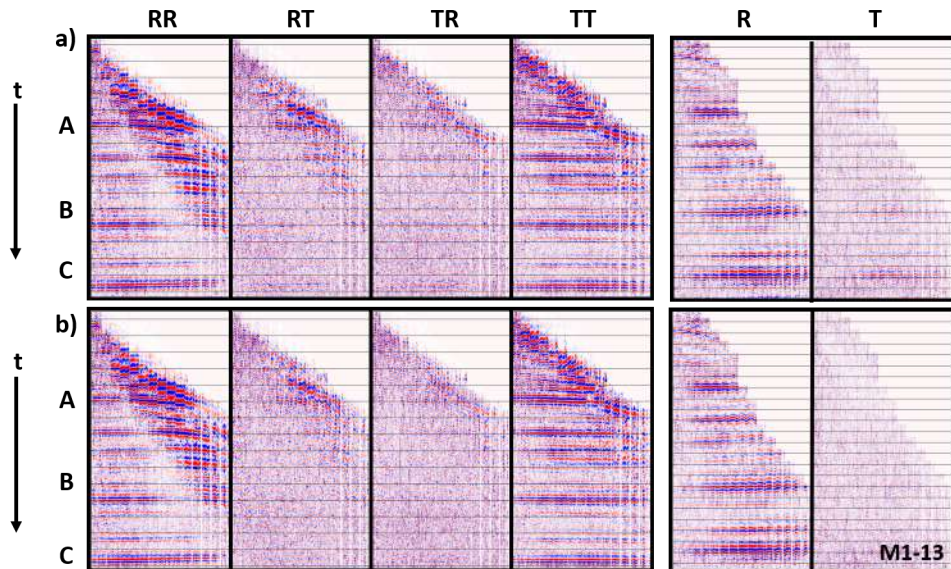
Figure 3.33: Monitor 1 COCA gathers. a) S-wave (**RR**, **RT**, **TR**, **TT**) and C-wave (**R**, **T**) obtained using the nominal $\phi_{H1}^{nom} = 0°$. b) COCA gathers obtained using the C-wave reflection scan ϕ_{H1}^{est} values.
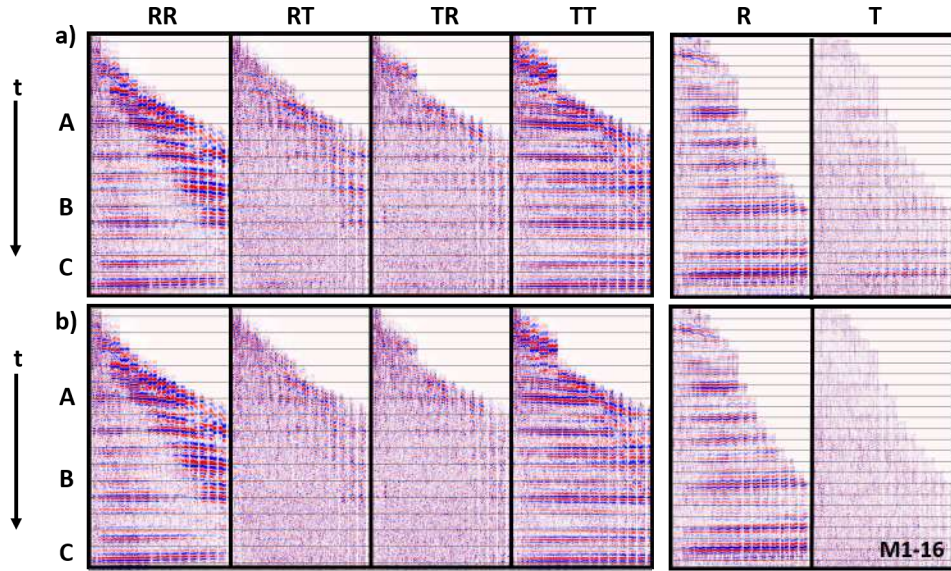
Figure 3.34: Monitor 1 COCA gathers. a) S-wave (**RR**, **RT**, **TR**, **TT**) and C-wave (**R**, **T**) obtained using the nominal $\phi_{H1}^{nom} = 0°$. b) COCA gathers obtained using the C-wave reflection scan ϕ_{H1}^{est} values.
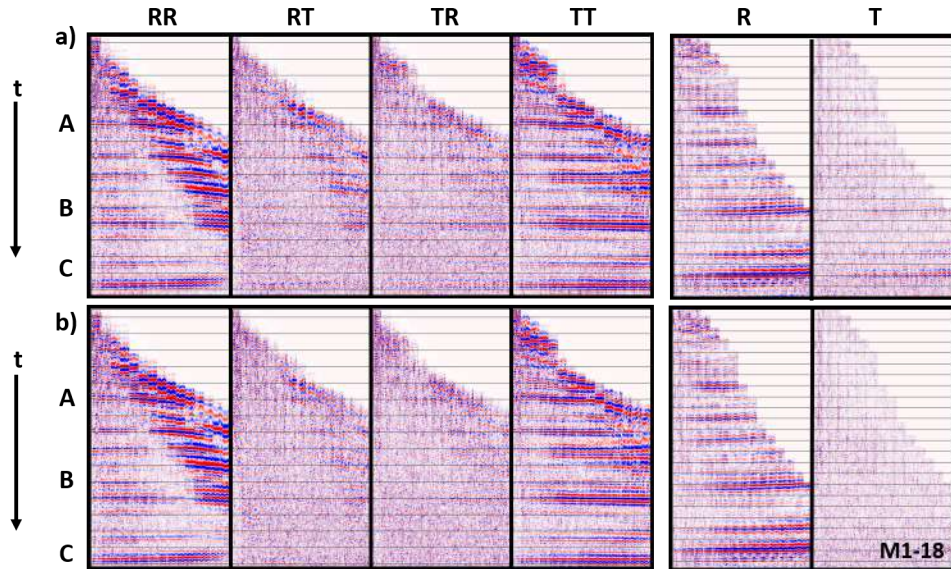
Figure 3.35: Monitor 1 COCA gathers. a) S-wave (**RR**, **RT**, **TR**, **TT**) and C-wave (**R**, **T**) obtained using the nominal $\phi_{H1}^{nom} = 0°$. b) COCA gathers obtained using the C-wave reflection scan ϕ_{H1}^{est} values.
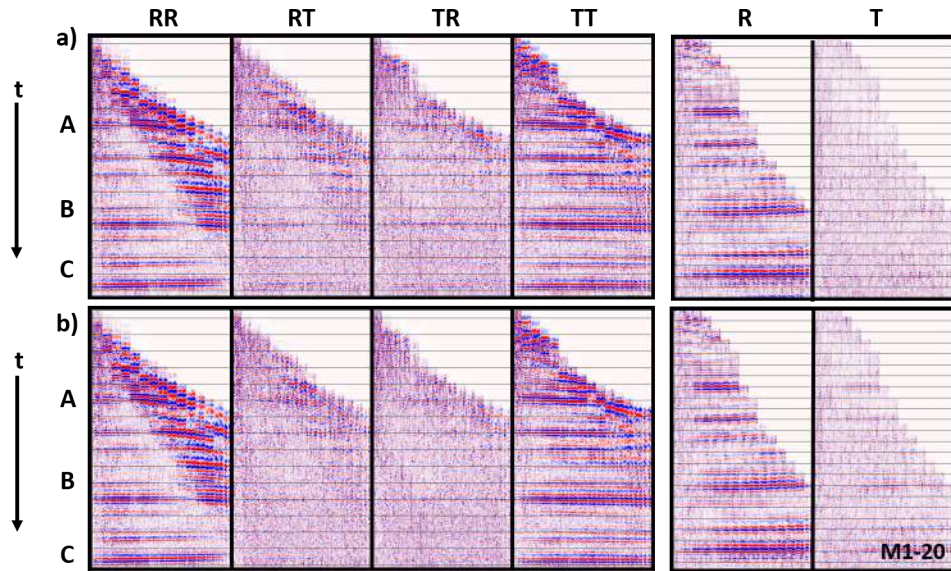
Figure 3.36: Monitor 1 COCA gathers. a) S-wave (**RR**, **RT**, **TR**, **TT**) and C-wave (**R**, **T**) obtained using the nominal $\phi_{H1}^{nom} = 0°$. b) COCA gathers obtained using the C-wave reflection scan ϕ_{H1}^{est} values.
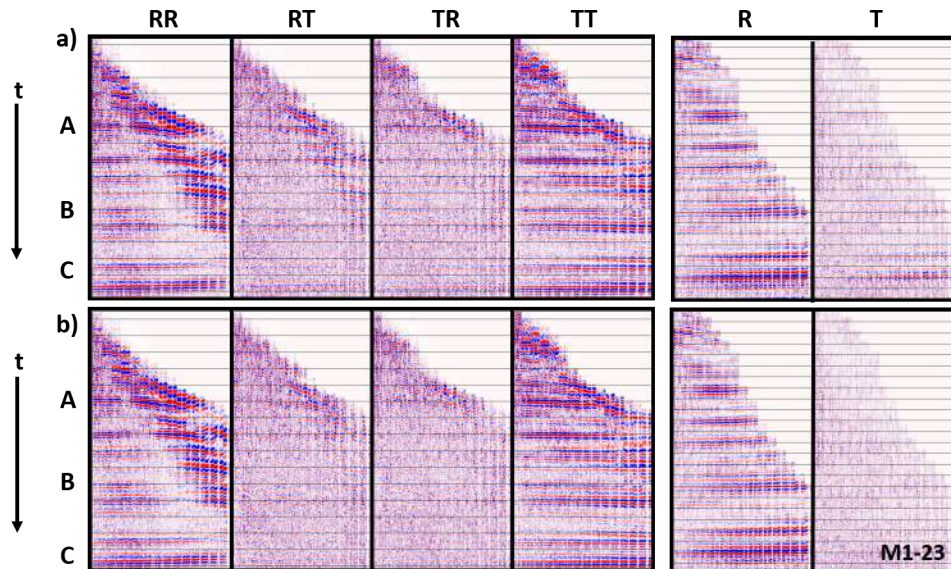
Figure 3.37: Monitor 1 COCA gathers. a) S-wave (**RR**, **RT**, **TR**, **TT**) and C-wave (**R**, **T**) obtained using the nominal $\phi_{H1}^{nom} = 0°$. b) COCA gathers obtained using the C-wave reflection scan ϕ_{H1}^{est} values.
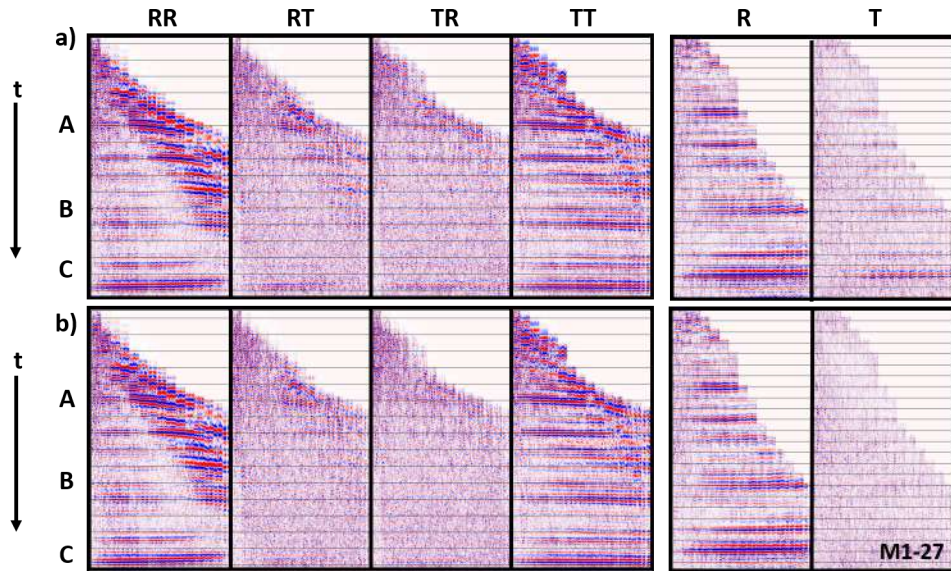
Figure 3.38: Monitor 1 COCA gathers. a) S-wave (**RR**, **RT**, **TR**, **TT**) and C-wave (**R**, **T**) obtained using the nominal $\phi_{H1}^{nom} = 0°$. b) COCA gathers obtained using the C-wave reflection scan ϕ_{H1}^{est} values.
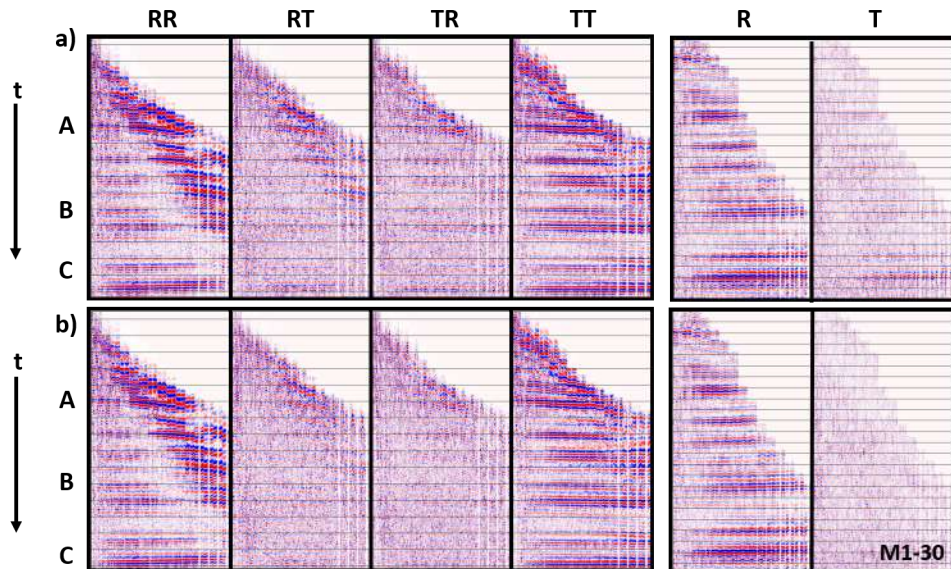
Figure 3.39: Monitor 1 COCA gathers. a) S-wave (**RR**, **RT**, **TR**, **TT**) and C-wave (**R**, **T**) obtained using the nominal $\phi_{H1}^{nom} = 0°$. b) COCA gathers obtained using the C-wave reflection scan ϕ_{H1}^{est} values.

66
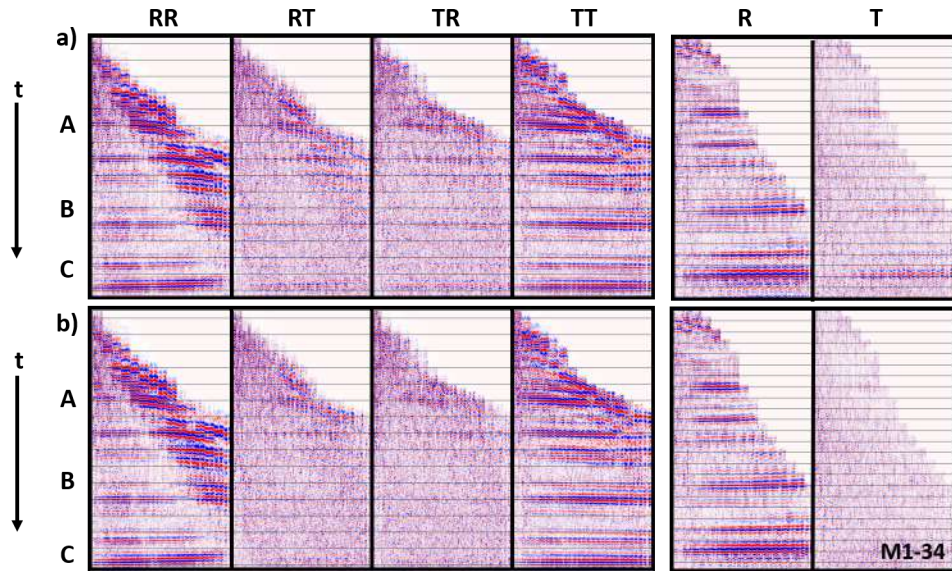
Figure 3.40: Monitor 1 COCA gathers. a) S-wave (**RR**, **RT**, **TR**, **TT**) and C-wave (**R**, **T**) obtained using the nominal $\phi_{H1}^{nom} = 0°$. b) COCA gathers obtained using the C-wave reflection scan ϕ_{H1}^{est} values.
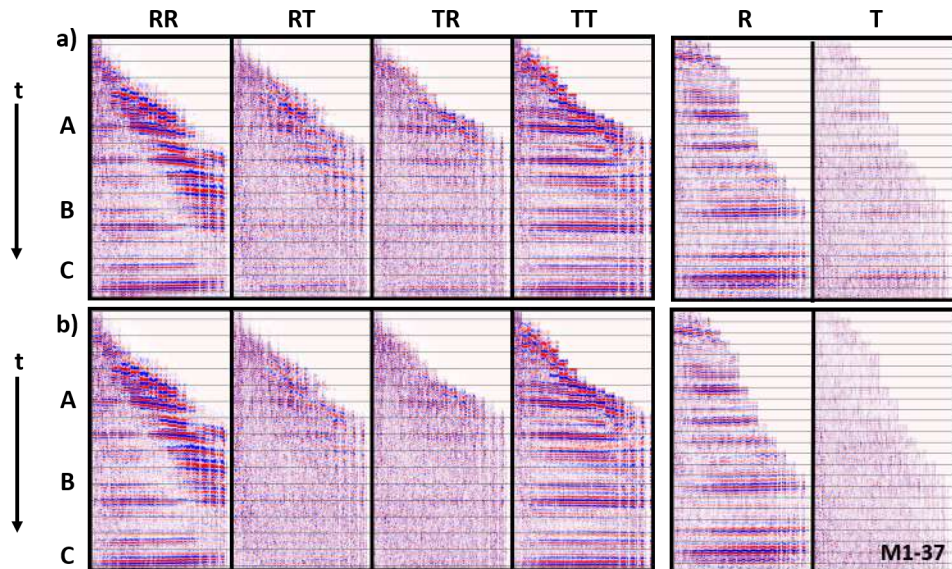
Figure 3.41: Monitor 1 COCA gathers. a) S-wave (**RR**, **RT**, **TR**, **TT**) and C-wave (**R**, **T**) obtained using the nominal $\phi_{H1}^{nom} = 0°$. b) COCA gathers obtained using the C-wave reflection scan ϕ_{H1}^{est} values.

67
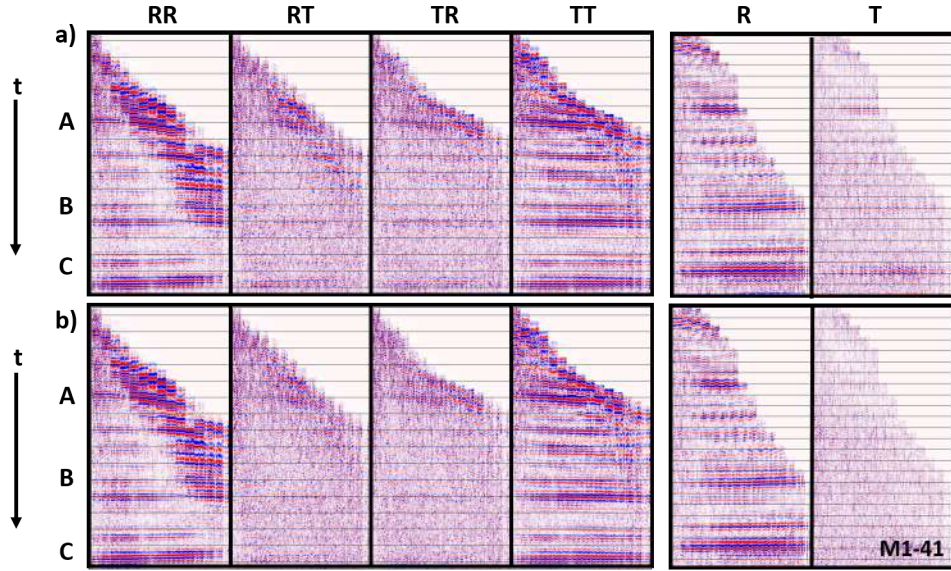
Figure 3.42: Monitor 1 COCA gathers. a) S-wave (**RR**, **RT**, **TR**, **TT**) and C-wave (**R**, **T**) obtained using the nominal $\phi_{H1}^{nom} = 0°$. b) COCA gathers obtained using the C-wave reflection scan ϕ_{H1}^{est} values.

Cross-component energy is reduced, in general, after using the ϕ_{H1}^{est} values, particularly for the Monitor 1 data. A verification in a different form is shown in Figure 3.43. These data are a single azimuth-sectored stack ($20° - 0°$, $-10°$ central angle) of the C-wave **T** component for all receiver gathers from Monitor 1. These are ordered arbitrarily from left to right within a the panel. The left panel shows the data received from the processing contractor which assumed $\phi_{H1}^{nom} = 0°$. The panel at the right shows the data after using the ϕ_{H1}^{est} values from the C-wave reflection-stack method.

Note the coherent energy in the overburden (expected to be isotropic) at ≈ 2.0, and the energy at the Niobrara level at ≈ 2.5 s on the left panel. These energy is considerably reduced upon using the ϕ_{H1}^{est} values in the radial-transverse rotation (right panel).

3.6   Discussion

The P-wave first arrival method identified, and corrected for, the global error of the Monitor 1 H_1 field-azimuth orientations. Cross-component leakage is removed, to first-order, by this compensation. The key step was recognizing the characteristics of the leakage on

Mon1: Transverse, C-wave: Receiver Stacks; Azimuth = -10

$H_1 = 0$ $H_1 =$ **Estimates**
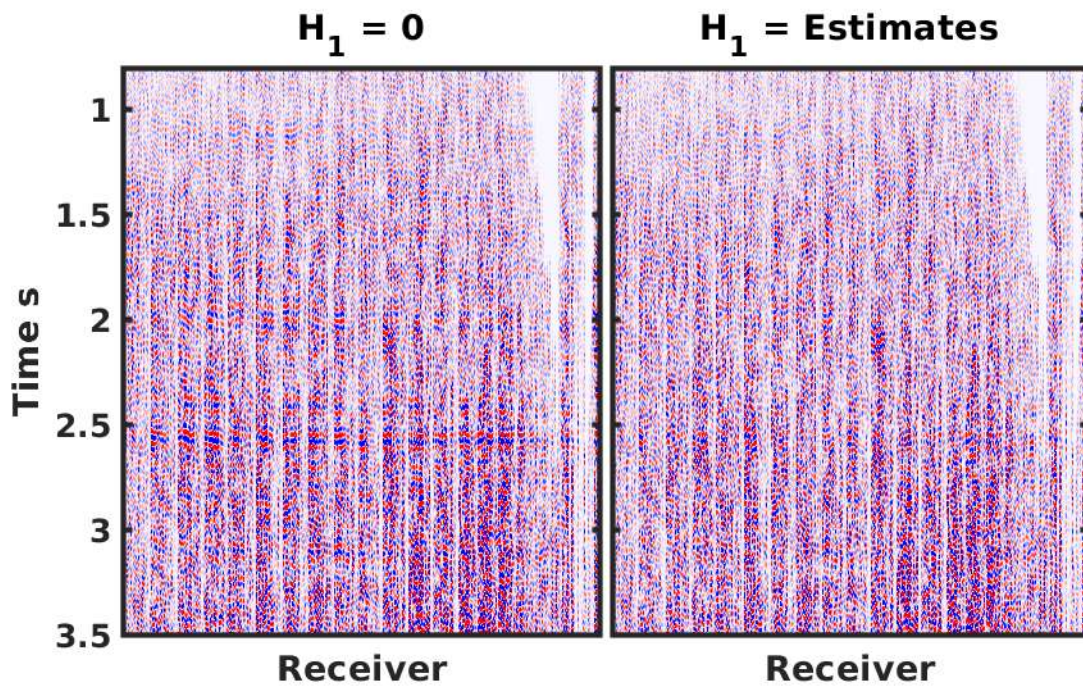
Figure 3.43: Monitor 1, transverse component (T) common-receiver, azimuth-sector stack, for the azimuth sector from $0° - 20°$. Each trace is a stack of the moveout-corrected $0° - 20°$ azimuth sector for each common-receiver gather (arbitrarily ordered). Left) Using $\phi_{H1}^{nom} = 0°$ from the production processing. Right) Using the ϕ_{H1}^{est} values from the reflection-stack method. Note the energy on the left panel, and the reduction in energy when the radial-transverse rotation is properly applied.

prestack S-wave and C-wave COCA gathers, and then using prestack modeling to verify the hypothesis that the leakage is caused by a global H_1 azimuth mis-orientation.

Histograms for both methods display a spread of H_1 orientations around the mode for each survey (Figure 3.26). This histogram spread could be masking shear-wave splitting signal, since the magnitude of the splitting is expected to be small ($\approx$ 2-7 ms for S-wave splitting, $\approx$ 1-3 ms for C-wave splitting, depending on the thickness of the fractured interval), and vary laterally (Omar, 2018).

The histogram spread from the P-wave first arrival method was not reliable and could not be used for local H_1 rotations. The C-wave reflection-stack approach produced more reliable estimates, and these ϕ_{H1}^{est} values were used to correctly rotate the C-wave and S-wave data into radial-transverse coordinates.

C-wave COCA gather analysis confirmed our hypothesis of a global H_1 orientation error. Lacking C-wave data, it would have been difficult to determine whether the acquisition orientation issue was receiver side, source side, shear-source non-orthogonality, or some combination thereof. We recommend such analysis as a standard for multicomponent data processing.

In addition, the P-wave first arrival method should be applied early in the processing sequence to determine an initial ϕ_{H1}^{nom} value for radial-transverse rotation. After data preprocessing, the C-wave reflection-stack method could be applied to refine the radial-transverse rotation to the data input to migration (Simmons and Backus, 2001b).

CHAPTER 4

SPARSE-LAYER REFLECTIVITY INVERSION

4.1 Introduction

The ultimate goal in oil and gas is to optimize exploration and exploitation of the reservoir of interest and the use of seismic to reach this goal is extremely important. Seismic exploration aids in the mapping of geological features associated with the petroleum system and seismic exploitation bolsters the characterization of subsurface static and dynamic reservoirs (Chopra and Marfurt, 2005). These specific parameters include, but are not limited to: horizon depth, reservoir thickness, faults, heterogeneity, porosity, permeability, and thermodynamics. Although logging programs measure a handful of these parameters, they are laterally sparse and incomplete. Seismically derived attributes provide estimates that are sensitive to geology and reservoir properties that help to infer parameters of interest (Chopra and Marfurt, 2005). Seismic inversion is considered a seismic attribute as it encompasses seismically derived parameters.

Post stack seismic inversion attempts to extract relative changes in impedance from post stack seismic data. Direct inversion methods estimate the impedance directly from the data. The least-mean-squared-error approach of Turin (1957), recursive trace-integration (Lindseth, 1979), and layer-stripping methods (Goupillaud, 1961; Robinson, 1978) are direct inversion methods. These direct methods assume that the data are noise free, and that the seismic wavelet is known exactly.

Another class of post stack inversion methods use an assumed forward-modeling operator to iteratively adjust an initial impedance model until a good fit between the observed and predicted data is achieved. These indirect methods require that the initial model be close to the true model (Cooke and Schneider, 1983; Russell and Hampson, 1991), and iteratively adjust/update the impedance model using a Generalized Linear Inversion (GLI) framework

(Keys and Weglein, 1983). Within the GLI framework, the user selectively weights the data misfit (Least-Mean-Squared-Error (LMSE) l_2 norm), and the model *reasonableness*. Model *reasonableness* is an arbitrary term, user (inverter) dependent, and is implemented mathematically through use of the model-covariance matrix (Tarantola 2005). Generally, the model covariance matrix limits adjustments to the current model at each iteration, but can also be specified to incorporate relationships between model parameters.

The post stack GLI inversion of Hampson-Russell (STRATA) is often used within RCP. Note that this inversion is heavily constrained. Horizons are required to guide the inversion, and a layer time-thickness (block size) is specified a priori. The model weighting factor weights the model reasonableness versus the data misfit (i.e. model covariance matrix in some form), and is rather insensitive, due to the horizon and layer time-thickness constraints (examples to be shown later).

Qualitative interpretation/inversion methods involve seismic attributes (Chopra and Marfurt, 2008), where the goal is to expose seismic anomalies. Typically, a variety of attributes are generated, and the user determines which attributes are meaningful for her/his particular prospect.

Spectral decomposition (Partyka et al., 1999) is a qualitative inversion that attempts to infer geological bed thicknesses in the frequency domain, and has found success exposing stream channels (Sinha et al., 2005), as well as differentiating hydrocarbons from brine (Chen et al., 2001; Chen et al., 2008). The vertical traveltime separation of seismic reflections produces a particular amplitude spectrum in the frequency domain. Spectral decomposition uses Short-Time-Fourier-Transforms (STFT) to decompose the poststack seismic volume into frequency bands which are related to bed thickness. Constant-frequency slides in plan view can expose lateral changes in layer thickness.

An extension to the spectral decomposition approach involves a more elaborate inversion that attempts to estimate bed thickness and *reflectivity* in the frequency (spectral) domain (Puryear and Castagna, 2008; Portniaguine and Castagna, 2004, 2005; and Chopra et al.,

2006; among others). This thin-bed reflectivity inversion uses STFT to spectrally decompose the seismic trace. Time, and space-variant (if specified), wavelets are deconvolved from the input data in a *constrained* fashion. Thin-bed thickness and the reflection coefficients at the top and base of the thin layer are estimated. The objective function includes the data misfit *and* a model-based term that controls the *sparsity* of the estimated reflection coefficients (Portniaguine and Castagna, 2004; Puryear and Castagna, 2008).

Thin-layer reflectivity-like inversion methods have also been cast in the time domain. The first application is that of Simmons and Backus (1994), and Simmons and Backus (1996). Post stack data are inverted (modeled) as a sparse set of thin-layer basis functions. In their offshore case-history, sparsity exposed that the assumption of a white reflectivity spectrum in the wavelet estimation process was incorrect. Consequently, their wavelet was modified for a blue reflectivity spectrum, which significantly reduced the data misfit of a known thin-layer reflection, and produced more accurate estimates of the thin-layer thickness.

Time-domain sparse-layer inversion has more recently been cast into a basis pursuit inversion by (Zhang and Castagna, 2011). This work is a rediscovery of the Simmons and Backus (1996) approach. The basis functions are now referred to as the basis pursuit dictionary (Chen et al., 2001), and the inversion is solved more elaborately than that of Simmons and Backus (1996).

I had hoped to evaluate the time-domain sparse-layer basis pursuit approach of Zhang and Castagna (2011) using Lumina Geophysical's Ultra^{TM} software package. Contractual arrangements could not be made in time so I moved forward with the thin-bed reflectivity code of Puryear and Castagna (2008), and Portniaguine and Castagna (2004, 2005).

The thin-bed reflectivity code is ThinMan, a commercial code provided by SigmaCubed. Seismic traveltime horizons are not needed, nor is a presumed layer time-thickness. My objective is to evaluate this approach for exposing lateral variations in thin-bed reflectivity and/or layer thickness, and comparing results with the more constrained GLI approach of Hampson-Russell.

I review the theory behind the ThinMan and GLI approaches. For completeness, I also discuss the time-domain sparse-layer inversion (Simmons and Backus, 1996; Zhang and Castagna, 2011) since this type of inversion may be suitable for use on the Eagleford project (RCP Phase XVII).

I apply spectral thin-layer reflectivity inversion to two synthetic datasets; the simple seismic wedge model, and a more elaborate 3-D synthetic based on the Wishbone section which was constructed from well logs, tops, and seismic horizons (Payson Todd, personal communication). ThinMan results are compared with those of HampsonRussell's poststack GLI inversion (STRATA). I perform parameter testing, and compare the best results from each method.

I then apply ThinMan to Baseline full stack data for a static interpretation of the geology. In addition, I apply the inversion to Baseline and Monitor 2 30° angle stacks as a proxy for time-lapse AVA, since ThinMan operates on post stack data. Results are then compared with those of Copley (2018), and Utley (2017).

4.2 The Convolutional Model

The advent of inversion of poststack seismic amplitude for acoustic impedance was a major contribution as estimations of the earth's acoustic impedance is a very desired attribute. Hampson and Russell's (1991) "comparison of poststack seismic inversion methods" provides a brief, yet thorough, summary of the post stack inversion methods at the time (Figure 4.1). All poststack inversion methods assume that a seismic trace can be modeled with the convolution equation:

$$d = W * r + n. \tag{4.1}$$

where d is the seismic trace, W is the seismic wavelet, r is reflectivity series to be estimated in the inversion, n is additive noise, and $*$ represents convolution. Equation 4.1 indicates that, in theory, if we deconvolve the wavelet, remove the additive noise and reverse the amplitude scaling, we should recover the reflectivity, and thus, the acoustic impedance (Russell and

Hampson, 1991).

The difference between the various poststack inversion methods (Figure 4.1) is the approach at which they solve this equation, but the general approach can be visualized in Figure 4.2.
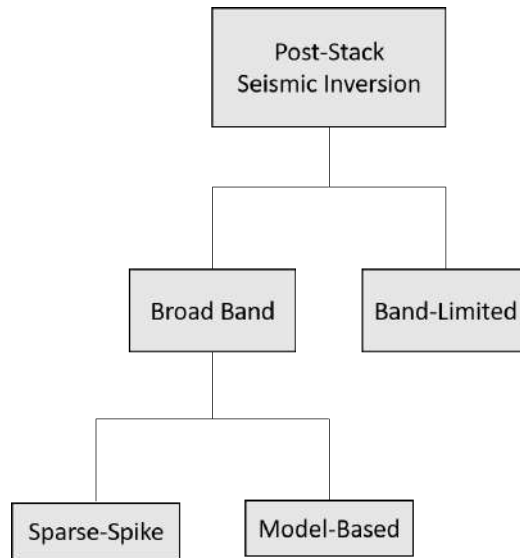
Figure 4.1: Summary of post stack inversion methods (Modified from Russell and Hampson, 1991).
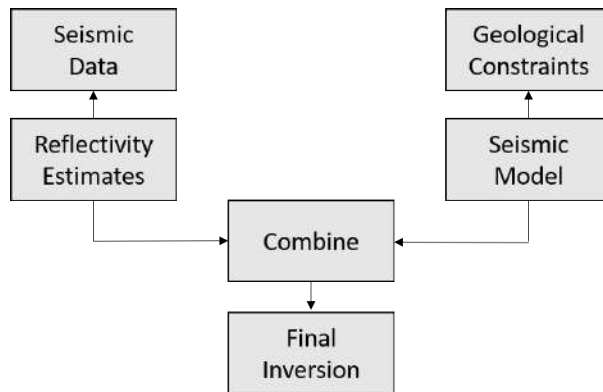
Figure 4.2: General approach to post stack inversion (Modified from Russell and Hampson, 1991).

Direct inversion methods assume that the wavelet is known exactly, and that the data are noise free (Turin, 1957; Lindseth, 1979; Goupillaud, 1961; Robinson, 1978). The indirect

GLI approach (Cooke and Schneider, 1983) uses a wavelet estimate obtained from a well log-based reflection coefficient time series, or derived directly from the data, and poststack data at the well location. The common approach within RCP has been to use a stochastic wavelet estimate. In this case, the main assumption is that the autocorrelation of the data is the autocorrelation of the seismic wavelet. A zero phase wavelet is then estimated that has the same autocorrelation. Note that errors in the wavelet estimate will map into errors in the reflectivity estimates.

4.3   Model-Based Post Stack Inversion Theory

As Figure 4.2 illustrates, poststack inversion attempts to find the reflection coefficients that when convolved with the wavelet, model (predict) the observed seismic trace. The objective function is a combination of the *data misfit*, and *model reasonableness* which tends to keep the updated model close to the previous model (i.e. geologic constraints). In this case, the model is an initial low frequency P-impedance model that is generated from well data and horizons. The inversion process iteratively solves for reflectivity by identifying differences between the input seismic data and the synthetic seismic formed from the model. The iterative process modifies the model to compensate for these discrepancies. This works to minimize the equation:

$$J = w_1 \times (d - W * r) + w_2 \times (M - Hr). \tag{4.2}$$

Where J is the objective function, d is the seismic trace, W is the wavelet, r is the reflectivity at the current iteration, M is the initial impedance model, H is the integration operator that when applied to the reflectivity estimate produces the updated impedance, and w_1 and w_2 are weighting factors (note that $w_1 + w_2 = 1$). A larger value for w_1 forces a solution that minimizes the data misfit (observed - predicted data), whereas a smaller value of w_1, and consequently a larger value of w_2, forces a solution update that stays close to the initial impedance model (HampsonRussell help documentation). To allow the model to deviate from the initial guess, I used the stochastic modeling inversion ("soft" constraint)

where a value for w_2 is set (thus indirectly choosing a value for w_1).

Multiple iterations (updates) are required because of $w_2 \neq 0$, and also because of the requirement that the reflectivity (impedance) updates mimic the input seismic time horizons, and updates are controlled by the pre-specified input layer time-thickness.

4.4 Thin-Bed Reflectivity Inversion Theory

The resolution of seismic data is the limiting factor for interpretation. The term "thin-bed" comprises of the idea of resolving power and the ability to distinguish individual properties of that bed. As the thickness of a bed decreases, the seismic response becomes a composite since the reflections from the top and base of the thin layer interfere. The top and base reflections are no longer resolved, and the amplitudes of the top reflection (now a composite) vary due to the interference. For a layer time-thickness $\leq 1/8\lambda$, where the seismic wavelength $\lambda = \frac{velocity}{frequency}$, the reflection response is the time derivative of the wavelet, and the amplitudes contain the information on layer thickness. At this point, the resolving power is lost. In the presence of noise, as field data inherently is, this value decreases to as low as $1/4 \lambda$. Thin-layer resolving power is dependent on both the dominate frequency of the incident wavelet and the signal to noise ratio (Widess, 1973). Therefore, to improve the resolution of seismic data, the frequency bandwidth must be improved; acquisition and processing parameters are what control the spectral bandwidth.

Deconvolution is a common and conventional method that attempts to increase resolution. The ultimate purpose of spiking deconvolution (applied prestack most commonly, or poststack) is to improve the temporal resolution through the compression of the source wavelet to a spike (Yilmaz, 2001). This process aims at increasing the resolution of reflected events by convolving the seismogram with a wavelet inverse filter to increase the bandwidth (whiten the amplitude spectrum) of the input data. Since the seismic signal is inherently band limited, the user determines the usable frequency range, and typically applies a band-pass filter to the deconvolved data.

Note that the concepts of inversion are applicable to spiking deconvolution. The user specifies a prewhitening factor that acts as damping in the deconvolution least-squares filter estimation. Prewhitening performs similarly to the model covariance matrix discussed earlier. A large prewhitening value causes the least-squares filter to *do less*, as does a large value of w_2 in Equation 4.2. Interpretive judgement is also involved in deciding the whitened frequency-bandwidth having sufficient signal-to-noise ratio (the passband for the subsequent band-pass filter). Deconvolution is a bit of an art, as is inversion, with the inherent compromise of *data fit versus model resolution*.

Thin-bed reflectivity inversion is a spectral inversion that attempts to resolve thin layers that lie below the conventionally-believed seismic resolution without any well-data input. Note that the ThinMan code is not documented, so inferences as to the details of the algorithm are made from Portniaguine and Castagna (2004, 2005), and Puryear and Castagna (2008).

The objective function is given by Portniaguine and Castagna (2004) as

$$min[||real(F(m)) - d||_2 + \lambda S(m).] \tag{4.3}$$

where $F(m)$ is the predicted (modeled) data, d is the observed data, m are the thin-bed reflectivity estimates, and $S(m)$ is a sparsity operator. A complex-valued wavelet library is contained in F, the details of which are not clear.

Theory behind the thin-bed reflectivity inversion is presented by Puryear and Castagna (2008). I attempt to illustrate the concepts behind ThinMan (and spectral decomposition) in Figures 4.3 - 4.5. Wedge model reflection coefficients as function of the layer time-thickness are shown in Figures 4.3a and 4.3b. Reflection coefficients are opposite sign at the top and base in Figure 4.3a, and the same sign in 4.3b. The corresponding amplitude spectra are shown in Figures 4.3c and 4.3d.

As the wedge model time-thickness varies, the notches (blue) in the amplitude spectra occur at different frequencies. Notches occur in the frequency domain at

$$f_{notch} = \frac{1}{\Delta t_{wedge}} \tag{4.4}$$

and consequently, the time-thickness can be inferred from the amplitude spectrum as

$$\Delta t_{wedge} = \frac{1}{f_{notch}} \tag{4.5}$$

where Δt_{wedge} is the time-thickness. Note that the above expressions are valid when the reflection coefficients at the top and base of the wedge are equal in magnitude but opposite in sign, as will be shown in Figure 4.4.

Spectral decomposition of 3-D data simply displays amplitude slices of various frequencies from the amplitude spectra in plan view. Naturally, more complicated reflectivity patterns produce more complicated amplitude spectra than those in Figure 4.3 but the principle is the same. Lateral changes in the frequency time slices may suggest changes in bed thickness and/or different depositional features. Note that spectral decomposition is a qualitative, attribute-like product.

Thin-bed reflectivity inversion attempts to use the magnitudes of the amplitude spectra, as well as infer the layer thicknesses. Amplitude spectra of the two wedge models are shown in Figures 4.4a, and 4.4b. Figures 4.4c, and 4.4d show the amplitude spectra for layer time-thicknesses of 10 ms (blue), 30 ms (green), and 50 ms (red). When the wedge reflection coefficients are equal in magnitude but opposite in sign, the spectra are sine functions (Figure 4.4c). For a layer thickness of 10 ms, the first notch in the amplitude spectrum is at 100 Hz (blue curve) as given by Equation 4.4. Similarly, for thicknesses of 30 ms and 50 ms, the first notch in the amplitude spectrum occurs at 33 Hz (green), and 20 Hz (red), respectively.

When the reflection coefficients at the top and base of the wedge are equal in magnitude and the *same* sign, the amplitude spectra are cosine functions (Figures 4.4b and 4.4d). Now the value of f_{notch} in Equation 4.4 is multiplied by 0.5.
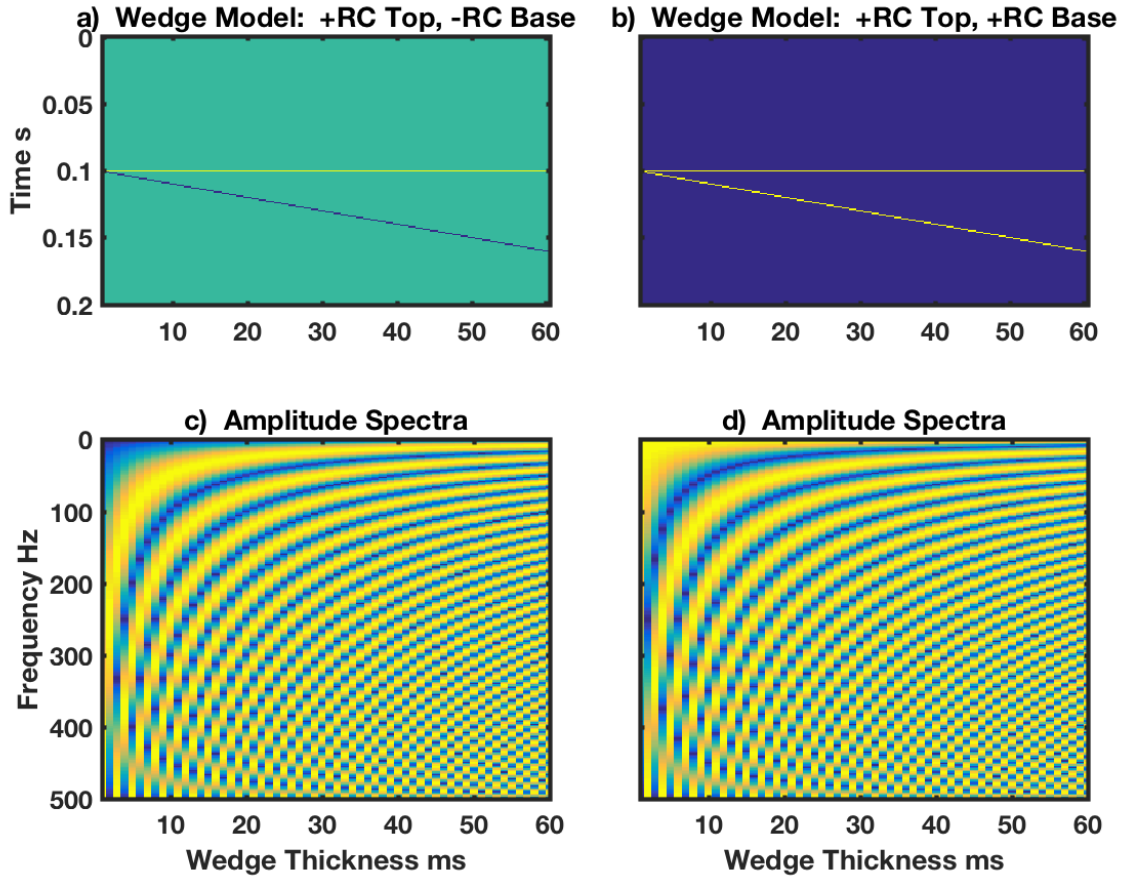
Figure 4.3: Wedge models in time and frequency domains. a) Wedge model with a positive (negative) reflection coefficient at the top (base). The magnitude of the reflection coefficients are the same. b) Wedge model with reflection coefficients of the same sign at the top and base. c) Frequency domain version of a). Blue values are low amplitude, yellow values are high amplitude. Different wedge time thicknesses produce a different pattern of amplitude highs and lows in the frequency domain. For a given wedge thickness, the amplitude spectra are sine functions. d) Frequency domain version of b). Note that these data are a cosine function since the reflection coefficients at the top and base are equal in magnitude and of the same sign.
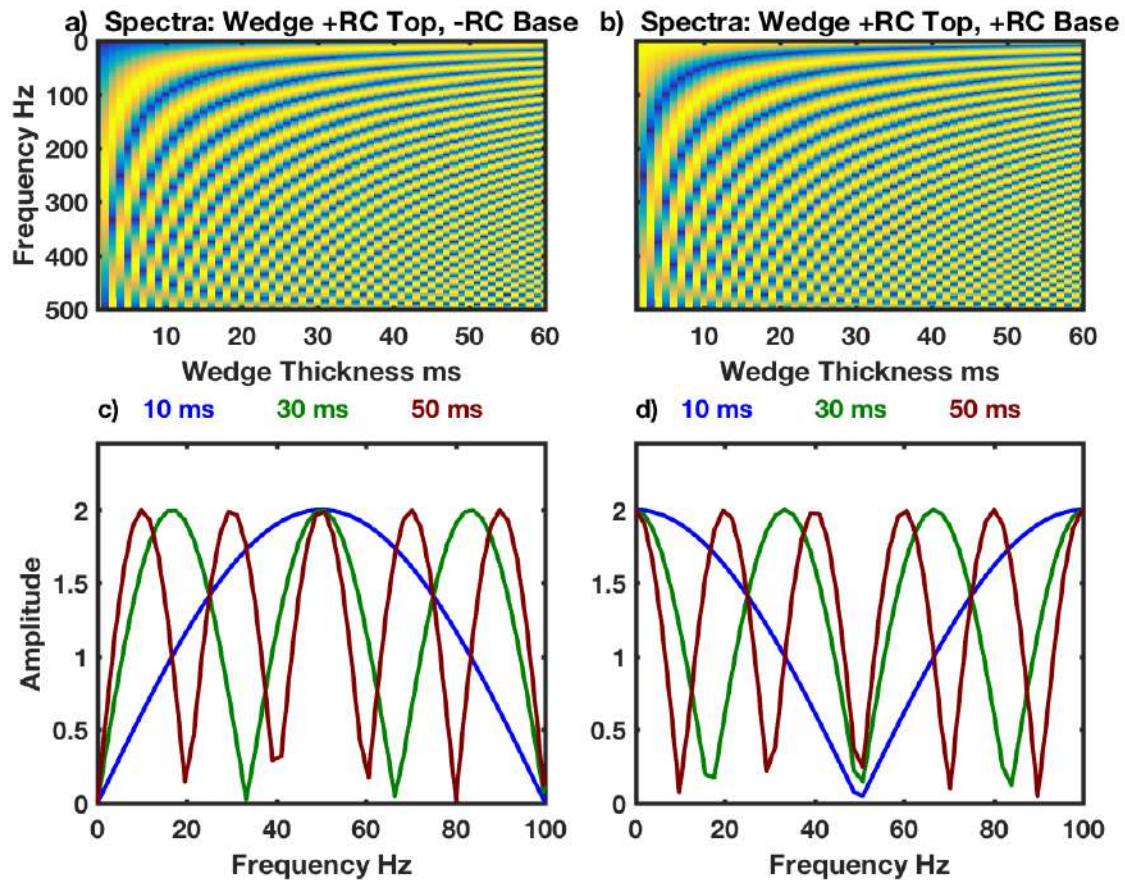
Figure 4.4: Wedge models in the frequency domain. a) Amplitude spectra as in Figure 4.3c. b) Amplitude spectra as in Figure 4.3b. c) Amplitude spectra corresponding to wedge thicknesses of 10 ms (blue), 30 ms (green), and 50 ms (red) from a). The sine curves are apparent. d) Amplitude spectra corresponding to wedge thicknesses of 10 ms (blue), 30 ms (green), and 50 ms (red) from b). The cosine curves are apparent.

When the reflection coefficients at the top and base of the wedge change, the amplitude spectra are scaled accordingly. Figures 4.3 and 4.4 assumed a reflection coefficient magnitude = 1 for illustrative purposes. Amplitude spectra for the wedge of Figure 4.3a with reflection coefficient magnitudes of 0.25 and 0.10 are shown in Figure 4.5. Maximum amplitude in the amplitude spectra is two times the reflection coefficient magnitude.

The thin-layer reflectivity inversion of Portniaguine and Castagna (2004, 2005), and Puryear and Castagna (2008), and consequently ThinMan (SigmaCubed purchased Fusion Geophysical where the algorithm was developed) make use of the reflection coefficient notches, the slope of the amplitude spectra, along with the magnitude of the spectra to produce an estimate of thin-layer reflection coefficients in the time-space (x,y) domain.

ThinMan attempts to reproduce the input data, while maintaining a level of *sparsity* of the reflection coefficient estimates (Equation 4.3). The user controls the level of sparsity; the reflectivity output becomes sparse as λ increases. Note that this is similar to the model covariance matrix in the GLI inversion, and the prewhitening factor in spiking deconvolution. As the reflectivity model becomes sparser, the data misfit increases, and the higher amplitude reflections are modeled. Again, all inverse problems have the inherent tradeoff between data fit and model resolution.

4.5 Sparse-Layer Inversion in the Time Domain

Perhaps a more intuitive approach is sparse-layer inversion in the time domain using thin-layer basis functions. Simmons and Backus (1996) detail a matched filter approach to impedance estimation that classifies selected reflection events (based on trace amplitudes) using a zero-lag cross correlation of the basis-function library (thin-layer seismic responses) with post stack data. In their case history, they maintained sparseness in the reflectivity estimates (no overlapping events) for the main purpose of exposing errors in their assumed seismic wavelet. An error in the wavelet estimate, produced coherent data misfit, which was then rectified by assuming a blue reflectivity spectrum in their wavelet estimation rather than using a white reflectivity assumption. Today their algorithm would be termed a *matching*
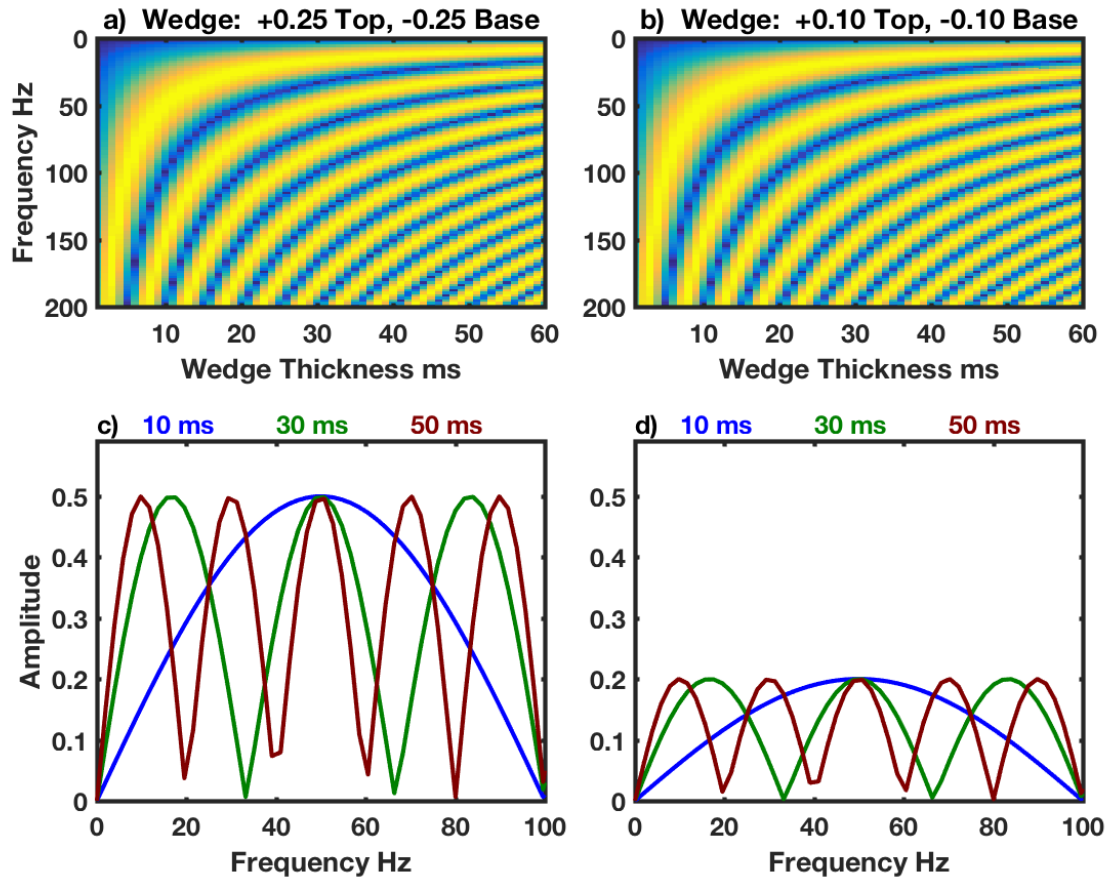
Figure 4.5: Wedge model of Figure 4.3a in the frequency domain. a) Amplitude spectra for all layer time-thicknesses. Reflection coefficients at the top and base of the wedge are +0.25 and -0.25, respectively. b) Amplitude spectra for all layer time-thicknesses. Reflection coefficients at the top and base of the wedge are +0.10 and -0.10, respectively. c) Amplitude spectra corresponding to wedge thicknesses of 10 ms (blue), 30 ms (green), and 50 ms (red) from a). The sine curves are apparent. d) Amplitude spectra corresponding to wedge thicknesses of 10 ms (blue), 30 ms (green), and 50 ms (red) from b). The cosine curves are apparent. The key point is that when the reflection coefficients differ, the amplitudes in the frequency domain differ as in c) versus d).

pursuit algorithm (Chen et al., 2001).

Zhang and Castagna (2011) rediscover the sparse-layer inversion of Simmons and Backus (1996), and term the thin-layer basis functions as a *dictionary* and employ a *basis pursuit* algorithm for their inversion. Both approaches involve a type of compressive sensing; seismic reflections are modeled as a combination of basis functions, or dictionary responses producing a sparse-layer reflectivity output. Sparse-layer inversion can output reflectivity estimates of higher temporal frequency than the input data without amplifying the noise, since deconvolution is not involved. The regularization parameter, λ, controls the *sparsity* of the reflectivity estimates. A sparse reflectivity model is produced when λ is relatively large. When λ is small, the data misfit is minimized, potentially at the expense of an unreasonable reflectivity model.

Sparse-layer inversion begins with forward modeling where basis-functions, or a wavelet/ wedge dictionary/library is specified. This first step attempts to model all possible events within the data by convolving a wavelet with a set of reflectivity series of known impedance. To start simple, the forward model is the convolution model (Equation 4.1).

The net response sourced from N calibrated seismic wavelets that have amplitudes and arrival times equivalent to the reflection coefficients results in a seismic trace. Simmons and Backus (1996) model the seismic responses as a combination of thin-beds and simple interfaces. For a simple interface, each seismic wavelet, w, is weighted by the reflection coefficient R_i and located at two-wave traveltime τ_i $d(t)$ are the modeled data, w is the wavelet that is weighted by the reflection coefficient R, τ_i is the two-wave travel time and n is additive noise.

$$d = \sum_{i=1}^{N} R_i w(t - \tau_j) + n. \tag{4.6}$$

Equation 4.7 details the extension of Equation 4.6 that includes the reflectivity of a thin-bed. The first term in this equation is the reflectivity of a thin-bed, where the top has a

reflection coefficient, R_i, located at time τ_i and a two-way time thickness $\Delta\tau_i$. The base of the reflector is equal in magnitude and opposite in sign. Where Figure 4.6 is an example of the basis-functions from Simmons and Backus (1996) that displays the impedance models (a), the reflectivity series (b), and the seismic response (c). Note that the basis functions take both high and low (or positive/negative, even/odd) impedances into consideration - polarity is controlled by this.

$$d(t) = \sum_{i=1}^{N} R_i[w(t - \tau_i) - w(t - \tau_i - \Delta\tau_i)] + \sum_{j=1}^{M} R_j w(t - \tau_j) + n(t).$$

(4.7)
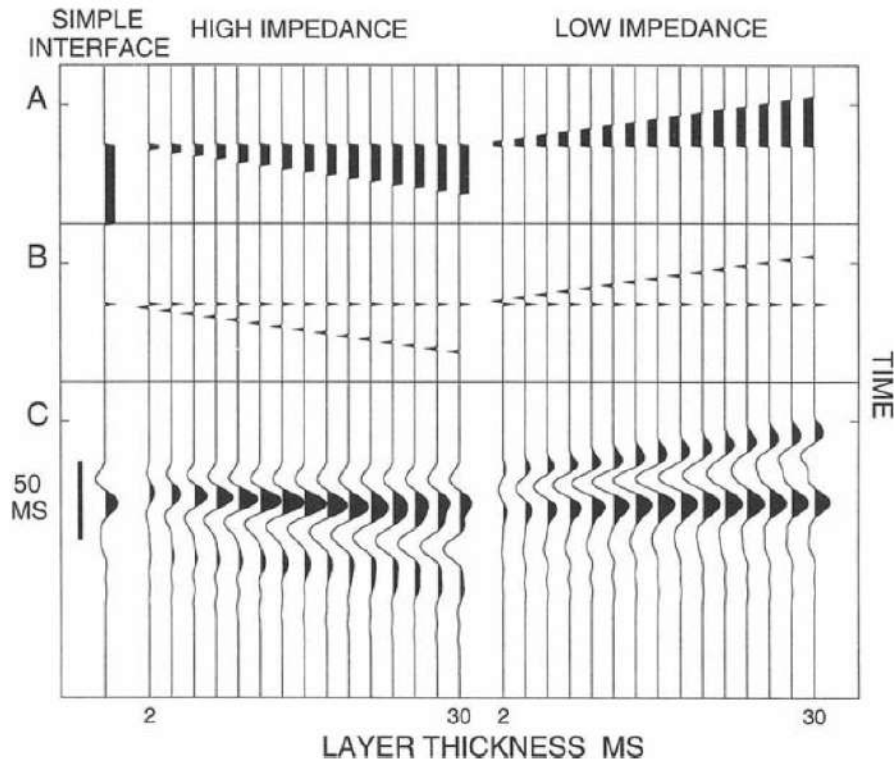
Figure 4.6: Example of the basis function that display the modeled impedance (a), the reflectivity series (b), and the seismic response (c) (Simmons and Backus, 1996).

Zhang and Castagna (2011) derive their basis library (wedge dictionary) by modeling the top and base reflectors as two impulse functions $c\delta(t)$ and $d\delta(t + n\Delta t)$, where $n\Delta t$ is time thickness of a thin-bed, Δt is the sample rate and c and d are the two reflection coefficients. To account for positive and negative reflectors, each pair is broken down into an even r_e and odd r_o pair with coefficients a and b (Equations 4.8, 4.9 and 4.10). The coefficients are varied from -1 to +1. To account for a range of bed thicknesses n ranges from zero to N to $N\Delta t$. The basis library this approach derives is very similar to Simmons and Backus (1996) (Figure 4.6). Even and odd are co-equivalent to high impedance and low impedance, respectively.

$$r_e = \delta(t) + \delta(t + n\Delta t)$$

$$(4.8)$$

$$r_o = \delta(t) - \delta(t + n\Delta t)$$

$$(4.9)$$

$$c\delta(t) + d\delta(t + n\Delta t) = ar_e + br_o$$

$$(4.10)$$

The inverse problem from Simmons and Backus (1996) is an iterative process that builds a model of the seismic response one event at a time starting with the largest absolute amplitude, similar to matching pursuit (MP). A match filter determines which basis function response best fits the data, Figure 4.7 shows the process. The algorithm first scans the trace to find the largest absolute amplitude, the real seismic trace is displayed on the right. The

basis functions are directly to the left of the seismic trace. The amplitudes of the basis functions are scaled to match those of the selected event. A normalized zero-lag cross-correlation of the event with the modeled basis functions determines which of the basis functions best matches the data (shown on the left of Figure 4.7). The basis function with the highest cross-correlation value is selected and then subtracted from the seismic to generate the misfit (or residual). The misfit is then used as the input for the next iteration. This process is repeated for a user-specified number of times.
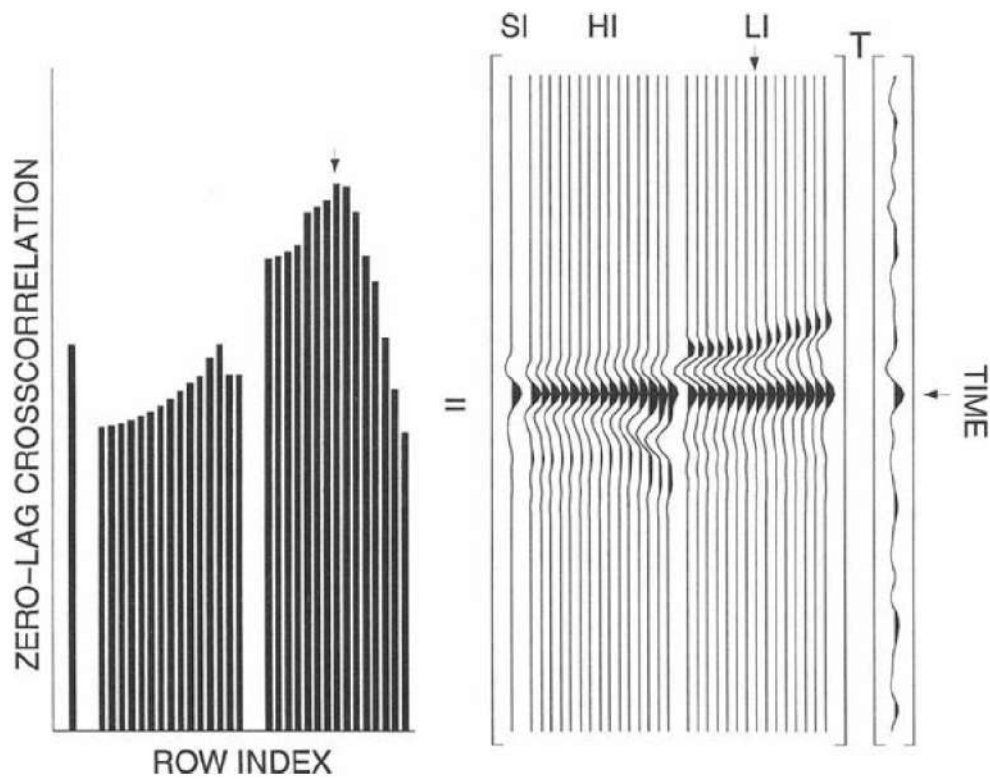
Figure 4.7: Method for determining which of the basis functions best models the data. This is a zero-lag cross correlation. The basis function with the highest cross correlation value is selected (Simmons and Backus, 1996).

Zhang and Castagna (2011) solve the inverse problem with the basis pursuit algorithm detailed fully in Chen et al. (2001). This process begins with rewriting the convolution model, Equation 4.1, in the form of Equation 4.11 where $\mathbf{d}$ is the data vector, $\mathbf{m}$ is the model parameter, $\mathbf{G}$ is the kernel and $\mathbf{n}$ is additive noise. Equation 4.12 is the result where

87

s is the column vector that represents the seismic response, **r** is the reflectivity series column vector, **W** is the diagonal wavelet kernel matrix and **n** is additive noise.

$$\mathbf{d} = \mathbf{G}m + \mathbf{n}.$$

(4.11)

$$\mathbf{s} = \mathbf{W}\mathbf{r} + \mathbf{n}.$$

(4.12)

$$min[||\mathbf{d\text{-}G}m||_2 + \lambda||m||_1].$$

(4.13)

The parameters in Equation 4.12 are solved with Basis Pursuit (BP) by minimizing the L_2 norm of error term and the L_1 norm of the solution (Equation 4.13). BP works by obtaining representations of the signal in an over complete dictionary where it works as an optimization principle rather than an algorithm. BP is useful in noisy data as it can suppress noise while preserving the structure built within the dictionary. In BP, λ controls the size of the residual and the sparsness of the solution, as well as balances the inverted reflectivity resolution and noise (Zhang and Castagna, 2011). As λ approaches zero, the residual goes to zero and may cause noise amplification. In contrast, as λ approaches ∞, the residual increases and decreases the resolution of the inverted reflectivity. For the L_1 norm of the solution, λ dictates the sparsness of the modeled data that gets inverted for (Chen et al. (2001)). The L_2 norm attempts to fit the data whereas the L_1 controls the sparsity.

Both methods heavily rely on the correct wavelet. As wavelets are commonly derived from the seismic data itself, the quality of the wavelet is directly dependent on the quality of the data. With any inversion, the integrity of the results will be on par with the condition of the wavelet. It is extremely important to begin the inversion with a wavelet that contains the appropriate amplitude and phase spectrum. The phase of the inversion and statistics of the reflectivity will be affected if it is run with an incorrect wavelet (Zhang and Castagna, 2011).

4.6 Wedge Model Testing

A synthetic wedge model (30 Hz Ricker wavelet) was run through both the ThinMan and HampsonRussell (HRS) post stack inversion packages to understand how the various parameters influence the results. Within ThinMan the three most critical variables are wavelet count, wavelet size and regularization. The regularization parameter pertains to λ from Equation 4.3 and is what controls the sparsity of the inversion. The larger this value, the more sparse the solution, and vice-versa. During testing the wavecount and wavelet size were held constant and the regularization value was varied between 5 and 0.2. The two most critical parameters controlling the output solution from HRS post stack inversion are the model weighting factor and the wavelet. During testing the wavelet was held constant and the weighting factor was varied between 0.1 and 0.8.

The wedge was run through ThinMan and the outputs include: modeled synthetic, relative acoustic impedance, reflection coefficients, and the error or data misfit. The two examples provided were run with a regularization parameter of 0.2 and 5. The output synthetics and the input wedge are displayed in Figure 4.8. The output synthetic run with a regularization parameter of 0.2 (a) appears to match the input wedge (c) better than the synthetic run with a value of 5. As the wedge becomes wider, the synthetic with the regularization parameter of 5 becomes jittery and discontinuous. For a direct comparison, Figure 4.9 displays the misfit which shows the difference between the output synthetic and input data with a consistent scale bar. When the scale bar is consistent, the misfit for the regu-

larization parameter of 0.2 (a) appears to be zero where there contains data in the misfit for the regularization parameter of 5 (b). The misfit for the regularization parameter of 0.2 is again displayed in Figure 4.10 with the same color bar as Figure 4.9 (a) and with a scale bar that allows for visualization of the amplitudes (b). In general, the misfit from the inversion with the regularization parameter of 0.2 is lower in amplitude than that with 5.

Figure 4.11 displays the respective output reflection coefficients compared to the input wedge. Both regularization parameters output reflection coefficients that give a general trend of a wedge and both contain events that are not related to the input wedge. The reflection coefficients run with a regularization parameter of 0.2 contains a significant amount of noise unrelated to the wedge, this output appears jittery. This output also contains events that look like "beds" above and below the actual events. ThinMan estimates time and space variant wavelets, so in this case, the wavelet estimates are likely getting confused by the variable time thickness of the wedge or there is an issue with the phase. The reflection coefficients run with a value of 5 also contain "beds" below and above the actual events that could be misleading during interpretation. As Portniaguine and Castagna (2005) detail, when there are issues with the phase of the wavelet, the inversion introduces artifacts as seen in both parameter tests. Although the inversion is not perfect, there are strong reflection coefficients with minor artifacts around them. Errors with the wavelet map into errors in model parameters, this is a fundamental issue for all inversions that can be considered over parameterized, or inversions that contain many user input model parameters.

Both relative acoustic impedance results, Figure 4.12, display the same wedge trend. The result of the 0.2 value (a) appears to be have a higher resolution, but artifacts do exist outside of the wedge. The results from a value of 5 (b) are lower in resolution, but contain less artifacts than the relative acoustic impedance volume with a value of 0.2. Although the synthetic and data misfit from the inversion run with the regularization parameter of 0.2 are more appealing as the synthetic data better matches the input data, the inversion results run with a value of 5 are overall, more appealing for interpretation.

In addition, the wedge was run through the poststack inversion within HampsonRussell and the outputs include the synthetic and the acoustic impedance. There is an option to output absolute acoustic impedance, but to directly compare to the ThinMan results, I output relative acoustic impedance. In addition, a difference volume (data misfit) was created by subtracting the initial data from the output synthetic. During these tests, the wavelet was kept consistent and the weighting factor was varied. Figure 4.13 shows the synthetic data run with a weighting factor of 0.1 (a), 0.5 (b) and, 0.8 (c). The synthetic for each test appear very similar and look like the input data. Additionaly, the data misfits (Figure 4.14) from 0.5 (b) and 0.8 (c) appear the same, whereas the misfit from 0.1 (a) is slightly different and contains erroneous amplitudes away from the wedge. Like the misfit, the relative impedance from 0.5 and 0.8 are very similar. The desired solution for this inversion is run with a weighting factor of 0.1 (as the background P-impedance volume is a constant value more weight should be placed on the input seismic traces rather than the initial model).

The comparison of the best results from ThinMan and HampsonRussell includes the relative acoustic impedance volumes in Figure 4.16 and the misfits in Figure 4.16. The relative acoustic impedance from HRS (a) are significantly smoother and contain more artifacts than the ThinMan results (b). The misfit from HRS (a) is much larger than the misfit from ThinMan (b). Looking at the relative impedance extracted from the top of the wedge model from both the results from HRS and ThinMan, as seen in Figure 4.18, the relative impedance as the bed thins differs between each output. The HRS relative impedance gradually increases as the bed thins and then stays at a constant value. The ThinMan relative impedance gradually increases to a maximum and then drops back off the the original value. In reality, the relative impedance of the top reflector is a constant value. The results from both HRS and ThinMan do not accurately resolve the relative impedance. Comparing the HRS and ThinMan results, ThinMan does a better job at modeling the data. Overall, this is not necessarily a bad thing, just something to keep in mind during interpretation.
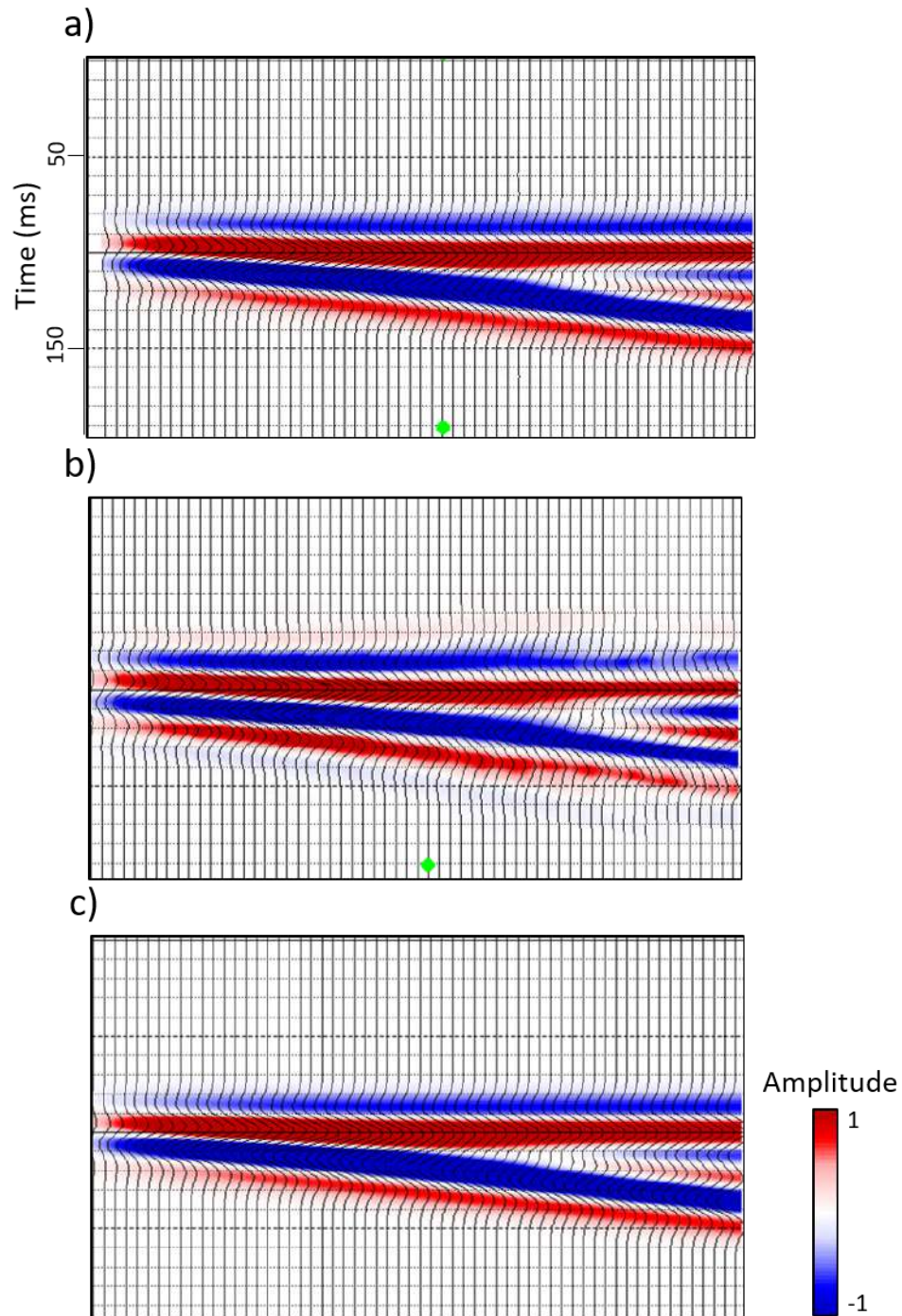
Figure 4.8: ThinMan inversion of wedge model a) Output synthetic wedge run with $\lambda = 0.2$. b) Output synthetic run with $\lambda = 5$. c) Input wedge model.
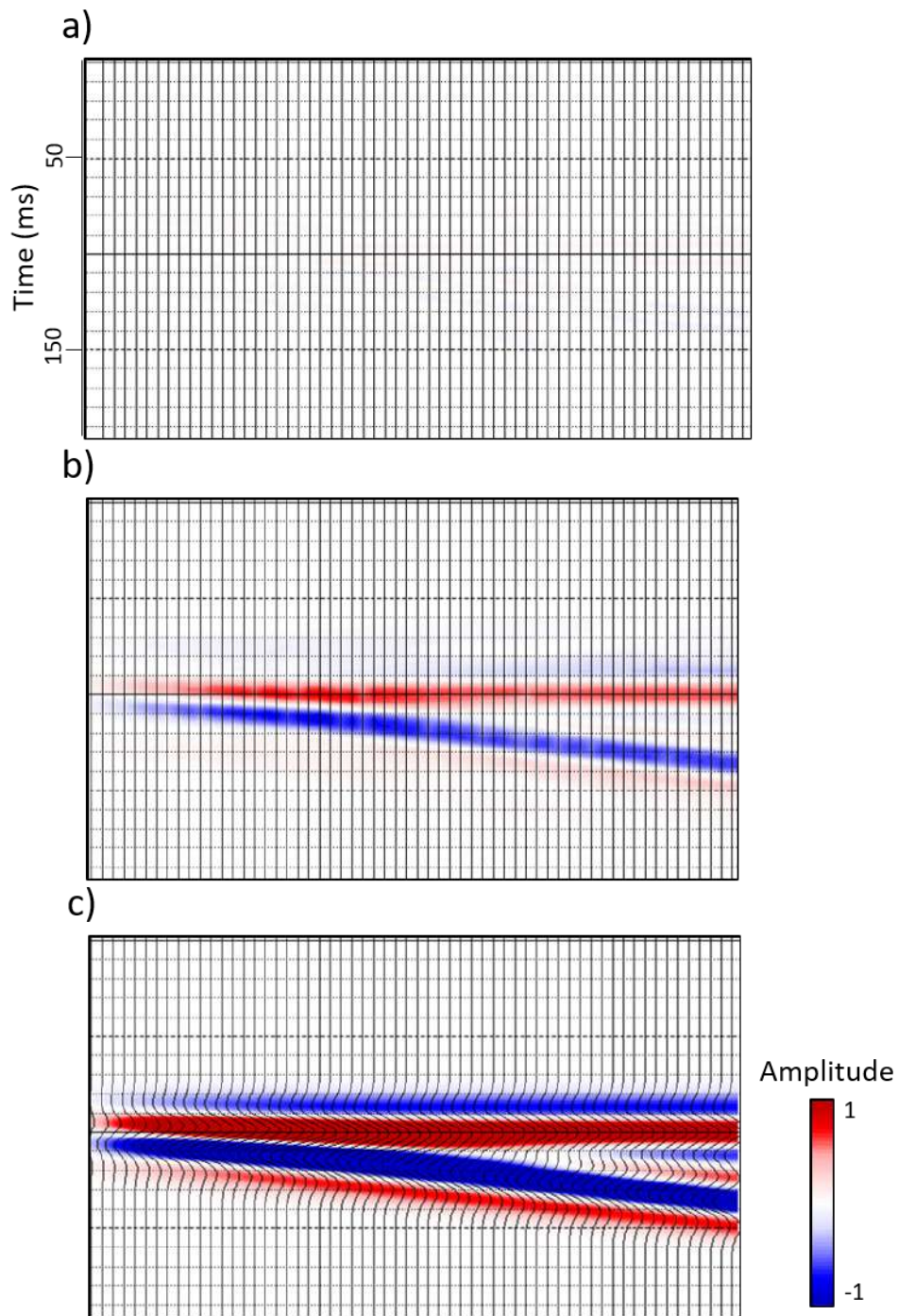
Figure 4.9: ThinMan inversion of wedge model - with a consistent color bar a) Misft of the output synthetic and input wedge run with $\lambda = 0.2$. b) Misft of the output synthetic and input wedge run with $\lambda = 5$. c) Input wedge model.
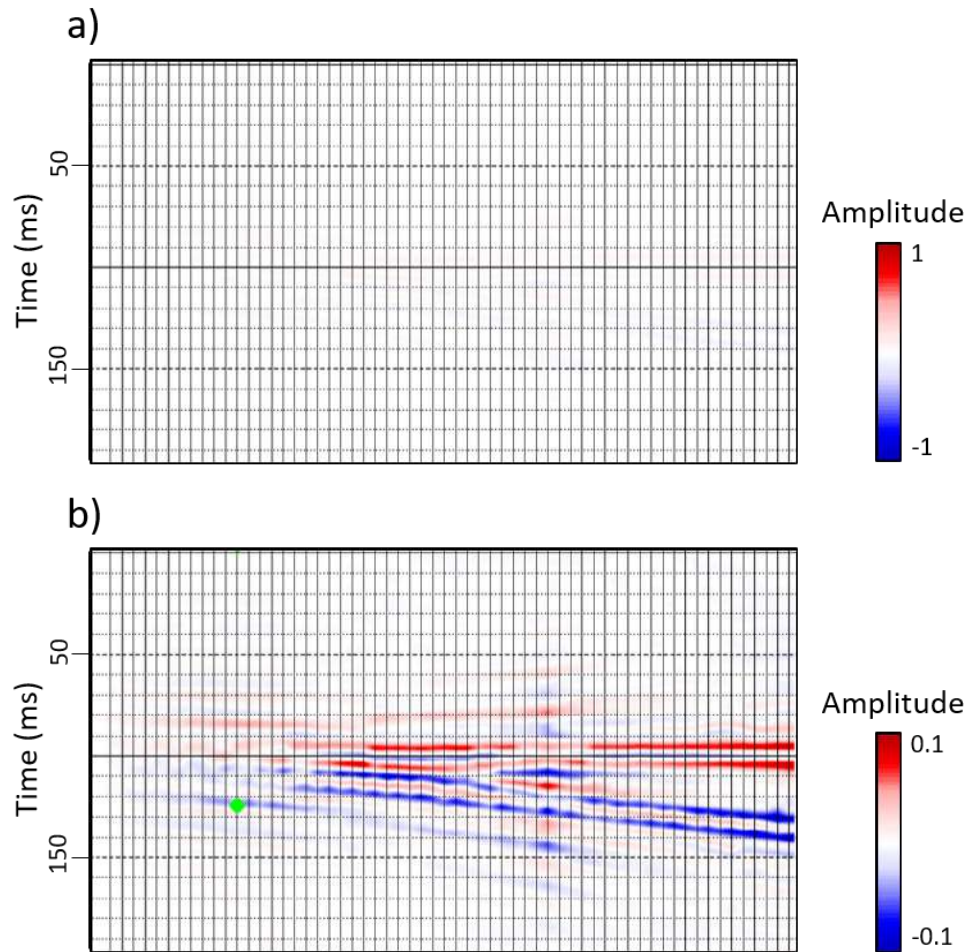
Figure 4.10: Misfit of the output synthetic from ThinMan and the input wedge model run with a $\lambda = 0.2$ a) Misfit with a color bar that ranges in amplitude from 1 to -1. b) Misfit with a color bar that ranges in amplitude from 0.1 to -0.1. This displays that the misfit decreases significantly when λ is small.
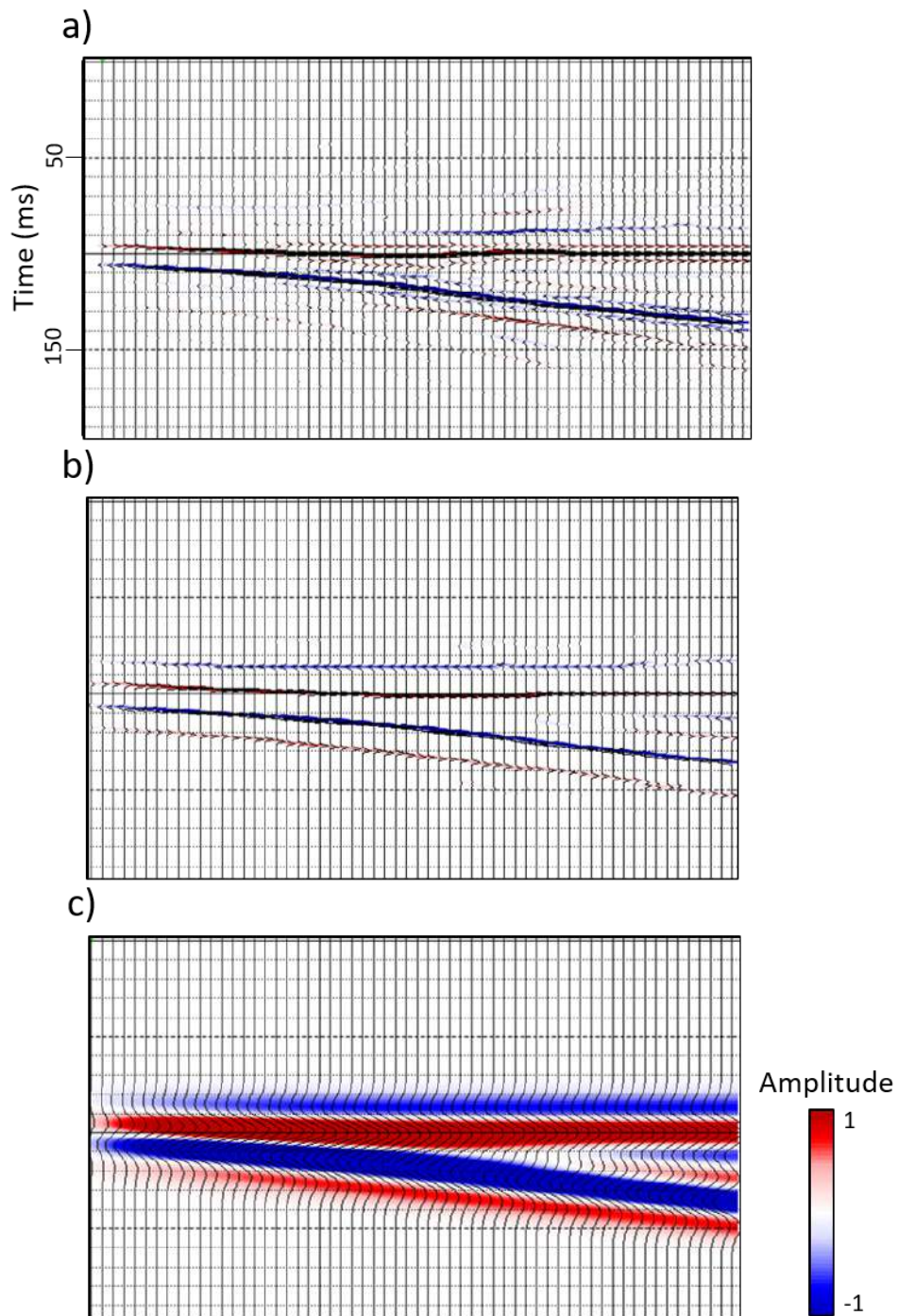
Figure 4.11: ThinMan inversion of wedge model a) Output reflection coefficients of the wedge run with $\lambda = 0.2$. b) Output reflection coefficients of the wedge run with $\lambda = 5$. c) Input wedge model.
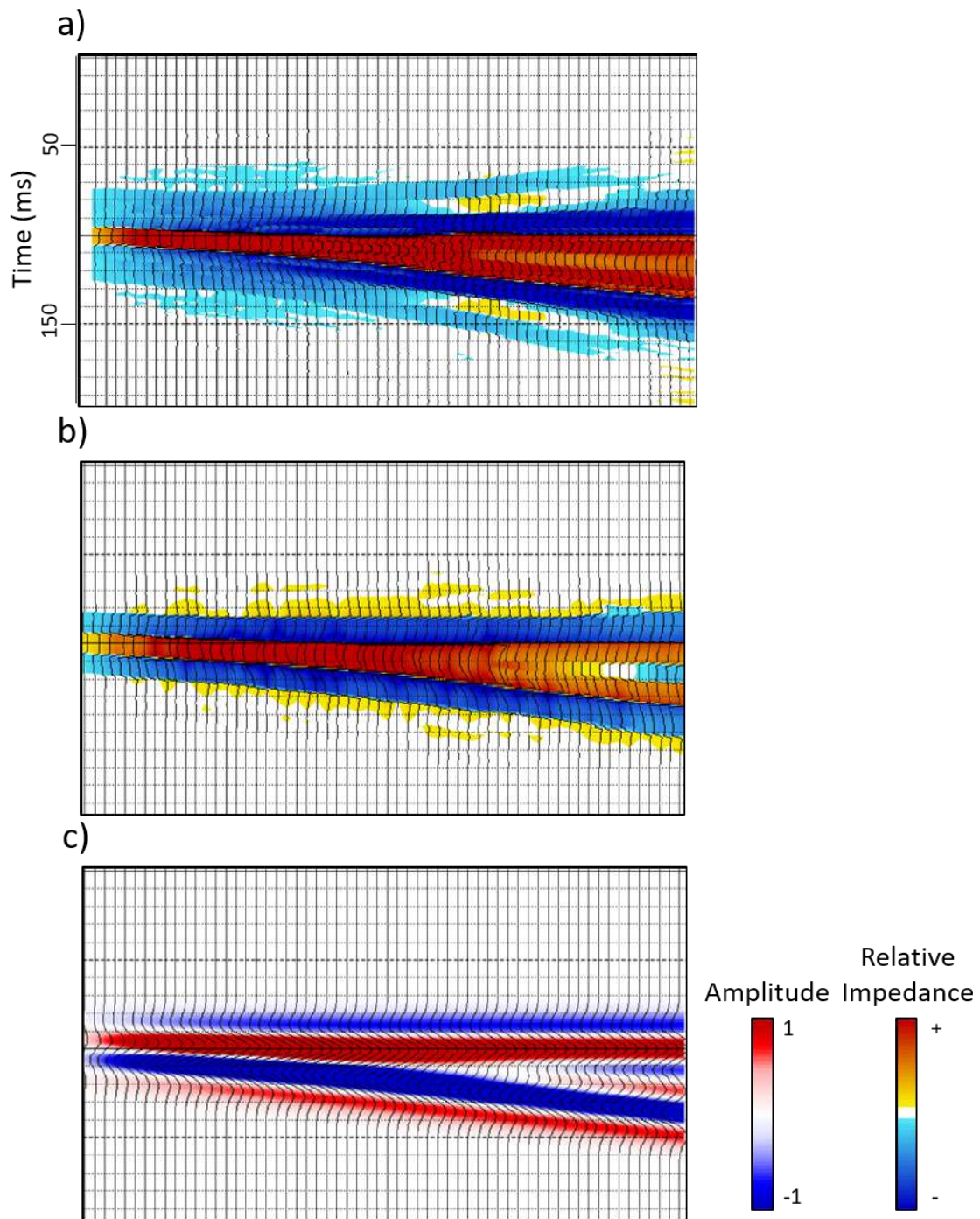
Figure 4.12: ThinMan inversion of wedge model a) Output relative acoustic impedance of the wedge run with $\lambda = 0.2$. b) Output relative acoustic impedance of the wedge run with $\lambda = 5$. c) Input wedge model
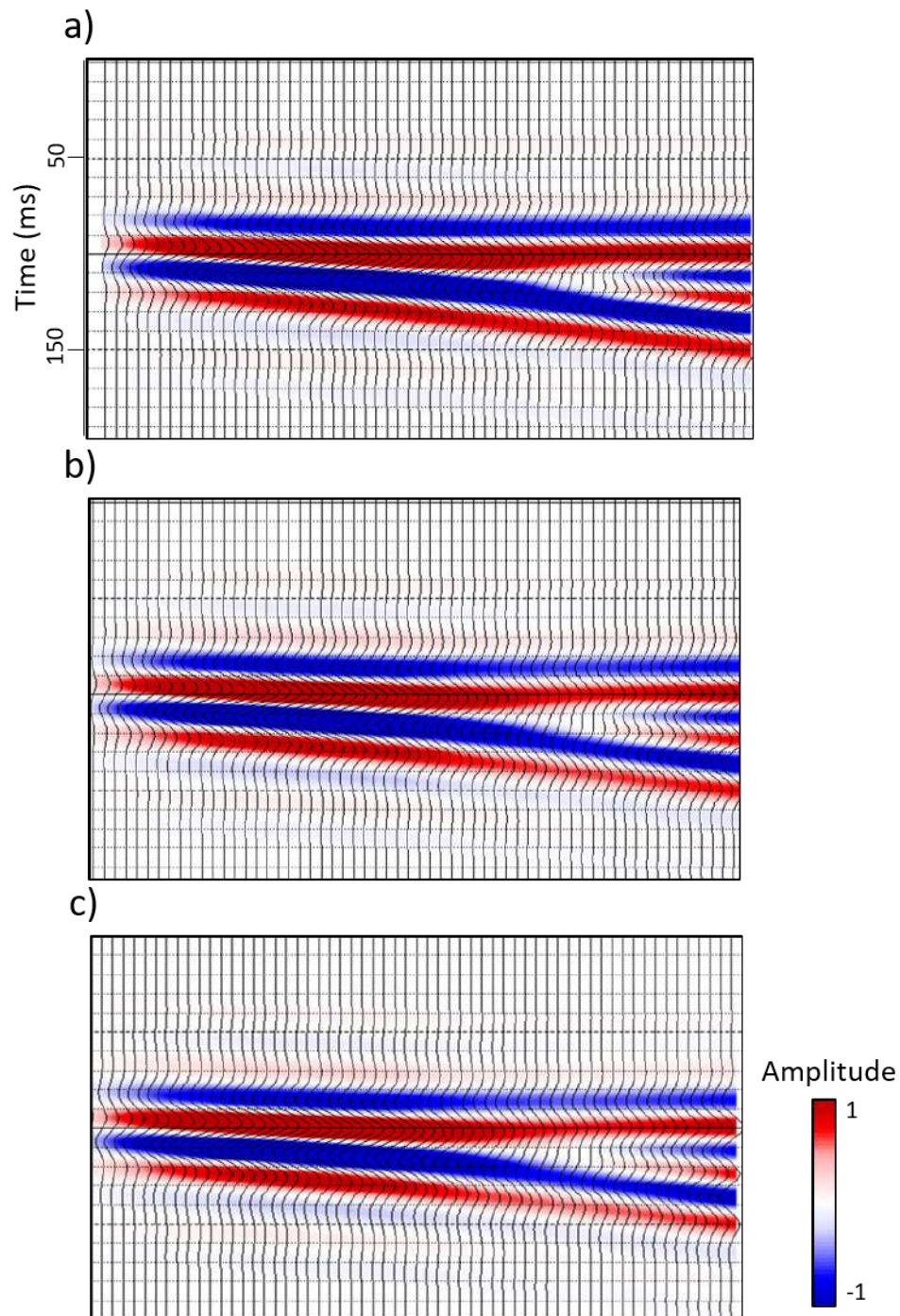
Figure 4.13: HampsonRussell post stack inversion of wedge model a) Output synthetic wedge run with a weighting factor = 0.1. b) Output synthetic wedge run with a weighting factor = 0.5. c) Output synthetic wedge run with a weighting factor = 0.8.
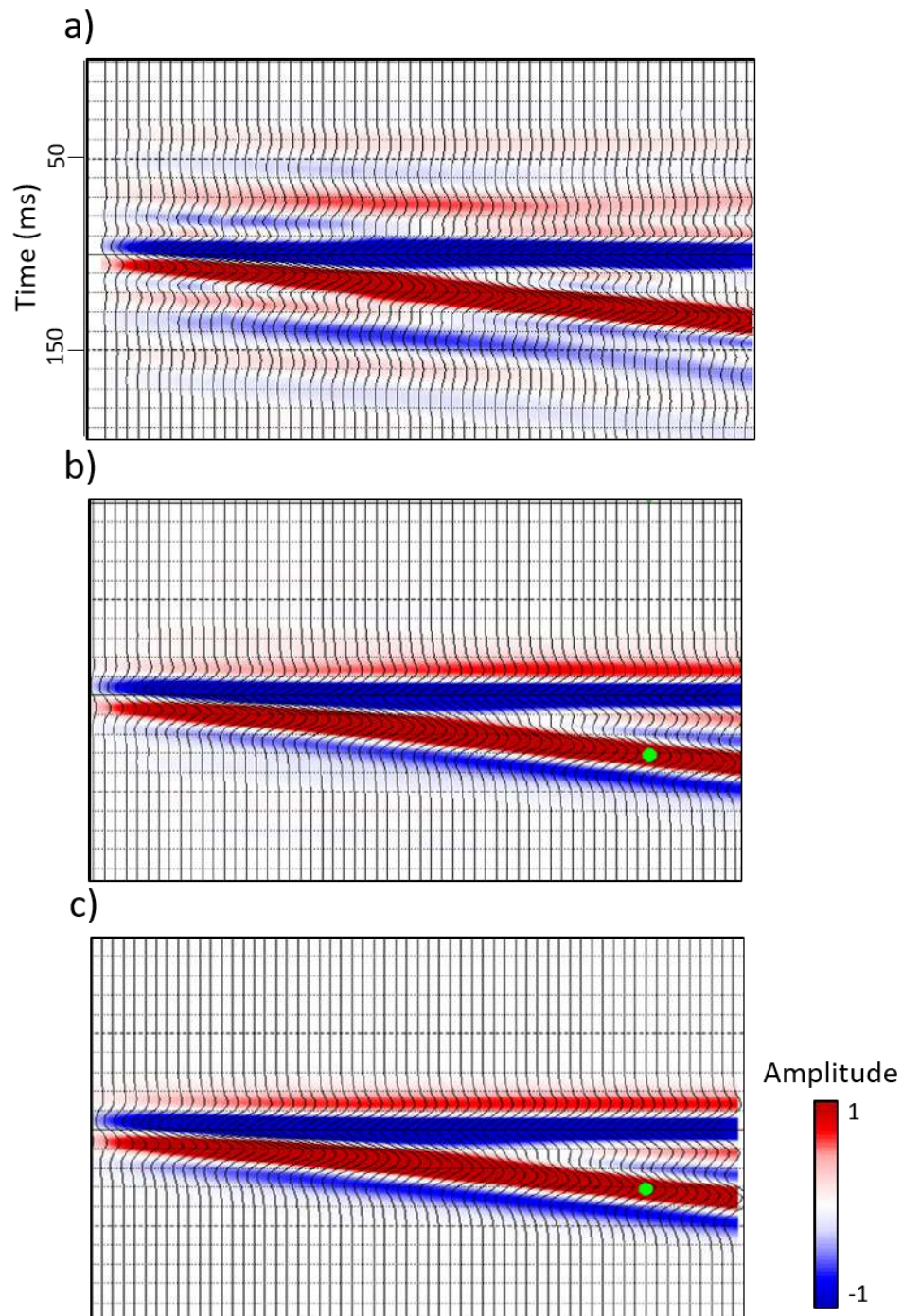
Figure 4.14: HampsonRussell post stack inversion of wedge model a) Misft of the output synthetic and input wedge run with a weighting factor = 0.1. b) Misft of the output synthetic and input wedge run with a weighting factor = 0.5. c) Misft of the output synthetic and input wedge run with a weighting factor = 0.8.
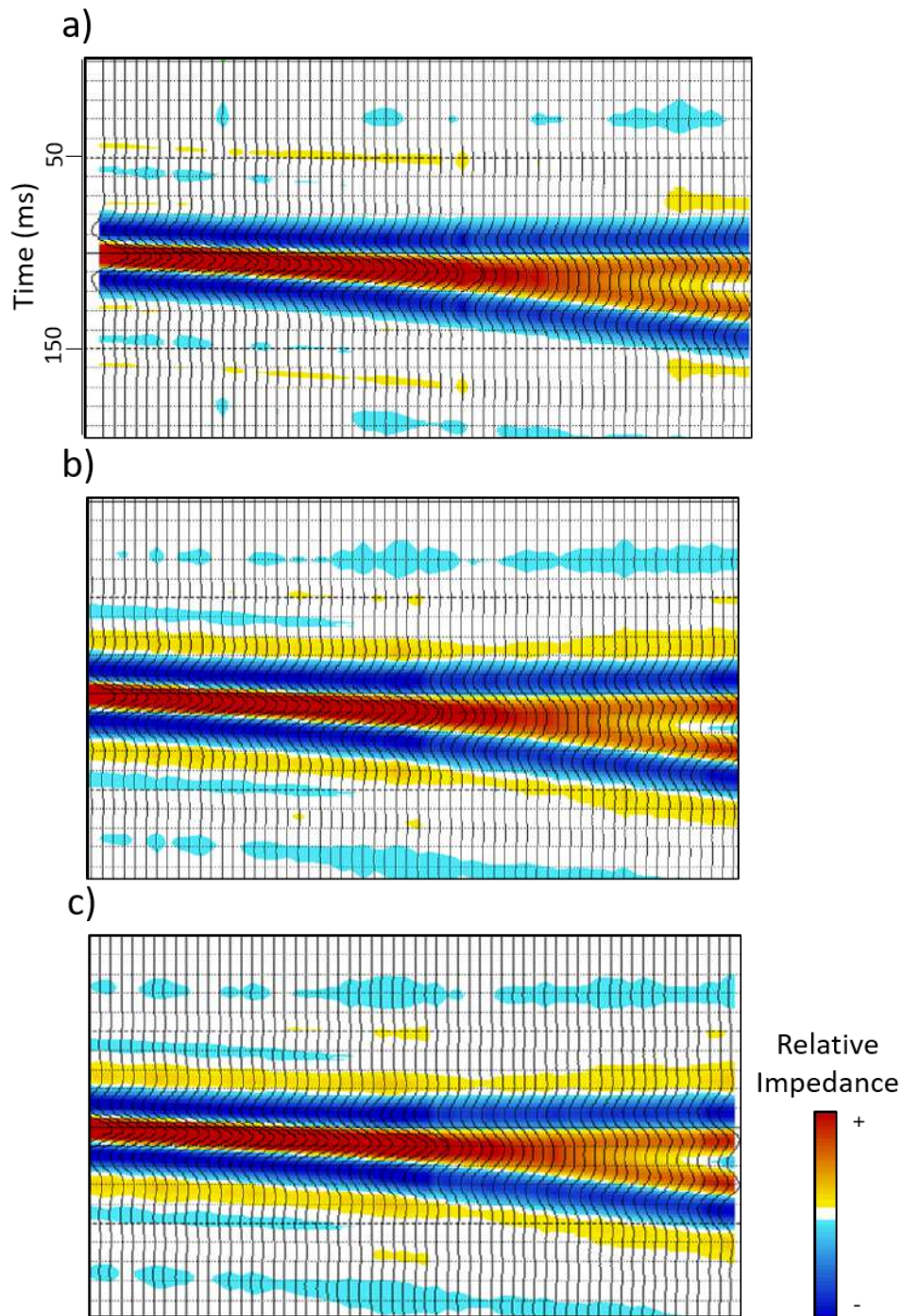
Figure 4.15: HampsonRussell post stack inversion of wedge model a) Inverted relative impedance run with a weighting factor = 0.1. b) Inverted relative impedance run with a weighting factor = 0.5. c) Inverted relative impedance run with a weighting factor = 0.8.
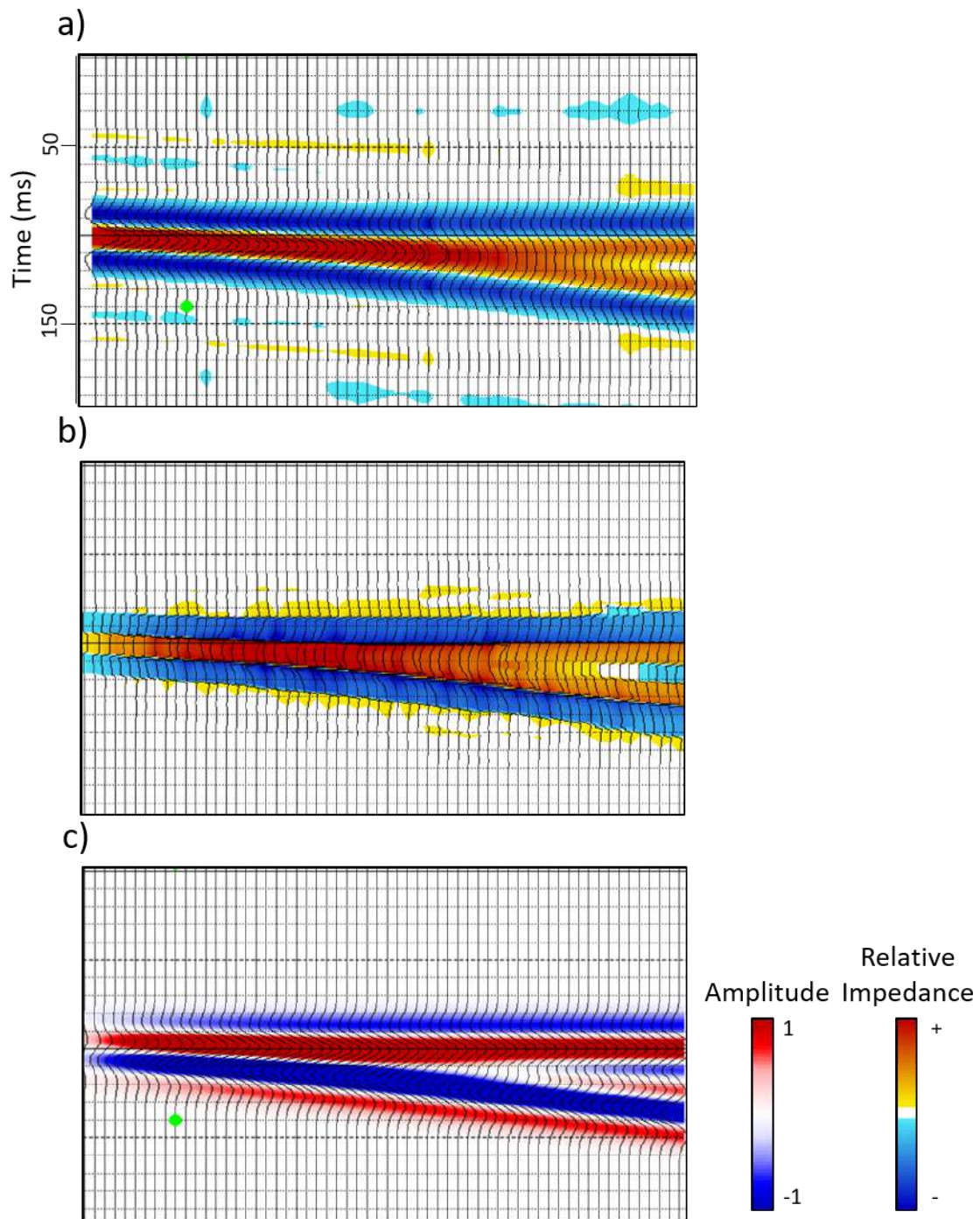
Figure 4.16: Comparison between ThinMan inversion and HampsonRussell post stack inversion a) HampsonRussell best result with a weighting factor = 0.1 b) ThinMan best result with a $\lambda = 5$. c) Input wedge model.
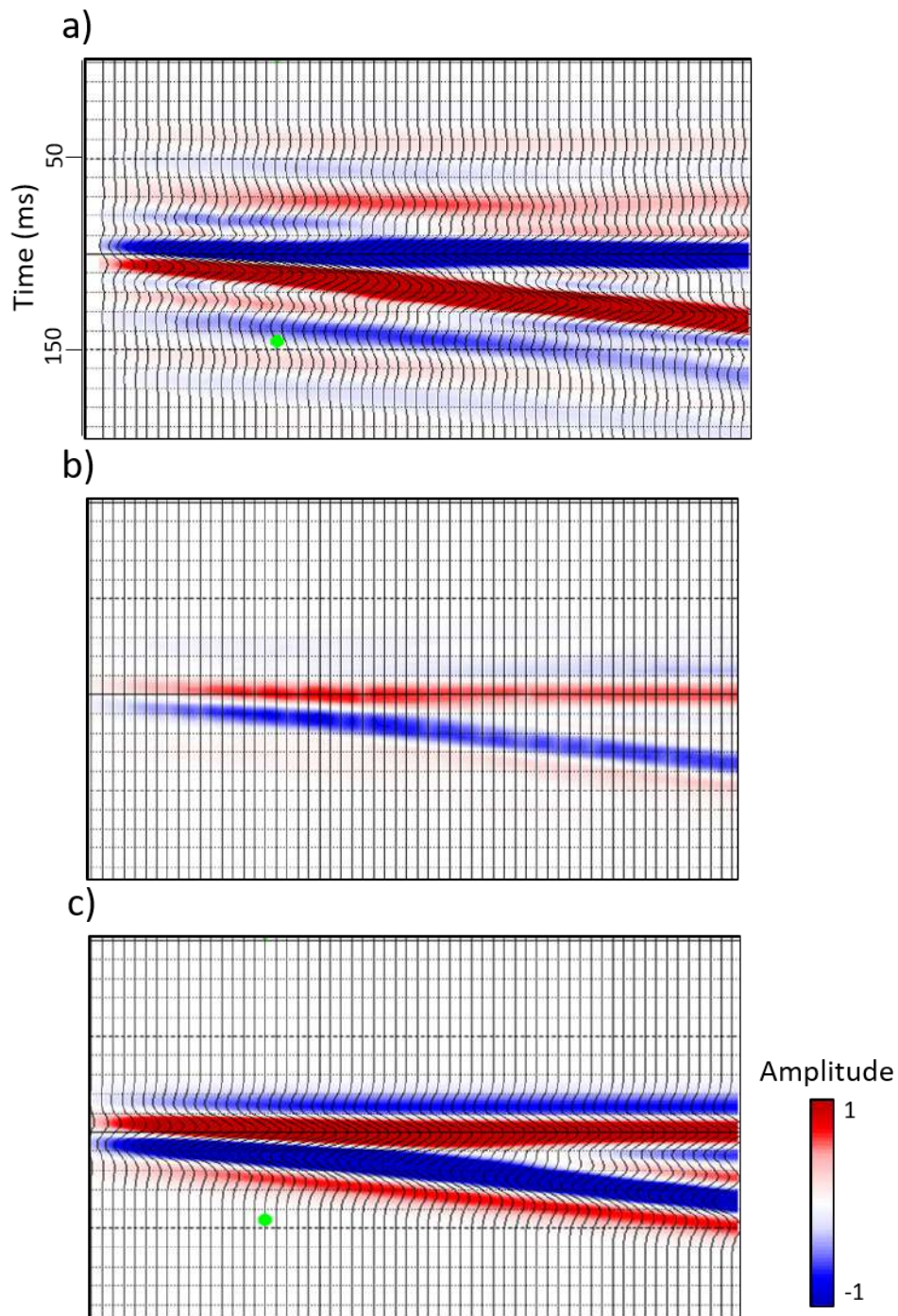
Figure 4.17: Comparison between ThinMan inversion and HampsonRussell post stack inversion a) Misfit between HampsonRussell best result synthetic and input wedge model. b) Misfit between ThinMan best result synthetic and input wedge model. c) Input wedge model.
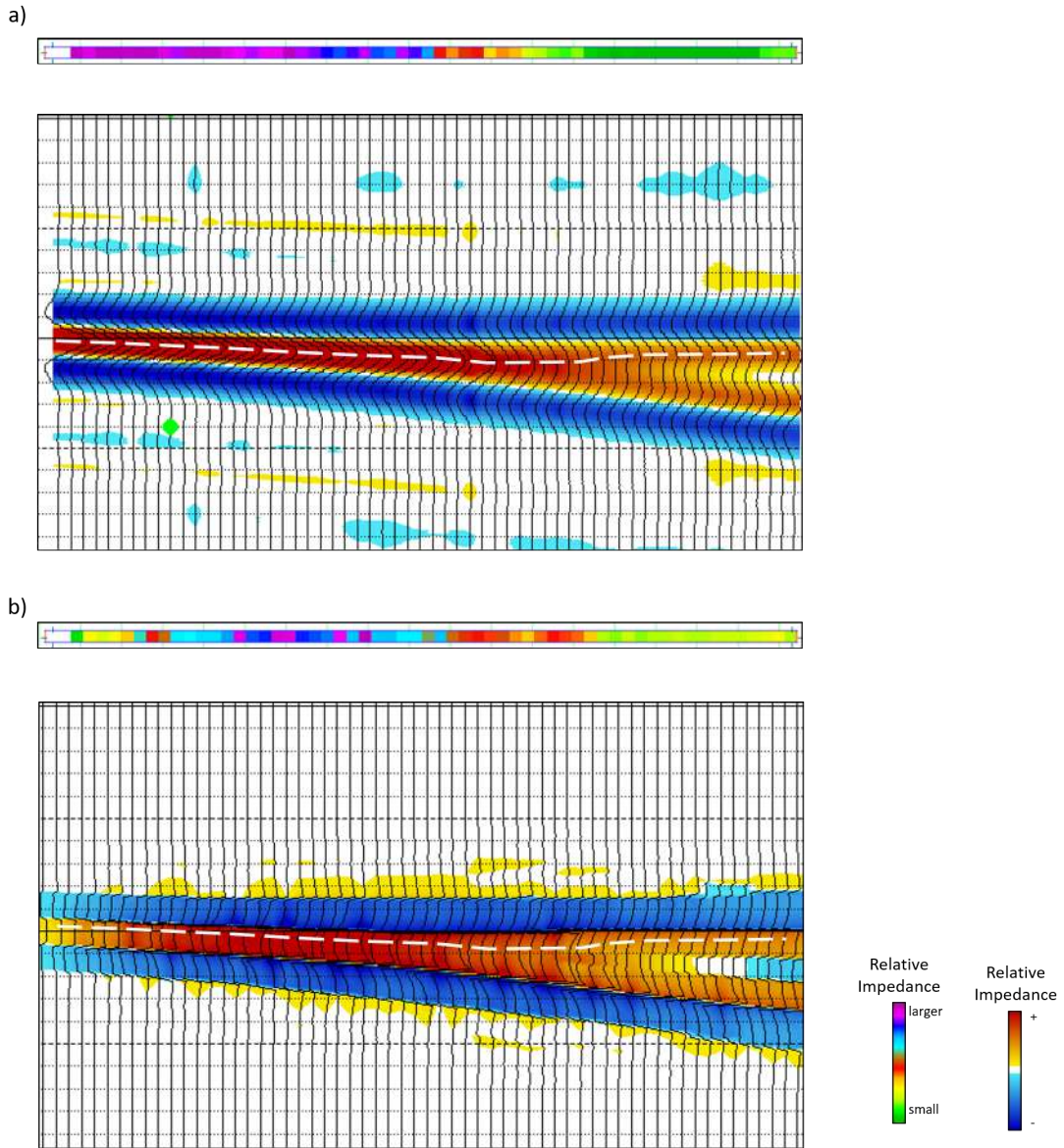
Figure 4.18: Comparison between the ThinMan inversion and HampsonRussell poststack inversion a) Bottom - Relative impedance from HampsonRussell best resuls. Top - Extracted relative impedance from the dash-white line. b) Bottom - Relative impedance from ThinMan best result. Top - Extracted relative impedance from the dash-white line.

4.7 Wattenberg Synthetic Testing

The Wattenberg synthetic volume was used to test the capabilities of the ThinMan and HRS inversions. The specifics of this synthetic volume are detailed in Chapter 1. The acoustic impedance volume created with the vertical wells in the section was converted into reflection coefficients. The reflection coefficients were then convolved with a 30hz wavelet to represent the Turkey Shoot Baseline survey, an example inline is shown in Figure 4.19. This volume was then run through both the ThinMan and HampsonRussel post stack inversion.
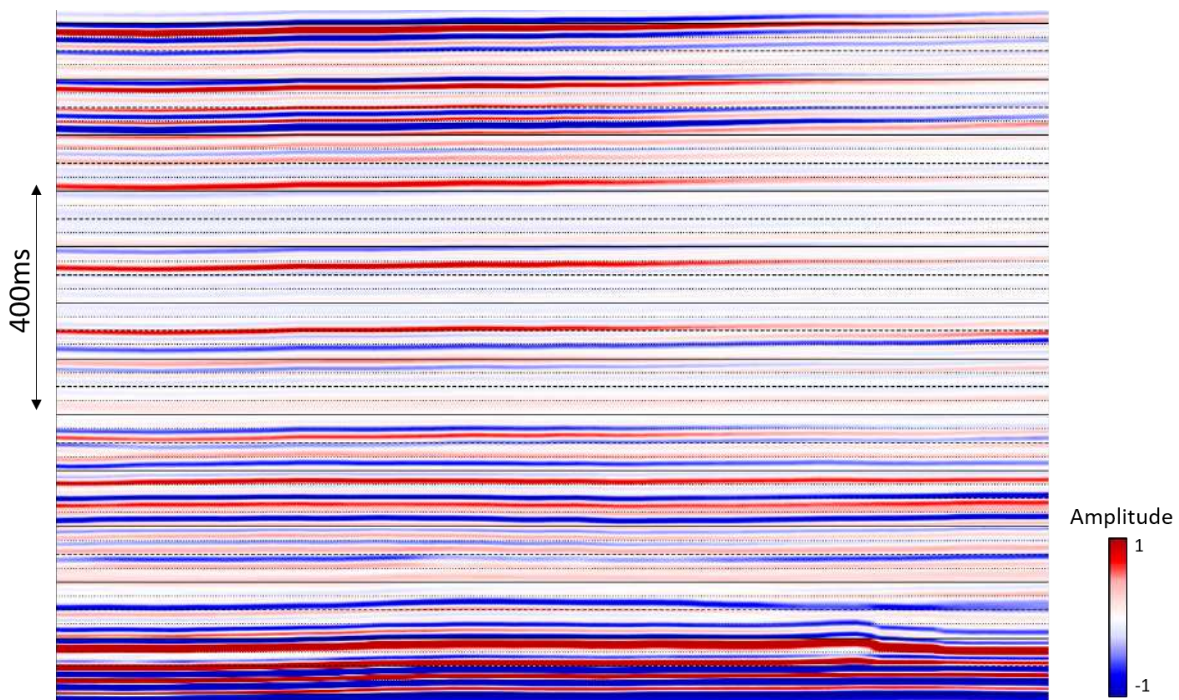
Figure 4.19: Example inline from the Wattenberg synthetic model.

The regularization parameter was tested at 1, 0.2, 0.02 and, 0.001. Figures 4.20-4.23 display the synthetic, the error or misfit, reflection coefficients and relative acoustic impedance from the test line. Images a-d were run with regularization parameters 1, 0.2, 0.02 and, 0.001, respectively. The output from the inversion can be viewed as spectrally broadened seismic data (Chopra et al., 2009).

Visually, the synthetic volumes, Figures 4.20a-d, do not contain any apparent differences. There exists some slight amplitude variations, but overall these appear to be the same. The misfit is the difference between the synthetic and the input volumes (Figure 4.21), this output volume provides insight as to how well the modeled data matches the input. The misfit from the sparsest result, Figure 4.21a, is the largest. This volume looks like a scaled down version of the input indicating this regularization parameter does not result in the best matched solution. Figure 4.21b contains a smaller misfit and less coherent energy than Figure 4.21a. Both Figures 4.21c and d have a very small misfit, although there is a small amount of coherent energy.

The output reflection coefficients in Figure 4.22 attempt to provide more detailed reflection information in both extra reflection cycles and fault detail (Chopra et al., 2009). Comparing Figures 4.22a and d we can observe the two extremes: Figure 4.22a is the volume with the regularization parameter = 1, i.e. the most sparse and, Figure 4.22d is the volume with the regularization parameter = 0.001, i.e. the least sparse. In the most sparse case, the inversion is still modeling more events than previously detectable on the input volume, yet it does not model as many events as the least sparse case. The reflection coefficient volumes can be useful in detecting the various chalk and marl benches within the Niobrara package.

The output relative acoustic impedance volumes are seen in Figure 4.23 where 4.23e is the relative impedance volume used to create the input synthetic volume. As the regularization parameter is decreased (less sparse), the inversion outputs a volume with increasing detail.

To determine how the thin-bed reflectivity inversion compares to the more commonly understood inversion process in CGG's HampsonRussell (HRS) package, a post stack inversion on the synthetic volume was completed. The two most critical parameters controlling the output solution are the weighting factor and the wavelet. Figures 4.24-4.26 display three example lines from the testing of the weighting factor. In each figure, a) was tested at 0.2, b) at 0.5 and, c) at 0.8. There is not a significant difference between a weighting factor
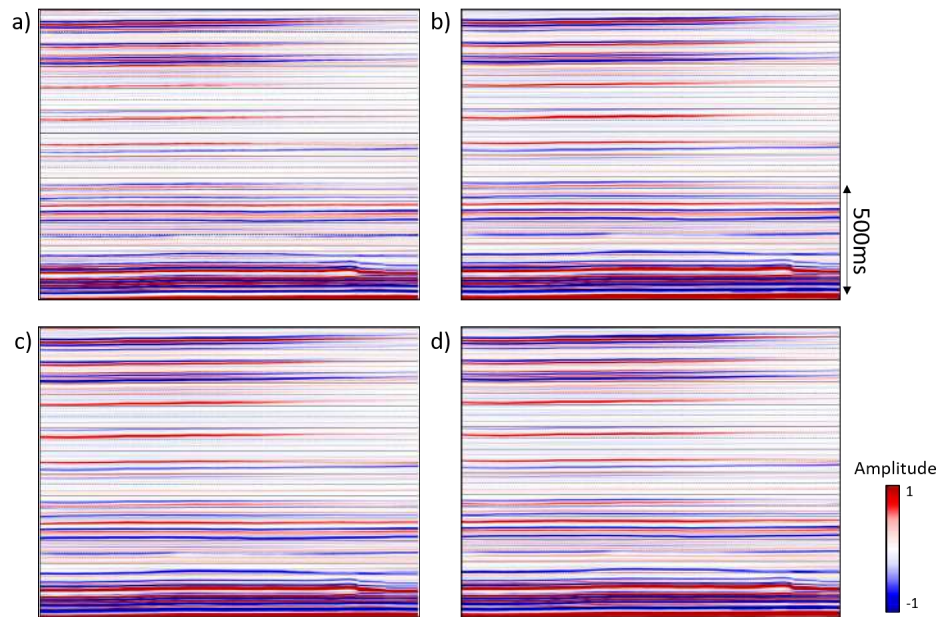
Figure 4.20: ThinMan inversion results from the Wattenberg Synthetic - inverted synthetic volumes with a) regularization parameter = 1. b) regularization paramter = 0.2. c) regularization paramter = 0.02. d) regularization paramter = 0.001. (red=positive).
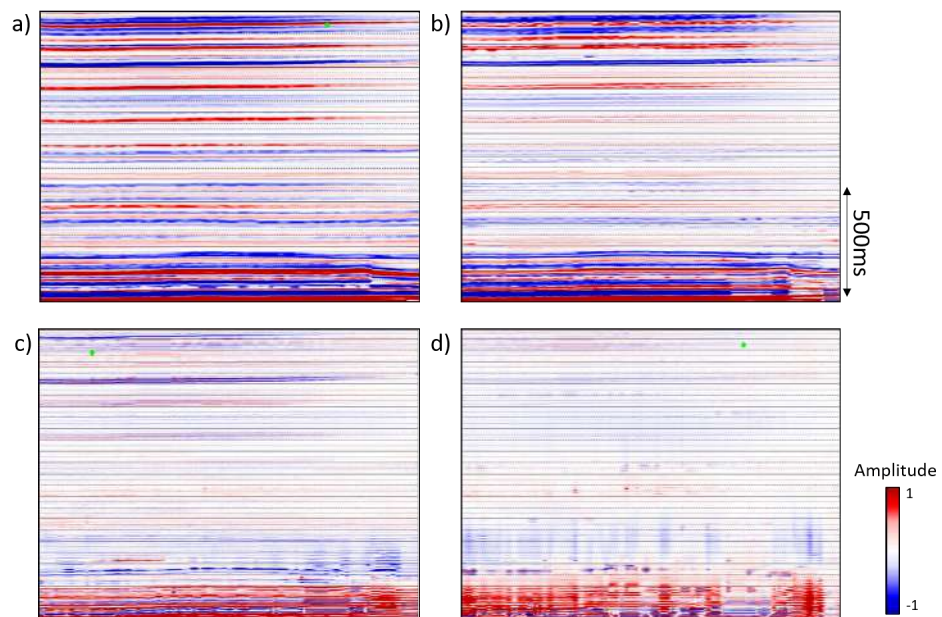
Figure 4.21: ThinMan inversion results from the Wattenberg Synthetic - misfit volumes (inverted synthetic - input data) with a) Regularization parameter = 1. b) Regularization paramter = 0.2. c) Regularization paramter = 0.02. d) regularization paramter = 0.001. (red=positive).
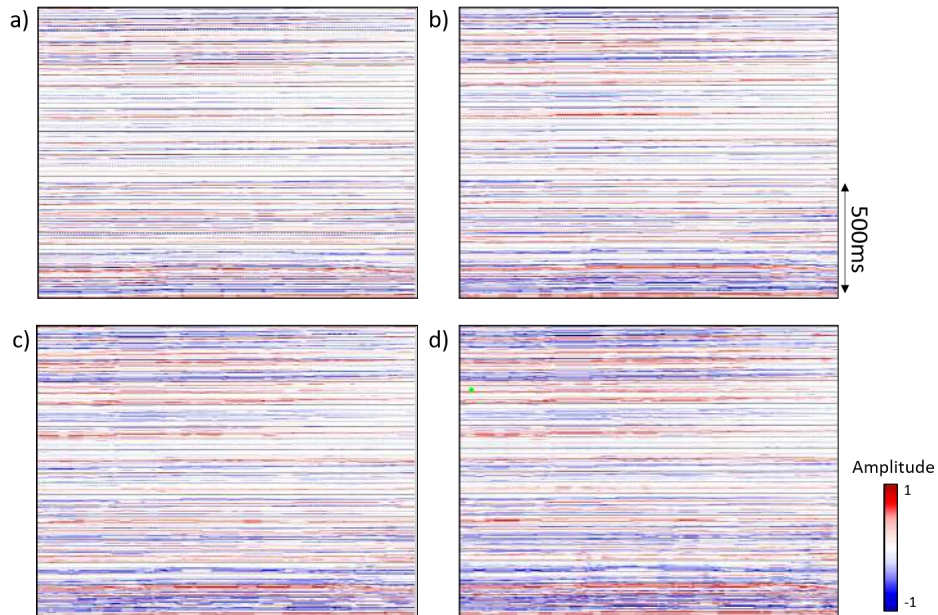
Figure 4.22: ThinMan inversion results from the Wattenberg Synthetic - inverted reflection coefficient volumes with a) Regularization parameter = 1. b) Regularization paramter = 0.2. c) Regularization paramter = 0.02. d) Regularization paramter = 0.001. (red=positive).

of 0.2 and 0.5. Increasing this parameter to 0.8 greatly impacts the results and outputs a solution with the greatest resolution and detail. In addition to weighting factors, two different wavelets (128ms and 100ms) were tested. The inversion results run with the 128ms and 100ms wavelets are shown in Figures 4.27a and b, respectively.

The inversion results run with a weighting factor of 0.8 and 128ms wavelets were compared with the thin-bed reflectivity results. Figures 4.28 and 4.29 show the relative acoustic impedance volumes from the HRS inversion (left), the ThinMan inversion (middle), and the input synthetic (right). The top row display the line fully zoomed out, the middle row zooms further in, and the bottom row zooms into the Niobrara reservoir interval.

The high resolution inversion results from ThinMan may be difficult for interpreters to believe as we conventionally believe the standard seismic resolution limitation to be $\lambda/4$. In Figure 4.31 the output reflection coefficients were convolved with both a 30hz and 50hz wavelet and then correlated with wells in the study area. The correlation coefficients for both the 30hz and 50hz ties were greater than 90%. These well ties were performed for quality
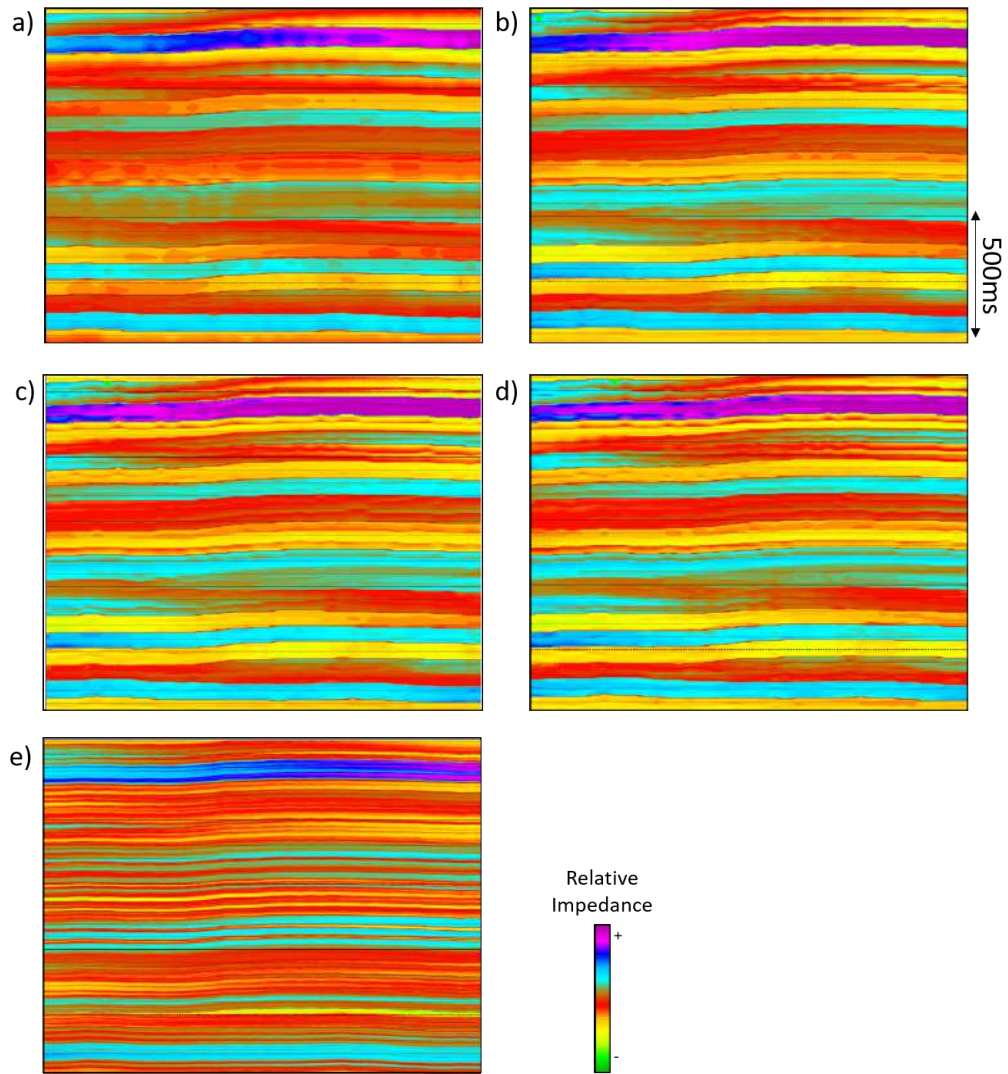
Figure 4.23: ThinMan inversion results from the Wattenberg Synthetic - inverted relative impedance volumes with a) Regularization parameter = 1. b) Regularization paramter = 0.2. c) Regularization paramter = 0.02. d) Regularization paramter = 0.001. e) The relative impedance volume used to derive the Wattenberg synethic.
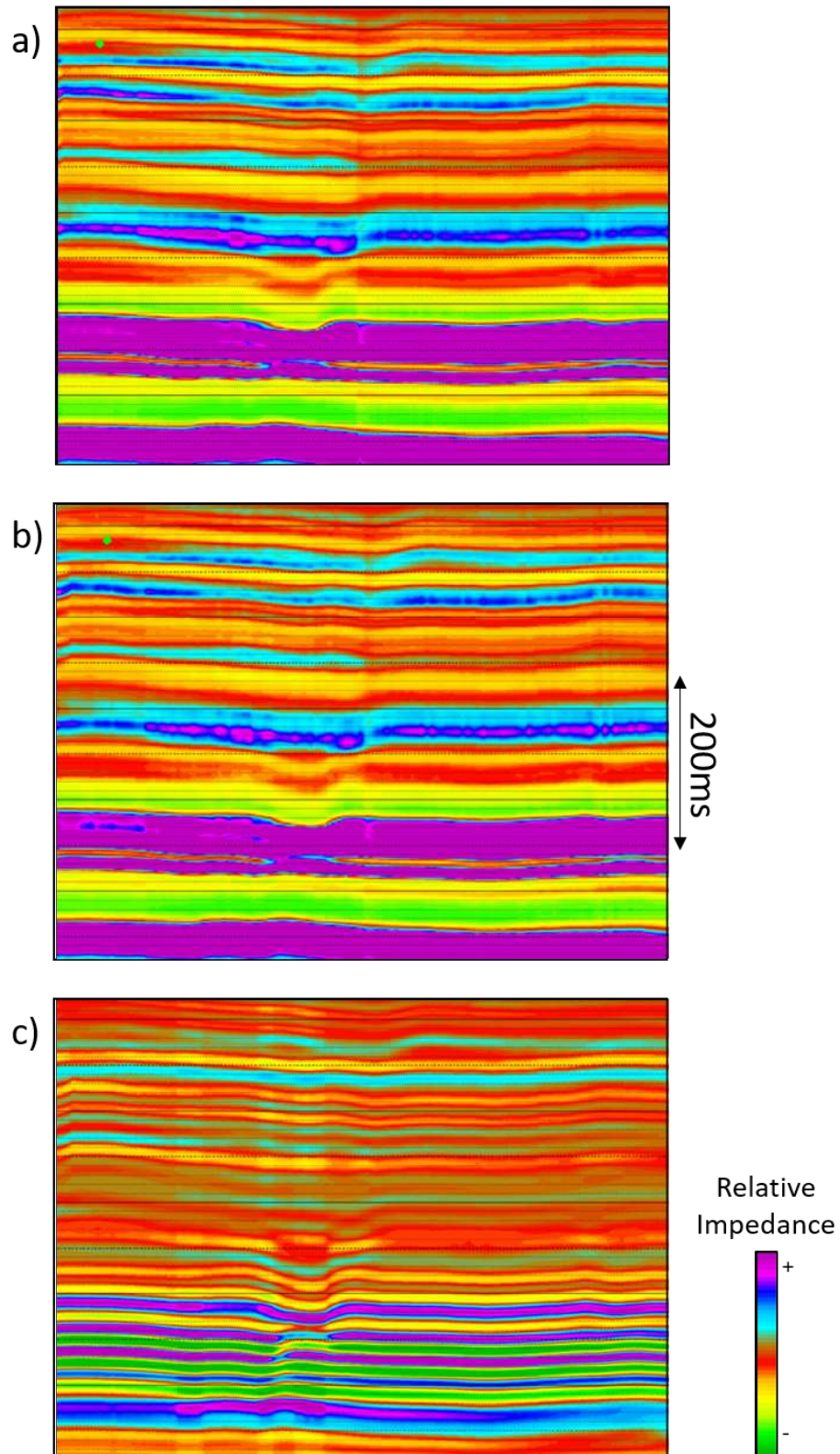
Figure 4.24: Example line 1 - HRS post stack inversion: testing weighting factors a) 0.2 b) 0.5 and c) 0.8.
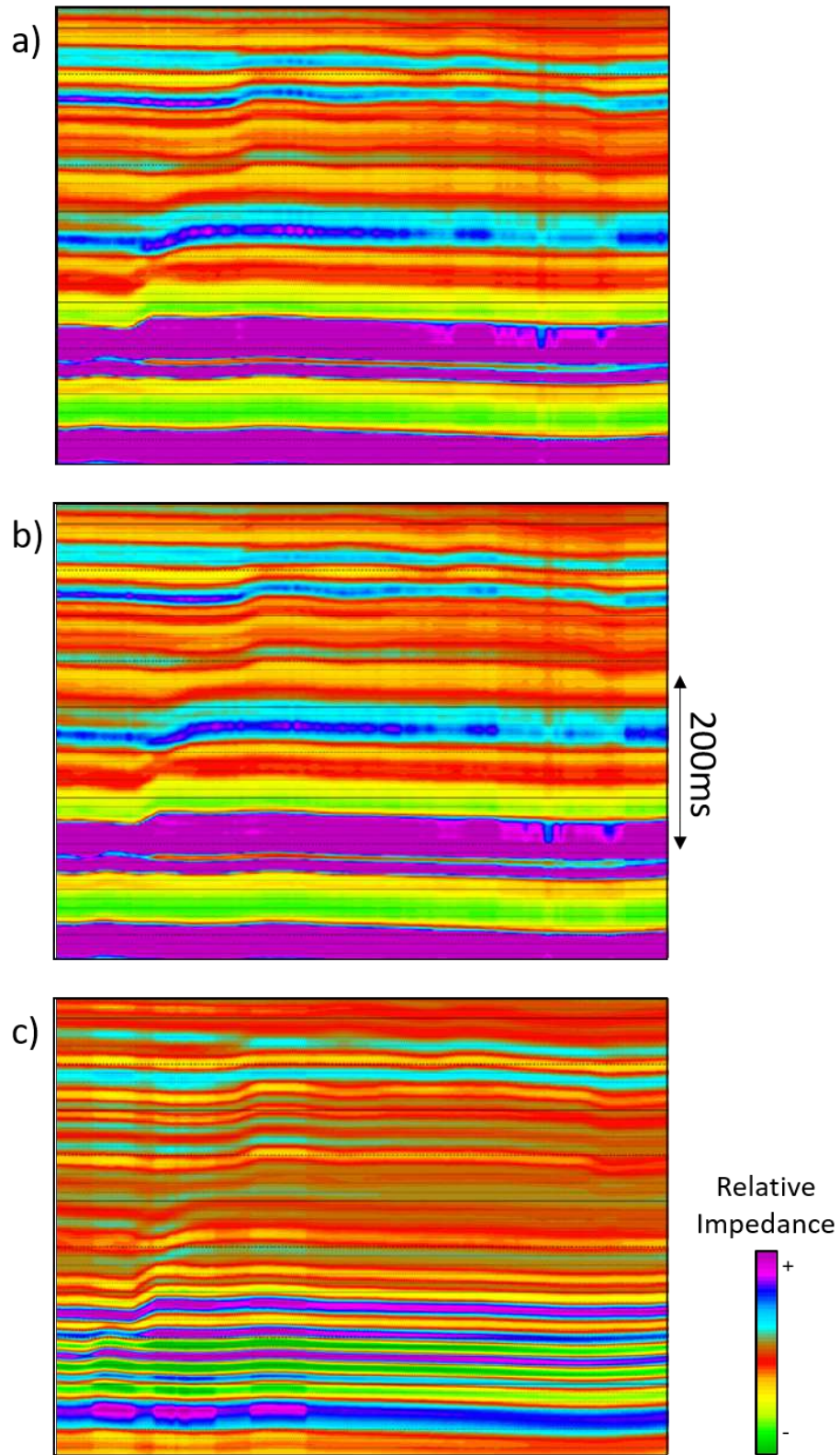
Figure 4.25: Example line 2 - HRS post stack inversion: testing weighting factors a) 0.2 b) 0.5 and c) 0.8.
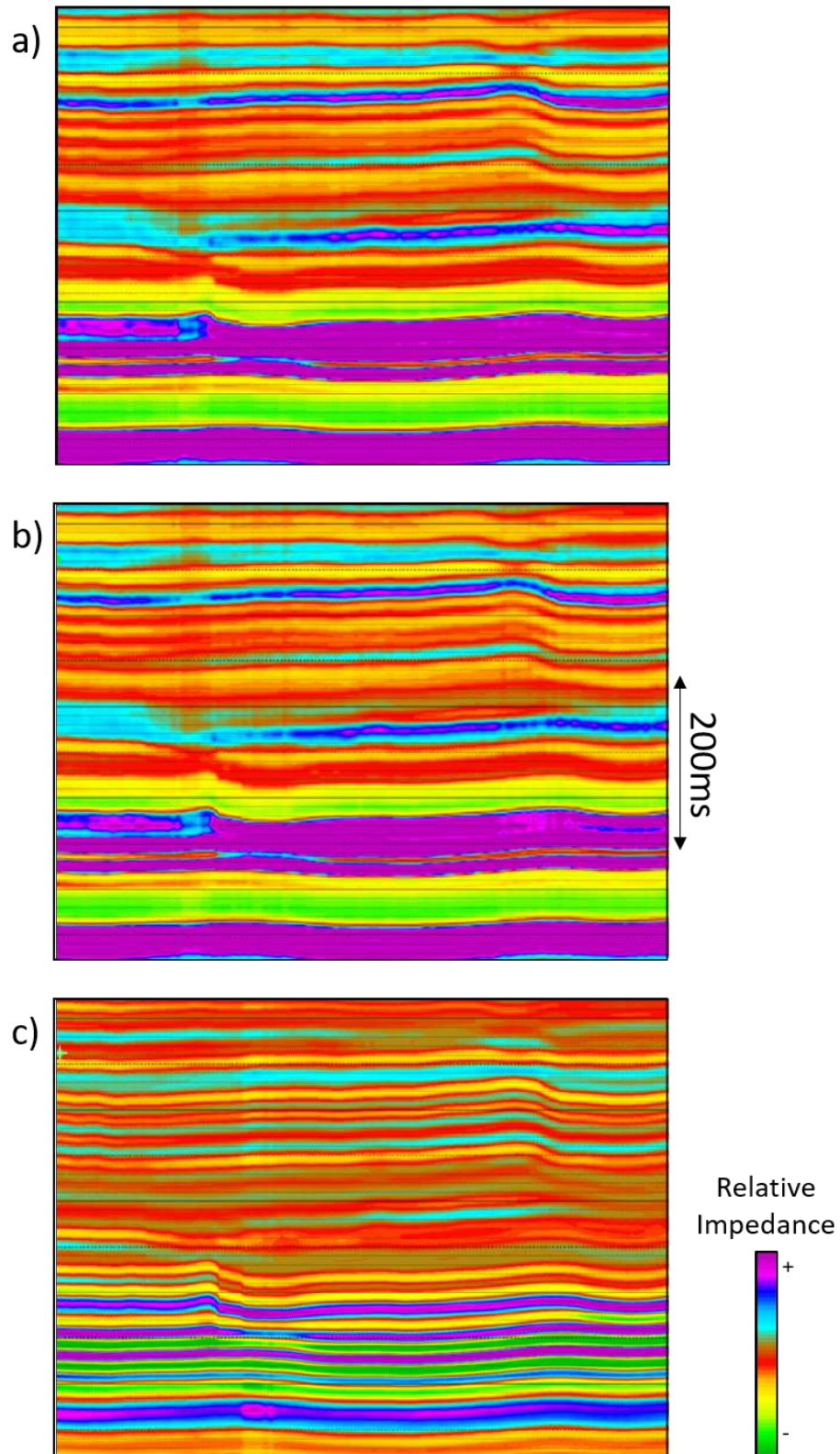
Figure 4.26: Example line 3 - HRS post stack inversion: testing weighting factors a) 0.2 b) 0.5 and c) 0.8.
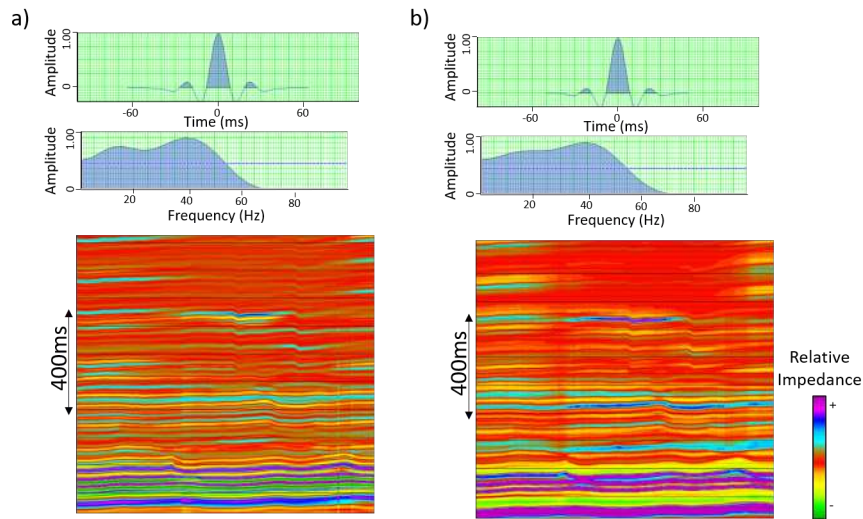
Figure 4.27: Example line 1 - HRS post stack inversion: testing wavelet length a) 128 ms b) 100ms.
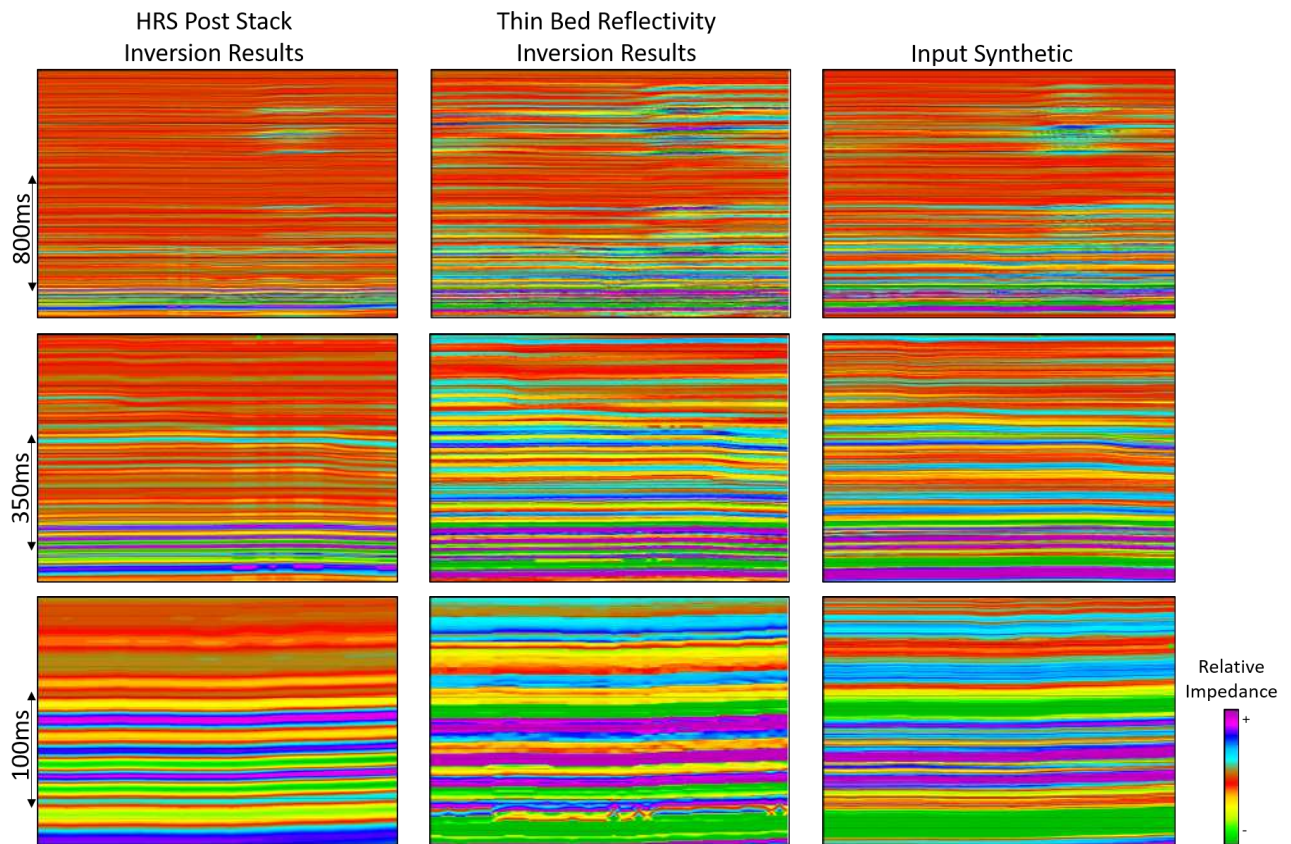
Figure 4.28: Post stack inversion results from HRS (left) and ThinMan (middle) compared to the relative imepedance volume used to create the input synthetic volume.
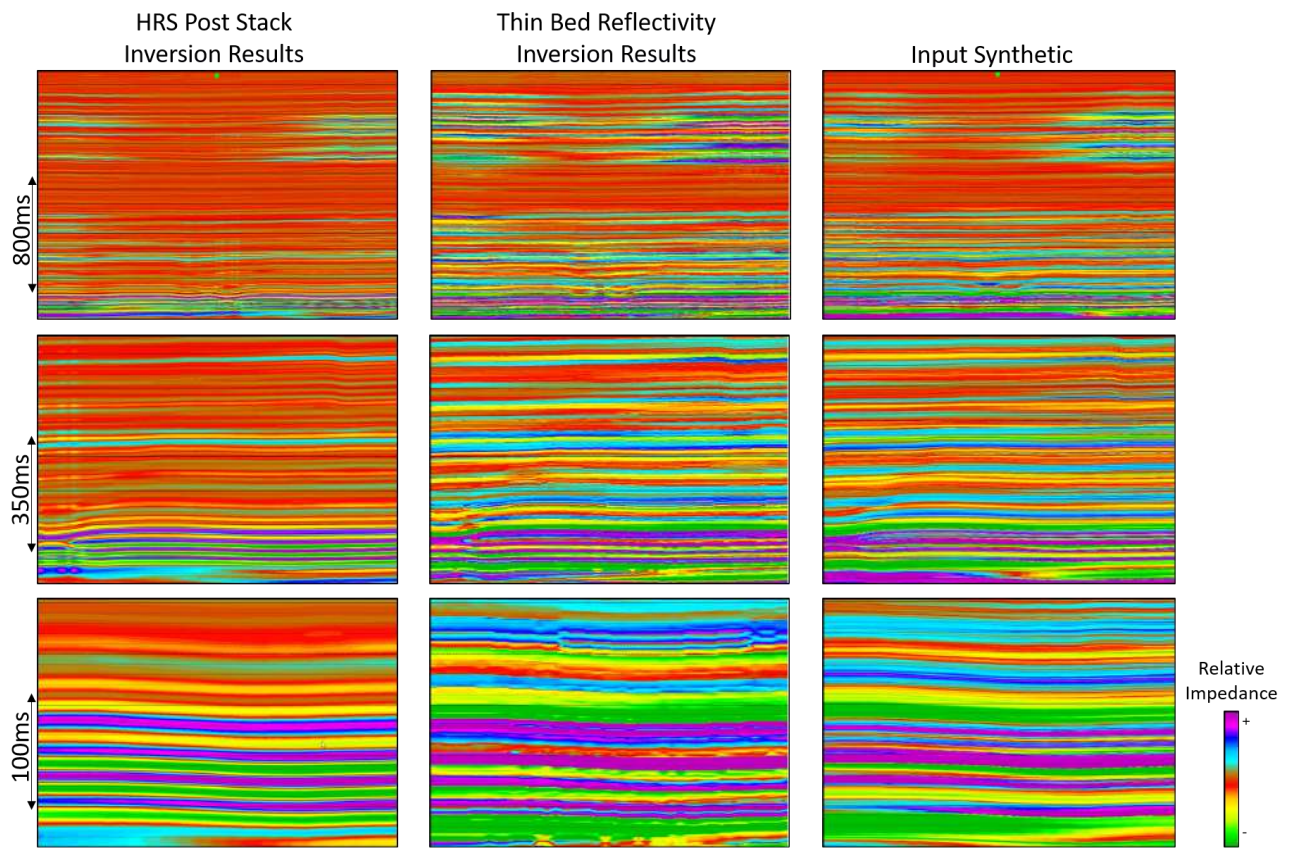
Figure 4.29: Post stack inversion results from HRS (left) and ThinMan (middle) compared to the relative imepedance volume used to create the input synthetic volume.

control purposes. As the inversions conducted with the Wattenberg synthetic volume is controlled, i.e., we know the solutions, this step in the quality control process verifies that the inversion is appropriately modeling the input data.

The next step in the quality control process is to compare the input and output reflection character. In Figure 4.30, the input seismic is shown on the left, the inverted reflection coefficients in the middle and the volume created from convolving the output reflection coefficients with a 50hz wavelet is on the right. This gives insight to how well the inversion matches the input data.
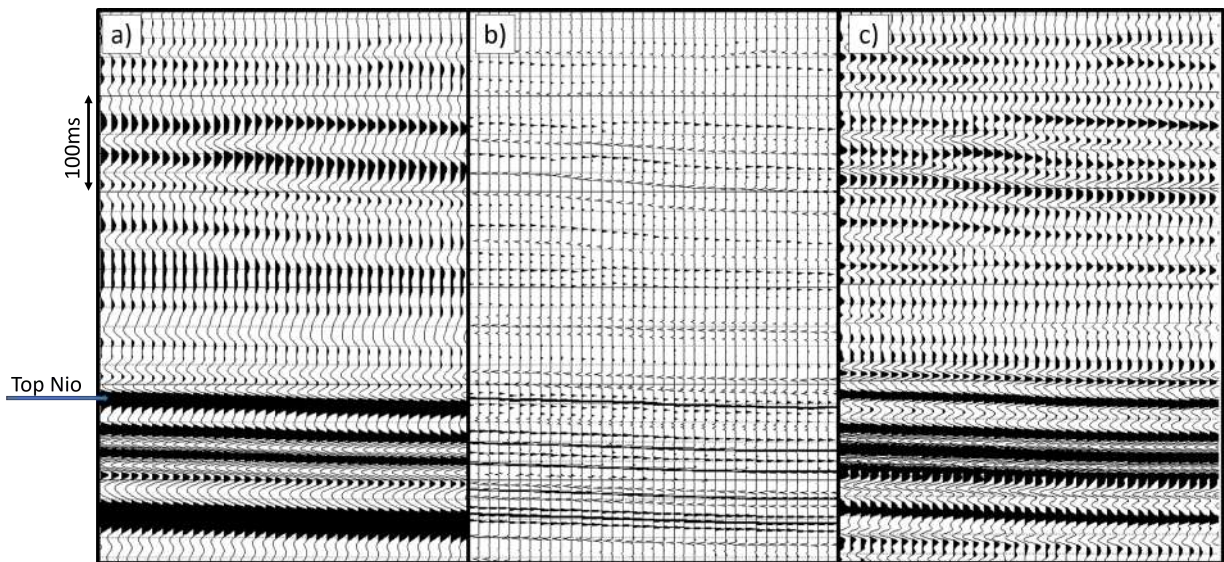
Figure 4.30: a) The Wattenberg modeled data convolved with a 30hz wavelet, general representation of our area of interest. b) The reflection coefficients output from the ThinMan inversion. c) The output reflection coefficients are convolved with a 50hz wavelet.
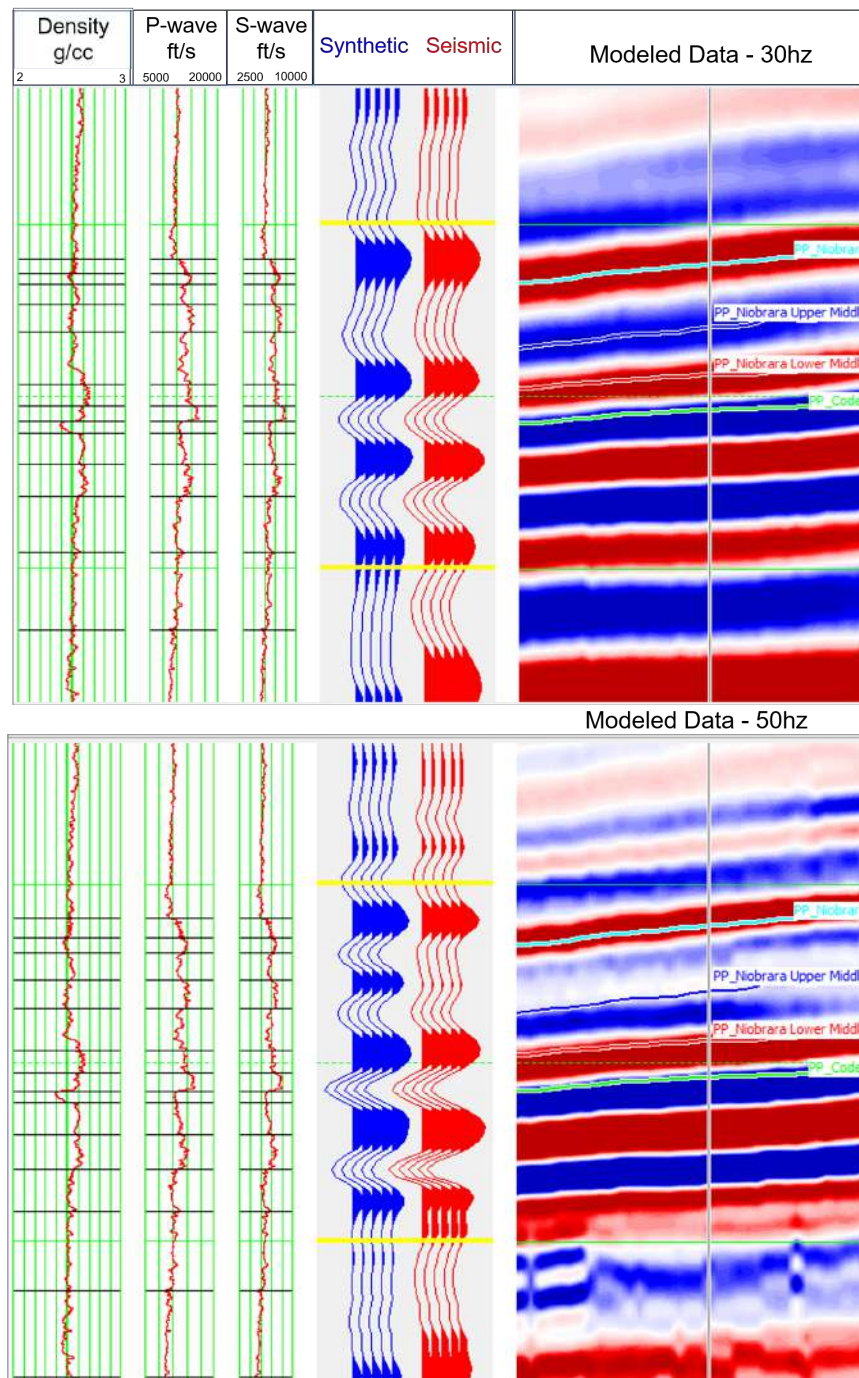
Figure 4.31: The inverted reflection coefficients from the Wattenberg synthetic volume are convolved with a 30hz (top) and 50hz (bottom) Ricker wavelet and then tied with a vertical well in the section. The cross correlations between these are above 90%.

4.8 Discussion

Although wedge tuning effects were present in both the ThinMan and HRS inversion, the ThinMan inverted relative impedance was more consistent than the HRS solution. The next step would be to compare these to the input acoustic impedance to determine how close they are to the actual answer. The ThinMan refelction coefficients indicate that there is an inherent issue with phase of the wavelet. The artifacts surrounding the strong events look similar to the case study from Portniaguine and Castagna (2005). This is something to keep in mind during interpretation. Overall, the ThinMan solution is superior.

The Wattenberg synthetic was useful in determining how both inversions match the input data (more complex and comparable to field data). Although ThinMan's inversion contains jittery-effects, the solution is more representative of the input than the HRS inversion. As the HRS inversion is very constrained, the solution is overly smooth and contains lower resolution than the ThinMan inversion. This is important to consider during interpretation of either inversions. If the goal of the inversion is to detect anomalous features, the overly smooth solution (from horizons and block size) may not resolve those features. I am recommending to model such an example to gain an understanding on how both HRS and ThinMan handle these effects and features.

Taking these results and brining them into interpretation, there are a few key things to keep in mind:

- HRS solutions are overly smooth

- ThinMan solutions contain jittery-effects that are not geological,but potentially controlled by the regularization parameter (testing is critical)

- ThinMan solutions are very high resolution, quality control of the results is essential

CHAPTER 5

APPLICATION AND INTERPRETATION OF THIN-BED REFLECTIVITY INVERSION

5.1 Static Conditions - Wattenberg Baseline QC

The ThinMan inversion of the Wattenberg synthetic volume indicates that the thin-bed reflectivity inversion produces high resolution relative impedance volumes while being robust (not requiring an initial model). Previous work within the RCP has determined that the landing position of the horizontal wells often went out of stage. As a result, the reservoir response varies from stage to stage by the varying geomechanical properties and that the geomechanical heterogeneity within the section is complex (Alfataierge, 2017). In addition, (Mabrey, 2016) conducted a rock quality index (RQI) analysis on the horizontal wells within the Wishbone section and proposed that the overall goal is to optimize completions by designing perforation clusters based on high rock quality and low stress. Harryandi (2017) used a pre-stack P-wave simultaneous seismic inversion for facies modeling where her results show probable chalk thickness. She proposes to use facies modeling during well planning to target the thickest and most continuous chalk intervals to optimize production. The motivation behind the thin-bed reflectivity inversion is similar to previous work as it is proposing to utilize geophysics to guide both the drill bit and completion designs. The thin-bed inversion is less laterally constrained than are HampsonRussell or Jason inversions. Consequently, thin-bed reflectivity inversion may be better suited for detecting anomalies Ultimately, we want to optimize production while maintaining relatively low costs.

The migrated, full-stack Turkey Shoot Baseline survey was run through the ThinMan inversion in attempts to resolve the chalk benches within the Niobrara formation. The ThinMan inversion attempts to increase the frequency content of the data without boosting noise. Figure 5.1 displays the amplitude spectrum from the input field data (blue) and the

inverted reflection coefficients (red). Note the significant increase in the frequency bandwidth of the reflection coefficients. This massive increase may draw red flags as is not part of the input data. Keep in mind that this inversion builds a known dictionary of all possible events (the model) and attempts to minimize the objective function by matching the model with the input data. The events within the dictionary contain information about the reflection coefficients and the relative acoustic impedance of those events. This is where the added bandwidth is derived. The inversion works to minimize the objective function while maintaining a level of sparsity.

To quality control (QC) these results, the output reflection coefficients were convolved with both a 30hz and 50hz Ricker wavelet and compared with data from the well locations. Data from the well locations were used for quality control purposes and were not used during the inversion process. These volumes were correlated with the vertical wells and RMS amplitude slices were extracted. In addition, the relative impedances at each well location is overlain on the inversion results. To visualize how the inversion results of the field data compare with the Wattenberg synthetic inversion, the reflection coefficients at each well are analyzed.

In Figure 5.2, the synthetic seismograms produced by convolving the output reflection coefficients with both a 30hz and 50hz Ricker wavelet are correlated with the sonic logs. This correlation checks the stability of the time variant set of extracted wavelets within the reservoir interval. There is a very good match between the seismic and the sonic logs, the correlation coefficients for both the 30hz and 50hz data are over 90% indicating that the time variant wavelet is stable.

Chopra and Marfurt (2005) claim that attributes run on frequency enhanced seismic data that produce more significant and detailed interpretations. These fine details include resolving channels, faults/fractures, and complex onlaps and off-laps. Figures 5.3-5.5 display the RMS amplitude slices on the lower Pierre, top Niobrara and Codell reflectors from both the input field data and the 50hz data. As the depositional environment of these

three formations would predict, the RMS amplitude slices are not resolving channels or onlaps/offlaps. Faults on each three slices from the 50hz data are higher resolution and better resolved than the slices from the input field data. Specifically on the top Niobrara, both grabens and the faults in the North-West corner are better resolved.

Figures 5.6-5.14 display the relative acoustic impedance from each well overlain on the inverted relative acoustic impedance. From top to bottom, the white arrow points to the top of the Niobrara and the black arrows point to the B chalk, C chalk and D interval, respectively. As one would expect, the actual relative impedance from the well is higher resolution than the inverted data, but overall there is a good match. The B and C chalk benches are consistently resolved throughout the entirety of the survey. The conventional seismic resolution of the P-wave data is approximately 65 ft. From the relative acoustic impedance volume, the measured thickness of both the B and C chalks are approximately 30-35 ft.

Taking a closer look at the fine details, Figures 5.15-5.17 show the reflection coefficients from the inverted Wattenberg synthetic (a), inverted Baseline survey (b), and the input seismic from the Baseline survey (c). Overlain on the data is gamma ray and the tops of the formations. The top Niobrara reflector is a strong positive (red) reflector. The strong event gets broken down into three positive reflectors with the event in the middle correlating to the top Niobrara and the one below it, the B chalk. Two events below the B chalk, the negative (blue) reflector correlates to the C chalk. Similar to what was observed on the relative acoustic impedance volumes, the reflection coefficients are consistently resolving the B and C chalk intervals. Note the lack in lateral smoothness, as this inversion is a trace-by-trace process, the solution works to detect small features and lateral anomalies.
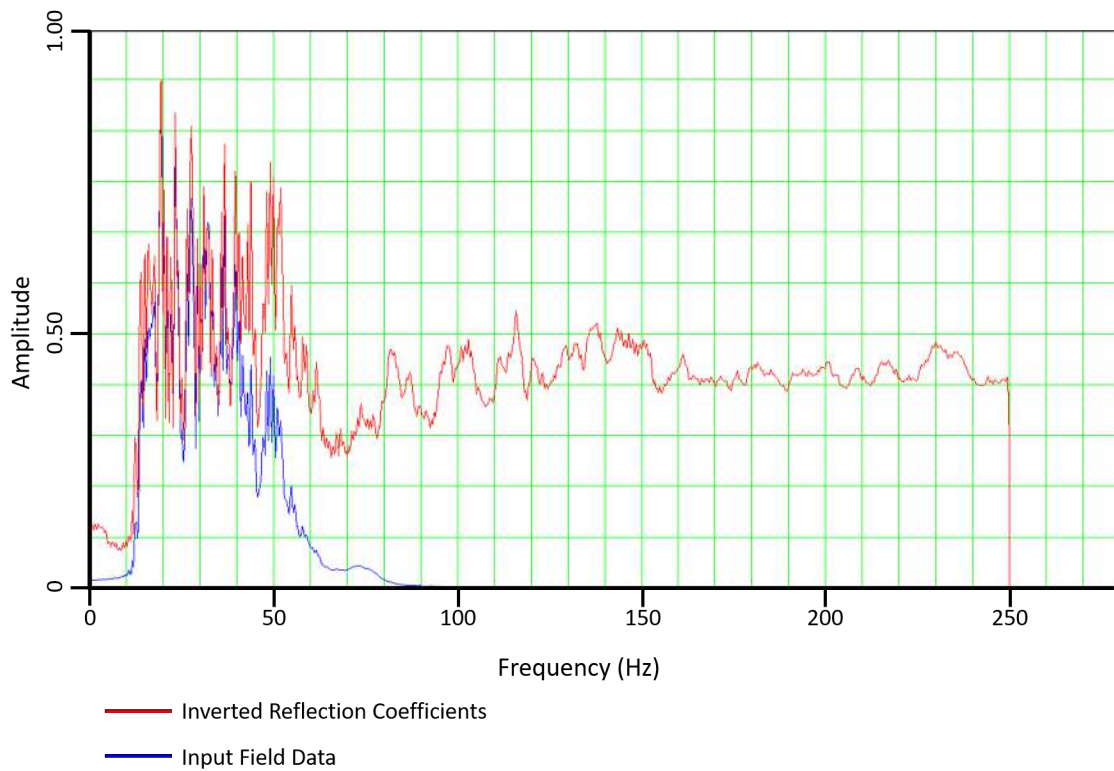
Figure 5.1: Comparison of the input amplitude spectrum with the inverted reflection coefficients. Note the large increase in frequency content on the reflection coefficients.
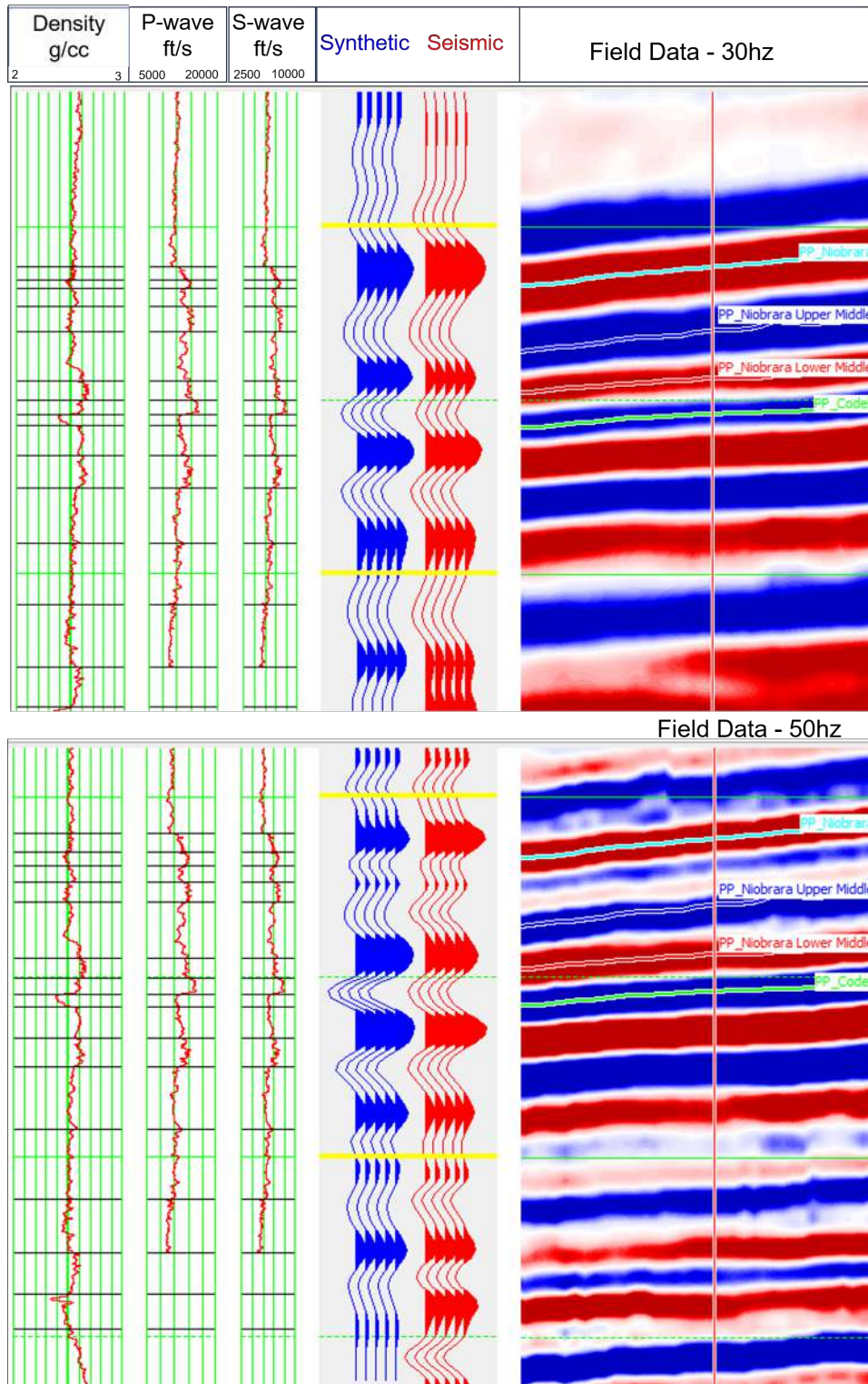
Figure 5.2: The inverted reflection coefficients from the Baseline field data are convolved with a 30hz (top) and 50hz (bottom) Ricker wavelet and then tied with a vertical well in the section. The cross correlations between these are above 90%.
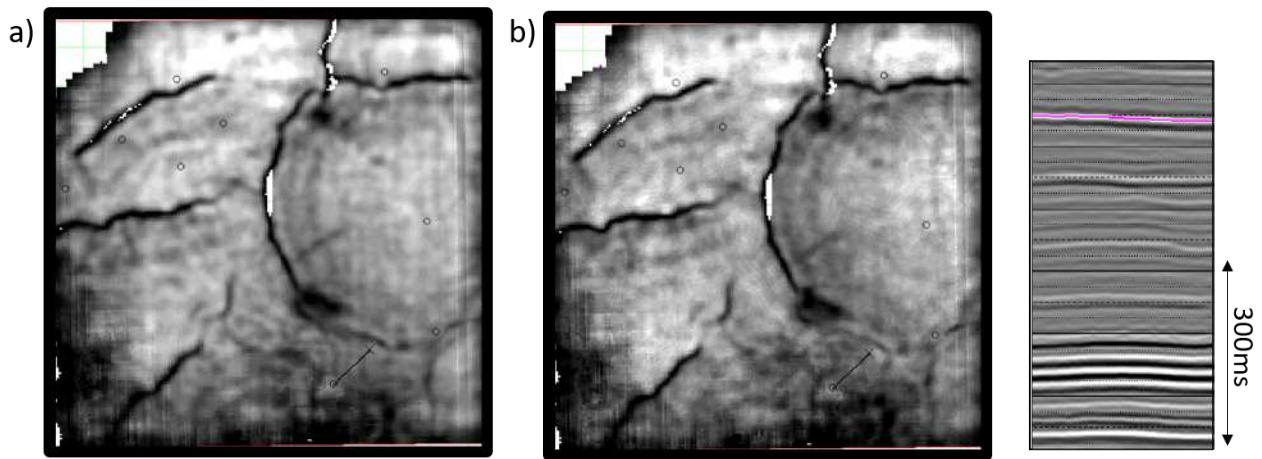
Figure 5.3: RMS amplitude slices on a lower Pierre reflector a) Data slice from the P-wave field data. b) Data slices from the reflection coefficients convolved with a 50hz wavelet.
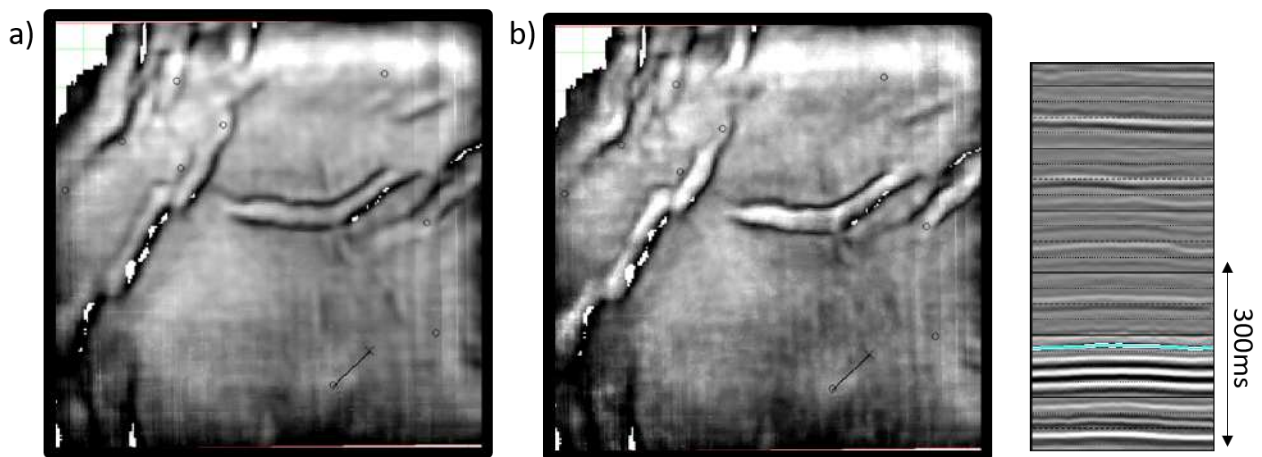
Figure 5.4: RMS amplitude slices on the top Niobrara reflector a) Data slice from the P-wave field data. b) Data slices from the reflection coefficients convolved with a 50hz wavelet.
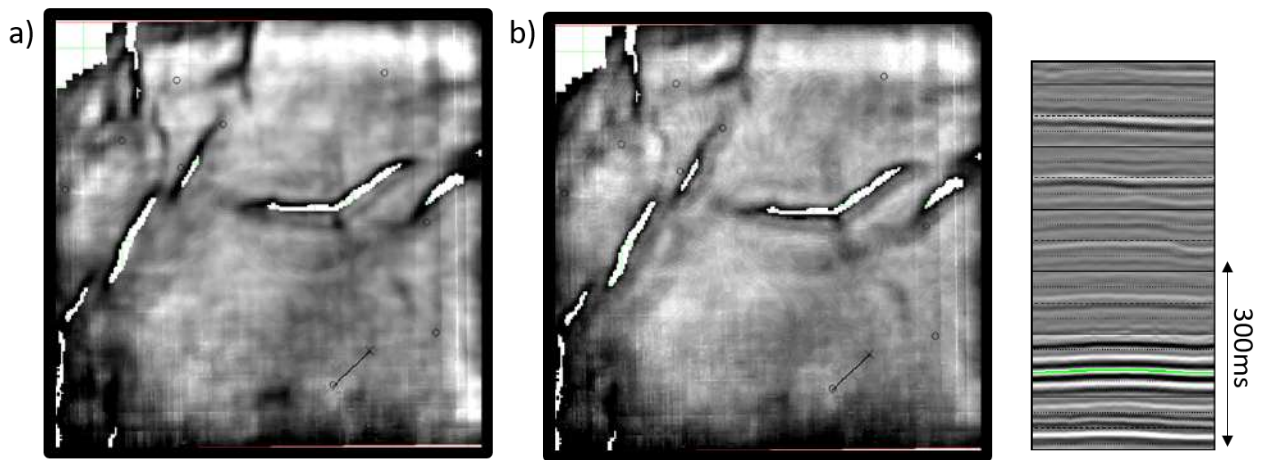
Figure 5.5: RMS amplitude slices on the Codell reflector a) Data slice from the P-wave field data. b) Data slices from the reflection coefficients convolved with a 50hz wavelet.
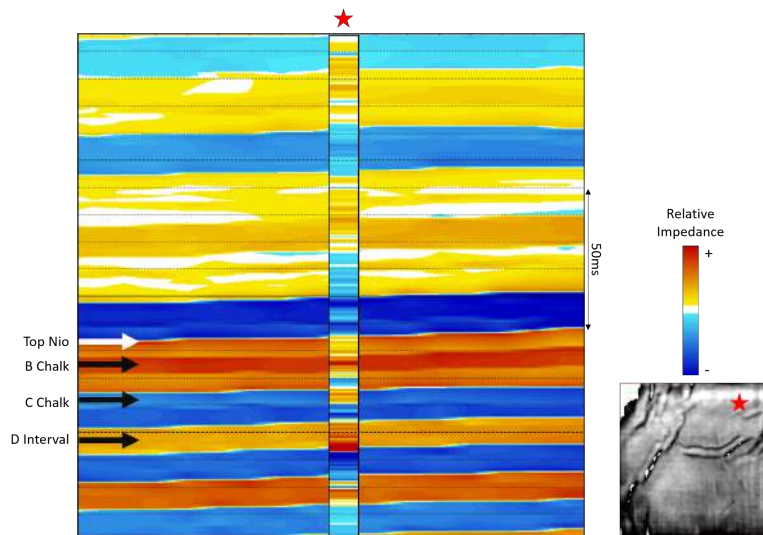
Figure 5.6: Relative acoustic impedance result from the Baseline survey (static condition) with relative impedance from the Wattenberg synthetic model overlain on the well location. The RMS amplitude slice on the top Niobrara reflector (from the input field data) is located in the bottom right corner as a basemap. The red star is the location of the well being used to QC the relative impedance results.
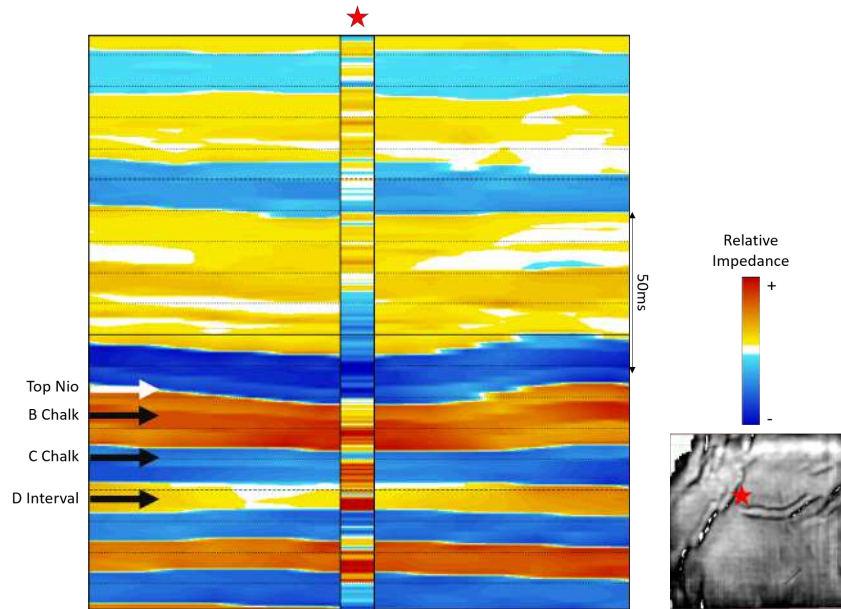
Figure 5.7: Relative acoustic impedance result from the Baseline survey (static condition) with relative impedance from the Wattenberg synthetic model overlain on the well location. The RMS amplitude slice on the top Niobrara reflector (from the input field data) is located in the bottom right corner as a basemap. The red star is the location of the well being used to QC the relative impedance results.
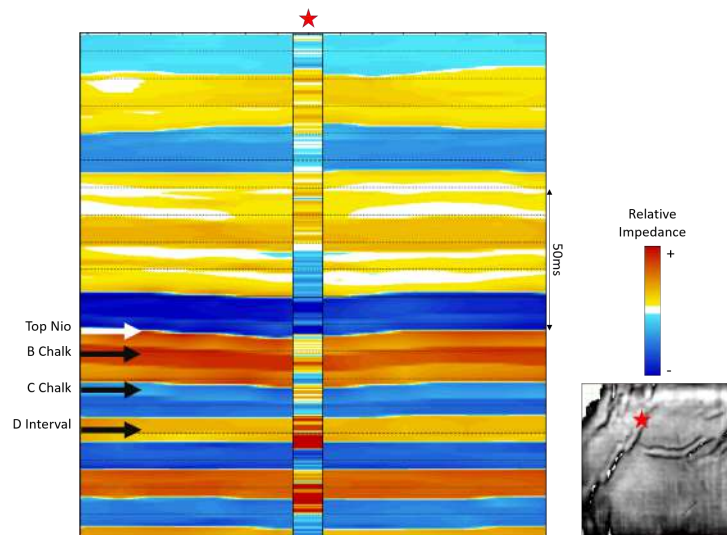
Figure 5.8: Relative acoustic impedance result from the Baseline survey (static condition) with relative impedance from the Wattenberg synthetic model overlain on the well location. The RMS amplitude slice on the top Niobrara reflector (from the input field data) is located in the bottom right corner as a basemap. The red star is the location of the well being used to QC the relative impedance results.
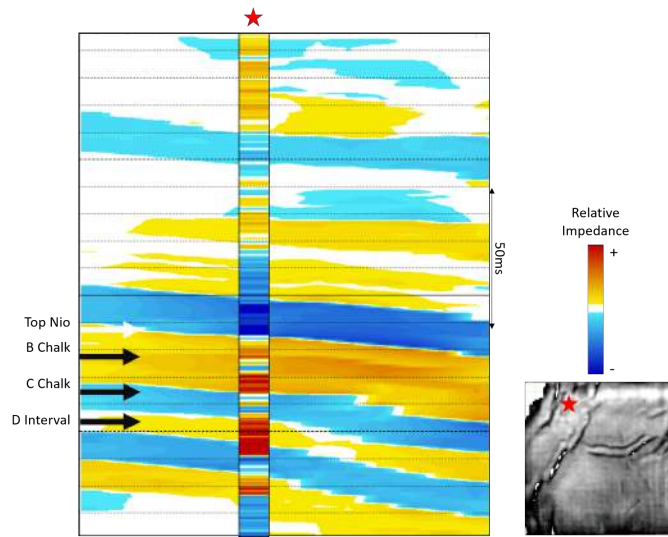
Figure 5.9: Relative acoustic impedance result from the Baseline survey (static condition) with relative impedance from the Wattenberg synthetic model overlain on the well location. The RMS amplitude slice on the top Niobrara reflector (from the input field data) is located in the bottom right corner as a basemap. The red star is the location of the well being used to QC the relative impedance results.
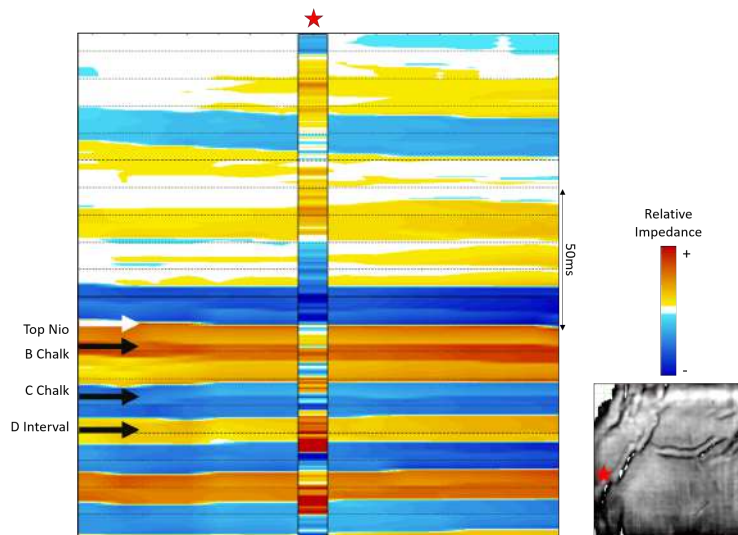
Figure 5.10: Relative acoustic impedance result from the Baseline survey (static condition) with relative impedance from the Wattenberg synthetic model overlain on the well location. The RMS amplitude slice on the top Niobrara reflector (from the input field data) is located in the bottom right corner as a basemap. The red star is the location of the well being used to QC the relative impedance results.
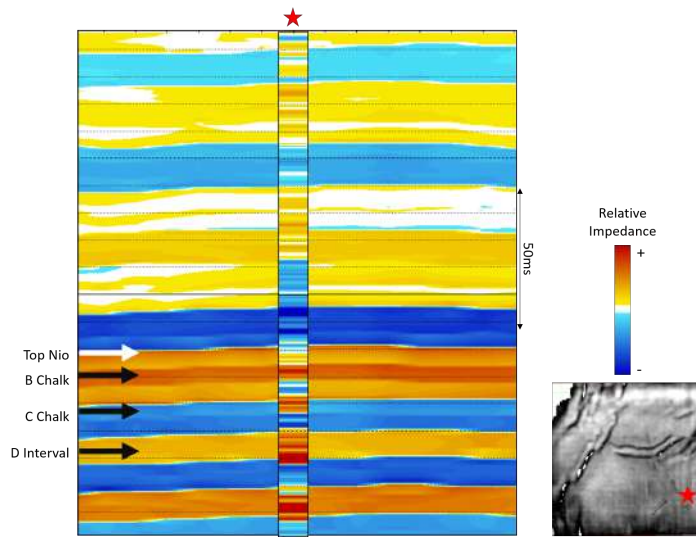
Figure 5.11: Relative acoustic impedance result from the Baseline survey (static condition) with relative impedance from the Wattenberg synthetic model overlain on the well location. The RMS amplitude slice on the top Niobrara reflector (from the input field data) is located in the bottom right corner as a basemap. The red star is the location of the well being used to QC the relative impedance results.
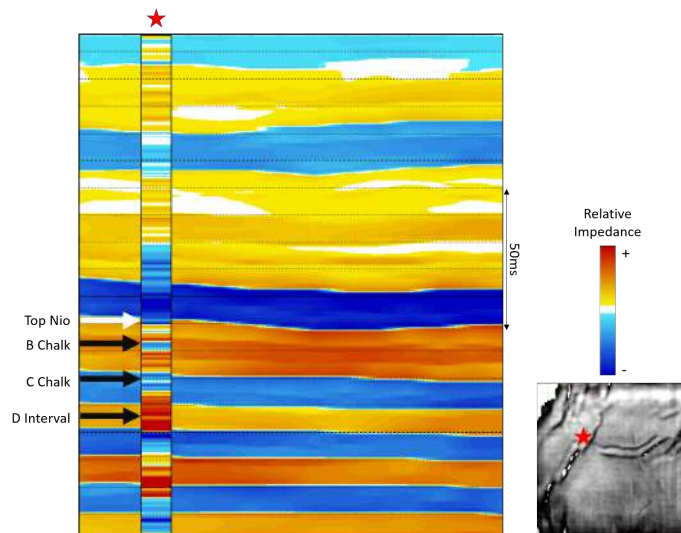
Figure 5.12: Relative acoustic impedance result from the Baseline survey (static condition) with relative impedance from the Wattenberg synthetic model overlain on the well location The RMS amplitude slice on the top Niobrara reflector (from the input field data) is located in the bottom right corner as a basemap. The red star is the location of the well being used to QC the relative impedance results.
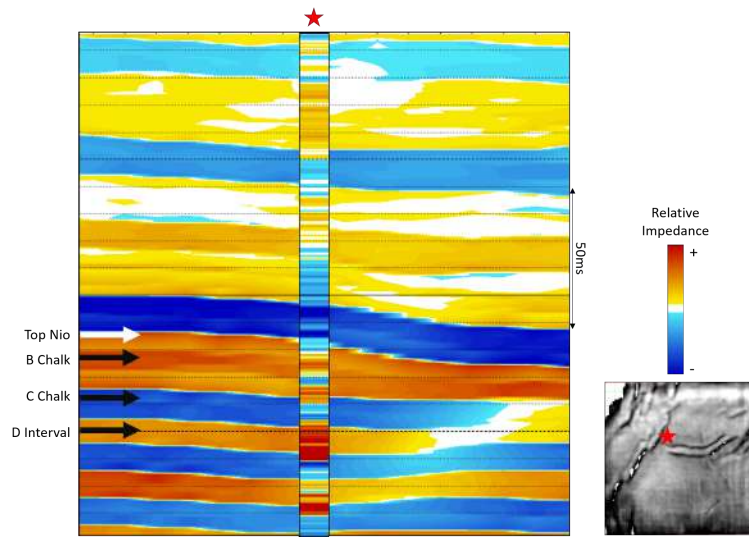
Figure 5.13: Relative acoustic impedance result from the Baseline survey (static condition) with relative impedance from the Wattenberg synthetic model overlain on the well location. The RMS amplitude slice on the top Niobrara reflector (from the input field data) is located in the bottom right corner as a basemap. The red star is the location of the well being used to QC the relative impedance results.
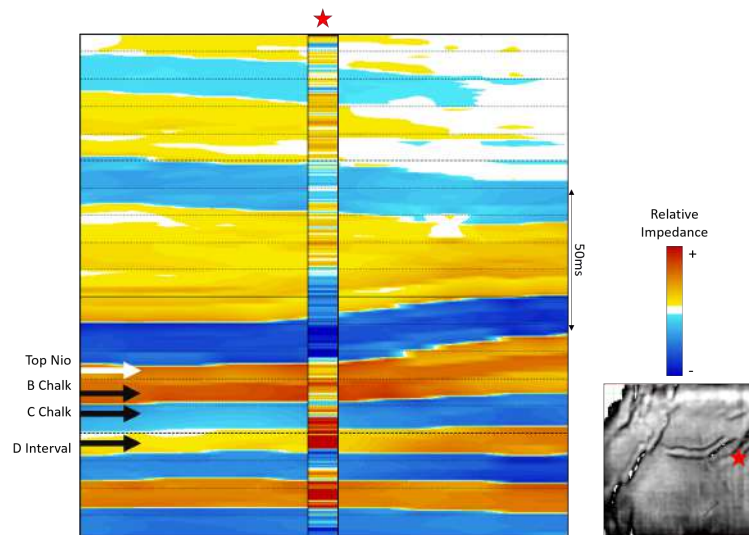
Figure 5.14: Relative acoustic impedance result from the Baseline survey (static condition) with relative impedance from the Wattenberg synthetic model overlain on the well location. The RMS amplitude slice on the top Niobrara reflector (from the input field data) is located in the bottom right corner as a basemap. The red star is the location of the well being used to QC the relative impedance results.
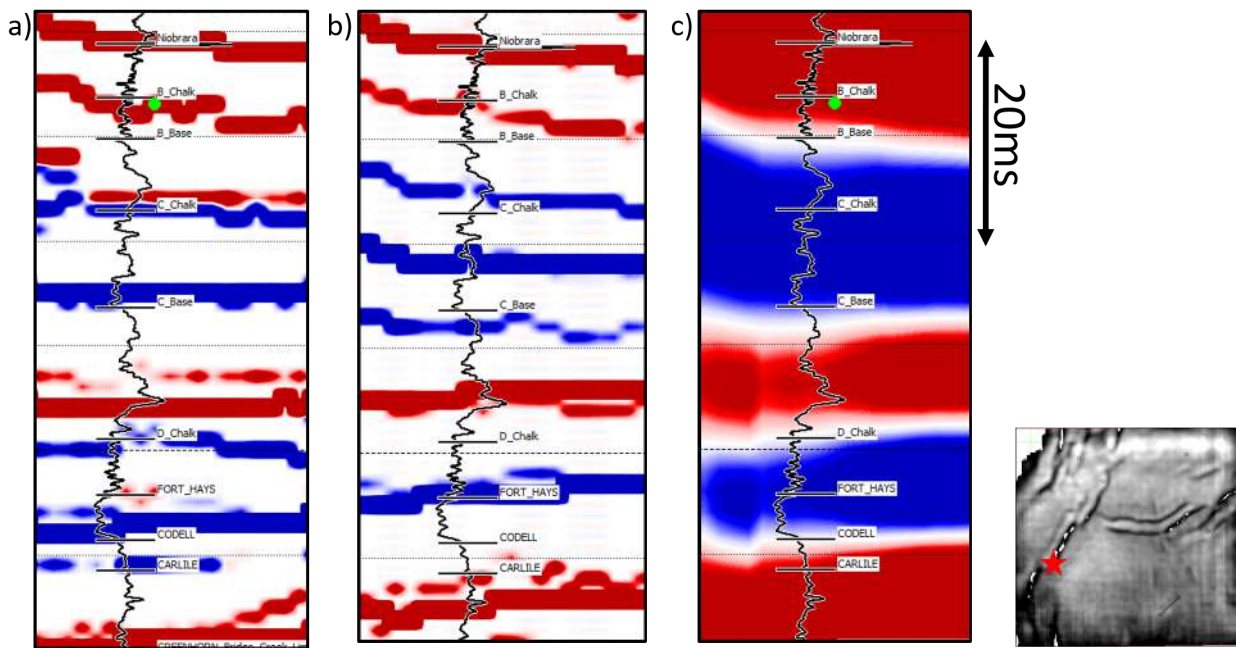
Figure 5.15: The inverted reflection coefficients from the Wattenberg synthetic volume (a) and the Baseline field data (b) are compared to the Baseline field data (c). The well location is depicted with the star on the basemap on the right. At the well location, gamma ray and well tops are displayed.
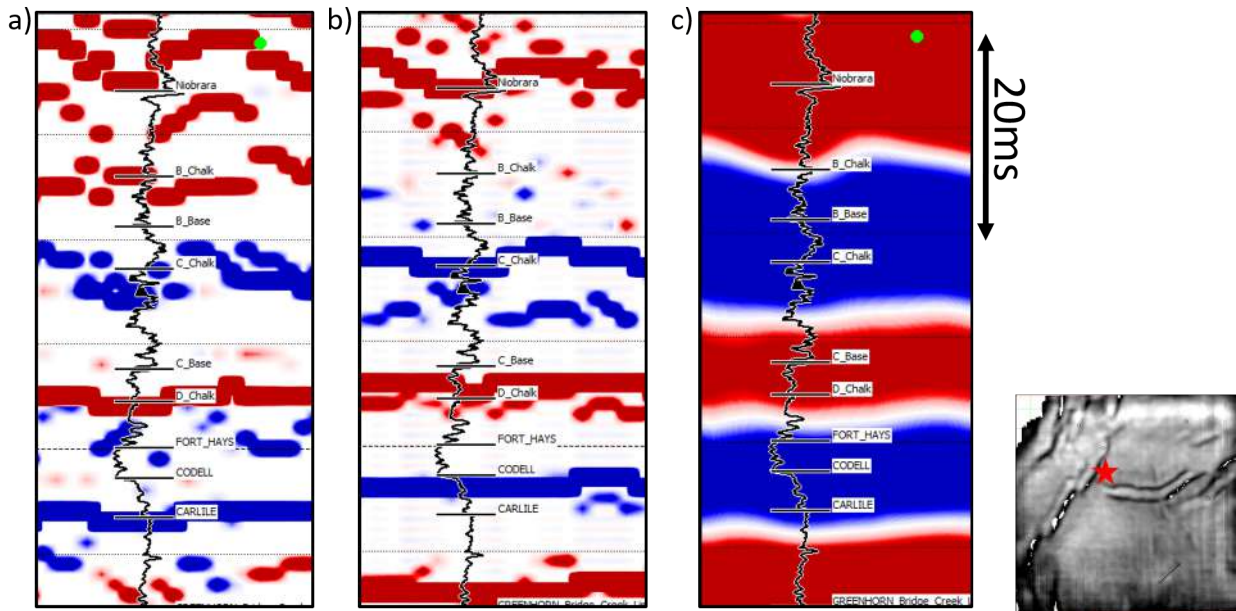
Figure 5.16: The inverted reflection coefficients from the Wattenberg synthetic volume (a) and the Baseline field data (b) are compared to the Baseline field data (c). The well location is depicted with the star on the basemap on the right. At the well location, gamma ray and well tops are displayed.
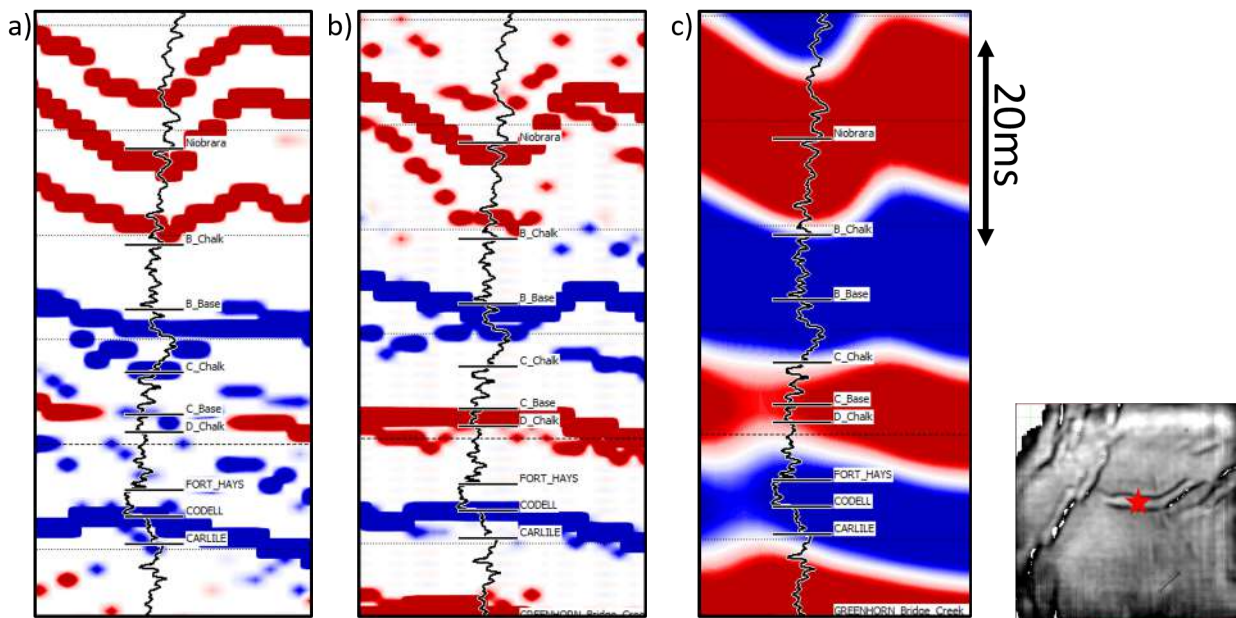
Figure 5.17: The inverted reflection coefficients from the Wattenberg synthetic volume (a) and the Baseline field data (b) are compared to the Baseline field data (c). The well location is depicted with the star on the basemap on the right. At the well location, gamma ray and well tops are displayed.

5.2 Static Conditions - Wattenberg Baseline Interpretation

Figure 5.18 shows a comparison of an inline from the Baseline survey and its corresponding reflectivity section. The ThinMan inversion outputs the reflection coefficients that provide extra detail, both in terms of extra reflection cycles and fault detail. Notice the extra reflection detail resolved on the top Niobrara reflector. The strong, positive event gets broken down into three and, relating this back to Figures 5.15-5.17, the positive event below the top Niobrara has been correlated to the B chalk interval. The potential doubt that the extra detail is not legitimate can be counter-argued by the correlated well ties in Figure 4.31. The correlation is very strong, both the 30hz and 50hz data have a correlation coefficient greater than 90%. Note that any correlation or comparison with well data is a blind well test as there was no well information utilized during the inversion process. The extra reflection cycles are matching with the corresponding cycles on the well data.
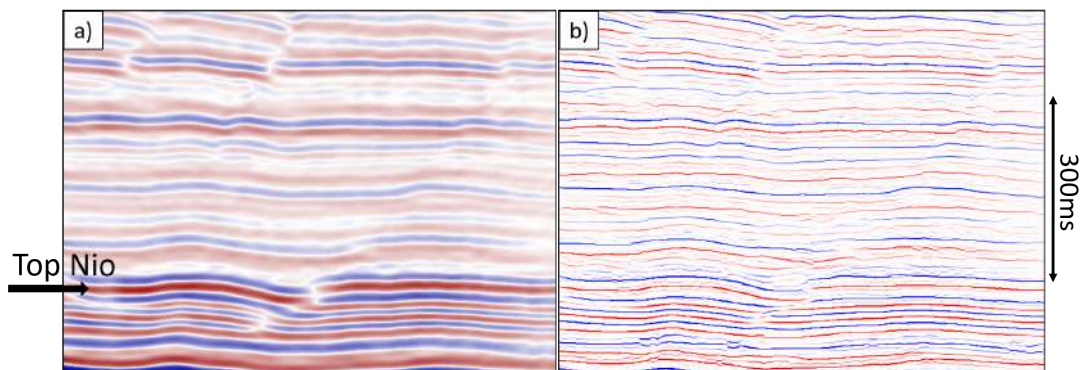
Figure 5.18: a) Example inline from the input seismic data. b) Inverted reflection coefficients. Note the extra reflection cycles and fault detail.

Drake and Hawkins (2012) presented a sequence stratigraphic framework for the Niobrara Formation in the DJ Basin in the Search and Discovery Article #50757 that is used to geologically verify the results from the Baseline/static thin-bed reflectivity inversion. The reference well used to build the sequence stratigraphic framework is located within a 10-square mile radius from our study area and is perfect for correlating and verifying the inversion results. Figure 5.19 displays the general paleogeography during the deposition of the Niobrara and

the geographical location of the reference well. Relating the inversion findings back to geology it is important to remember that the sedimentary record is inherently complicated by relative sea level and that the various chalk and marl benches display general trends within the DJ Basin (Drake and Hawkins, 2012). The sequence stratigraphic framework is generally preferred over the lithostratigraphy (Figure 5.20), as mapping the stratigraphic sequence trends correlate better to the preservation and non-preservation of organic material. The chalk benches were deposited during highstands where there was a shoreward shift in facies and can be correlated with the maximum flooding surfaces. Figure 5.21 correlates the maximum flooding surfaces on gamma ray and resistivity from the reference well, to the well data derived relative acoustic impedance and the inverted relative impedance from the Baseline survey within the Wishbone section.
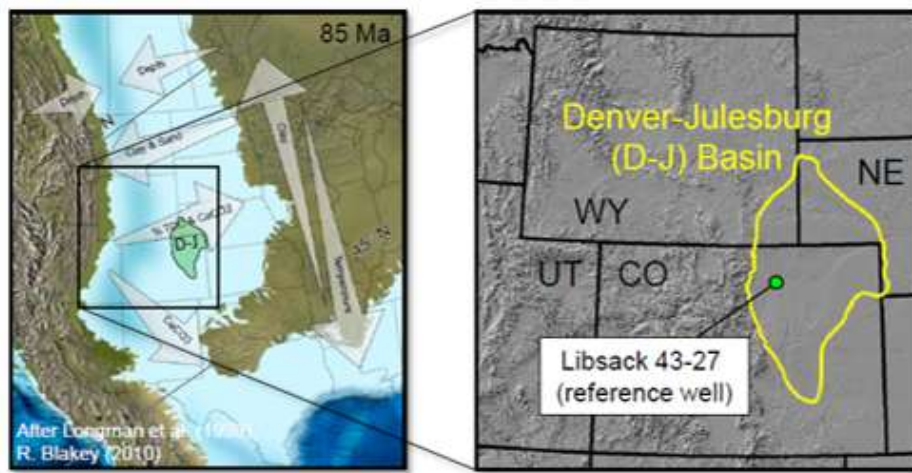
Figure 5.19: Paleogeographic map depicting depositional environment (left). The black box indicates the regional study area. Zooming into the study area (left), the DJ Basin is outlined in yellow and the green dot indicates the location of the reference well (Drake and Hawkins, 2012).

The inverted relative impedance is not fully resolving the D interval as it is lumping together the D marl and the Fort Hays. The inverted relative impedance and reflection coefficients are resolving both the B and C chalk intervals. As the Wishbone is heavily faulted, the inverted relative impedance volume was flattened on the top Niobrara and
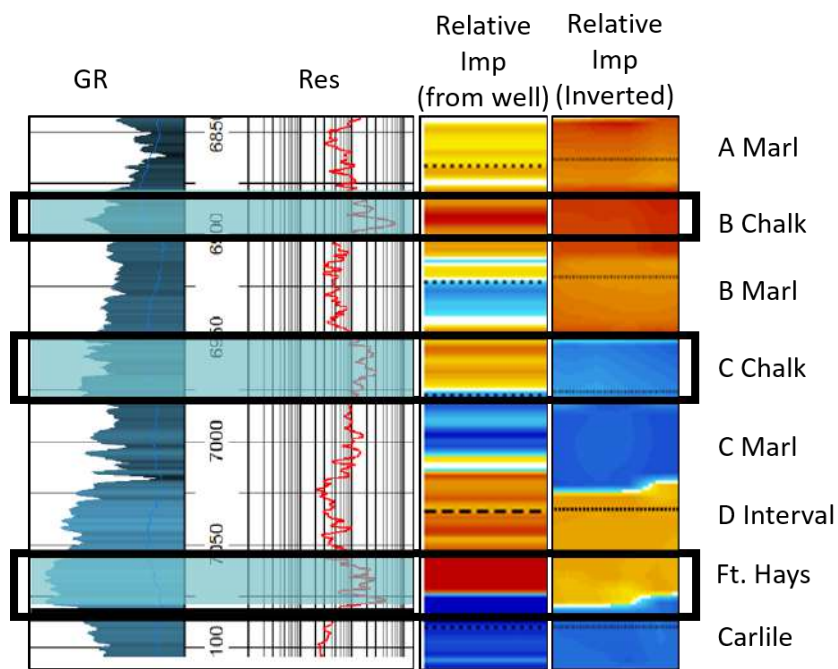
Figure 5.20: Gamma ray and resistivity from the Pioneer reference well interpreted with the relative impedance from the Wishbone section and the inverted relative impedance from the seismic. The black boxes shadded in blue depict the different intervals established in the sequence stratigraphic framework (Modified from Drake and Hawkins, 2012).
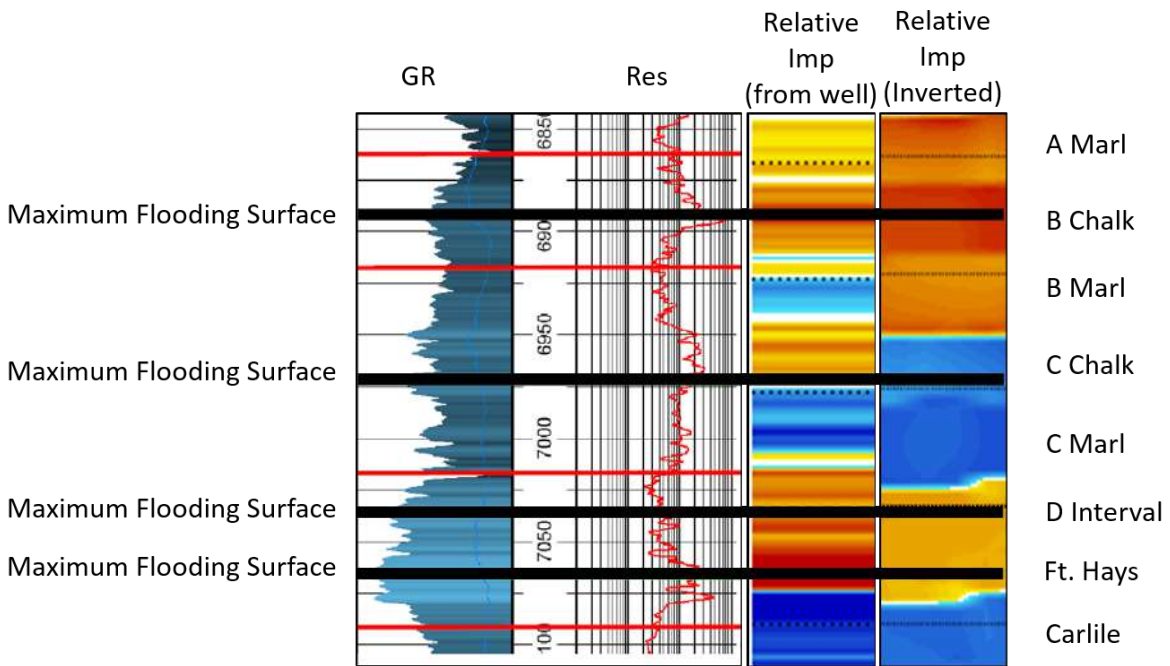
Figure 5.21: Gamma ray and resistivity from the Pioneer reference well interpreted with the relative impedance from the Wishbone section and the inverted relative impedance from the seismic. The black lines indicate the maximum flooding surfaces (Modified from Drake and Hawkins, 2012).

the Greenhorn formation in order to perform stratal slicing. The goal behind the stratal slicing is to characterize the distribution and physical properties of the reservoir (Zeng, 2018; Zeng et al., 1998a; Zeng et al., 1998b). As I have inverted the seismic for relative acoustic impedance and correlated these relative values back to geology at the well locations, the next step is to map their spatial variability and discontinuities/continuities. To relate these results back to stratigraphy, the stratal slices are compared with the isochron maps from Drake and Hawkins study. Figure 5.22 displays the flattened inline A-A' that cuts through the Wishbone Section. The arrow and the dotted black line indicate where in time the relative impedance slice is located. The relative impedance of the B chalk within this area can be correlated to the isochron thickness map of the B chalk in Figure 5.23. The relative impedance of the B chalk tends to be very positive. On the inversion results the B chalk appears to be very continuous, yet the its unique character seems to decrease to the south. Looking at the isochron map, the B chalk thickness appears to be decreasing just south of the reference well (i.e. the location of the Wishbone section.) Moving down in section, the C chalk character within the relative impedance slice in Figure 5.24 appears very continuous and does not seem to be changing within the study area. Spatially around the reference well, Figure 5.25 shows that the isochron thickness is not changing. Similar to the character of the C chalk, the D interval (D marl and Ft. Hays) is very continuous without any lateral variation (Figure 5.26). Around the reference well in Figure 5.27, there is a gradual increase in thickness to the south, but in general, the thickness within the study area is continuous.

The facies inversion from Harryandi (2017) produces a RMS amplitude map of the pure chalk facies that include the B and C chalk benches of the Niobrara (Figure 5.29). The warm colors indicate areas that have a high probability of having thicker chalk benches. Within the center of the Wishbone section there is high probability of a thick chalk interval. This decreases to the North and South. Comparing this result to the ThinMan relative impedance maps of the B and C chalk benches, each map observes a decrease to the South. These maps differ to the North, as the B chalk increases in relative impedance.

133
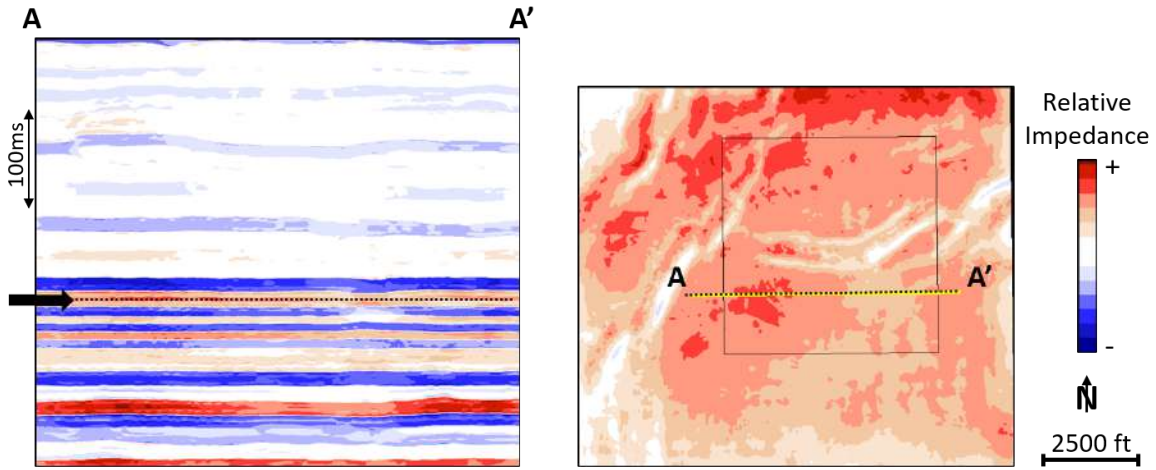
Figure 5.22: Seismic line A-A' flattened on the Top Niobrara and the Graneros (left).The black dotted line and black arrow indicate the interval the stratal slice (b) is extracted from. This stratal slice is representative of the B chalk.
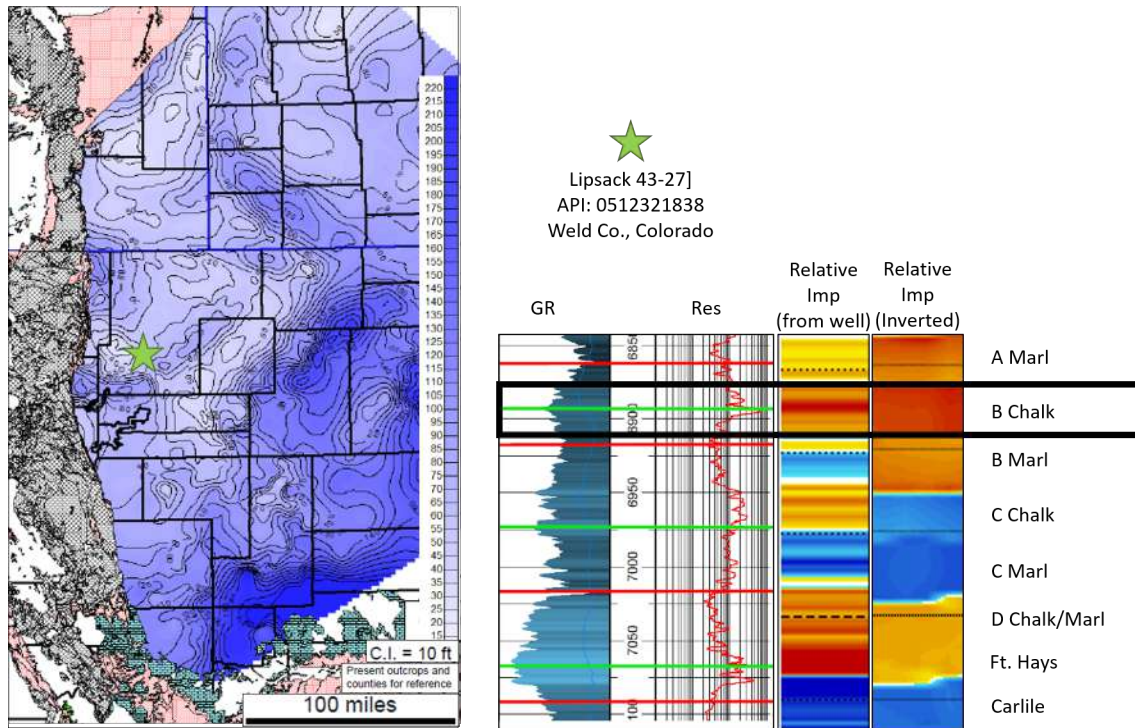
Figure 5.23: Isochron map of the B chalk (left). The green star is the Pioneer reference well location. Gamma ray and resistivity from the Pioneer reference well interpreted with the relative impedance from the Wishbone section and the inverted relative impedance from the seismic (right) (Modified from Drake and Hawkins, 2012).

134
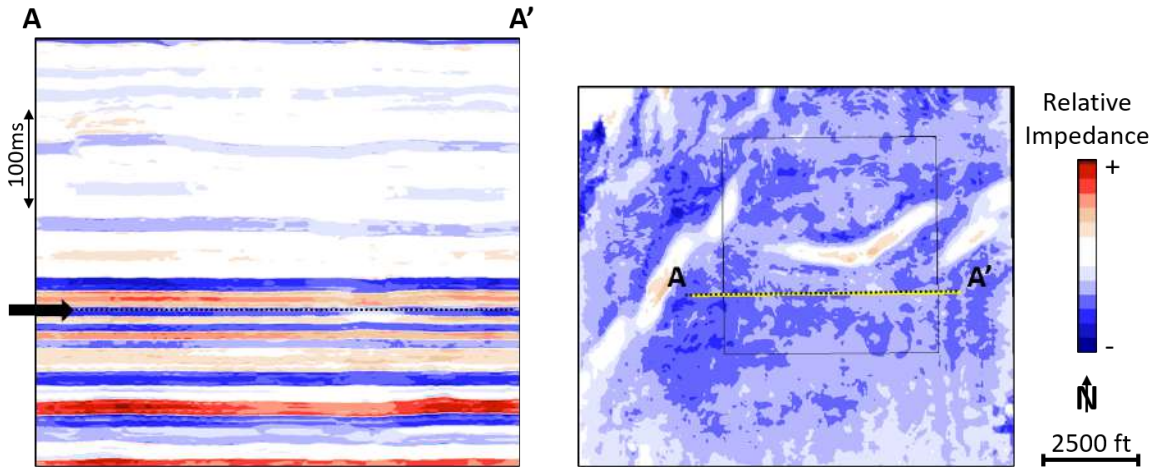
Figure 5.24: Seismic line A-A' flattened on the Top Niobrara and the Graneros (left).The black dotted line and black arrow indicate the interval the stratal slice (b) is extracted from. This stratal slice is representative of the C chalk.
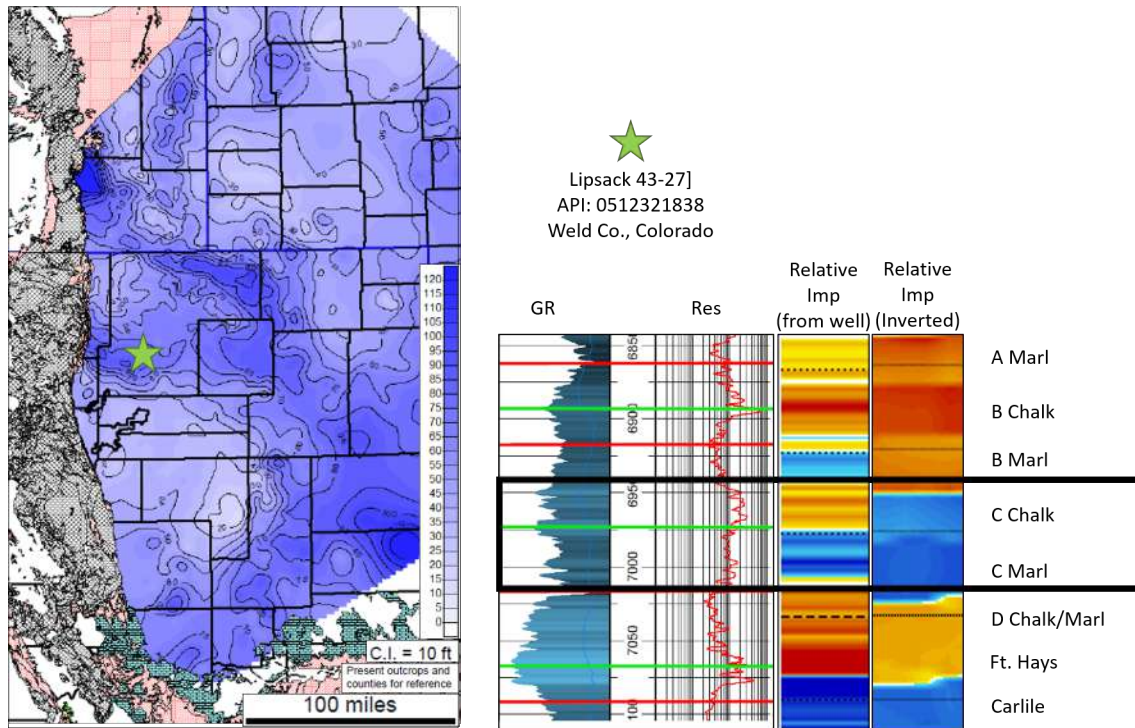
Figure 5.25: Isochron map of the C chalk (left). The green star is the Pioneer reference well location. Gamma ray and resistivity from the Pioneer reference well interpreted with the relative impedance from the Wishbone section and the inverted relative impedance from the seismic (right) (Modified from Drake and Hawkins, 2012).

135
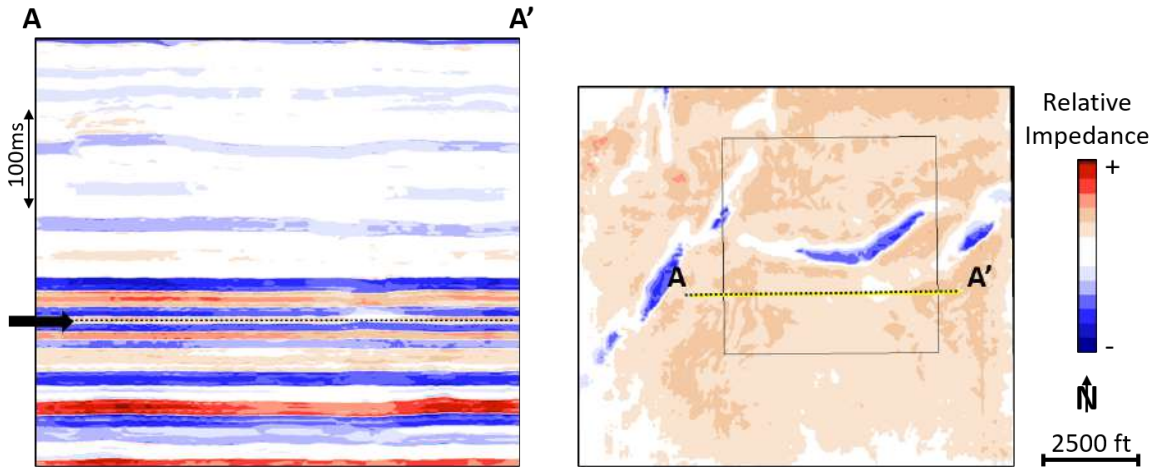
Figure 5.26: Seismic line A-A' flattened on the Top Niobrara and the Graneros (left).The black dotted line and black arrow indicate the interval the stratal slice (b) is extracted from. This stratal slice is representative of the D interval.
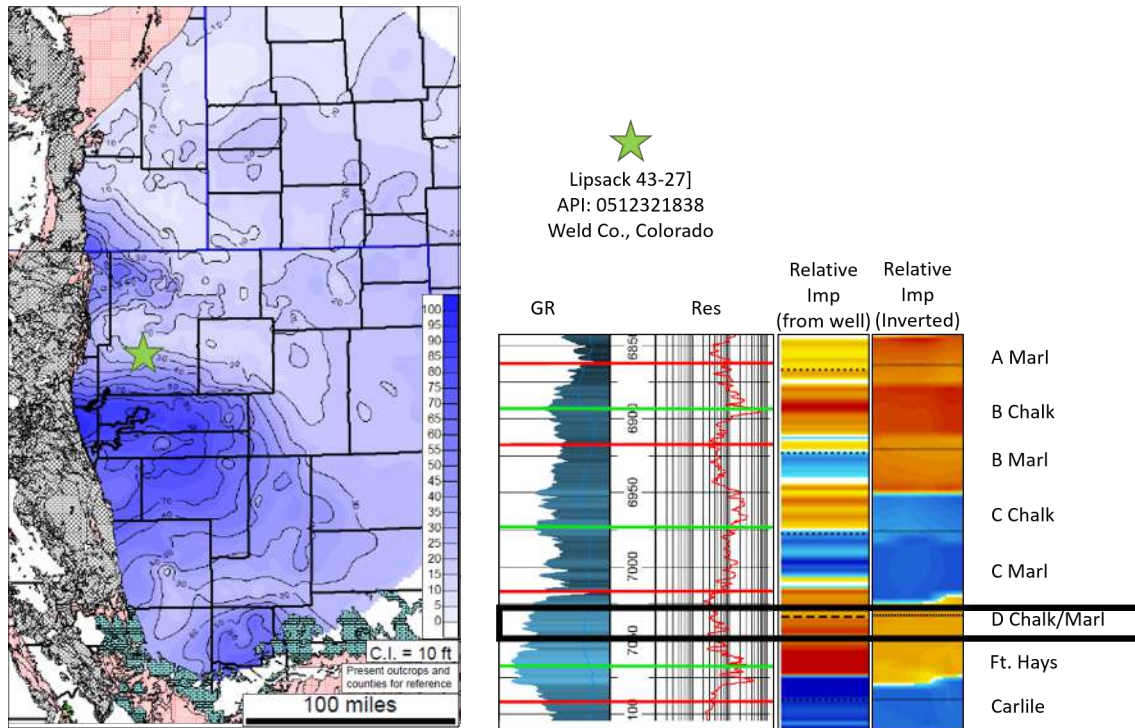
Figure 5.27: Isochron map of the D interval (left). The green star is the Pioneer reference well location. Gamma ray and resistivity from the Pioneer reference well interpreted with the relative impedance from the Wishbone section and the inverted relative impedance from the seismic (right) (Modified from Drake and Hawkins, 2012).

136
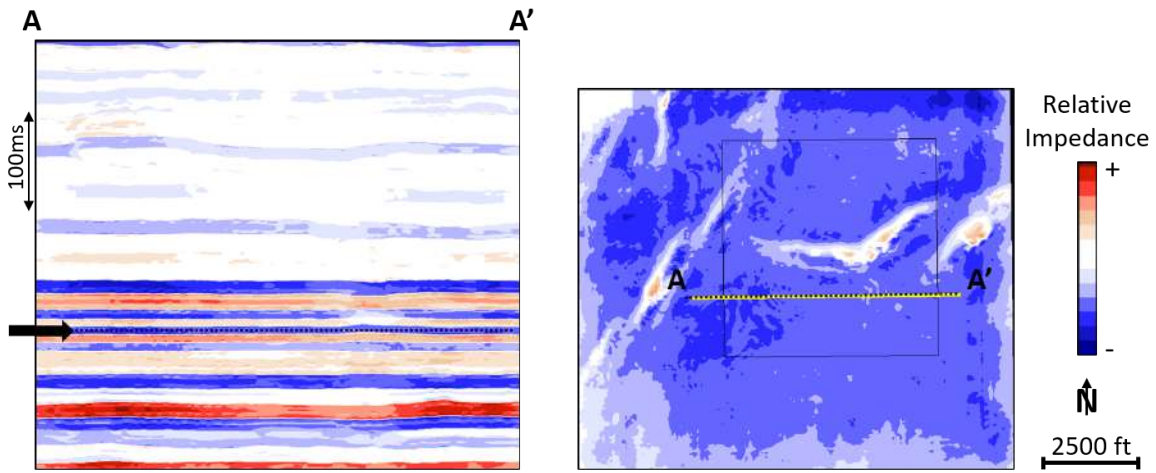
Figure 5.28: Seismic line A-A' flattened on the Top Niobrara and the Graneros (left).The black dotted line and black arrow indicate the interval the stratal slice (b) is extracted from. This stratal slice is representative of the Codell formation.
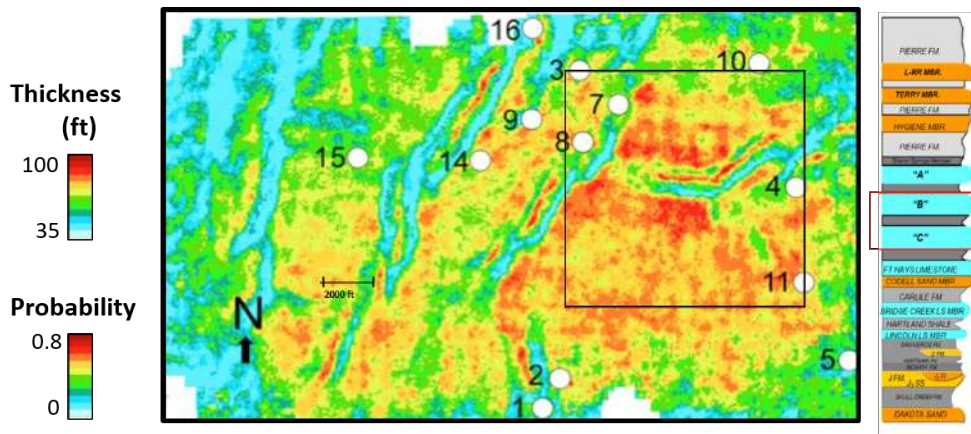
Figure 5.29: Extraction map of the pure chalk facies probability. RMS amplitude of the pure chalk facies probability from the Top Niobrara horizon to 20ms below, including the B and C chalk benches. The outlined box displays the location of the Wishbone section (Modified from Harryandi, 2017).

137

5.3 Dynamic Conditions - Wattenberg Production

Previous work in the Wishbone section has theorized that the reservoir is experiencing the most change in the Western portion of the section. Figure 5.30 displays the simulated gas saturation (a) and the 2D microseismic events (b). Here it is observed that the heavier microseismic activity coincides with the higher modeled gas saturation. In addition to gas saturation and microseismic, there is higher fracture conductivity, a zipper fracture, and more proppant and hydraulic fracture fluid used during completions that are correlated to higher producing wells to the West. But, through the analysis recently conducted, this theory is refined.

The Turkey Shoot survey contains a Baseline survey that was acquired after the wells in the Wishbone section were drilled, and a Monitor 2 survey that was acquired after two years of production. To gain an understanding of how the reservoir is changing after two years of production, the inversion was preformed in a time-lapse sense. Stacks with an angle range of $30 - 40°$s from the Baseline and Monitor 2 surveys were utilized for a pseudo AVO analysis (as we expect the greatest changes around this angle range). The gather conditioning and cross-equalization of these data was performed by Copley (2018). Preconditioning included trim-statics and division into the angle stacks. The cross-equalization process consisted of global amplitude scaling, frequency shaping filtering, global phase-time shifts, trace-by-trace amplitude scaling and trace-by-trace phase-time shifts. NRMS was calculated within the overburden and within the reservoir and for an angle range $30 - 40°$s this value was 0.149 in the overburden and 0.151 within the reservoir. The goal is to minimize this value in the overburden to below 0.3 (as a value of 0.3 would indicate that the seismic in the Monitor 2 survey was reproduced within 30% of the seismic in the Baseline survey). The NRMS values calculated for these surveys show the Monitor 2 survey was reproduced within 15% of the seismic in the Baseline survey. Minimizing NRMS in the overburden ideally maximizes real changes within the reservoir (Copley, 2018).

As the inversion outputs relative acoustic impedance, the extraction of absolute changes within the reservoir is not possible. The extraction of the relative changes is more appropriate. A difference volume was created by subtracting the Baseline relative impedance volume from the Monitor 2 relative impedance volume. In Figure 5.31a, I extracted the root-mean-square (RMS) values from the Top Niobrara to the Greenhorn Lincoln Limestone formation to observe relative changes within the entire reservoir. In Figure 5.31b I smoothed the RMS surface to observe general trends.

The theory behind doing a time-lapse analysis of the inversion is to identify which portions of the reservoir have been effectively drained. Figure 5.32 displays the RMS surface with the horizontal wells color coded according to how well they produce (green = best producer, yellow = moderate producer, red = poor producer), below is the relative well placement in cross-sectional view. The largest changes observed from the inversion are the western portion of the survey and north of the central graben. Although it is difficult to discern, it is observed that the best producers do correlate with the largest changes from Baseline to Monitor 2.

In Figure 5.33, I have overlain the microseismic events on the RMS surface. In general, there are significantly more events in the north-west portion of this section. Those events align with the larger differences observed on the RMS surface, potentially indicating that the rock that has been affected by hydraulic fracturing (i.e. the microseismic events) has produced more adequately. When I overlay the hydraulic fracture conductivity established from the 3D hydraulic fracture modeling (Alfataierge, 2017), it appears that the larger relative impedance changes correlate to the more effectively stimulated intervals. The effective fracture length corresponds to the changes within the reservoir. The larger hydraulic fracture conductivity values are color-coded purple. The areas with the highest hydraulic fracture conductivity are primarily North of the central graben and secondarily in the West.

In Figure 5.35 the lithology that the horizontal wells have intersected are overlain on the RMS surface. When analyzing the lithology with the reservoir changes, it is observed

that the larger 4-D seismic changes generally coincide in locations where the wells intersect the chalky intervals. It is also observed that there are larger changes to the reservoir on the western portion of the survey and north of the central graben. These larger changes correlate to areas where the reservoir was effectively stimulated and where the wells landed within chalky intervals. Figure 5.36 displays the 4-D seismic changes with both the intersecting lithologies and the microseismic events. The larger 4-D changes are observed in the areas with heavier microseismic activity and chalky lithologies.

Figure 5.37 compares the relative impedance changes from ThinMan with a previous inversion performed in HampsonRussell. The previous inversion contributed to the theory that the reservoir is being effectively drained in the West. Overall, these results exhibit the same changes within the reservoir. The main difference is that the older inversion displays reservoir changes south of the central graben, whereas the ThinMan results do not.

Figure 5.38 shows the updated 4-D inversion from HampsonRussell of $\lambda\rho$ (bottom) and the relative impedance changes from ThinMan (top). The updated HampsonRussell inversion shows the largest 4-D changes in the North-West corner of the Wishbone section. The area with the highest change is outlined with a dotted black line and overlain on the relative impedance changes from ThinMan. Both inversions agree that the largest changes to the reservoir are observed in the North-West. Both updated inversions, microseismic, lithology and fracture conductivity all agree that the largest changes to the entire reservoir are observed in the North-West portion of the Wishbone section. The wells within this area are spaced closer together contain a zipper fracture and were treated with more hydraulic fracture fluid and proppant. This integrated analysis refines the initial theory of where the reservoir is experiencing the most change and where it is effectively producing from. From this analysis, I believe the largest changes are experienced in the North-Western portion of the Wishbone section.

One of the benefits of the ThinMan inversion is that the results have higher vertical resolution than conventional inversions. To observe the changes to each chalk bench in the

140

Niobrara and the Codell Formation, RMS values from smaller intervals were extracted from the difference volume (Figures 5.39-5.43). The red dotted line overlain on the wells within each map indicate which wells intersect the interval extracted from. The warm colors on the map are the areas with the highest relative changes and the seismic section on the left shows the well tops on the left and the seismic horizons on the right. The yellow horizontal lines overlain on the seismic section indicate what interval the RMS slices was calculated from. Figure 5.39 is the RMS map from the Sharon Springs to the top Niobrara reflector. The well farthest to the West intersects the B chalk that is included within this extraction. This slices shows the largest changes to the reservoir on the Western portion of the Wishbone section. Figure 5.40 shows the RMS map from the top Niobrara to the middle Niobrara reflector that includes the B and C chalks. This interval includes all 7 Niobrara wells that have tighter spacing to the West (600 ft) and sparer to the East (900-1200 ft). The 4-D seismic response observes changes all across the Wishbone section. Figure 5.41 is extracted from the bottom Niobrara to the Codell reflector and includes all four Codell wells. The largest changes to the reservoir are observed to the North-West where the Codell wells are present. Figure 5.42 displays the 4-D seismic response from the Sharon Springs to the Codell. Similar to the interval containing all 7 Niobrara wells, the 4-D response is observed throughout the entirety of the section, although there is a high concentration of large changes in the North-West. To include all changes, Figure 5.43 was extracted from the Sharon Springs to the Greenhorn Lincoln Limestone interval (like Figure 5.31). As we previously saw, the largest overall change to the reservoir is observed in the North-West. When extracting over the largest interval (Figure 5.43, Sharron Springs to Greenhorn Lincoln Lime) the contribution from the Codell wells is entirely incorporated.

a)

b)
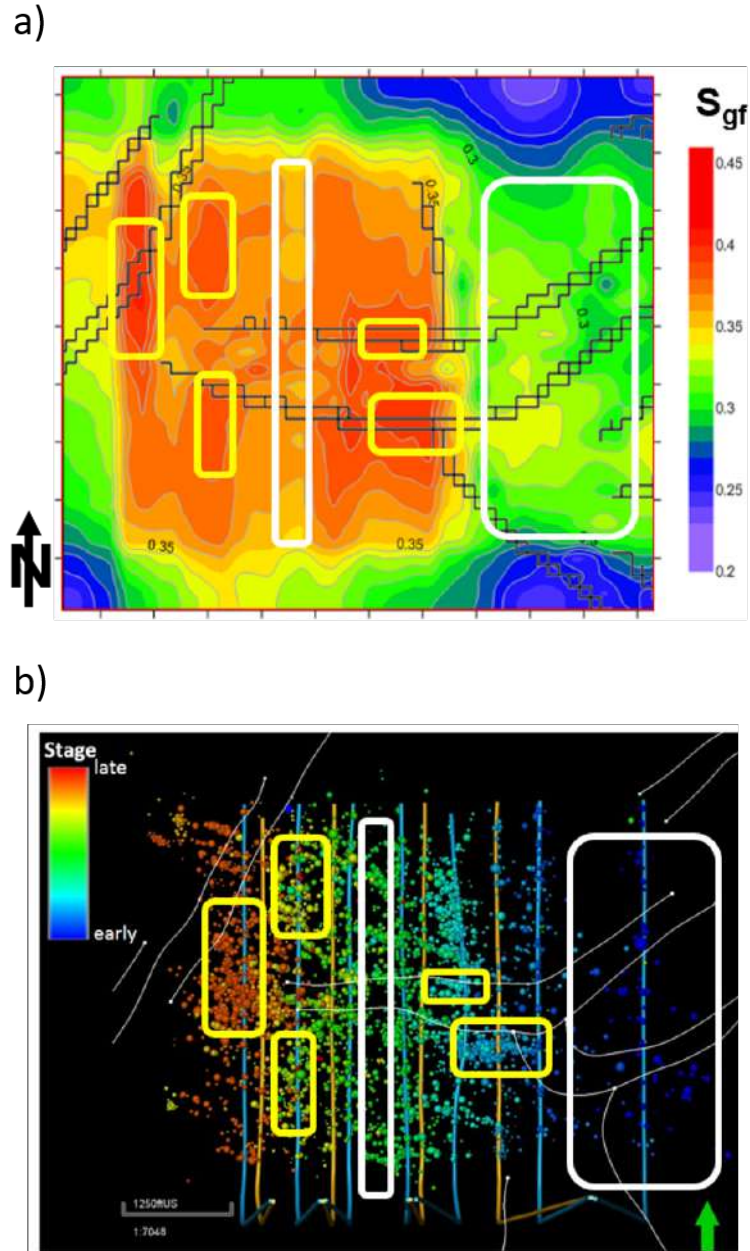
Figure 5.30: Comparison between simulated gas saturation distribution (a) and surface microseismic events (b). Higher gas saturation (yellow rectangles) correlates with microseismic clusters (Modified from Ning, 2017).
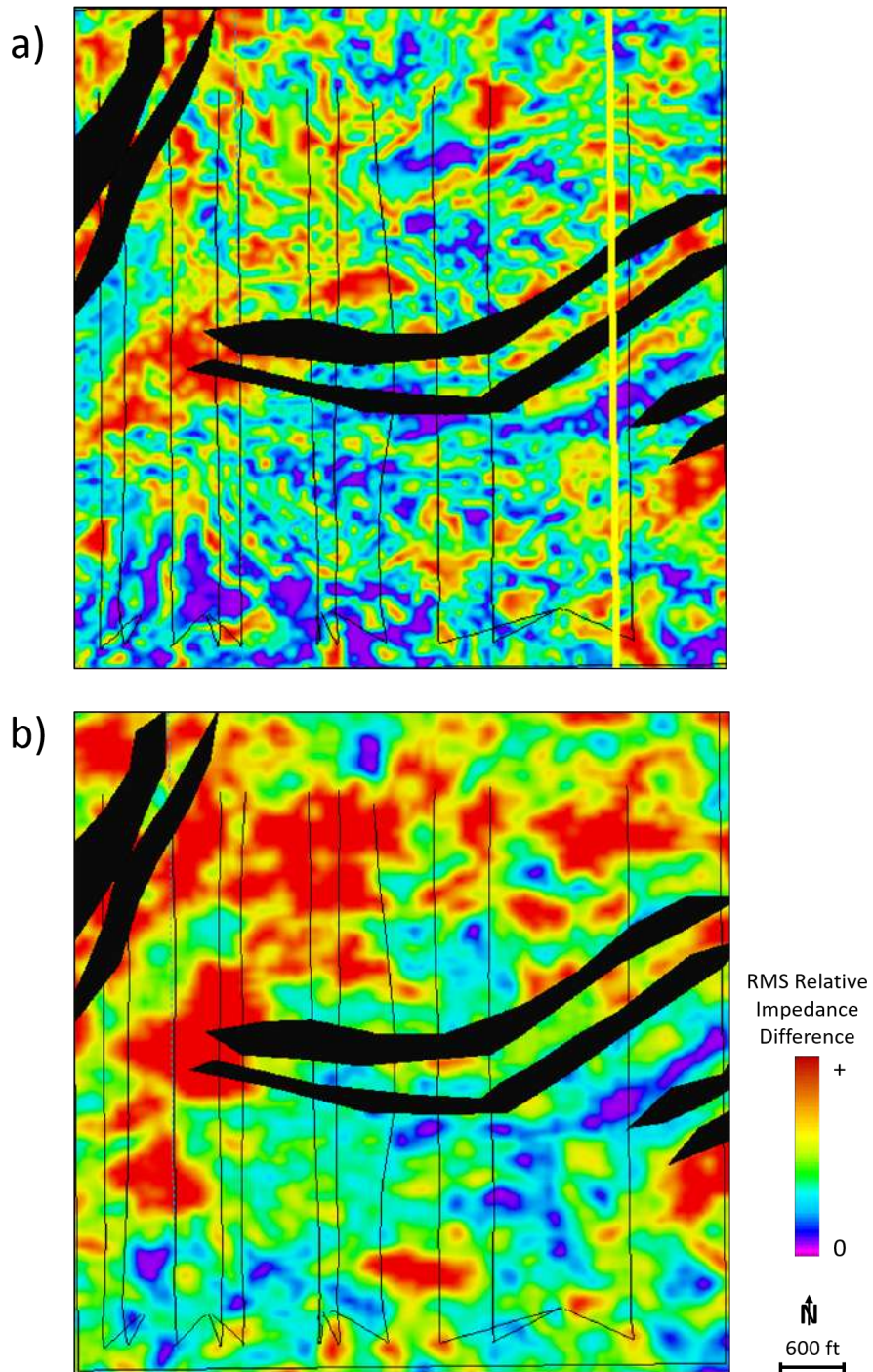
Figure 5.31: Extracted root-mean-square (RMS) values from the Top Niobrara to the Green-horn Lincoln Limestone formation to observe relative changes within the reservoir (a). Smoothed surface (b). The 11 horizontal wells are shown with the black lines trending North-South.

143
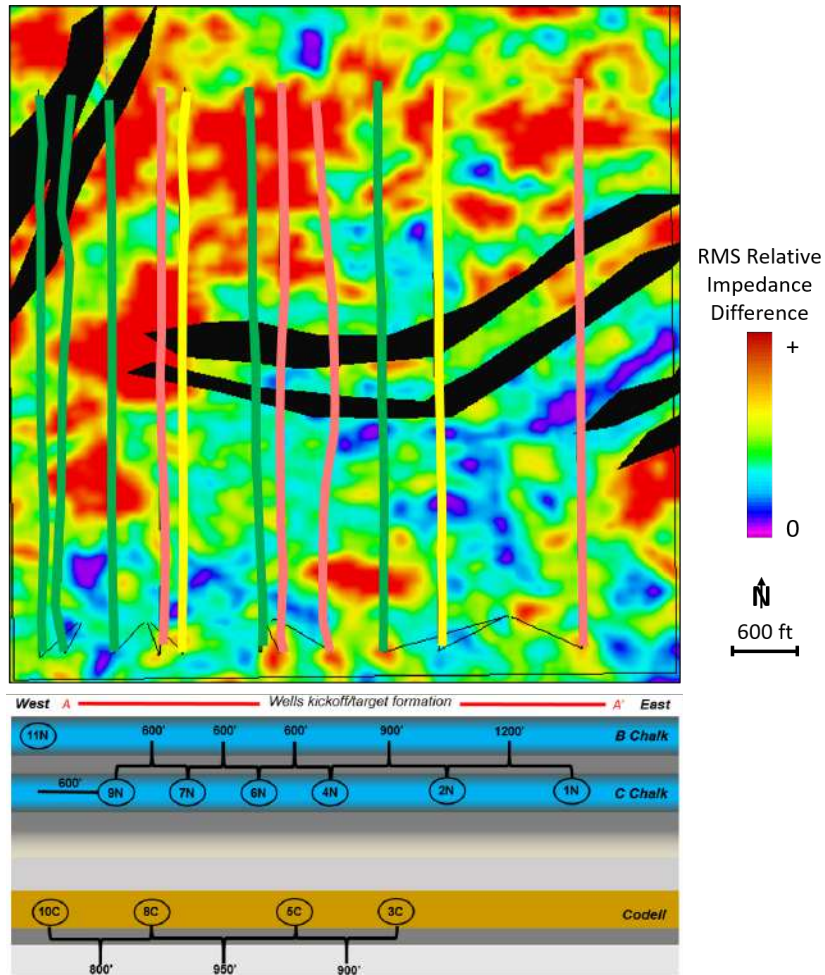
Figure 5.32: Smoothed RMS surface (top). Cross section schematic displaying the general location in depth of the horizontal wells. The horizontal wells are overlain on the RMS surface colored green = good producer, yellow = moderate producer, red = poor producer.
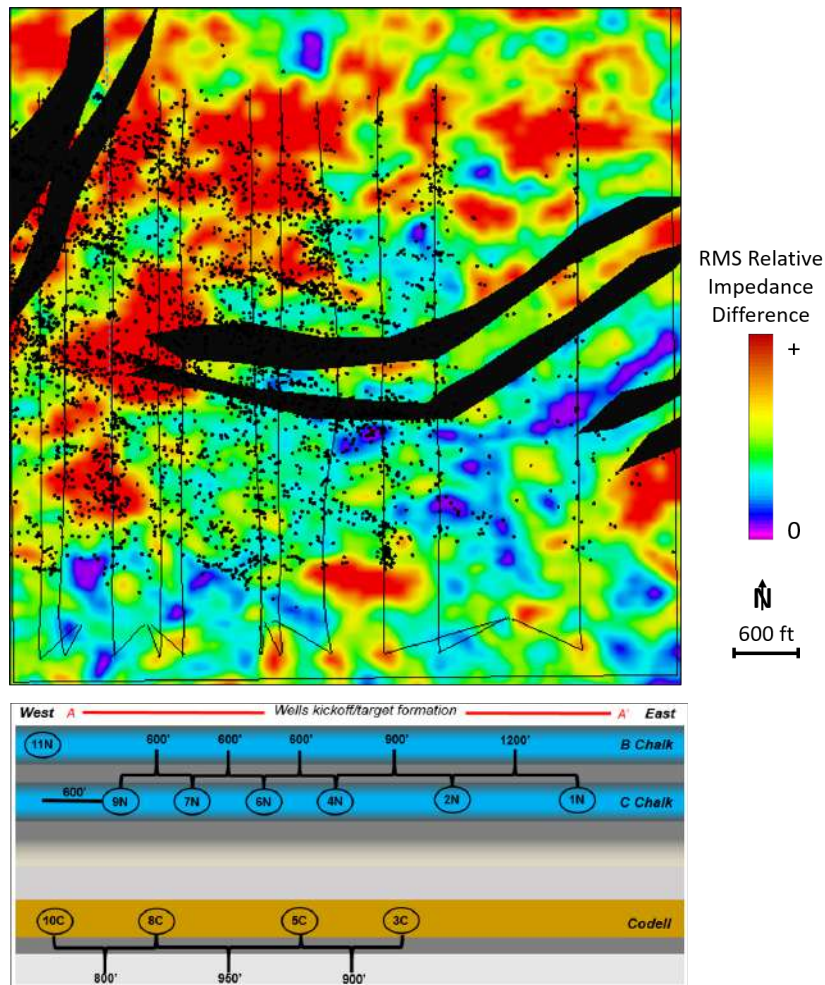
Figure 5.33: Smoothed RMS surface (top). Cross section schematic displaying the general location in depth of the horizontal wells. The horizontal wells are overlain on the RMS surface are the microseismic events. The trend in the microseismic events correlate with the larger changes observed on the time-lapse seismic.
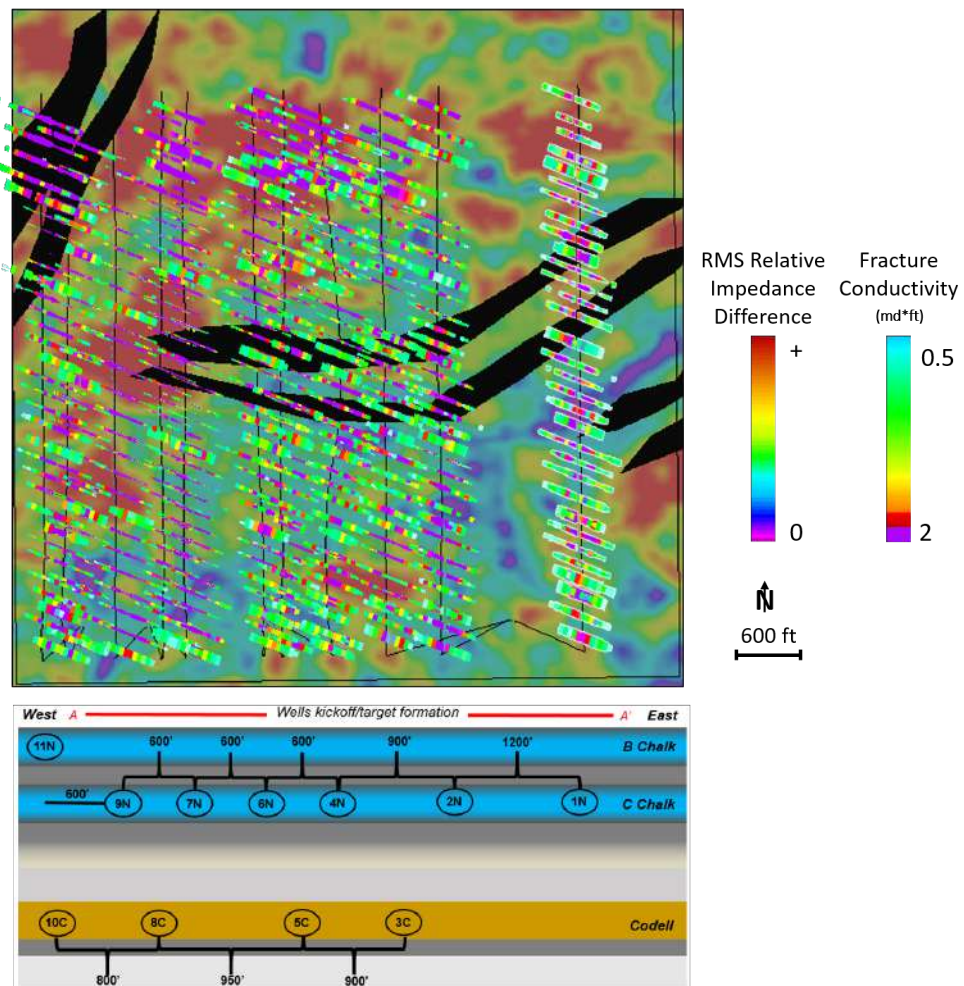
Figure 5.34: Smoothed RMS surface (top). Cross section schematic displaying the general location in depth of the horizontal wells. The hydraulic fracture conductivity is overlain on the RMS surface. There is a strong correlation with high fracture conductivity and the larger changes observed on the time-lapse seismic.
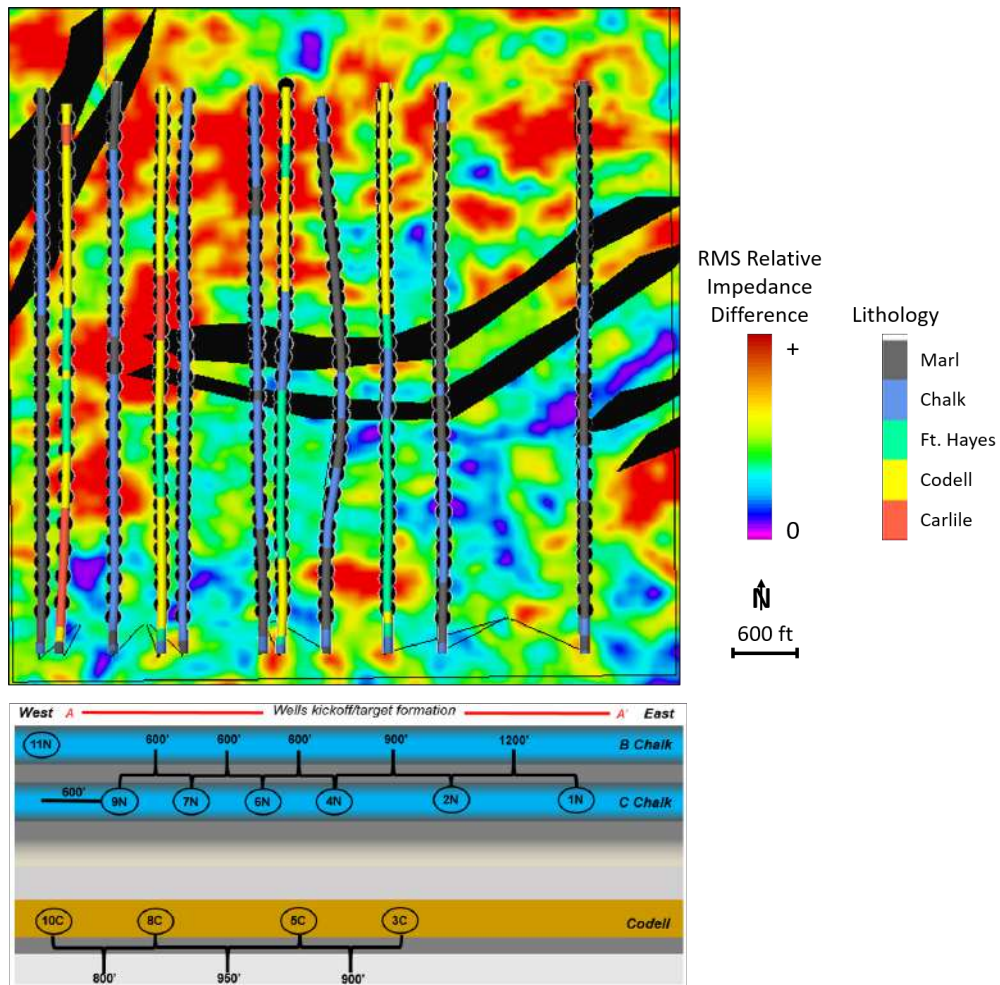
Figure 5.35: Smoothed RMS surface (top). Cross section schematic displaying the general location in depth of the horizontal wells. The lithologies that the horizontal wells intersect are overlain on the RMS surface. The areas where the wells intersect the chalk benches correlate to the larger changes observed on the time-lapse seismic.
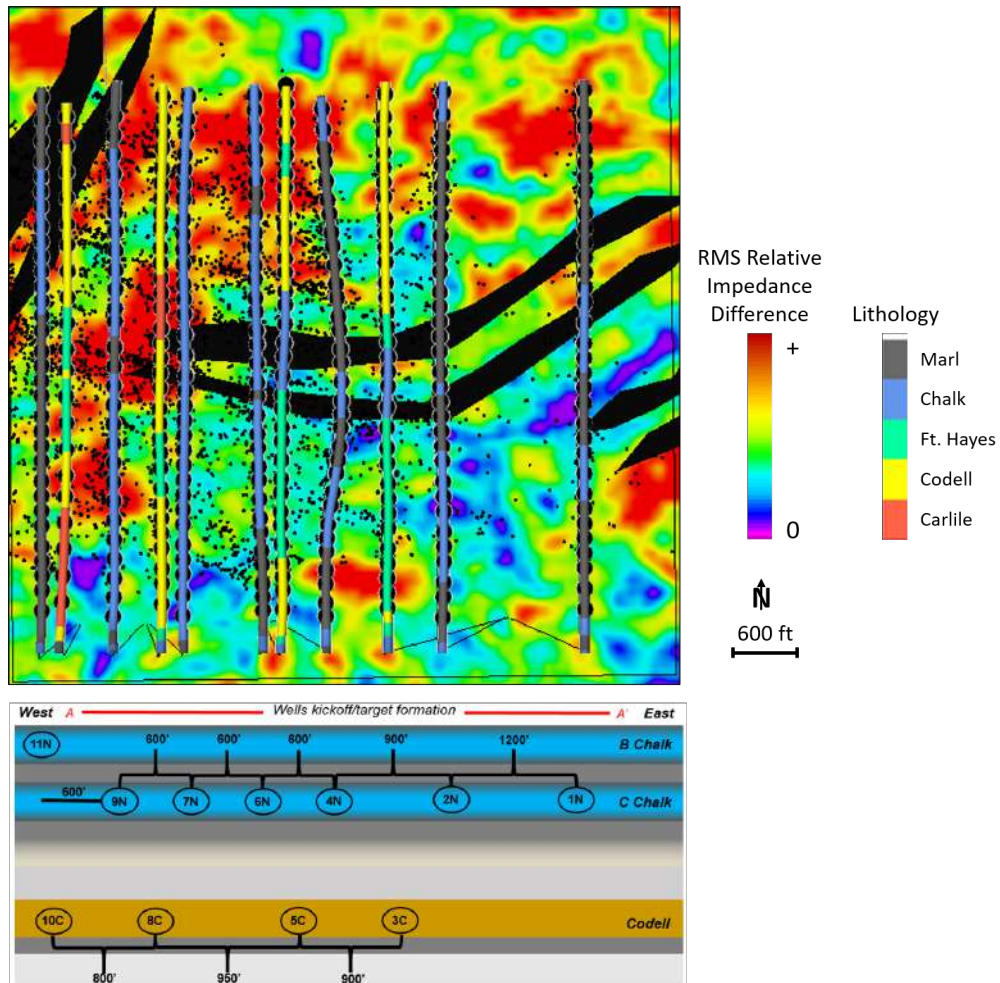
Figure 5.36: Smoothed RMS surface (top). Cross section schematic displaying the general location in depth of the horizontal wells. The lithologies that the horizontal wells intersect are overlain on the RMS surface and the microseismic evetns. The areas where the wells intersect the chalk benches and have higher microseismic density correlate to the larger changes observed on the time-lapse seismic.
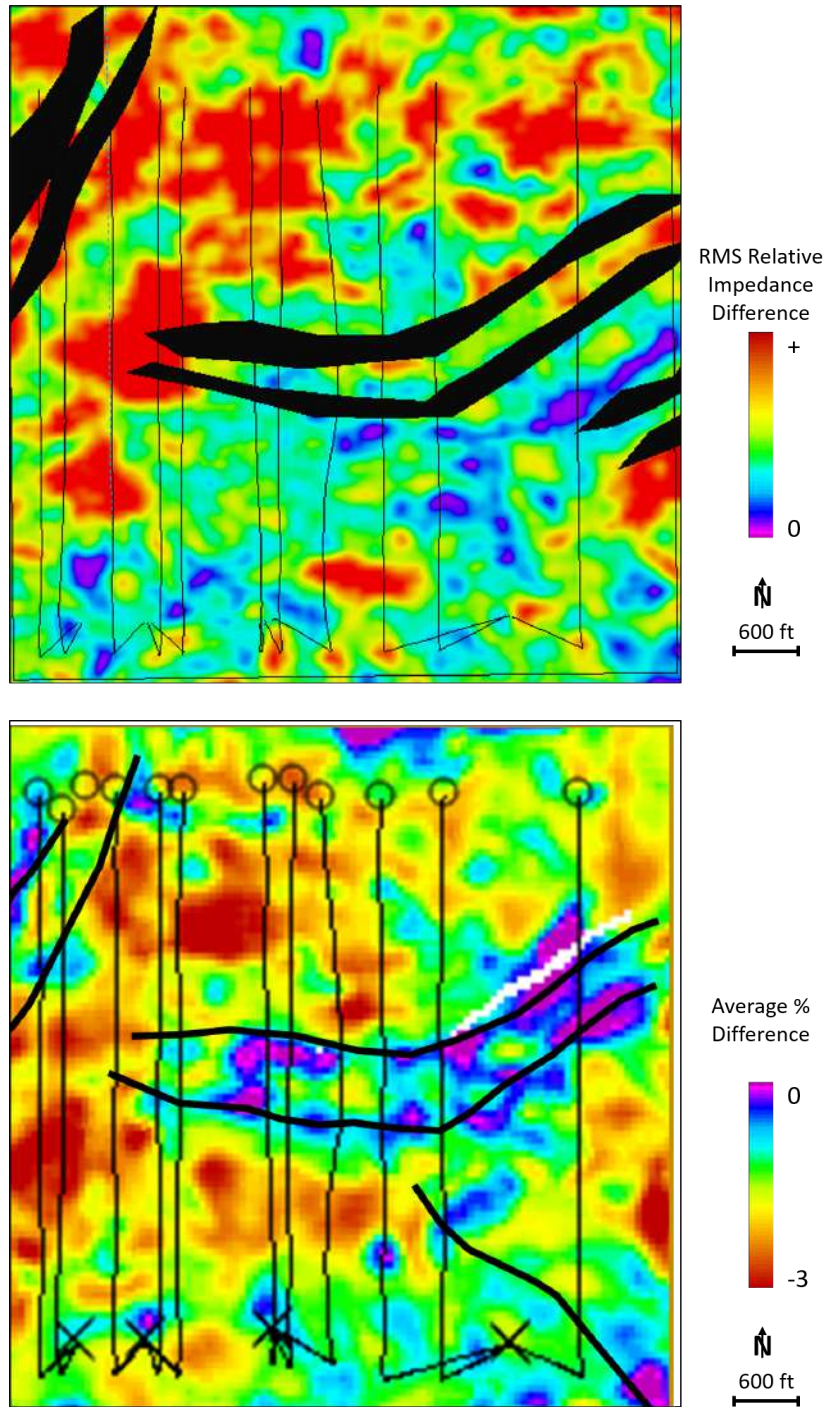
Figure 5.37: Smoothed RMS surface established from the ThinMan inversion (top). Previous time-lapse inversion relating to production showing changes to the reservoir. Both maps are extracted over the same intervals. These inversions show similar trends North of the central graben but contain differences South of the Graben. (Modified from Utley, 2017).

ThinMan Time-Lapse Results
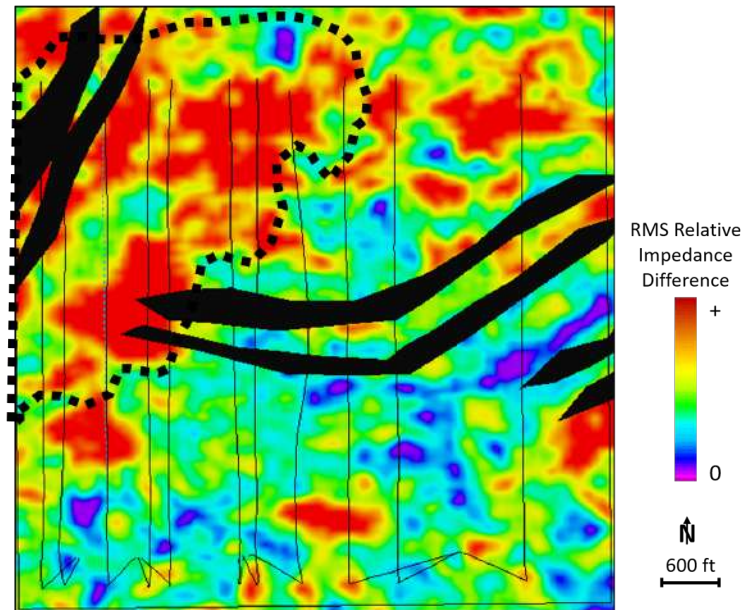
Δλρ Extracted to Niobrara Interval
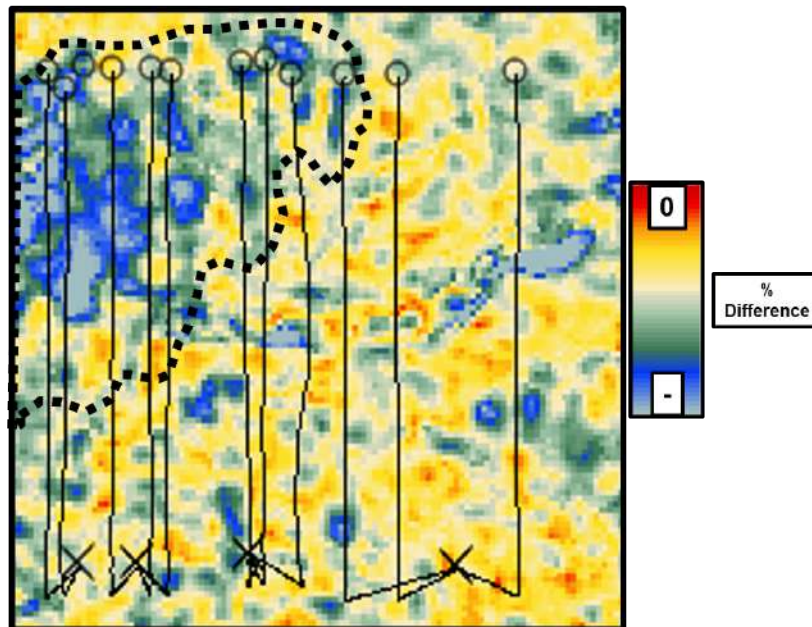
Figure 5.38: Smoothed RMS surface established from the ThinMan inversion (top). Updated time-lapse inversion relating to production showing changes to the reservoir. Different from the previous time-lapse results, both updated time-lapse results show the largest changes to the reservoir within the North-Western portion of the Wishbone section. (Modified from Copley, 2018).
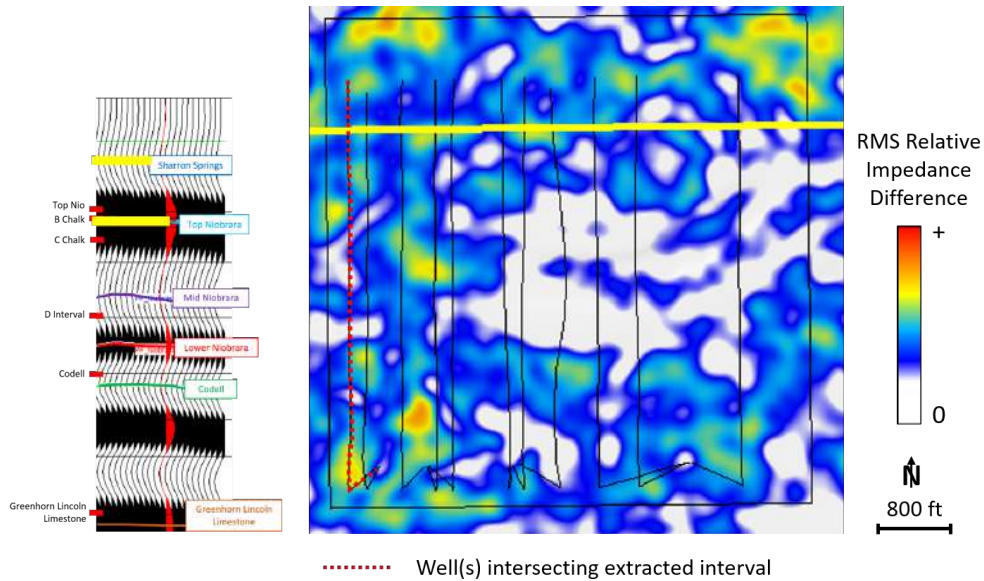
Figure 5.39: Smoothed RMS surface established from the ThinMan inversion extracted from the Sharron Springs interval to the Top Niobrara reflector. This extraction includes the B chalk interval. The red dotted line represents the well that intersects this formation.
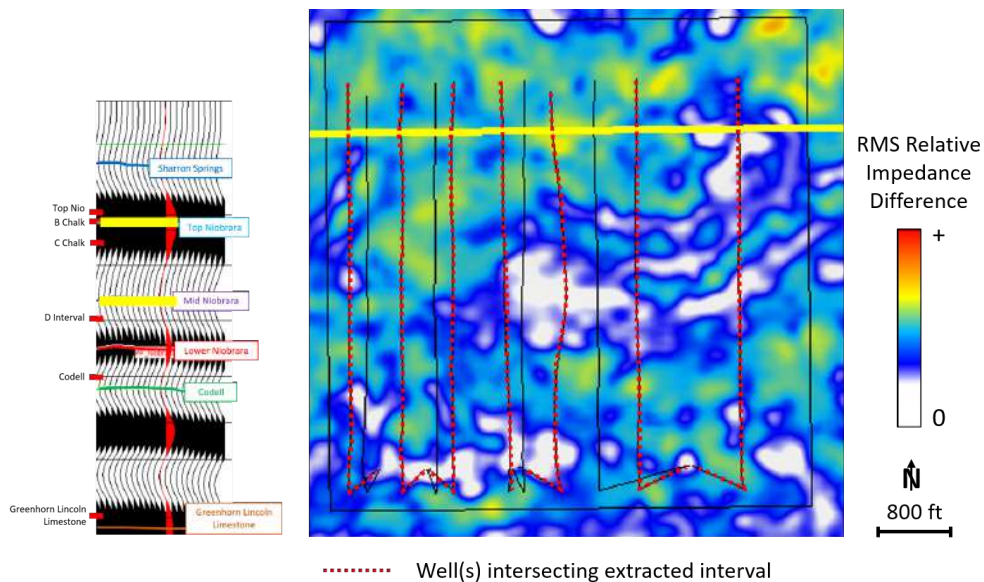
Figure 5.40: Smoothed RMS surface established from the ThinMan inversion extracted from the Top Niobrara reflector to the Middle Niobrara reflector. This extraction includes the B and C chalk intervals. The red dotted lines represent the wells that intersects these formations.
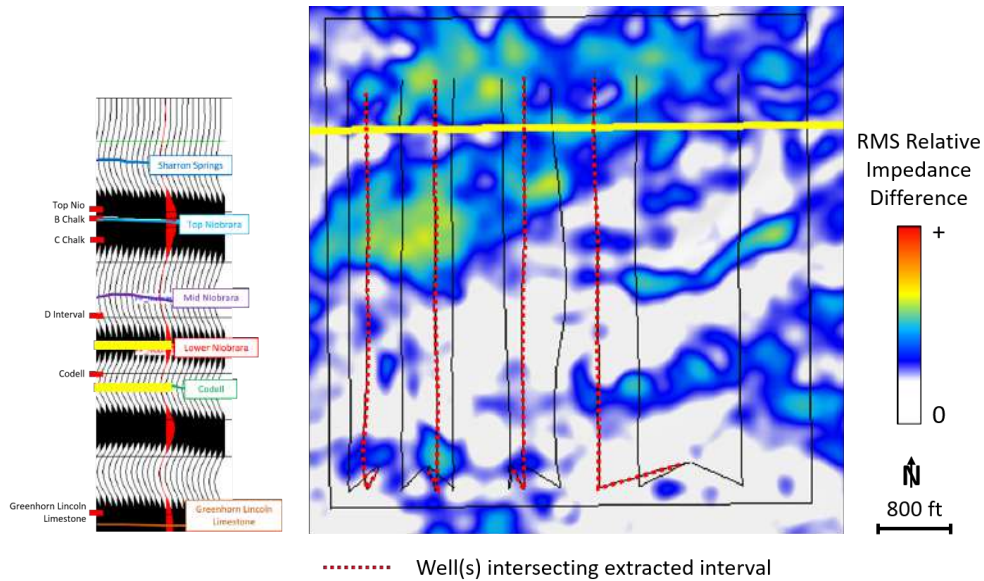
Figure 5.41: Smoothed RMS surface established from the ThinMan inversion extracted from the Lower Niobrara reflector to the Codell reflector. This extraction includes the Codell Formation. The red dotted lines represent the wells that intersects this formation.
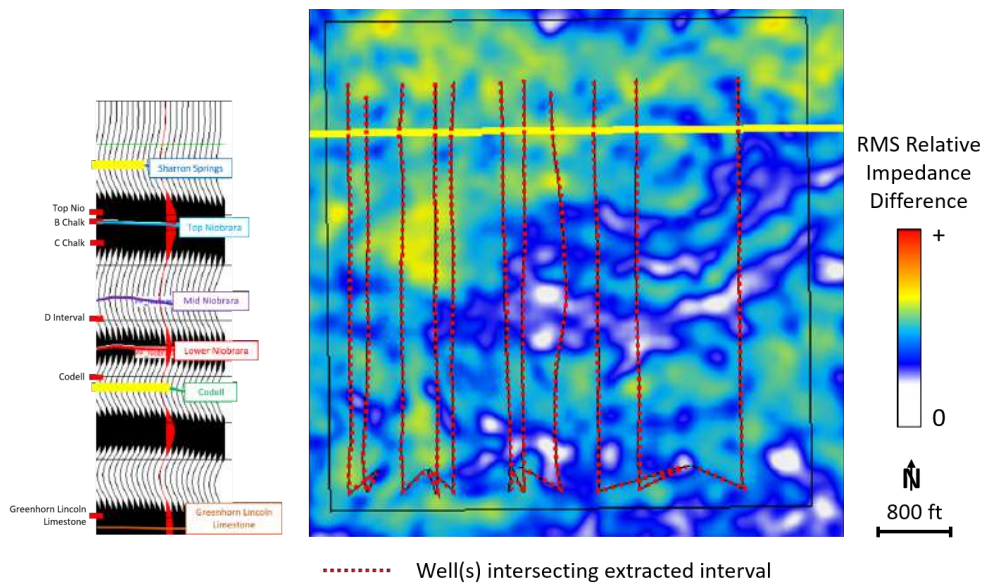
Figure 5.42: Smoothed RMS surface established from the ThinMan inversion extracted from the Sharron Springs reflector to the Codell reflector. This extraction includes the B chalk, C chalk and Codell Formation. The red dotted lines represent the wells that intersects these formations. Note this extraction depth interval includes all 11 horizonal wells.
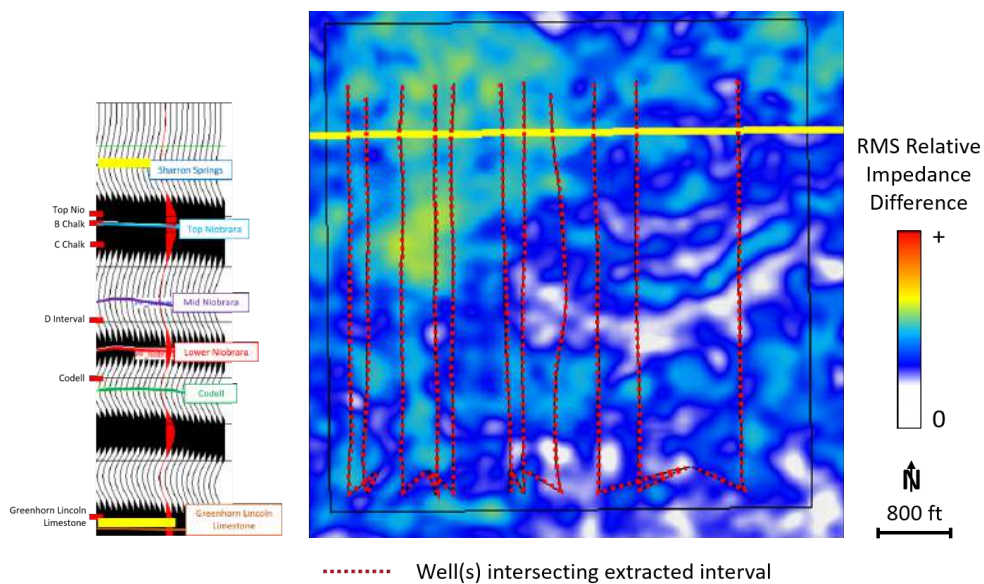
Figure 5.43: Smoothed RMS surface established from the ThinMan inversion extracted from the Sharron Springs reflector to the Greenhorn Lincoln Limestone reflector. This extraction includes the B chalk, C chalk and Codell Formation. The red dotted lines represent the wells that intersects these formations. Note this extraction depth interval includes all 11 horizonal wells.

CHAPTER 6

CONCLUSIONS AND RECOMMENDATIONS

6.1 Horizontal-Receiver Azimuth Estimation

The process that lead to the discovery of the cross-component leakage was viewing of prestack COCA gathers. Analysis of the shear components during processing is usually conducted with LAS and was not recognized during processing. The use of the COCA gathers to recognize the data issue was essential. The cross component leakage was initially identified on the pure shear COCA gathers and it was determined that there was an issue with the horizontal sources and/or receivers. Analysis of the C-wave data confirmed that it was a receiver-side issue, errors in the azimuth orientation of H_1 during data acquisition.

Multicomponent prestack synthetic modeling verified my hypothesis. Critical steps in this analysis were the use of S-wave *and* C-wave prestack COCA gathers, and analyzing COCA gathers in overburden as well as in the Niobrara target interval. Conventionally, multicomponent data is analyzed in LAS during processing. In this case, LAS would not highlight the signal leakage. Sorting the data into COCA gathers was essential and key to the signal leakage identification.

The P-wave first-arrival method was initially used and detected the global H_1 azimuth error for Monitor 1. This global error is attributed to H_1 oriented to magnetic North. The large histogram spread suggested that the local variations in the H_1 estimates were possibly not reliable. As the P-wave first-arrival method does not handle near surface complexities well, the C-wave reflection method was evaluated. Histograms from this method were more refined (the spread of the histogram decreased), and the local variations were deemed trustworthy. The C-wave reflection method can handle near surface complexities and performs well in the presence or absence of anisotropy. Both methods indicated the global orientation of the H_1 azimuths for each survey.

H_1 azimuth estimates obtained from the C-wave reflection method were used to properly rotate the C-wave and S-wave data to radial-transverse coordinates. These data are now better suited for further analysis, and to potentially expose/detect that subtle fracture-related seismic signal produced by the hydraulic fracturing within the Niobrara reservoir interval. Also, with the radial and transverse components rotated incorrectly, preprocessing parameters derived from the radial component (and applied to transverse) will be in error (surface consistent amplitude compensations, surface consistent deconvolution, etc.). These errors impact amplitude work, in addition to shear-wave splitting.

6.2   Horizontal-Receiver Azimuth Estimation Recommendations

I recommend using the P-wave first arrival method for a brute rotation into radial-transverse coordinates early in processing. Once the data has been cleaned and refined, the C-wave reflection method should be used for refinements in the rotation. If the data are going to be used for an assessment of shear wave splitting, these rotations need to be analyzed and quality controlled, since poor rotations may lead to false indicators of shear-wave splitting. When the magnitude of shear-wave splitting delay is small, the C-wave and S-wave crossterm reflection signal is weak. Improper rotation to radial-transverse coordinates may mask this weak signal what we wish to detect, expose, and invert.

6.3   Sparse-Layer Reflectivity Inversion

The conventional method of performing a post stack inversion involves the input of a background P-impedance model. The sparse-layer reflectivity inversion is significantly more robust (as it does not require a a background model), relatively simple to use, while outputting results that are just as good, if not superior to the model-based inversion results. Performing the inversion on the Wattenberg synthetic volume provided confidence in the process as the results have high resolution and do a great job at accurately modeling the subsurface.

For a comparison of ThinMan and Hampson-Russell's post stack inversion (STRATA) both the wedge model and the Wattenberg synthetic were used. When comparing the actual impedance results for the Wattenberg results with the input relative impedance volume, the ThinMan results were preferred. Although the results from the HRS inversion match the data well, this result is very smooth and is lower resolution than the ThinMan results.

To gain confidence in the ThinMan inversion of the field data, a handful of quality control steps were necessary:

- Comparison of the field data results with the Wattenberg synthetic results

- Convolving the output reflection coefficients with 30hz and 50hz Ricker wavelets and performing well ties

- Using the relative impedance values from each well and comparing those with the inverted relative impedance from the field data

Through the quality control process, it was determined that the B and C chalk benches of the Niobrara were resolved. Once confidence was established, the field data results from the Baseline survey (static conditions) were integrated and interpreted within a regional sequence stratigraphic framework to determine if there is a relationship between relative impedance and thickness. The inverted relative impedance volume was flattened on the Top Niobrara and the Graneros for stratal slicing. Stratal slices from the B chalk, C chalk, D interval and Codell were compared with the regional isochron maps. The relative impedance over the B chalk decreases to the south, a similar trend is observed on the isochron map. From the C chalk isochron, it is observed that this interval has a constant thickness over our study area. The relative impedance of this interval also remains relatively constant. From the isochron maps, both the B and C chalk benches are around 30-40ft. The measured thickness of those benches from the inverted relative impedance are also 30-40 ft. The D interval appears to thicken to South of our study area. Its relative impedance decreases in the same direction. It is observed that the relative impedance trends do correspond to the thicknesses from the

isochron maps, although more work is needed to confirm this as a correlation. Overall, it should be noted that the seismic volume covers a total of 4 square miles, so it is difficult to determine lateral variations in geology in such a limited area.

The dynamic inversion results show strong impedance changes in the North-West corner of the Wishbone section. This anomaly correlates to heavy microseismic activity, high hydraulic fracture conductivity established from reservoir modeling and well landing positions relative to chalk benches. The results from the ThinMan inversion are a decent match to the previously established time-lapse seismic response to production. These results match to the North of the central graben, but disagree in the South.

6.4 Thin-Bed Reflectivity Inversion Recommendations

To potentially match the inverted impedance response to reservoir sweet spots, the results from Mabrey's (2016) RQI should overlain on the inversion. If a relation between relative impedance values with high quality rock could be established, more efficient completion designs could be from the seismic. In addition, the inversion should be run on every angle stack. It has been shown that we can resolve the chalk benches, it would be even more powerful if we could determine the AVO response of the sweet spots. To verify the 4-D seismic response and it's correlation to production, the 4-D response at each horizontal well should be extracted and compared to the production from each well. In addition, the work completed by Copley (2018) determined that the largest 4-D changes were observed on the $40 - 50°$ angles. I am recommending to do a similar 4-D ThinMan inversion of this angle range for another pseudo-AVA analysis.

REFERENCES CITED

Alfataierge, A. (2017). *3D Modeling and Characterization of Hydraulic Fracture Efficiency Integrated with 4D/9C Time-lapse Seismic Interpretations in the Niobrara Formation, Wattenberg Field, Denver Basin.* Master's, Colorado School of Mines.

Alford, R. M. (1986). Shear data in the presence of azimuthal anisotropy: Dilley, texas. *SEG Technical Program Expanded Abstracts*, pages 476–479.

Burch, D. N., Calvert, A. S., and Novak, J. M. (2005). Vector fidelity of land multicomponent measurements in the context of the earth sensor system: misconceptions and implications. *SEG Technical Program Expanded Abstracts*, pages 904–907.

Cary, P. W. (2002). Detecting false indications of shear-wave splitting. *SEG Technical Program Expanded Abstracts*, pages 1014–1017.

Chen, G., Matteucci, G., Fahmy, B., and Finn, C. (2008). Spectral-decomposition response to reservoir fluids from a deepwater West Africa reservoir. *Geophysics*, 73(6):C23–C30.

Chen, S. S., Donoho, D. L., and Saunders, M. A. (2001). Atomic Decomposition by Basis Pursuit. *SIAM Review*, 43(1):129–159.

Chopra, S., Castagna, J., and Portniaguine, O. (2006). Seismic resolution and thin-bed reflectivity inversion. *CSEG recorder*, 31(1):19–25.

Chopra, S., Castagna, J., and Xu, Y. (2009). Thin-bed reflectivity inversion and some applications. *First Break*, 27(MAY):55–62.

Chopra, S. and Marfurt, K. J. (2005). Seismic attributes — A historical perspective. *Geophysics*, 70(5):3SO–28SO.

Chopra, S. and Marfurt, K. J. (2008). Emerging and future trends in seismic attributes. *The Leading Edge*, 27(3):298–318.

Cooke, D. A. and Schneider, W. A. (1983). Generalized linear inversion of reflection seismic data. *Geophysics*, 48(6):665–676.

Copley, M. (2018). *Seismic characterization of Niobrara fluid and rock properties: a 4D study and multicomponent (3C) analysis.* PhD thesis, Colorado School of Mines.

DiSiena, J. P., Gaiser, J. E., and Corrigan, D. (1984). Horizontal components and shear wave analysis of three-component VSP data. In Toksoz, M. N. and Stewart, R. R., editors, *Vertical seismic profiles, Part B: Advanced concepts*. Geophysical Press.

Drake, W. R. and Hawkins, S. J. (2012). A Sequence Stratigraphic Framework for the Niobrara Formation in the Denver-Julesburg Basin. *Search and Discovery #50757*, 50757(September):29.

Farfour, M. and Yoon, W. J. (2016). A review on multicomponent seismology: A potential seismic application for reservoir characterization. *Journal of Advanced Research*, 7(3):515–524.

Fryer, G. J. and Frazer, L. N. (1984). Seismic waves i n stratified anisotropic media. (December).

Fryer, G. J. and Frazer, L. N. (1987). Seismic waves in stratified anisotropic media - II. Elastodynamic eigensolutions for some anisotropic systems. *Geophysical Journal of the Royal Astronomical Society*, 91(1):73–101.

Gaiser, J. (2003). Vector fidelity differences between P-wave first breaks and PS-wave reflections: Implications for compensation of full-azimuth data. *SEG Technical Program Expanded Abstracts*, pages 822–825.

Gaiser, J. E. (1999). Applications for vector coordinate systems of 3-D converted-wave data. *The Leading Edge*, 18:1290.

Goupillaud, P. L. (1961). An approach to inverse filtering of near-surface layer effects from seismic records. *Geophysics*, 26(6):754–760.

Gray, D. (2007). Observations of Seismic Anisotropy in Prestack Seismic Data. *SEG 2007 Annual Meeting*, pages 119–123.

Grechishnikova, A. (2017). *Niobrara discrete fracture networks: From outcrop surveys to subsurface reservoir models*. Phd, Colorado School of Mines.

Grossman, J. P. and Couzens, R. (2012). Preserving sensor vector fidelity using automated multicomponent receiver-azimuth detection. (November):46–50.

Harryandi, S. (2017). *Facies Modeling Using 3D Pre-Stack Simultaneous Seismic Inversion and Multi-Attribute Probability Neural Network Transform in the Wattenberg Field, Colorado*. Master's, Colorado School of Mines.

Hettinger, R. D. and Kirschbaum, M. A. (2002). U . S . Department of the interior U . S . Geological survey stratigraphy of the upper Cretaceous Mancos shale (upper part) and Mesaverde group in the southern part of the Uinta and Piceance Basins , Utah and Colorado.

Higley, Debra K and Cox, D. O. (2007). Oil and gas exploration and development along the front range in the Denver Basin of Colorado, Nebraska, and Wyoming. *Petroleum Systems and Assessment of Undiscovered Oil and Gas in the Denver Basin Province, Colorado, Kansas, Nebraska, South Dakota, and Wyoming—USGS Province*, 39.

Kanasewich, E. R. (1981). *Time Sequence Analysis in Geophysics*. University of Alberta Press.

Kennett, B. L. N. (1983). *Seismic wave propagation in stratified elastic media*. Cambridge University Press.

Keys, R. G. and Weglein, A. B. (1983). Generalized linear inversion and the first Born theory for acoustic media. *Journal of Mathematical Physics*, 24(6):1444–1449.

Lindseth, R. O. (1979). Synthetic sonic logs—a process for stratigraphic interpretation. *Geophysics*, 44(1):3–26.

Locklair, R. E. and Sageman, B. B. (2008). Cyclostratigraphy of the Upper Cretaceous Niobrara Formation, Western Interior, U.S.A.: A Coniacian–Santonian orbital timescale. *Earth and Planetary Science Letters*, 269(3-4):540–553.

Mabrey, A. (2016). *Rock quality index for Niobrara horizontal well drilling and completion optimization, Wattenberg field, Colorado*. Master's, Colorado School of Mines.

MacBeth, C., Zeng, X., Yardley, G. S., and Crampin, S. (1994). Interpreting data matrix asymmetry in near-offset, shear-wave VSP data. *Geophysics*, 59(2):176–191.

MacFarlane, T. (2014). *Amplitude inversion of fast and slow converted waves for fracture characterization of the Montney Formation in Pouce Coupe Field, Alberta, Canada*. PhD thesis, Colorado School of Mines.

Nagarajappa, N., Cary, P., and Ursenbach, C. (2013). 3C receiver orientation estimation by stack power optimization of reflected PS data. *SEG Technical Program Expanded Abstracts*, pages 1684–1688.

Ning, Y. (2017). *Interpretation, Production potential of Niobrara and Codell : integrating reservoir simulation with 4D seismic and microseismic*. Phd, Colorado School of Mines.

Omar, S. (2018). *Multicomponent analysis for HTI-Related VVAZ effects*. PhD thesis, Colorado School of Mines.

Partyka, G., Gridley, J., and Lopez, J. (1999). Interpretational applications of spectral decomposition in reservoir characterization. *The Leading Edge*, 18(3):353–360.

Portniaguine, O. and Castagna, J. (2004). Inverse spectral decomposition. In *SEG Technical Program Expanded Abstracts 2004*, pages 1786–1789. Society of Exploration Geophysicists.

Portniaguine, O. and Castagna, J. (2005). Spectral inversion: lessons from modeling and Boonesville case study. In *SEG Technical Program Expanded Abstracts 2005*, pages 1638–1641. Society of Exploration Geophysicists.

Puryear, C. I. and Castagna, J. P. (2008). Layer-thickness determination and stratigraphic interpretation using spectral inversion: Theory and application. *Geophysics*, 73(2):R37–R48.

Riazi, N. and Clarkson, C. (2017). The Use of Time-Lapse Seismic Attributes for Characterizing Hydraulic Fractures in a Tight Siltstone Reservoir. In *Proceedings of the 5th Unconventional Resources Technology Conference*, Tulsa, OK, USA. American Association of Petroleum Geologists.

Robinson, E. (1978). Dynamic predictive deconvolution. *Geophysical Prospecting*, 23:780–798.

Russell, B. and Hampson, D. (1991). Comparison of poststack seismic inversion methods. In *SEG Technical Program Expanded Abstracts 1991*, pages 876–878. Society of Exploration Geophysicists.

Simmons, J. and Backus, M. (2001a). Shear waves from 3-D–9-C seismic reflection data. *The Leading Edge*, 20(6):604–612.

Simmons, J. and Backus, M. (2001b). Shear waves from 3-D–9-C seismic reflection data. *The Leading Edge*, 20(6):604–612.

Simmons, J. L. (2009). Converted-wave splitting estimation and compensation. *Geophysics*, 74(1):D37–D48.

Simmons, J. L. and Backus, M. M. (1994). AVO modeling and the locally converted shear wave. *Geophysics*, 59(8):1237–1248.

Simmons, J. L. and Backus, M. M. (1996). A matched-filter approach to impedance estimation. *Geophysics*, 61(2):484–495.

Sinha, S., Routh, P. S., Anno, P. D., and Castagna, J. P. (2005). Spectral decomposition of seismic data with continuous-wavelet transform. *Geophysics*, 70(6):P19–P25.

Smith, K. H. (2015). Codell Sandstone , DJ Basin *. 10760:1–18.

Sonnenberg, S. A. (2013). New reserves in an old field, the Niobrara resource play in the Wattenberg Field, Denver Basin, Colorado. *URTeC*, 1562913(December):1–13.

Tarantola, A. (2005). *Inverse problem theory and methods for model parameter estimation.* siam.

Tatham, R. and McCormack, M. (1991). *Multicomponent seismology in petroleum exploration.*

Todd, C. (2018). *No Title.* PhD thesis, Colorado School of Mines.

Turin, G. (1957). On the estimation in the presence of noise of the impulse response of a random, linear filter. *IEEE Transactions on Information Theory*, 3(1):5–10.

Utley, J. W. (2017). *Time-lapse PP Seismic to Characterize Stimulation and Production Behavior in the Niobrara and Codell Reservoirs Wattenberg Field, Colorado, US.* Master's, Colorado School of Mines.

White, M. (2015). *Time-lapse interpretation of P-wave data for a hydraulically fractured reservoir, Wattenberg Field, Colorado.* PhD thesis, Colorado School of Mines.

Widess, M. B. (1973). How thin is a thin bed? *Geophysics*, 38(6):1176–1180.

Yilmaz, Ö. (2001). *Seismic Data Analysis.* Society of Exploration Geophysicists.

Zeng, H. (2018). What is seismic sedimentology? A tutorial. *Interpretation*, 6(2):SD1–SD12.

Zeng, H., Backus, M. M., Barrow, K. T., and Tyler, N. (1998a). Stratal slicing, Part I: Realistic 3-D seismic model. *Geophysics*, 63(2):502.

Zeng, H., Henry, S. C., and Riola, J. P. (1998b). Stratal slicing, Part II: Real 3-D seismic data. *Geophysics*, 63(2):514–522.

Zeng, X. and McMechan, G. A. (2006). Two methods for determining geophone orientations from VSP data. *Geophysics*, 71(4):V87–V97.

Zhang, R. and Castagna, J. (2011). Seismic sparse-layer reflectivity inversion using basis pursuit decomposition. *Geophysics*, 76(6):R147–R158.